

UNIVERSITÀ DEGLI STUDI DI PERUGIA

XXXIV CICLO DEL DOTTORATO DI RICERCA IN SCIENZA E TECNOLOGIA PER LA  
FISICA E LA GEOLOGIA



---

**Development of the external tracker of the  
FOOT experiment.**

---

*Studente:*

Gianluigi SILVESTRE

*Relatore:*

Leonello SERVOLI

A.A. 2018/2021



*"Really, you should always discuss the defeats because you can learn much more from failure than from success."*

—Niki Lauda



## **Ringraziamenti**

Un ringraziamento a tutte le persone che mi hanno seguito e aiutato durante tutto il percorso che ha portato a questa tesi, ma soprattutto a chi ha sempre sopportato le mie innumerevoli lamentele rimanendo comunque al mio fianco.



---

## Contents

---

<b>Introduction</b>	<b>V</b>
<b>1 Tumour treatments and Charged Particle Therapy</b>	<b>1</b>
1.1 Commonly used therapies . . . . .	3
1.1.1 Surgical treatment . . . . .	3
1.1.2 Chemotherapy . . . . .	3
1.1.3 Radiotherapy . . . . .	5
1.1.4 Other types of therapy . . . . .	8
1.2 Charged Particle Therapy . . . . .	9
1.3 Interactions of charged particles with matter . . . . .	10
1.3.1 The Bethe-Bloch formula . . . . .	12
1.3.2 Range of particles and the Bragg peak . . . . .	14
1.4 Nuclear interactions and nuclear fragmentation . . . . .	16
1.5 Biological effects of charged particles . . . . .	20
1.6 Fundamental Radiobiology principles . . . . .	21
1.6.1 Fundamental Quantities and Units . . . . .	22
1.7 Advantages of Charged Particle Therapy . . . . .	27
<b>2 The FragmentatiOn Of Target experiment</b>	<b>31</b>
2.1 Goals and motivations of the experiment . . . . .	32

2.2	The inverse kinematics approach . . . . .	32
2.2.1	Double differential cross-sections . . . . .	35
2.3	Experimental setups . . . . .	37
2.3.1	Electronic detector setup . . . . .	38
2.3.2	Emulsion spectrometer . . . . .	52
2.4	Expected performances . . . . .	56
<b>3</b>	<b>Silicon position detectors</b>	<b>61</b>
3.1	Short introduction to track detectors . . . . .	61
3.2	Charged particle signals in thin detectors . . . . .	62
3.2.1	Energy loss in thin silicon layers . . . . .	62
3.3	Interaction of photons with silicon detectors . . . . .	65
3.4	Current technology: silicon detectors . . . . .	68
3.4.1	Signal generation in a microstrip detector . . . . .	72
<b>4</b>	<b>The FOOT Micro Strip Detector</b>	<b>79</b>
4.1	The first prototype PE001 . . . . .	81
4.1.1	Assembly procedure . . . . .	81
4.1.2	Data Acquisition system for the first prototype . . . . .	84
4.1.3	Noise performance of the detector . . . . .	85
4.1.4	Characterization with cosmic muons data . . . . .	94
4.1.5	Signal dependence on DAQ parameters . . . . .	102
4.2	Characterization of the detector with photon sources . . . . .	105
4.2.1	Energy calibration with a radioactive photon source . . . . .	105
4.2.2	Characterization of the detector with an infrared laser . . . . .	111
4.3	The new DAQ system for the FOOT MSD . . . . .	112
4.3.1	CAEN A7585DU Silicon Power Supply . . . . .	117
4.4	Construction and testing of the complete MSD subsystem . . . . .	119
<b>5</b>	<b>Detector response to charged particles at the accelerators</b>	<b>123</b>
5.1	Experimental setups . . . . .	124
5.1.1	Trento 2021 Data Campaign . . . . .	124

5.1.2	GSI 2021 Data Campaign . . . . .	126
5.1.3	CNAO 2021 Data Campaign . . . . .	129
5.1.4	Noise performance at the accelerators . . . . .	130
5.2	Detection efficiency . . . . .	131
5.3	Response of the detector to charged particles . . . . .	135
5.3.1	Response to protons . . . . .	135
5.3.2	Response of the detector to heavy ions . . . . .	144
5.4	Computation of alignment parameters . . . . .	150
5.5	Spatial resolution of the detectors . . . . .	156
<b>6</b>	<b>Conclusions</b>	<b>161</b>
	<b>Bibliography</b>	<b>165</b>



---

## Introduction

---

The work presented in this thesis is part of the FOOT (FragmentatiOn Of Target) experiment approved by the National Institute of Nuclear Physics.

The experiment aims to measure the double differential cross section of the fragmentation of the atoms that make up the healthy tissue of the human body, crossed by protons during Hadrontherapy before reaching the tumour area. The fraction of energy released by fragmentation is about 12.5% of the energy released by ionisation during the pathway.

Since there are no sufficiently precise measurements in the energy range of therapeutic interest (100-400 MeV) to allow modelling of the dose imparted by the proton to the tissues traversed, and therefore an accurate assessment of the damage induced during therapy, the FOOT experiment will make this measurement using the technique of inverse kinematics, i.e. sending ions of the appropriate energy onto a proton rich target, and studying the type, energy and angle of emission of the fragments.

The experiment was therefore designed with the following requirements:

1. it must be transportable to the various accelerators where the ion beams will be available.
2. be capable of measuring in a redundant manner: A, Z, E, p, v of the various fragments.

---

The main objective of the PhD research project was to help develop prototype sensors to be used for the Micro Strip Detector (MSD), which is the last station of the tracking and one of the two systems to measure  $dE/dx$ .

The performances under realistic conditions, i.e. with beams of protons and ions, have been tested and the most suitable solution has been chosen, both from a scientific and a technical feasibility point of view.

The research project also included a contribution to the construction of the modules that made up the tracker outside the magnetic volume and the consequent verification of performance from the point of view of reconstructing the track of the individual ions, and the measurement of their  $dE/dx$ .

Finally, a contribution has been made in the installation of the tracker inside the experiment, in the integration in the analysis software framework implementation and in the first global data taking at the accelerators.

# CHAPTER 1

---

## Tumour treatments and Charged Particle Therapy

---

A tumour, or *neoplasm* (from the Greek νέος, *nèos*, 'new', and πλάσις, *plásis*, 'formation'), is the abnormal and uncontrolled proliferation of cells in a tissue or organ of the body caused by alterations in their genetic material.

Tumours are divided into benign, if they tend to remain localised in the organ of origin and have a slow and expansive growth, and malignant, if they grow rapidly, with extensive infiltration of the organs in which they develop and the ability to spread throughout the body.

Neoplasms are, after cardiovascular diseases, the leading cause of death in the world, with some 20 million new cases and 10 million deaths in 2020 alone.[1]

The global rates of development of neoplasms have increased mainly due to a general ageing of the population, and although it can occur at any age, the majority of people diagnosed with malignant tumours are over 65.

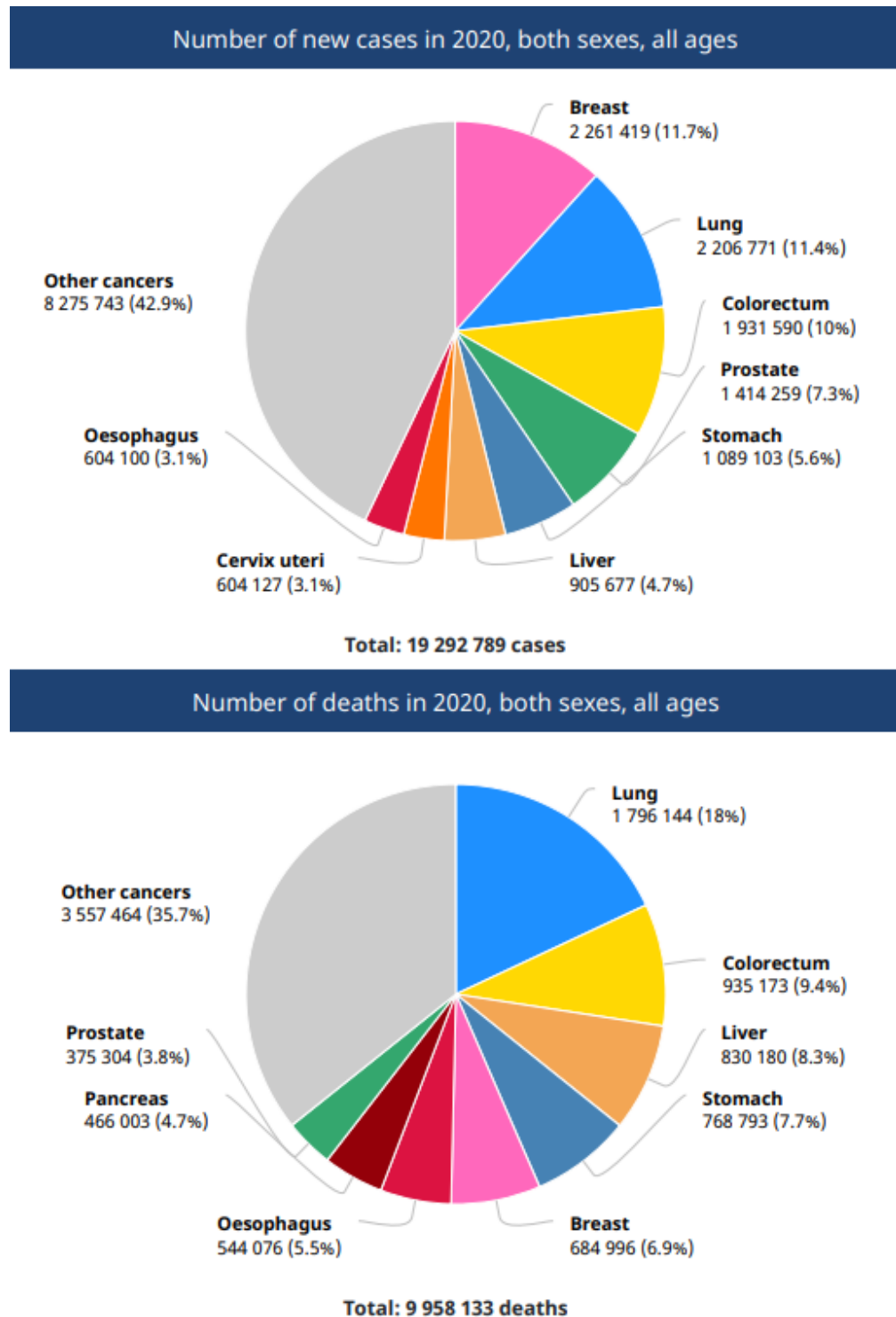


Figure (1.1) – All cancer statistics from IARC for 2020 (data from [2])

## 1.1 Commonly used therapies

Treatment of tumours is aimed at eliminating neoplastic proliferation and preventing local or distant recurrence.

There are many options available for the treatment of both benign and malignant tumours, including surgery, chemotherapy, radiotherapy and palliative care.

The decision on which treatment to use depends largely on the location and type and grade of the tumour, as well as the patient's health and life expectancy.

### 1.1.1 Surgical treatment

Surgery treatment to remove the tumour is generally indicated in case of early diagnosis and when the tumour mass is sufficiently small and localized, to remove isolated metastases or to reduce symptoms caused by compression of surrounding organs and improve the patient's quality of life, even when complete eradication of the tumour is not possible.

Surgery can be used as the only procedure or combined with other treatments: it is not always possible to ascertain with certainty before surgery whether the tumour has spread.

During surgery, doctors often remove lymph nodes near the tumour (sentinel lymph nodes) to check if the tumour has affected them.

If it has, there may be a risk of relapse and the person may need chemotherapy or radiation therapy after surgery to prevent recurrence.

In any case, surgery is not the treatment of choice for all types of early-stage cancer. Some tumours grow in inaccessible locations or, in other cases, removal of the tumour may require removal of an essential organ or impairment of organ function. In these cases, another type of treatment is necessary.

### 1.1.2 Chemotherapy

Chemotherapy (from English chemo- and greek θεραπεία, therapèia, "therapy") is the branch of pharmacology that develops substances with the ability to target and selec-

tively treat various diseases. When related to the oncological field it is more properly referred to as *antineoplastic chemotherapy*.

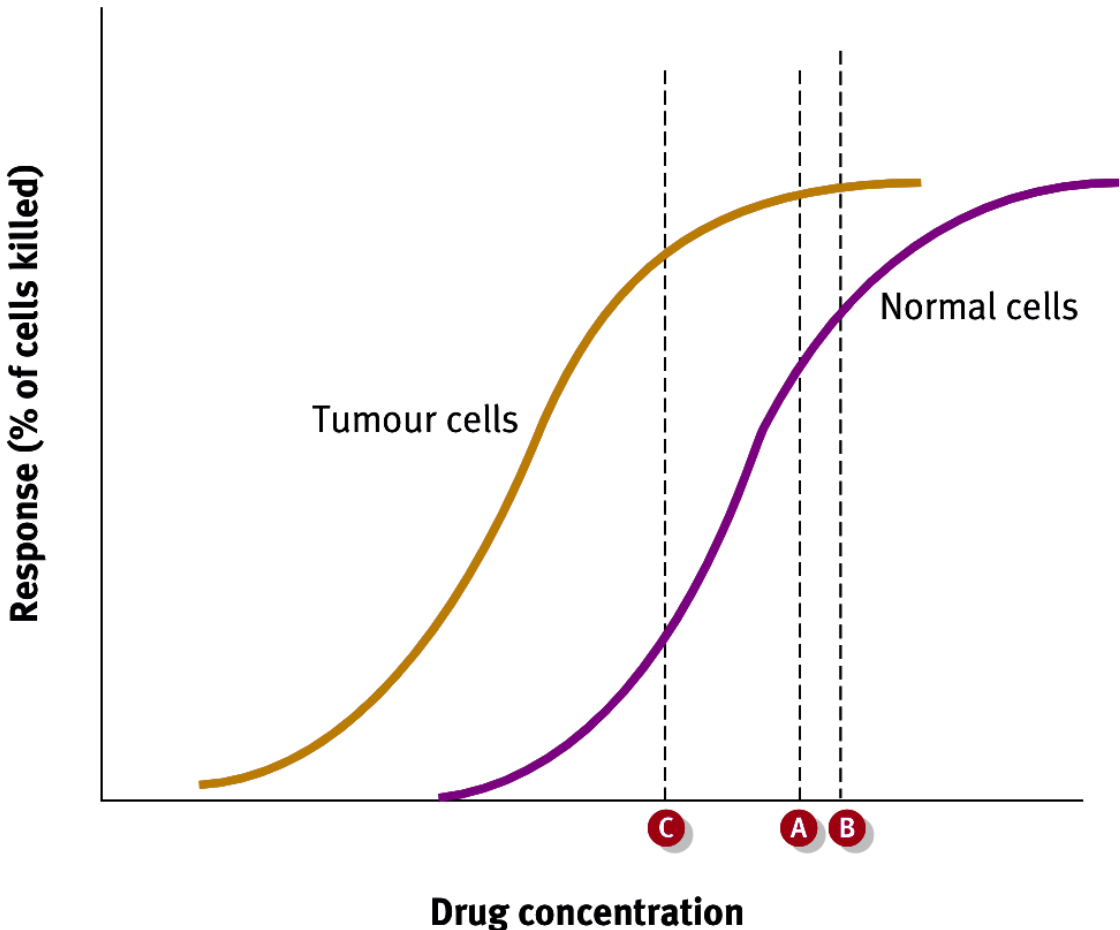


**Figure (1.2)** – Dose response curves for a chemotherapy drug: the therapeutic dose (A) is close to the toxic dose (B) where normal cells die. The safe dose (C) is chosen for administration. (Adapted from [3])

The chemotherapeutic substances used in oncology prevent cell multiplication by interfering with the mechanisms related to this process, and thus eliminate cancer cells by inducing their death (cytotoxic action).

Tumour cells reproduce much more rapidly than normal cells, so the effect of chemotherapy is most effective especially on tumours that grow quickly, because it is able to block or slow down the development or even to reduce its volume.

Given its characteristic of systemic treatment, i.e. spread throughout the patient's body, the use of chemotherapy, however, involves side effects that need to be weighed in relation to the expected benefits.

The action of radiopharmaceuticals has also consequences on some types of healthy cells subject to rapid replication such as hair bulbs cells, blood and those lining the mucous membranes with common side effects such as hair loss, anemia and decline in immune defenses.

As such, the choice to subject a patient to chemotherapy is usually taken in the following cases:

- to eliminate the disease definitively, in the case of tumours that are very sensitive to these treatments;
- to reduce the volume of the tumour mass before surgery or before radiotherapy (*neoadjuvant chemotherapy*);
- to prevent a possible relapse after surgery or radiotherapy (*adjuvant or precautionary chemotherapy*);
- to prolong survival or to delay the progression of the disease when it cannot be eliminated completely;
- to alleviate the symptoms caused by the tumour mass when it cannot be removed surgically;
- to prepare the organism for a bone marrow or stem cell transplant.

### 1.1.3 Radiotherapy

Radiotherapy (or radiation therapy, often abbreviated RT, RTx, or XRT) is a localized, non-invasive therapy capable of causing necrosis of tumour cells through the use of ionizing radiation, either administered externally via *external beam radiotherapy* (EBRT) or internally via *brachytherapy*.

Considered an alternative to traditional surgery, especially in the case of tumours such as prostate or those of the nasopharynx, which are difficult to operate due to

their location, it is often associated with other treatments, such as surgery itself or chemotherapy.

Historically, radiotherapy uses X-rays: discovered more than a century ago they have been since used both for diagnostic purposes, as in the case of radiography, and for therapeutic purposes, as in the case of radiotherapy.

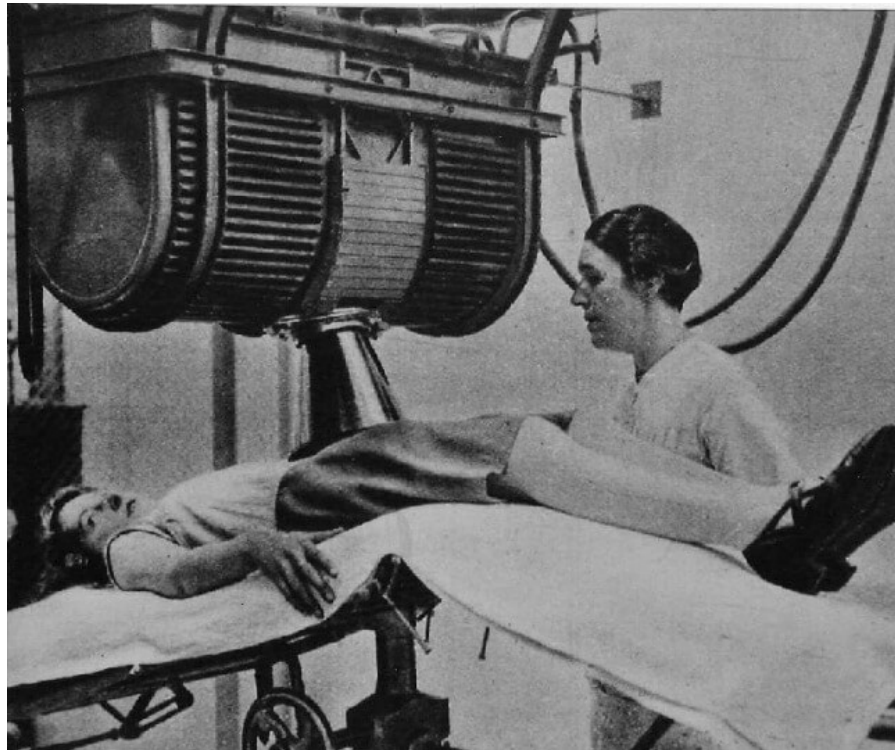


*Figure (1.3) – Radiation therapy with a high power x-ray tube in 1930 at National Cancer Institute in Milan, Italy*

The high energy ionizing radiation used in radiotherapy is capable of damaging the DNA of the target tissue: tumour cells have, in general, poor abilities in repairing their damage and therefore undergo cell death by apoptosis.

To spare healthy tissues, such as skin or organs that the radiation must pass through to reach the tumour, the radiation beams are shaped and directed from different angles, intersecting in the center of the area to be treated, where therefore there will be a greater amount of total absorbed dose than in adjacent parts.

Although the precision of radiotherapy has increased more and more over the years, it may happen that some healthy cells, close to the diseased area, are affected by radiation.

Compared to cancer cells, however, healthy cells are more capable to repair the damage inflicted by radiation, which is why effective radiation therapy treatments can be carried out with generally low side effects.

Depending on the type of tumour and the clinical condition of the patient, radiation therapy can be used with different objectives:

- **curative radiotherapy:** aims to completely eliminate the tumour;
- **preoperative or *neoadjuvant* radiotherapy:** it is performed before surgery to reduce the tumour size and the risk that a small number of tumourous cells may spread during surgery;
- **postoperative or *adjuvant* radiation therapy:** is prescribed after surgery to increase the chances of eliminating any remaining cancer cells;
- **intraoperative radiotherapy:** also known as *IORT (Intra-Operative RadioTherapy)* it consists in the administration of a dose of radiation during surgery to remove the tumour;
- **palliative radiotherapy:** to stop tumour growth and alleviate symptoms, including pain in advanced and metastatic forms, thus improving the quality of life of patients;
- **total body radiotherapy:** the entire patient's body is irradiated in order to destroy the diseased cells in some particular tumours that affect the cells of the blood and lymphatic system, usually performed before a bone marrow or stem cells transplant;
- **ablative or *stereotactic* radiotherapy:** high doses from a highly focused radiation treatment are administered to small volume tumours, limiting the dose to the surrounding organs and limiting the number of treatment sessions needed

### 1.1.4 Other types of therapy

**Targeted therapies** Unlike traditional chemotherapy, that affects cancer cells by acting on their tendency to multiply more than normal ones, they act in a much more targeted way with a specific molecule or process of cancer cells, not causing damage to normal cells and thus reducing side effects.

Most of the drugs used in targeted therapies are called biopharmaceuticals because they mimic substances present in the body despite being produced in a laboratory.

In another strategy the therapeutic agent is an antibody which specifically binds to a protein on the surface of the cancer cells.

**Immunotherapy** Immunotherapies are treatments that aim to stimulate the body's ability to defend itself against cancer, retraining the immune system to control and effectively eliminate the transformed cells.

Laboratory-produced substances that closely mimic the natural ones involved in the inflammatory reaction underlying the immune response are commonly used.

They are also called *non-specific immunological therapies*, because they are not used exclusively for the treatment of cancer or for a specific patient.

Research in recent years has investigated the molecular mechanisms underlying the interaction between cancer cells and immune cells.

From these researches have been developed treatments based on *immune checkpoint inhibitors*, molecules that, among other things, send intra-cellular inhibitory signals capable of slowing down the activity of the immune system when, for example, pathogens have been eliminated.

In the tumour, cancer cells can control this physiological regulatory system to halt the anti-cancer immune response and escape immune system surveillance.

**Hormonal therapy** Hormone therapy is used to treat tumours whose growth is stimulated by hormones.

For example, estrogen or testosterone can stimulate the growth of certain breast or prostate cancers.

Hormone therapy, also called *endocrine therapy*, aims to prevent the production of these hormones or to block their action in stimulating the multiplication of cancer cells.

Hormone therapy can reduce the risk of relapse after other treatments (surgery, radiotherapy and/or chemotherapy) have been completed, or it can help reduce the symptoms of an advanced stage of the tumour and is also used as neoadjuvant therapy, i.e. to reduce the size of the tumour before surgery.

Surgical removal of endocrine organs, such as orchectomy and oophorectomy can also be employed as a form of hormonal therapy.

## 1.2 Charged Particle Therapy

When treating tumours with conventional radiotherapy, ideally only the tumor volume gets irradiated, while the surrounding healthy tissues are completely avoided, resulting in only malignant cells being harmed and eliminated.

However, in practice, this is not possible due to the unavoidable irradiation of tissues located upstream and downstream of the tumor, which receive a dose that varies depending on particle type, energy, and other parameters.

The first intuition that proton beams could be an effective method for radiotherapy treatment was formulated by Robert R. Wilson in a paper published in 1946, with the help of the Harvard Cyclotron Laboratory (HCL).[4]

Wilson's theory was based on the fact that, unlike photons, charged particles do not release their energy constantly as the depth of penetration into the tissue increases.

A charged particle beam's energy release, instead, is characterized by a low dosage deposition in the entrance channels, followed by a peak of deposited energy (Bragg peak, figure 1.4), and then essentially no more energy release.

Hadrontherapy's strength is the ability to precisely change the position of the Bragg peak in order to get a considerable release of energy at the tumor area of interest.

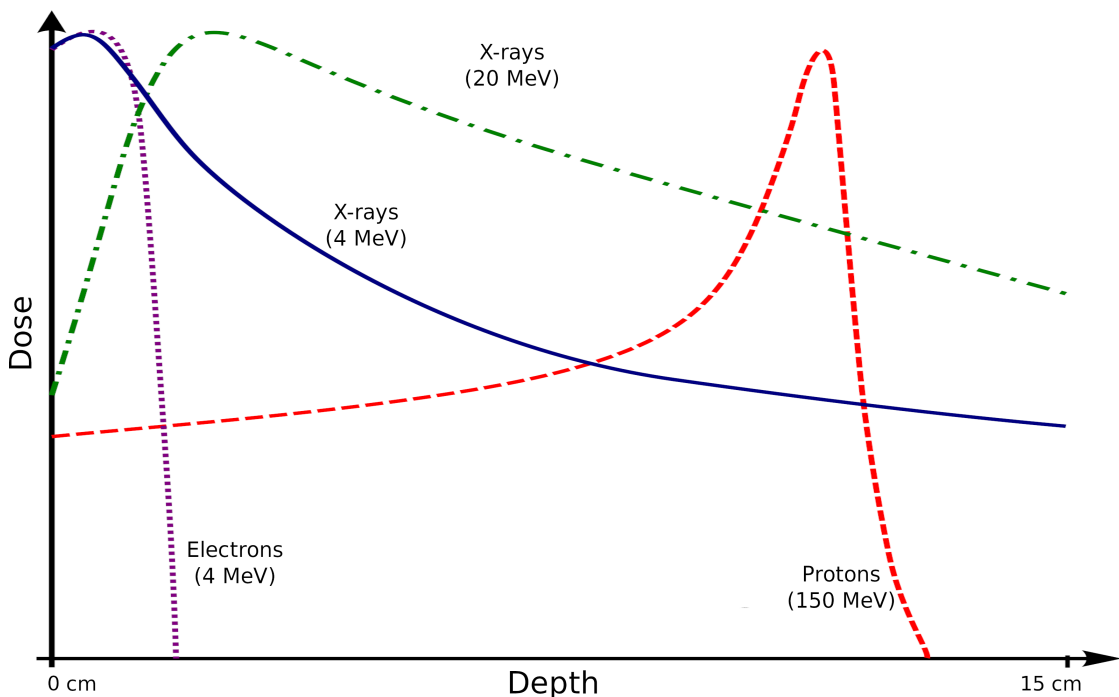


**Figure (1.4)** – Dose-depth profiles for various particles in the same material (Adapted from [5])

Furthermore, the low energy deposits in the entrance channel and the area following the Bragg peak allow for the least amount of harm to healthy tissues around the neoplastic area at therapeutic levels.

The first treatments with protons were performed with particle accelerators built for physics research, notably at Berkeley Radiation Laboratory in 1954 and Uppsala in Sweden in 1957.

The first dedicated medical proton therapy center went into operation in 1990 at Loma Linda (California) while the first carbon ion therapy facility, the HIMAC (Heavy Ion Medical Accelerator in Chiba), opened 4 years later in Chiba (Japan).

### 1.3 Interactions of charged particles with matter

Charged particles primarily interact with matter mainly by means of the Coulomb forces between their positive charge and the negative charge of the orbital electrons within the absorber atoms.

Although interactions between the particle and nuclei (such as, for example, Rutherford scattering) are possible, they are uncommon and usually negligible.

Whenever a charged particle enters an absorbing medium, it interacts with a large number of electrons at the same time.

The transferred energy may be sufficient to either move the electron to a higher-lying shell within the atom (*excitation*) or to remove the electron completely from the atom (*ionization*), depending on the proximity of the encounter.

The energy transferred to the electron comes at the expense of the charged particle, and its velocity is therefore decreased as a result of the interaction.

The maximum energy that can be transferred from a charged particle of mass  $m$  with kinetic energy  $E$  to an electron of mass  $m_0$  in a single collision is  $4Em_0/m$ : because this value is usually a small fraction of the total energy, the primary particle loses its energy in many such interactions during its passage through the medium, with the net effect of decreasing its velocity continuously until the particle is stopped.

It is thus possible to define the *linear stopping power*  $S$  for charged particles in a given material as the differential energy loss for that particle within the material divided by the corresponding differential path length

$$S = \frac{dE}{dx} \quad (1.1)$$

and the *mass stopping power*, which for a material with density  $\rho$  can be simply defined as  $S_\rho = S/\rho$ .

The stopping power can be further divided into three independent parts that are linked to the different energy loss mechanisms in the medium:

$$S = S_e + S_n + S_r \quad (1.2)$$

where  $S_e$  is the energy loss associated to excitation or ionization of the electrons in the target medium,  $S_n$  is the result of the elastic collisions with the nuclei of the medium and  $S_r$  arises from radiative emission of energy of the charged particle (*i.e. Bremsstrahlung*).

For very slow non-relativistic particles  $S_r$  is usually negligible while  $S_n$  is much more relevant, and viceversa for fast relativistic particles.

### 1.3.1 The Bethe-Bloch formula

For heavy charged particles with intermediate energies (in the range  $0.1 \lesssim \beta\gamma \lesssim 1000$ ) the mean rate of energy loss is well described by the “*Bethe equation*” [6]

$$-\frac{dE}{dx} = \frac{2\pi N_A e^4 \rho z^2 Z}{m_e v^2 A} \left[ \ln \left( \frac{2m_e v^2 W_{max}}{I^2 (1 - \beta^2)} \right) - 2\beta^2 - \delta(\beta\gamma) \right] \quad (1.3)$$

where

- $m_e$  is the electron rest mass
- $z$  is the charge number of the incident particle
- $Z$  is the charge number of the target particle,  $A$  its mass number
- $\rho$  is the target density expressed in g/cm<sup>3</sup>
- $I$  is the mean excitation energy of the atoms of the target
- $N_A$  is the Avogadro number
- $W_{max}$  is the maximum possible energy transfer to an electron in a single collision
- $\delta(\beta\gamma)$  is the density effect correction to ionization energy loss

For this particular range of  $\beta\gamma$  ions lose energy mainly through inelastic electromagnetic interaction with atomic electrons, that is, they lose energy by ionizing and exciting atoms in the absorption medium.

Ionization causes also the generation of secondary electrons, usually called  $\delta$ -rays.

Nuclear interactions start having an important role for  $\beta\gamma \approx 0.1$ , where the free electron assumption, upon which the theory of energy loss by ionization and excitation given by Bethe is based on, is not accurate.

In this region the particle velocity is comparable to the one of the atomic electrons of the material the contribution to the stopping power from  $K$  and lower shell electrons decreases, requiring the introduction of a *shell correction* factor  $(C_K + C_L + \dots)/Z$ .

For even lower values of  $\beta\gamma$  the particles captures electrons from the medium, which results in a reduction of its effective charge and the rate of energy loss decreases again.

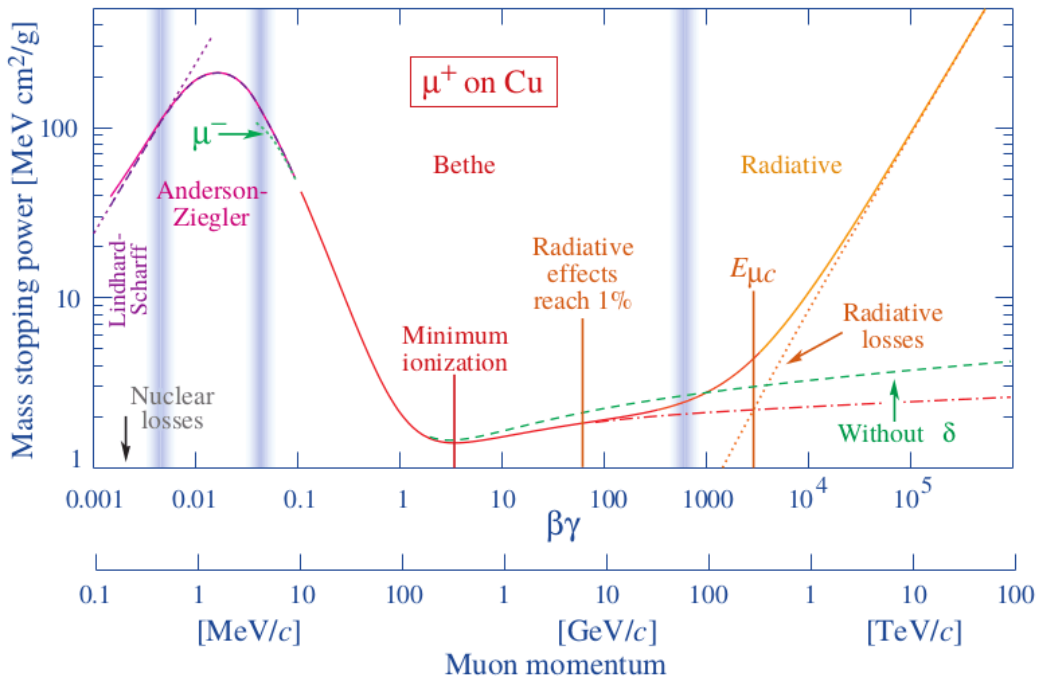


Figure (1.5) – Muon stopping power in Cu target (Image from [6])

For values of  $\beta\gamma \gtrsim 0.1$  the stopping power first decreases as  $1/\beta^\alpha$  with  $\alpha \approx 1.4 - 1.7$  and a slight dependence on the particle's mass and  $Z$ .

At  $\beta\gamma \approx 3$  the stopping power reaches a minimum with  $dE/dx \approx 2 \text{ MeV g}^{-1}\text{cm}^2$  for a wide range of  $Z$  values, followed by a *relativistic raise* for increasing energies following a  $\ln(\beta\gamma)$ , as showed in figure 1.5 as an example for the case of muons interacting with copper.

A significant part of the relativistic raise arises from Lorentz contraction that extends the electric field of the particle: this field also polarizes the medium, reducing the increase for the highest energies, and the effect is taken into consideration by the density-effect correction factor  $\delta(\beta\gamma)$ .

Another part of the increase is introduced by the explicit  $\beta^2\gamma$  dependence of  $W_{max}$ , the maximum possible energy transfer to an electron from the medium: events with an high energy transfer to a single electron become possible, extending the tail of the energy loss distribution with a resulting increase of the energy loss mean.

For  $\beta\gamma \approx 1000$  radiative processes become more important and the Bethe-Bloch formula is not valid anymore.

### 1.3.2 Range of particles and the Bragg peak

For energies high enough for shell corrections to be negligible, but low enough to be able to neglect also relativistic effects the Bethe-Bloch formula (1.3) can be approximated as follows

$$-\frac{dE}{dx} \approx \bar{K}z^2 \frac{1}{\beta^2} \left[ \ln \frac{2m_e c^2 \beta^2}{I(1 - \beta^2)} - \beta^2 \right] \quad (1.4)$$

Under these conditions it is possible to observe a direct dependence of  $dE/dx$  on  $z^2$  and  $1/\beta^2$ , confirmed also experimentally. The dependence on these two quantities, especially on the second one, manifests itself with an increase in the ionization of the medium for low energies.

The number of electron-hole pairs created per centimetre by ionisation (defined as *ionisation density*) reaches a maximum value when the incident particle has lost almost all its energy and is therefore at the end of its path in the medium.

This peak is called Bragg peak (BP), and is represented in figure 1.6 in the case of protons at different energies ranging from 120 MeV to 220 MeV: in the first part of the particle's path, the energy released is lower and almost constant, while in the last part of the path the sudden growth of energy release with the subsequent collapse indicates that the particle has stopped in the medium.

The total path length traversed by the charged particle before it is stopped is called its *range* and it's a fundamental parameter to characterize the dose deposited along the beam direction.

For a fixed particle type, beam energy and material it is firstly possible to define a *mean range* over an ensemble of incident particles. Due to the stochastic nature of the

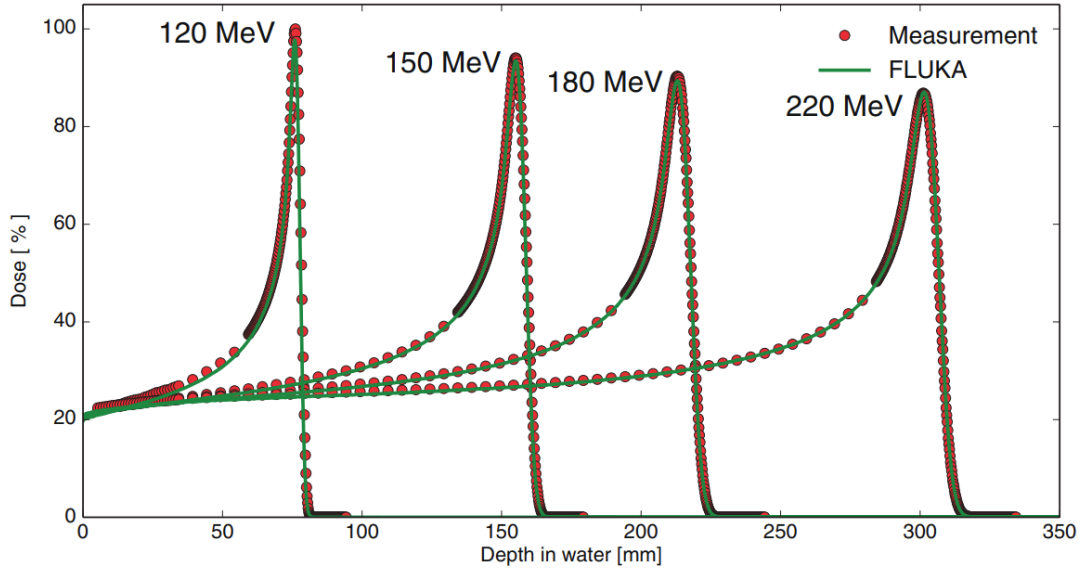


**Figure (1.6)** – Measured (red circles) and FLUKA simulated (green lines) depth dose curves of protons at different energies (from [7])

interactions, particles in the same medium have varying path lengths between the same initial and final energies.

Such fluctuations are usually called *straggling*, and it was originally showed by Bohr [8] that for long path lengths (that is, for targets that are thick with respect to the particle energy) the range distribution is approximately Gaussian, arising from the contribution of many small independent energy releases.

For thinner targets, fewer energy depositions event occur, and single large energy transfer collisions cause a tail in the high energy region of the distribution.

A very close approximation to the average path length traveled by a charged particle up to rest position is found in the CSDA (*Continuous Slowing Down Approximation*) Range.

Assuming the rate of energy loss at every point along the track to be equal to the total stopping power, and neglecting energy loss fluctuations, nuclear interactions,  $\delta$ -rays production and Multiple Coulomb Scattering, it is defined as

$$R_{CSDA}(E_0) = \int_0^{E_0} \left( \frac{dE}{dx} \right)^{-1} dE \quad (1.5)$$

where  $E_0$  is the energy of the incident particle.

$R_{CSDA}$  is measured in  $\text{g}/\text{cm}^2$  and is not directly measurable experimentally: it is usually derived by evaluating the fraction of protons that pass through an absorber of thickness  $R$ . Figure 1.7 shows the case of electrons, protons and  $\alpha$  particles interacting with water.

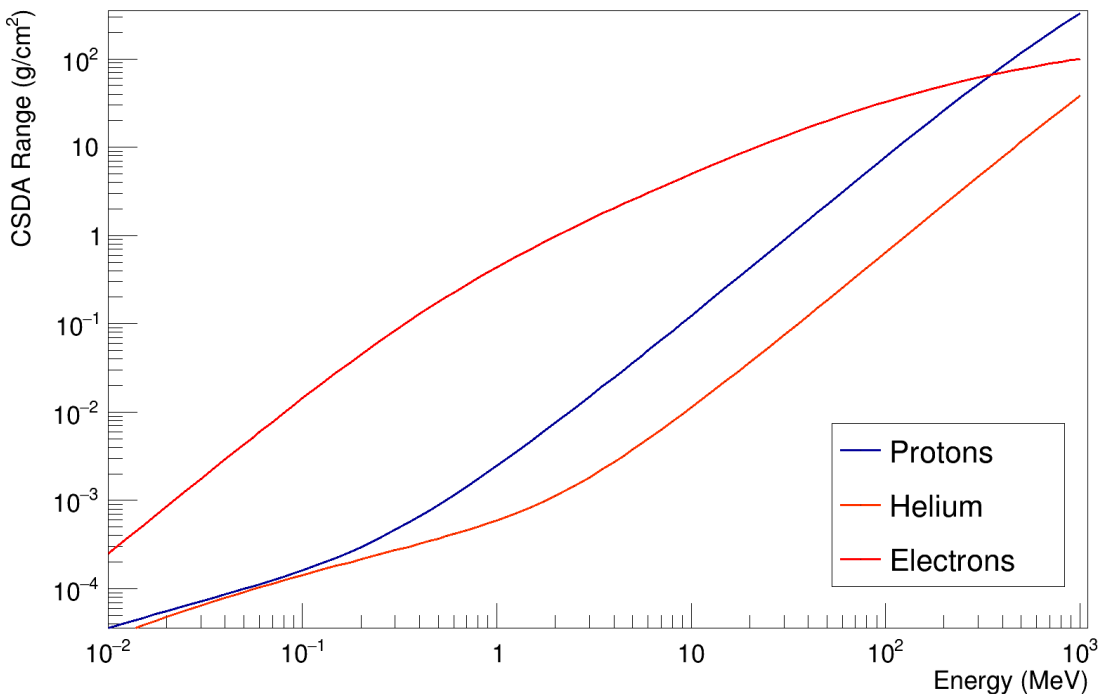


Figure (1.7) –  $R_{CSDA}$  range of electrons, protons and  $\alpha$  particles in water (data from [9])

## 1.4 Nuclear interactions and nuclear fragmentation

Nuclear interactions can be classified at first order as elastic and inelastic collisions.

In the case of elastic collisions, which conserve kinetic energy, the main result is a slight broadening of the beam, which is well described by the *Multiple Coulomb Scattering* effect, as outlined in figure 1.8.

The distribution of scattering angles due to multiple scattering for a high number of small angle deviations can be approximated to a Gaussian distribution around  $\theta = 0$  with standard deviation equal to

$$\theta_0 = \frac{13.6}{\beta pc} z \sqrt{\frac{x}{X_0}} \left[ 1 + 0.038 \ln \frac{x}{X_0} \right] \quad (1.6)$$

where  $p$  is the momentum of the incident particle,  $z$  is its charge and  $x/X_0$  is the thickness of the material expressed in units of radiation length  $X_0$ .

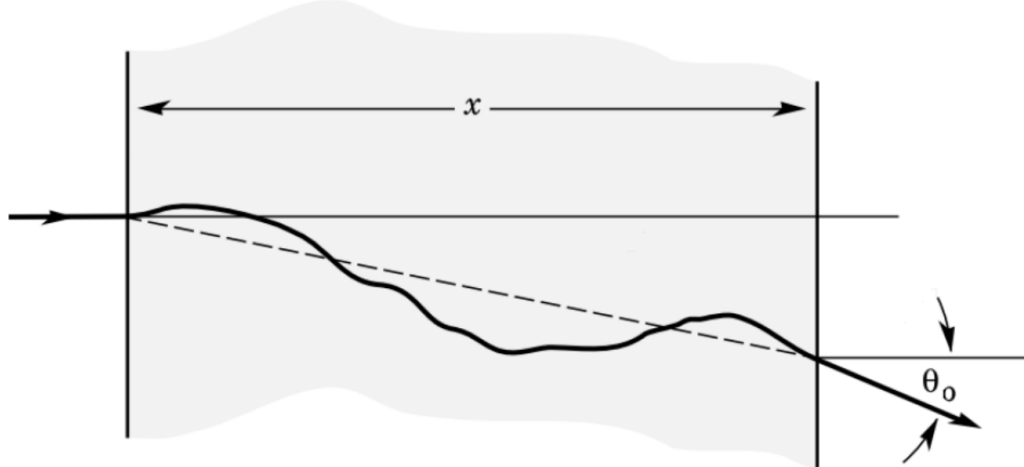


Figure (1.8) – Effect of Multiple Coulomb Scattering (adapted from [6])

When analysing the effects of collimated beams of high-energy hadrons used in Hadrontherapy, it is also necessary to look at inelastic processes: in general, this type of nuclear reaction is less likely to occur than multiple scattering, but the effects it produces are significant, especially when the radiation passes through a thick medium.

For high energies (several hundreds of MeV per nucleon) there is the possibility for the particles in the beam to overcome the Coulomb barrier of the target nuclei, and they can therefore interact strongly with them, causing fragmentation and/or fragmenting themselves (except, of course, in the case of protons).

When these events occur, collisions between the projectile and the atoms of the medium can be central (or *head-on*), resulting in the disintegration of both nuclei and

the emission of fragments, or peripheral, in which the primary particle loses one or more nucleons.

The latter collisions are the most frequent and the process can be described by the abrasion/ablation model devised by Serber [10], as outlined in figure (1.9).

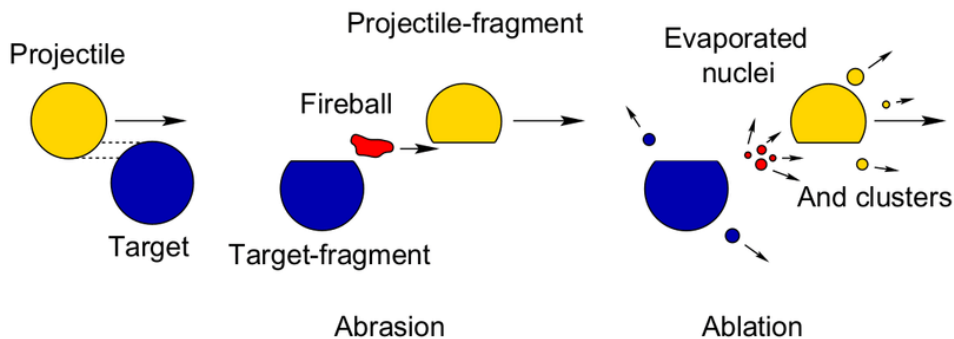


*Figure (1.9) – Abrasion/ablation model as described by Serber (from [11])*

The abrasion/ablation process takes place in two distinct phases with clearly defined characteristic times:

**Abrasion** after the peripheral collision between the particles, fragments of the projectile and the target are generated and a zone of very high excitation, called a "fireball", is formed. This process takes place in a very short time, in the order of  $10^{-22}$  to  $10^{-23}$  s.

**Ablation** consists in the de-excitation of the fireball and of the fragments of the projectile and target, through the emission of photons and massive fragments, until stability is achieved. This process takes a relatively longer time, in the order of  $10^{-16}$  to  $10^{-18}$  s.

The fragments originating from the primary particles present a forward peaked angular distribution in the laboratory frame due to the high projectile velocity and have approximately the same velocity and direction of the originating beam.

Fragments originating from the target nucleus at rest, on the other hand, are emitted in an almost isotropic manner and at a much lower velocity, with a consequently very short range.

For therapeutic beams the energetic contribution of these secondary fragments produced becomes important, especially for correct treatment planning, as the dose deposited and the consequent damage in the first part of the particle path is non negligible (Figure 1.10).

When fragmentation of the beam particles occur due to nuclear inelastic processes, a monochromatic incoming beam turns into a mixed beam containing neutrons and lower-Z fragments, with a resulting broadening of the energy distribution and an increase in penetration depth accordingly.

These fragments are responsible for a further energy deposition which results in some of the dose being deposited after the Bragg Peak expected for the incoming beam.

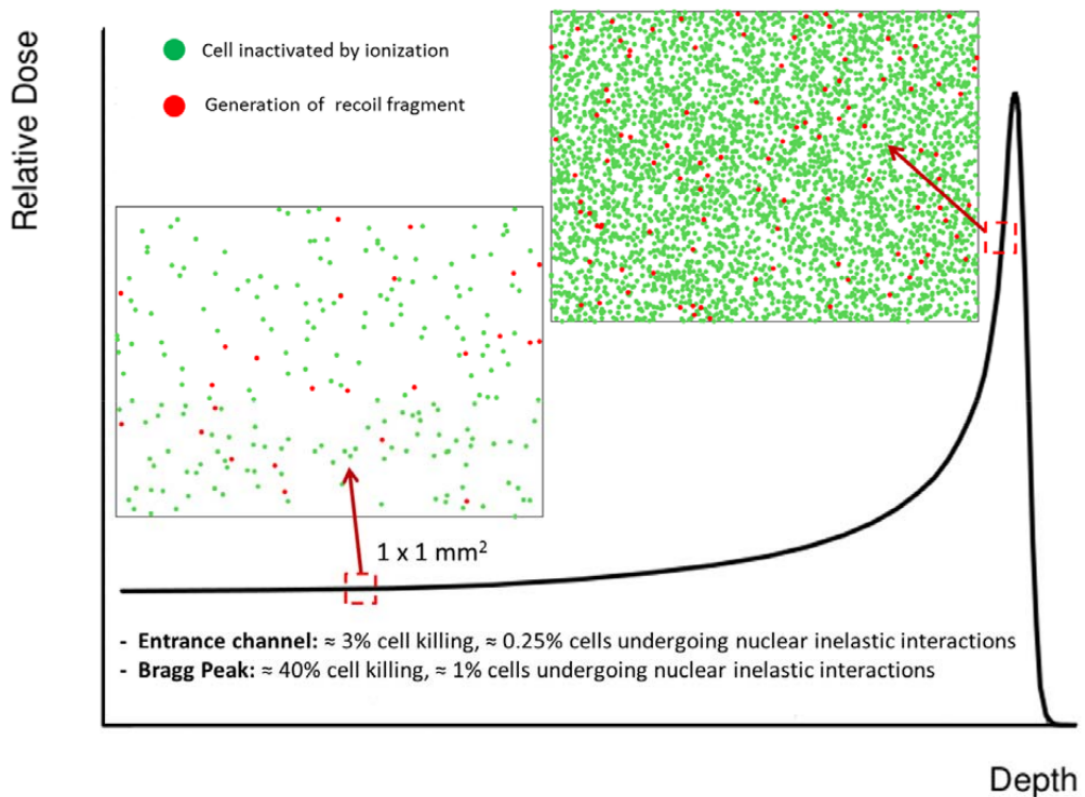


Figure (1.10) – Effects of nuclear fragmentation on a therapeutic beam (from [12])

## 1.5 Biological effects of charged particles

When the human body is exposed to any kind of radiation, the primary interactions in the different tissues are similar to those in any other material.

However, after the exposure, a series of secondary effects involving new processes like chemical reactions can occur, leading to what is called *radiation injury*.

Conversely, living tissues in the human body respond to the damage with a series of repair mechanisms, so that the steps involved in the biological damage can be various and complex: some interactions occur very quickly as the energy is transferred to the tissue, while further effects can manifest over a period of several days to weeks.

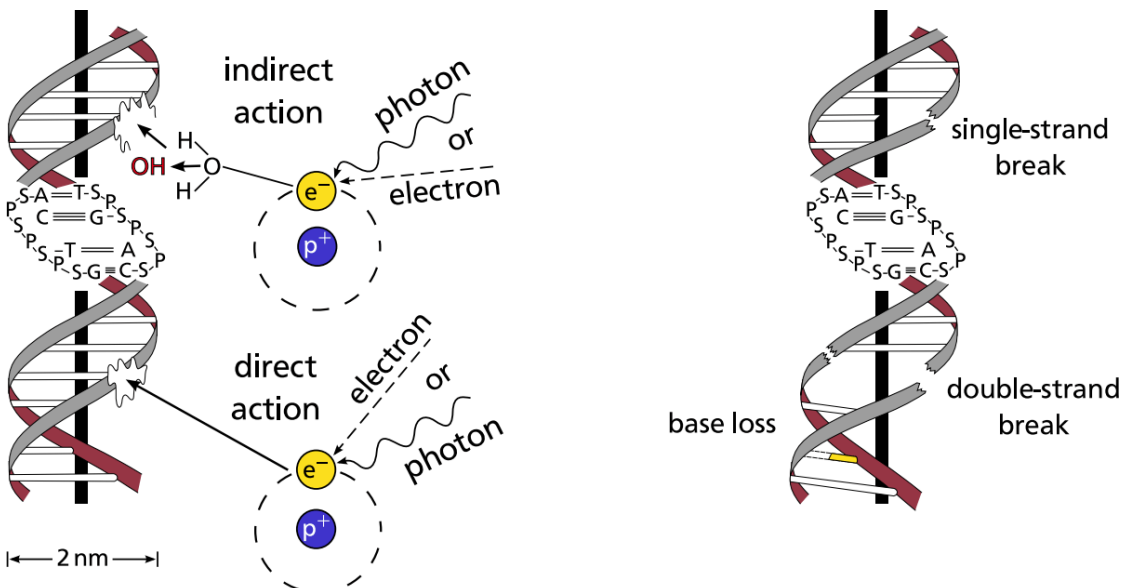


*Figure (1.11) – Direct and indirect radiation damage to the DNA (left) and different types of radiation damage (right) (from [13])*

Regarding the initial effects, it is possible to discriminate between direct and indirect physical damage (Figure 1.11):

**Direct damage** due to the deposition of energy into the tissue

**Charged particles (protons,  $\alpha$  particles and heavier ions)** : interaction with the atoms of the tissue, mainly with colliding with its electrons, losing energy

according to the Bethe-Bloch formula (as discussed in section 1.3.1)

**Electrons** interaction with the electrons of the tissue similarly to heavier particles, with the addition of the energy release due to bremsstrahlung radiation in the form of photons

**Neutrons** low energy neutrons (under 100 eV) mainly lose energy through a  $(n, \gamma)$  capture reaction (primarily with the hydrogen atoms of a water molecule).

Higher energy neutrons lose on average a large fraction of their energy in elastic collisions with other nucleons, with a subsequent release of energy in the form of ionization by the recoiling protons.

**Photons** energy transferred to the electrons of the atoms in the tissue via Compton scattering, photoelectric effect and pair production, depending on the composition of the tissue.

**Indirect chemical damage** While some of the physical interaction processes can cause direct and irreversible damage to part of the tissue most of the primary interactions result in the ionization of molecules in the target, mostly with those of water present in the whole body.

The ionization of these molecules can result in the creation of chemically active *free radicals*, electrically neutral atoms or molecules with an unpaired electron.

Free radicals are extremely reactive and can be both oxidizers (accepting an electron from other molecules) or reducing agents (donating their extra electron), and can diffuse far enough to induce chemical changes in fundamental biological structures of the cell.

## 1.6 Fundamental Radiobiology principles

The branch of science dedicated to the study of the action of ionizing radiation on living things, especially health effects of radiation, is commonly called *Radiobiology*, and follows three fundamental principles [14]:

### Justification

*"Any decision that alters the radiation exposure situation should do more good than harm"*

## Optimisation of Protection

*“Doses should all be kept as low as reasonably achievable, taking into account economic and societal factors”*

## Dose Limitation

*“The total dose to any individual . . . should not exceed the appropriate limits”*

Given the high number of different processes involved in the interaction of radiation and charged particles with the human body, it is necessary to define a set of fundamental quantities to be used in order to obtain the desired effects and avoid undesirable effects when planning a therapy.

### 1.6.1 Fundamental Quantities and Units

#### Dose

The fundamental quantity, strictly related to the induced radiation damage, is the dose  $D$ , or *absorbed dose*, which is defined as the ratio between the mean energy  $dE$  released by ionizing radiation in a volume element and the mass  $dm$  contained in that volume

$$D = \frac{dE}{dm} \quad (1.7)$$

The modern SI unit for the absorbed dose is the gray (Gy), where  $1 \text{ Gy} = 1 \text{ J kg}^{-1}$

#### Dose rate

The absorbed-dose rate is defined as the ratio

$$\dot{D} = \frac{dD}{dt} \quad (1.8)$$

The modern SI unit for the absorbed dose rate is gray per second ( $\text{Gys}^{-1}$ ).

### Linear Energy Transfer

The Linear Energy Transfer (LET) is strictly related to the stopping power, and is a quantity frequently used in radiodosimetry and radiobiology.

It is defined as the amount of energy that an ionizing particle transfers to the material traversed per unit distance and, differently from stopping power, it does not take into account radiative energy loss (i.e. the radiative stopping power or Bremsstrahlung) or delta-rays.

LET is defined as:

$$\text{LET}_\Delta = \left( \frac{dE}{dx} \right)_\Delta \quad (1.9)$$

where  $dE$  is the mean energy loss due to the interaction with the atomic electrons for events with energy transfer under the cut-off value  $\Delta$ .

For any given value of  $\Delta$  the LET is properly defined as *restricted linear energy transfer* and the value is usually chosen to exclude the events (like  $\delta$ -rays) that release energy far from the trajectory of the incident particle.

For values of  $\Delta \rightarrow \infty$  the LET becomes the *unrestricted linear energy transfer*, which is identical to the linear electronic stopping power in absolute value.

### Relative Biological Effectiveness

To take account of the fact that, for the same dose, a different LET leads to different biological effects, the *Relative Biological Effectiveness* (RBE) is introduced.

It is defined as the ratio between the dose of a reference radiation ( $D_X$ ), generally photons ( $\gamma$ -rays from  $^{60}\text{Co}$  or X-rays), required to produce a certain biological effect and the dose of the radiation under investigation ( $D_R$ ) whose efficacy is to be verified, required to create the same biological effect (Figure 1.12):

$$\text{RBE} = \frac{D_X}{D_R} \quad (1.10)$$

The RBE is a complex quantity, and several factors determine its value: the type

of radiation, the dose, the number of times in which the dose delivery is fractionated, particle mass, cell radiosensitivity, to name a few.

The RBE is strongly dependent on dose and survival levels derived from dose-response curves: as the LET increases, the RBE grows slowly in the first part, then increases more and more steeply until it reaches a maximum corresponding to about  $100\text{keV}/\mu\text{m}$ , as shown in figure 1.13 in the case of the irradiation of different cell types.

At this ionisation density, the average separation between two consecutive ionisation events is about the diameter of DNA ( $\approx 2 \text{ nm}$ ) and has a high probability of causing biological damage with the passage of a single charged particle.

After the maximum, the RBE decreases and this decrease as a function of LET is due to the *overkilling effect*: so much dose is deposited in a single cell, more than needed to completely kill the cell, that part of the dose is in excess and therefore "wasted".

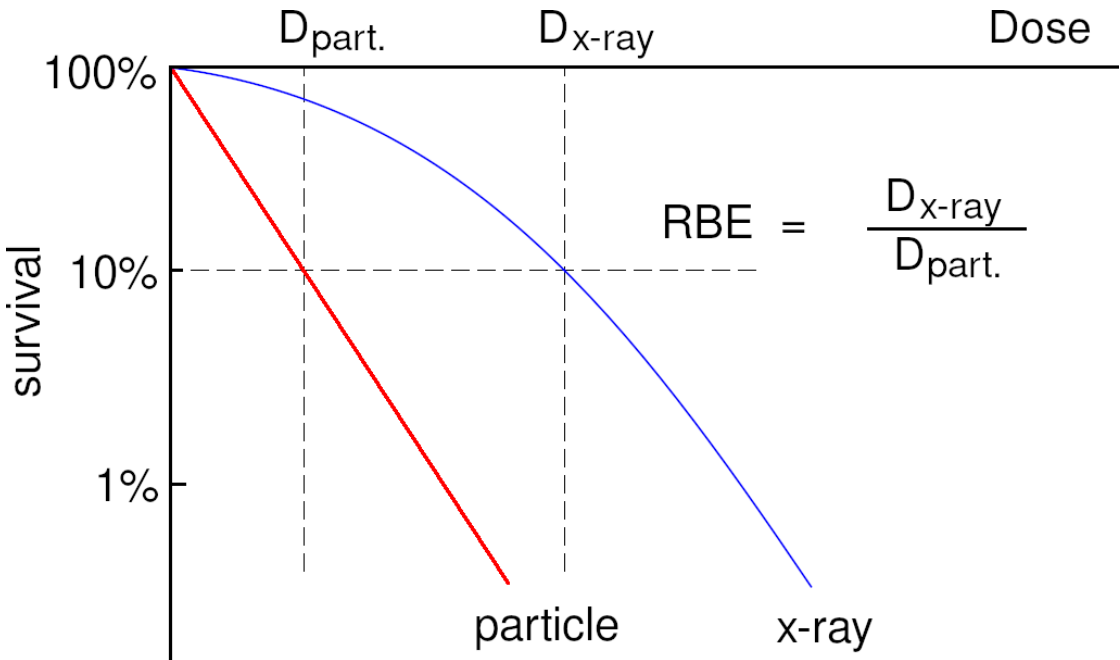


*Figure (1.12) – Definition of RBE and its relation to survival rate (adapted from [15])*

In clinical practice, proton RBE is considered constant and equal to 1.1 according to ICRU [16] recommendations: *protontherapy* is thus considered about 10% more effective than classical radiotherapy because it has higher values for RBE than for photons.

Protons also have the advantage of an LET along the track that does not increase as much as for heavier ions. RBE for heavier ions, in fact, varies significantly up to values  $> 3$  in case of carbon ions.

This also influences the position of the RBE maximum, that ranges from about 100 to 200 keV/ $\mu$ m for  $Z > 1$  ions, typically shifted towards higher LET values than those of protons.

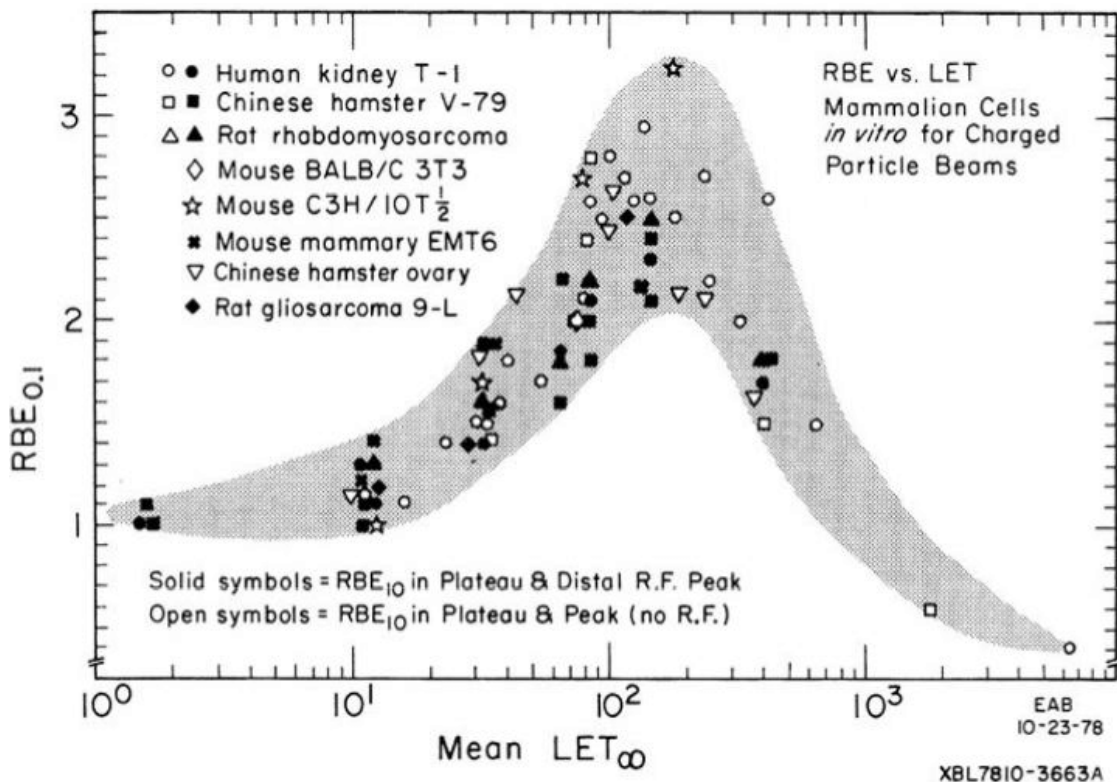


*Figure (1.13) – Comparison of different RBE curves for different cell types irradiated using a different ions and energies. The shaded area shows the general trend of the data. (from [17])*

### Oxygen Enhancement Ratio

When a tumour grows in size it usually develops its own blood supply system with the creation of new blood vessels in a process called *angiogenesis*, in order to supply oxygen to the cells in the tumour center that are too far from the original vessels present in the tissue.

However, even if the same mediators that are responsible for physiological angiogenesis are involved in tumour angiogenesis, their production is irregular.

The vessels that are formed are abnormal, presenting a tortuous course and excessive leakiness that generate irregular blood flow [18].

This leads to the formation of hypoxic regions, especially in the core of larger tumours, that have been long proven to be more radioresistant [19].

This effect is quantified by the *Oxygen Enhancement Ratio* (OER), defined as the ratio between the radiation dose in hypoxia condition ( $D_{hyp}$ ) over the radiation dose in an aerobic condition ( $D_{ox}$ ), for the same biological effect

$$\text{OER} = \frac{D_{hyp}}{D_{ox}} \quad (1.11)$$

OER is independent on the dose, and generally is about 3 for photons, while it is significantly reduced for ions that have higher LET: hypoxic and aerobic conditions are similar for high-LET particles, while they appear very different for low-LET particles (fig 1.14).

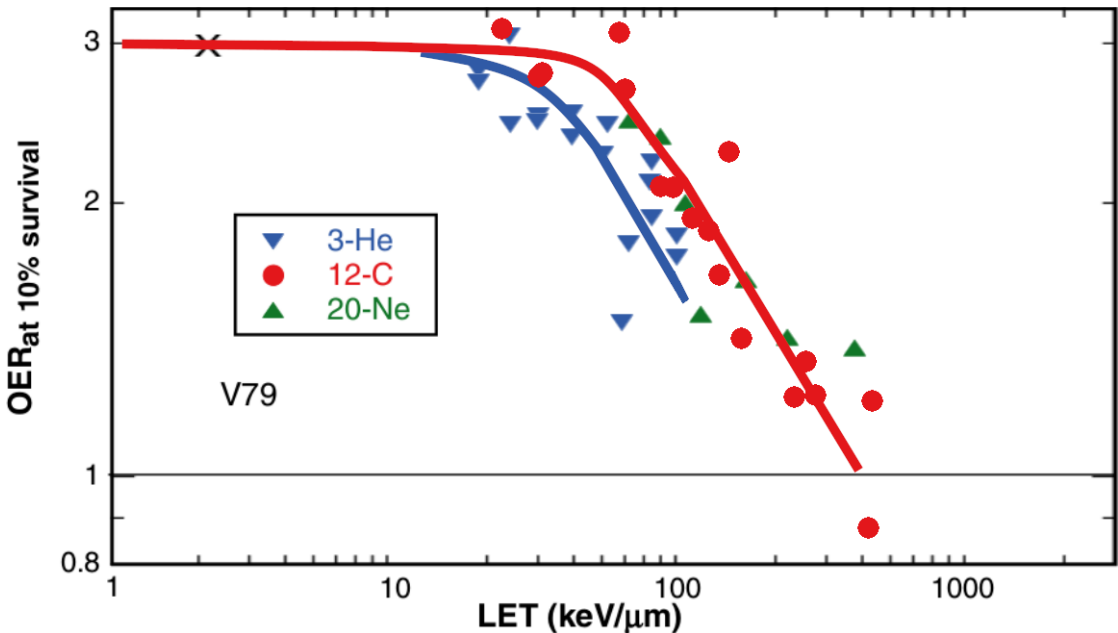


*Figure (1.14) – OER at different LETs for different ions (from [20])*

The oxygen fixation hypothesis (OFH), developed in the late 1950s [21], is widely regarded as the most satisfactory explanation of this effect: the presence of molecular oxygen permanently fixes the DNA damage produced by free radicals, leading to irreparable damage.

Since the role of indirect damages is not predominant for high LET radiation, the hypothesis also gives an explanation for the almost unity value of the OER for that kind of radiation.

## 1.7 Advantages of Charged Particle Therapy

The first attempt at radiation therapy were made in the 1890s using x-rays and  $\gamma$ -rays from radioactive isotopes such as  $^{60}\text{Co}$ .

Since then, improved technology and research results have led to the popularity and growth of radiation therapy as a well-established technique for cancer treatment.

The state-of-the-art photon radiation therapy is the *Intensity Modulated Radiation Therapy* (IMRT), in which the intensity of the radiation beam is modulated for each small volume to be treated, adjusting the radiation dose deposition in a 3-dimensional shape.

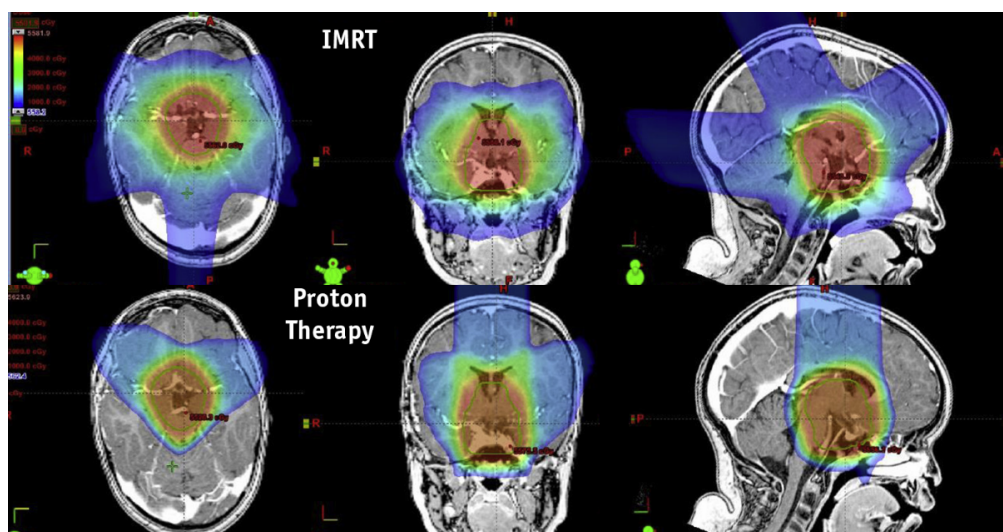


Figure (1.15) – Comparison of craniopharyngioma treatment with photons (IMRT, top) and protons (bottom) in 3 different planes (from [22])

The rationale for the use of ions in radiotherapy lies instead in their favorable deep-dose profiles and increased biological efficacy, as showed in section 1.6.1: while electromagnetic radiation (x-rays and photon beams) show a large exponential dose reduction with depth, charged particles profiles are characterized by the Bragg peak.

With particle therapy it's possible to use only a small number of beam entry sites and preserves healthy tissue better than conventional radiotherapy (fig. 1.15).

The position of the Bragg peaks can, in fact, be precisely tuned to the desired depth in the tissue by varying the kinetic energy of the incident ions.

Protons used in the therapy are usually accelerated to energies between 60 and 250 MeV, which corresponds to a range of 15-35 cm in water.

However, a single beam of energy produces a deposition area that is usually too narrow to radiate the entire tumour.

Thus, several beams with different energies are combined to produce what is known as the *Spread Out Bragg Peak* (SOBP), so that a uniform dose is distributed through the tumor volume (fig. 1.16).

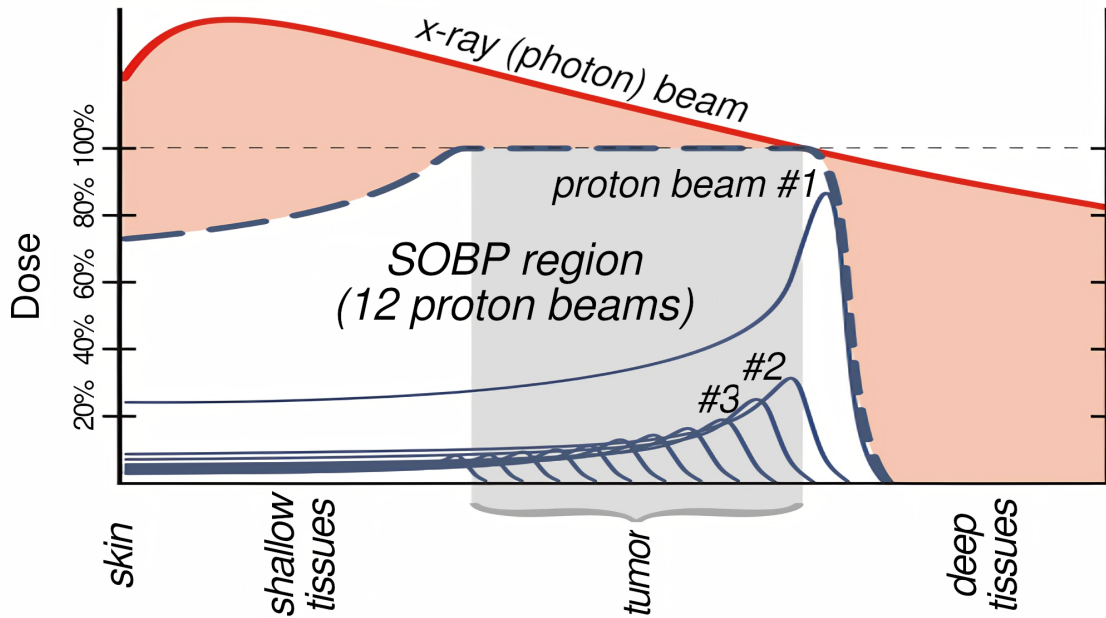


**Figure (1.16)** – Comparison of dose profiles for single protons, Spread Out Bragg Peak and x-ray radiotherapy

A Spread Out Bragg Peak is generated by varying the beam's energy with either passive or active modulations: in the first case it is done by placing layers of passive filtering material to degrade the beam energy to the desired value, while in the latter the target volume is divided into *voxels* that can be reached by equal beam energies and a pencil beam is then controlled by a magnetic scanning system that varies the beam's energy.

Due to the high spatial accuracy of the charged particle dose deposition, the PT treatment is more sensitive to uncertainty in the range of the beam than the conventional radiotherapy processing method.

A wrong range estimation can produce a shift in the position of the Bragg peak, leading to under-dosage in the tumor volume and over-dosage of healthy tissue placed before or after the tumor.

Common sources of error are patient movements (e.g. due to breathing), anatomic changes (e.g. due to tumor regression or patient weight loss) that have occurred during treatment sessions.

Models used in Treatment Planning System (TPS), which are computer based system used to calculate and optimize the treatment for each patient, take into account both this effects and the effects of nuclear fragmentation, as discussed in section 1.4.



## CHAPTER 2

---

### The FragmentatiOn Of Target experiment

---

Although currently a constant RBE value of 1.1 for protons is used in treatment planning, it is known that this quantity can actually vary depending on many parameters.

A physical process, which occurs when hadrontherapy beams pass through the human body, which is not taken into account with sufficient accuracy in any of the models currently available is that of nuclear fragmentation.

Depending on the type of particle used it is possible to get fragmentation of both the projectile or the target, causing the production of secondary particles and heavy fragments.

Unfortunately at present this effect is difficult to explore due to the missing cross sections measurements related to the production of heavy fragments induced by the proton irradiation with energies in the range of interest for particle therapy, with the only available measurements cover the light fragment ( $Z < 3$ ) production.

For this reasons the contribution of nuclear fragments is not included in any of the models for the RBE but simulations [23] have shown that this contribution can be very significant in some areas of the Bragg profile.

The fragmentation of ions on targets is also of interest in the field of radioprotection in space, with ESA, NASA and other space agencies doing risk assessment studies for their astronauts in view of long duration space missions [24].

## 2.1 Goals and motivations of the experiment

The *FragmentatiOn Of Target* (FOOT) experiment is a nuclear physics project approved and funded by the Istituto Nazionale di Fisica Nucleare (INFN) in 2017 with the aim of measuring the double differential cross sections related to nuclear fragmentation processes in an energy range typical of Hadrontherapy and space radiation protection.

To date, the project counts more than 100 members from 10 different INFN sections and involves several Italian and international laboratories and universities.

For the typical energy range used for therapeutic beam applications (50-250 MeV for protons and 50-400 MeV/u for carbon ions) the fragmentation process is not fully covered by experimental measures and it is necessary to rely on simulation models.

However, these simulations present several uncertainties because there is no exact analytical theory for these nuclear processes.

In recent years, some experiments have studied the effects of fragmentation of  $^{12}\text{C}$  ion projectiles, but such measurements have only been performed for a few energies in the lower part of the energy range of interest.

Therefore, the FOOT experiment was designed to perform a series of nuclear fragmentation cross-section measurements that will be used to improve the accuracy of Treatment Planning Systems for proton and ion therapy.

## 2.2 The inverse kinematics approach

A major experimental difficulty encountered in planning such an experiment is the very short range of fragments produced.

The fragment production reaction can be represented as

$$p + X \rightarrow X' + p' \quad (2.1)$$

where  $p$  are the protons and  $X$  the target nuclei undergoing inelastic interaction, and  $p'$  and  $X'$  are the protons and fragments produced after the interaction.

These fragments can travel at most only few tens or hundreds of  $\mu\text{m}$  which makes it difficult to detect them outside the target. A target thin enough to let the fragments outside would be too thin for any practical use and the interactions rates with the beam would be too low to get any significant statistics.

To overcome this difficulty the FOOT experiment uses the approach of inverse kinematics: the basic principle of this technique is the inversion of the roles of projectile and target within the reaction between protons and nuclei belonging to the human body.

For example, instead of shooting a proton beam on a tissue-like material (so rich in carbon or oxygen), tissue-like nuclei can be accelerated to the same kinetic energy and shoot on a fixed proton target: this results in a change from the *patient reference frame* to a new *laboratory reference frame*.

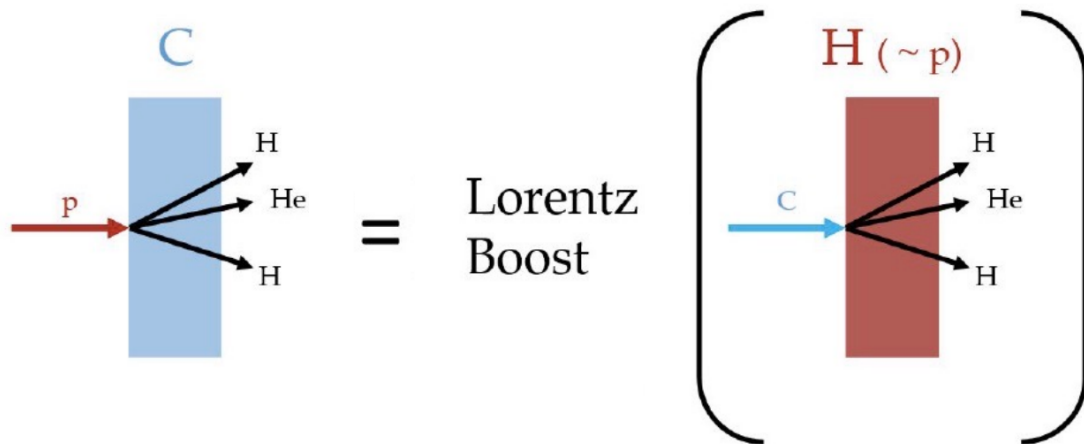


Figure (2.1) – Inverse kinematics strategy

By colliding beams with a kinetic energy of 100-200 MeV/u on the target, the kinetic energy of the fragments produced will be similar to that of the incident beam and their mean range will be much higher than in the direct kinematics approach.

It is then possible to obtain the cross-section of interest, i.e. the cross-section in which the proton beam strikes the materials making up the human body, by applying a Lorentz transformation.

Assuming the beam direction is towards the positive part the z-axis, we define  $S$  as the laboratory reference frame, where the ion beam moves along  $z$  with a constant  $\beta$  towards the fixed proton target, and  $S'$  the patient reference frame, where the heavy ions are at rest and the proton is moving along the  $z$  axis with the same  $\beta$ , but in opposite direction.

If  $E$  and  $E'$  are respectively the ion and the proton energies, their 4-momentum in the reference frame  $S$  will be  $\mathbf{P} = (E/c, p)$  and  $\mathbf{P}' = (E'/c, p')$ .

We can then express the components of the proton's 4-momentum in the frame  $S'$  as:

$$\left\{ \begin{array}{l} \frac{E'}{c} = \gamma \left( \frac{E}{c} - \beta p_z \right) \\ p'_x = p_x \\ p'_y = p_y \\ p'_z = \gamma \left( -\beta \frac{E}{c} + p_z \right) \end{array} \right. \quad (2.2)$$

Or, in a more compact matrix form as:

$$\mathbf{P}' = \Lambda \mathbf{P} \quad (2.3)$$

where  $\Lambda$  is the 4x4 matrix that represents the Lorentz transformation from  $S$  to  $S'$

$$\Lambda = \begin{pmatrix} \gamma & 0 & 0 & -\beta\gamma \\ 0 & 1 & 0 & 0 \\ 0 & 0 & 1 & 0 \\ -\beta\gamma & 0 & 0 & \gamma \end{pmatrix} \quad (2.4)$$

It is now possible to calculate the inverse Lorentz transformation  $\mathbf{P} = \Lambda^{-1} \mathbf{P}'$ , where the inverse matrix  $\Lambda^{-1}$  is

$$\Lambda^{-1} = \begin{pmatrix} \gamma & 0 & 0 & \beta\gamma \\ 0 & 1 & 0 & 0 \\ 0 & 0 & 1 & 0 \\ \beta\gamma & 0 & 0 & \gamma \end{pmatrix} \quad (2.5)$$

To properly apply Lorentz boost transformation, the described reverse kinematic strategy requires a resolution for the emission angles of the order of a few mrad, both for the projectile and the fragments. Additionally, target thickness density needs to be of the order of  $g/cm^2$  or less, in order to minimize the probability of secondary fragmentation within the target.

A good compromise to have a good level of interaction to acquire a sufficient number of events in a reasonable time frame while also minimizing the possibility of secondary fragmentation in the target has been found to be a thickness of about 2-10mm.

### 2.2.1 Double differential cross-sections

In view of the inverse kinematics approach, the FragmentatiOn Of Target experiment was designed with a fixed target setup: the beams of interest representative of human tissue will hit targets composed of carbon and hydrogen for the fragments to be detected and measured.

While a pure carbon target, in the form of a graphite block, is easy to obtain, a pure hydrogen target poses a series of challenges.

The use of hydrogen in a gaseous state would greatly reduce the probability of interaction with the beam particles, while the use of a liquid hydrogen target would imply the use of a special container to keep it in the right pressure/temperature conditions.

To overcome the difficulties of using a pure hydrogen target, a hydrogen-enriched target like  $C_2H_4$  (polyethylene), can be used.

The cross sections on hydrogen can be then retrieved by means of a subtraction technique between the cross sections for carbon and polyethylene targets

$$\sigma(H) = \frac{\sigma(C_2H_4) - 2\sigma(C)}{4} \quad (2.6)$$

or, in the case of differential cross sections

$$\frac{d\sigma}{dE}(H) = \frac{\frac{d\sigma}{dE}(C_2H_4) - 2\frac{d\sigma}{dE}(C)}{4} \quad \text{and} \quad \frac{d\sigma}{d\Omega}(H) = \frac{\frac{d\sigma}{d\Omega}(C_2H_4) - 2\frac{d\sigma}{d\Omega}(C)}{4} \quad (2.7)$$

This method has been already successfully adopted in the past [25] [26]: figure 2.2 shows the results obtained for a cross sections study involving a  $CH_2$  and  $C$  targets.

The main disadvantage of this method is that the resulting cross section uncertainties for hydrogen, coming from the quadratic sum of the uncertainties of the two single targets measurements, are affected by a larger error than would be achievable with a pure hydrogen target.

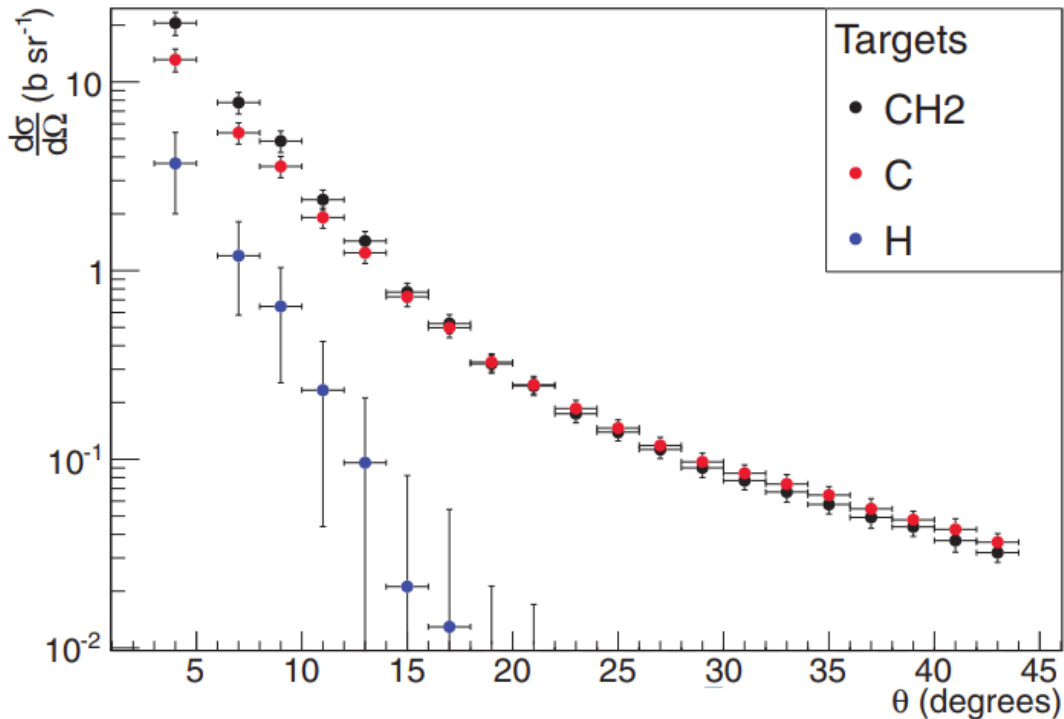


Figure (2.2) – Combination of carbon and  $CH_2$  targets angular distribution are used to determine the hydrogen angular distribution (from [26])

## 2.3 Experimental setups

The FOOT experimental apparatus has been designed to be easily transportable since it will use ion beams, in an energy range of 150 to 400 MeV/u.

Data will be acquired in various Hadrontherapy centres in Europe, like the Centro Nazionale di Adroterapia Oncologica in Pavia (Italy) and the GSI Helmholtz Centre for Heavy Ion Research in Darmstadt (Germany) to name but a few.

This also implies important space constraints: the apparatus will have to be placed inside several treatment and experimental rooms, so its overall length will not exceed 2-4 metres, in a "table top" configuration.

Two different configurations are foreseen: one with electronic detectors for the measurement of heavier fragments and one mainly based on an emulsion chamber for the measurement of lighter fragments.

**Setup for heavy fragments** : based on a magnetic spectrometer, it is optimized for fragments heavier than  ${}^4\text{He}$ .

This configuration is characterised by an angular acceptance of about  $10^\circ$  with respect to the axis of the primary beam

**Setup for light fragments** : based on an emulsion chamber as already tested in the past with the FIRST experiment [27], it is optimized for light fragments such as protons, deuterons, tritium or He nuclei.

This configuration has an angular acceptance of  $70^\circ$  with respect to the beam direction.

Preliminary MC simulations during the design, construction and operation phases have been performed with FLUKA (FLUktuierende KAskade) [28] [29] a general simulation tool widely employed in different physics branches.

When performing a simulation, FLUKA takes into account both electromagnetic physical processes and hadronic interactions, adopting the microscopic models whenever possible and continuously benchmarking against latest experimental data in each new release.

One of the field in which FLUKA is particularly used due to this characteristic is in Particle Therapy studies [30].

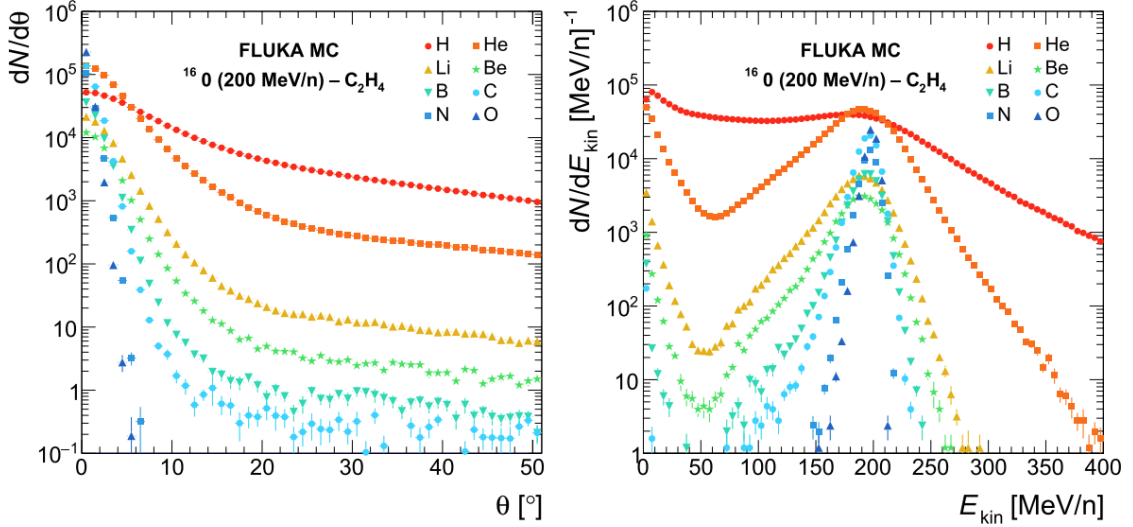


**Figure (2.3)** – MC calculation of the angular (left) and kinetic energy (right) distributions of different fragments produced by a 200 MeV/nucleon  $^{16}\text{O}$  beam impinging on a  $\text{C}_2\text{H}_4$  target (from [31])

### 2.3.1 Electronic detector setup

The adoption of the inverse kinematics approach requires for a few % level accuracy on the measurement of the energy and momenta of the produced fragments, together with an emission angle resolution with respect to the beam of the order of few mrad.

To achieve such an angular resolution, both the beam particles direction before the target and the fragment emission angle after the target must be tracked with an angular accuracy at the mrad level.

The setup has been designed to perform, for each fragment, redundant measurements of independent quantities, all with adequate accuracy to achieve a low error in the measurements of the double differential cross sections of interest.

The charge of each fragment can be identified by combining the  $\Delta E$  measurements with TOF or kinetic energy, while the mass can be extracted by momentum and kinetic energy measurements.

The performances that FOOT aims to achieve are [32]:

- Momentum resolution  $\sigma(p)/p$  of 5%
- Kinetic energy resolution of the fragments  $\sigma(E_{kin})/E_{kin}$  of 2%
- Fragments' energy resolution  $\sigma(E)/E$  of 2%
- Fragments' Time-Of-Flight resolution of 100 ps

The detector geometry is based on two main factors: the emission angle of the heavy fragments and the angular separation between two fragments emitted in the same events, with the former dictating the needed angular acceptance while the latter gives constraints on the granularity of the measurements.

Most of the the design of the detectors was thus driven by the FLUKA simulation of the expected fragmentation angular distributions for different fragments produced (fig. 2.3) and their angular separation.

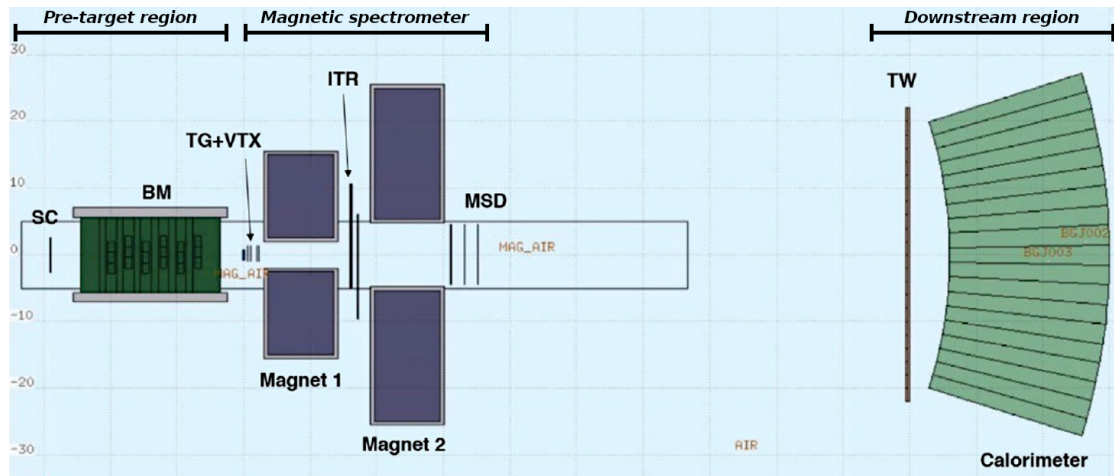


*Figure (2.4) – Schematic view of the FOOT electronic detectors setup generated from MC geometry with FLAIR [33]*

The total length of the apparatus can be varied between 1 and 4 meters according to the energy of the beam and three different regions can be identified for the electronic configuration: the *pre-target region*, the *magnetic spectrometer* and the *downstream region* (fig. 2.4).

### Pre-target region

The pre-target region is composed of detectors that reconstruct the incoming primary particle track, provide the beam's direction and part of the triggering system

- **Start Counter (SC)**

The SC consists of a sheet of EJ-228 plastic scintillator  $250\mu\text{m}$  thick with a  $5 \times 5\text{cm}^2$  active area, placed about 30 cm before the target by means of an aluminum frame enclosed in a black 3D printed box to provide the light tightness.

The scintillation light is collected by 48 *AdvanSiD ASD-NUV3S-P* Silicon Photo Multipliers [34], biased and readout in 8 groups [35] by *WaveDAQ* [36] system.

The SC monitors the rate of the primary particles, provides the trigger signal for acquisition and gives the start time of the event.

The latter information, together with the time reported by the scintillator in the downstream region, provides the time-of-flight (ToF) measurement.

Since the measurement of ToF is crucial to be able to identify the mass of the fragments with sufficient resolution, the Start Counter it's expected to guarantee a time resolution of about 60 ps.

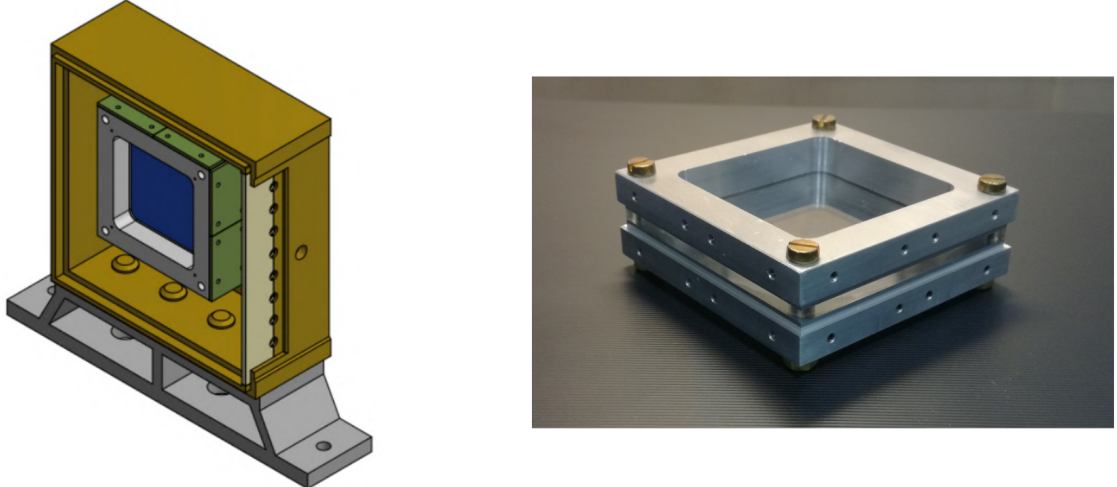


*Figure (2.5) – CAD of the Start Counter in its holder box (left) and photo of its mechanical frame (right)*

- **Beam Monitor (BM)**

The Beam Monitor consists of a drift chamber filled with 80/20% Ar/CO<sub>2</sub> gas and composed of 12 alternating horizontal and vertical wire planes enclosed by two films of mylar with a thickness of 100  $\mu\text{m}$  placed at the beam entrance and exit.

Originally built for the FIRST experiment [37], the drift chamber was chosen due to the low density of the gas, as it minimises multiple Coulomb scattering and the production of fragments inside the detector.

Twelve dedicated front-end electronic boards are adopted to read all the sense wire signals.

The function of the Beam Monitor is to measure the direction and point of impact of the beam on the target, which is necessary to resolve the ambiguity due to pile-up in the vertex detector.

The calibration and the performance assessment of the detector resulted in a spatial resolution of about 100  $\mu\text{m}$  in the central part of the cell and a related angular resolution of the order of few mrad, with an hit detection efficiency of  $\approx 93\%$  [38]

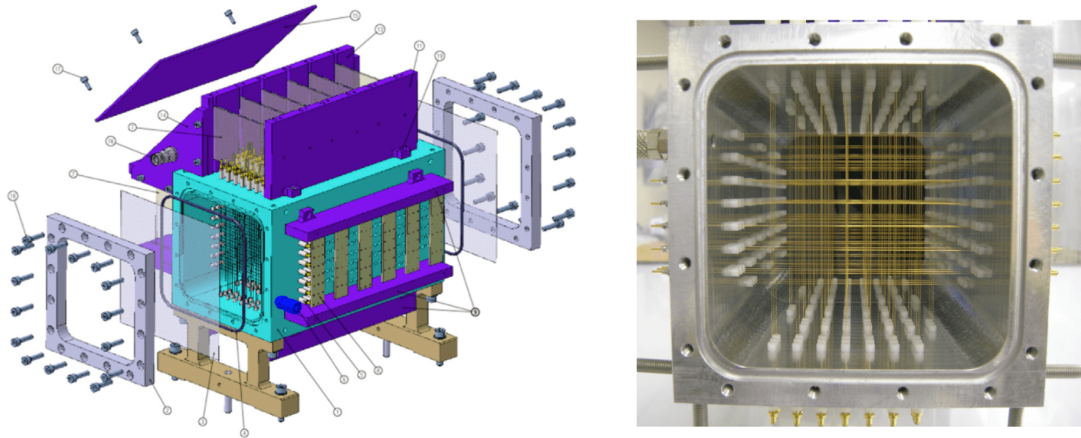


*Figure (2.6) – Technical drawing of the Beam Monitor (left) and photo of its inside (right)*

## Magnetic spectrometer

The magnetic spectrometer includes pixel and microstrip detector together with permanent magnet system that provides the required magnetic field.

It is designed to measure the fragments production vertex and momentum.

- **Vertex Detector (VTX)**

The VTX detector is composed of four layers of  $50\mu\text{m}$  thick silicon pixel detectors placed just after the target, for a resulting geometrical acceptance of about  $40^\circ$ .

Each layer is equipped with a MIMOSA-28 Monolithic Active Pixel Sensor (previously known as ULTIMATE and originally developed for the STAR pixel detector [39][40]) composed by  $928 \times 960$  pixels with a  $20.7\mu\text{m}$  pitch, for a total sensitive area of  $20.22\text{mm} \times 22.71\text{mm}$ .

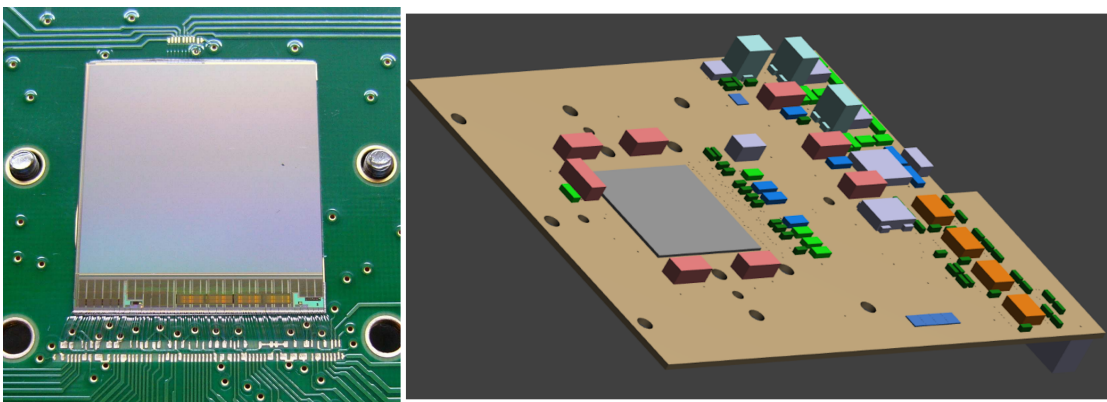


*Figure (2.7) – Close up of one of the MIMOSA-28 CMOS sensors (left) and technical drawing of one of the VTX boards (right)*

Each pixel includes an amplification and a Correlated Double Sampling (CDS) circuit that, with a binary readout and a zero suppression in-chip logic to reduce the amount of data transferred for each  $185.6\mu\text{s}$  frame time.

The VTX contributes to the measurement of the particles momentum in the magnetic field and will evaluate for each event the vertex of interaction inside the target.

By means of dedicated reconstruction clusterization algorithms an accuracy of  $< 5\mu\text{m}$  on the particle position can be achieved.

The VTX readout has been implemented by means of a DE10 board housing an Intel System-on-Chip (SoC) FPGA (Cyclon V) with a dual-core CortexA9 CPU [41].

- **Permanent Magnet (PM)**

The Permanent Magnet is the key element for the FOOT spectrometer, used to bend the fragments produced in the target making the particles momentum detection possible.

While a magnetic dipole in vacuum with two tracking stations placed at the extremities would provide the needed momentum resolution, the solution is not viable for a portable table top experiment: for this reason a magnetic system in air composed of two magnets in Halbach configuration was chosen.

In a Halbach configuration, the magnetic field increases with the external cylinder radius while decreases with the gap radius.

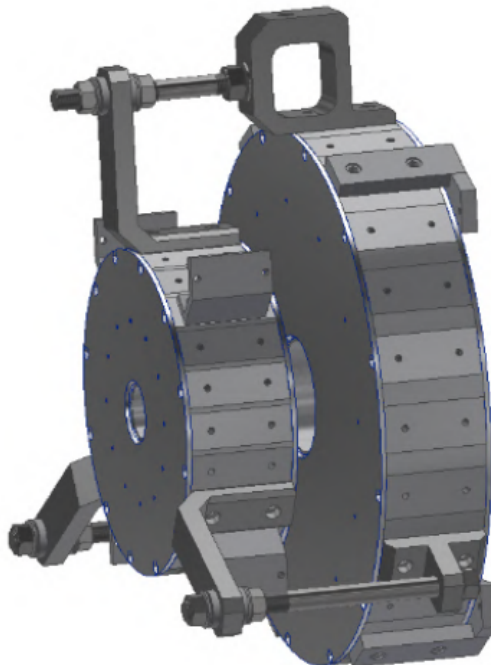


*Figure (2.8) – Technical drawing of the two magnets in their containing structure*

In order to match the final momentum resolution needed while also maintaining an angular acceptance of  $10^\circ$  for the emitted fragments, two different magnet dimensions have been chosen.

The first upstream magnet, close to the vertex detector, has an internal diameter of 5 cm and it provides a maximum magnetic field of 1.4 T. The second magnet has a gap diameter of 10.6 cm and the maximum magnetic field is of 0.9 T. Considering the axis of the magnets coincident to the  $z$ -axis, the chosen configuration of the Halbach array gives a dipolar field with the main component directed along the  $y$ -axis.

A gap of 50 cm between the two magnets is left where the Inner Tracker detector is installed. Each magnet is composed of twelve single pieces of  $Sm_2Co_{17}$ , selected for its capability to maintain its magnetic properties even in a high radiation environment [42].

The two magnets will be assembled into a single mechanical structure that is robust enough to withstand the generated magnetic force and ensure high accuracy in the alignment with the tracking stations.

The ability to move the magnets about 40 cm perpendicular to the beamline will give the ability to align the tracking stations in dedicated runs without bending the primary particles of the beam.

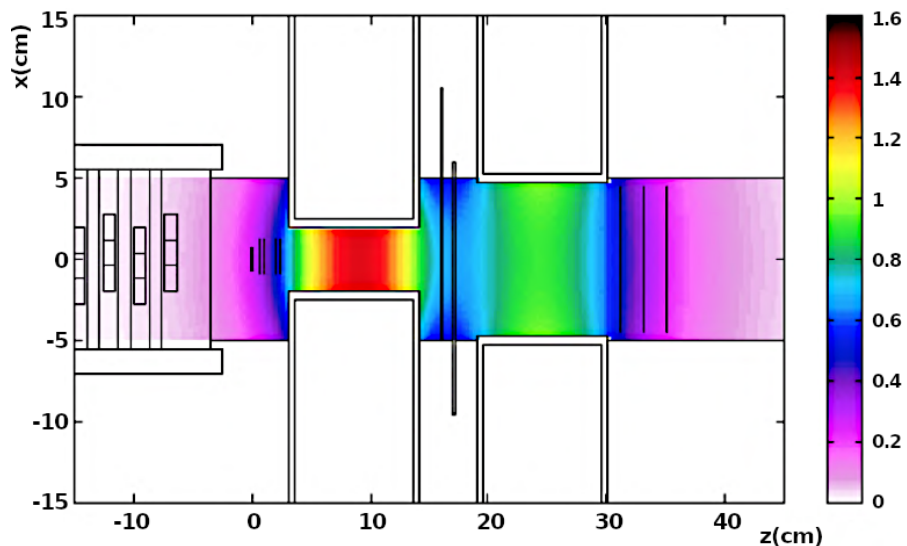


*Figure (2.9) – Computed magnetic field map of the two permanent magnets*

- **Inner Tracker (ITR)**

The Inner Tracker (ITR) is the second station of the magnetic spectrometer and is placed between the two permanent magnets.

It adopts the same M28 sensor as the VTX detector. The choice of the M28 sensors was made because they are not expected to be significantly affected by the foreseen residual magnetic field in between the permanent magnets [43].

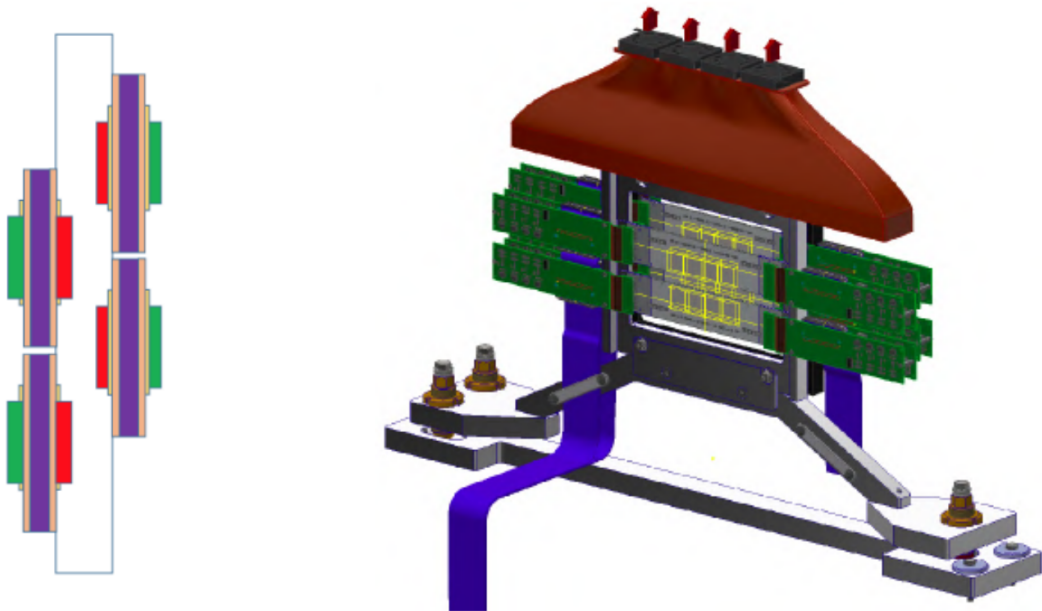


*Figure (2.10) – Scheme of the top view of the ITR (left) and technical drawings of the assembled detector (right)*

However, since the fragment spatial distribution is broader between the magnets than at the VTX position, the area to be covered is larger: this required a different arrangement of the sensors, with two planes of pixel sensors, each one characterized by a sensitive area of  $8\text{cm}^2$

Each plane is composed of two ladders similar to the ones implemented in the PLUME project [44] with eight M28 sensors, four on each side, glued on a 2 mm thick support structure made of low density silicon carbide (*SiC*) foam, supported by a mechanical frame.

To minimize the horizontal dead area the distance between two consecutive M28 sensors in the same module is about  $30\ \mu\text{m}$ , with all the sensors then glued and bonded on a kapton-metal flex cable that provides the communication with the outside world.

- **Microstrip Silicon Detector (MSD)**

The Microstrip Silicon Detector (MSD) is the last station of the FOOT magnetic spectrometer, composed of three layers of silicon microstrip detectors placed after the two permanent magnets.

It will be mainly used to reconstruct the position of the fragments with a spatial resolution  $< 35\mu\text{m}$ , to match the reconstructed tracks with the downstream scintillator and calorimeter hits, with the possibility to also give a redundant measurement of the energy release  $\Delta E$  of the particles, complementing the measurements performed by the Tof-Wall scintillator necessary for the charge identification of the fragments.

The tracking station consists of three MSD x-y planes with an active area of  $9.6 \times 9.3\text{cm}^2$ , separated by a 2 cm gap along the beam direction, to ensure the needed angular acceptance to measure ions with  $Z > 2$ .

In order to reduce the amount of material two perpendicular Single-Sided Silicon Detector (SSSD) sensors thinned down to  $150\ \mu\text{m}$  are used for each MSD x-y plane, each glued on a hybrid PCB that provides the needed mechanical support and the interface with the readout, and with light tightness of each plane ensured using only the metallized sensors backplane.

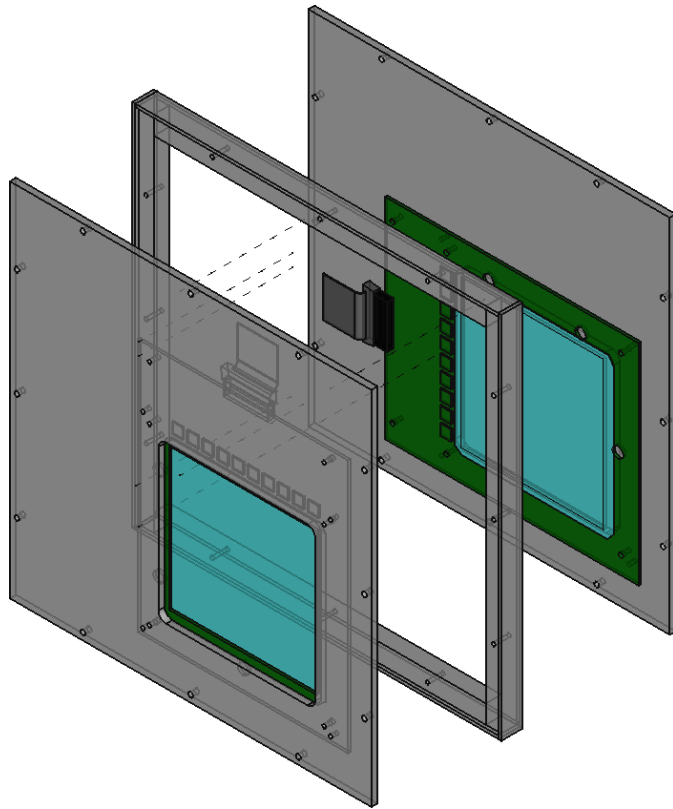


*Figure (2.11) – Exploded view of one of the MSD X-Y planes*

### Downstream region

It is the final part of the setup and consists of two orthogonal planes of plastic scintillator rods that allow TOF stop signal and energy loss measurements, and a BGO calorimeter that provides kinetic energy measurements of the fragments.

Depending on the primary beam energy, the distance to the target position changes from about 1 m to about 3 m to increase the lever arm, improving fragment estimation.

- **TOF-Wall Scintillator (TW)**

The TOF-Wall is composed of two layers of 20 orthogonally oriented plastic scintillator bars made of EJ-200. Each bar is 0.3cm thick, 2cm wide and 44cm long, wrapped with reflective aluminum and darkening black tape [45].

The thickness of the bar has been chosen as a compromise between the require-

ments on the energy resolution and the necessity to reduce the secondary fragmentation probability, while the channel granularity was chosen according to the fragments expected separation.

The total detector active area is then of  $40 \times 40\text{cm}^2$ , corresponding to an angular aperture of  $10^\circ$  at 1 m from the target.

The bars are coupled at the two edges to four SiPMs with a  $3 \times 3\text{mm}^2$  active area and  $25\ \mu\text{m}$  microcell pitch. The channels are then digitized at rates up to 5 Gsamples/s by the WaveDAQ system.

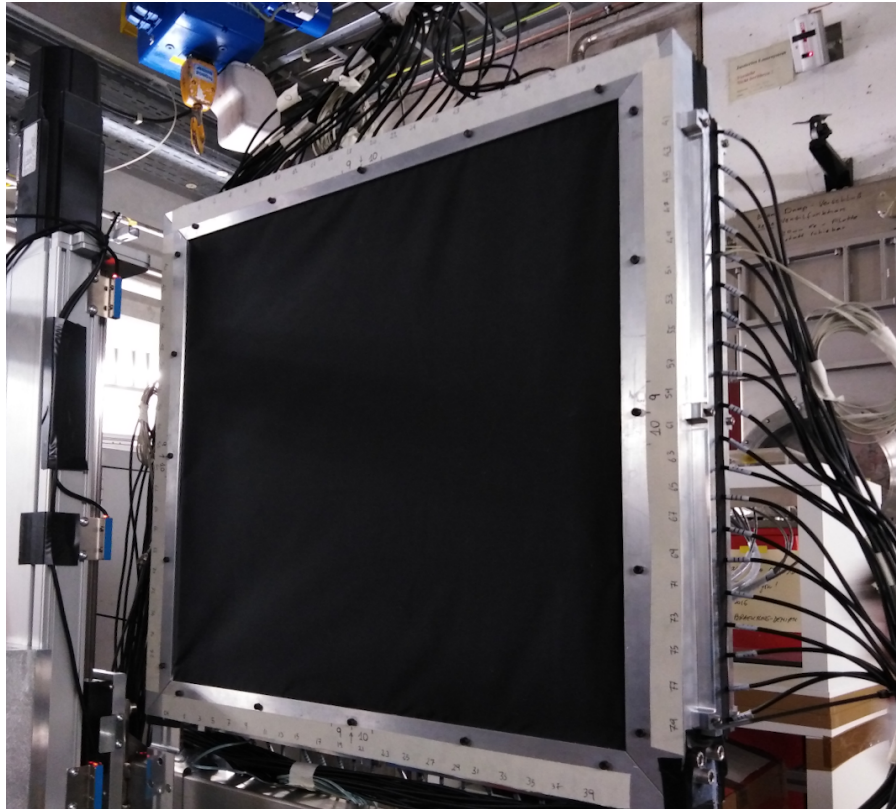


*Figure (2.12) – The assembled TOF-Wall detector*

The high number ( $4 \times 14400$ ) of pixels per channel of the SiPM result in a dynamic range spanning over two orders of magnitude and allow the identification of fragments from proton to oxygen with different kinetic energies, with a resolution on the TOF and energy measurements better than 100 ps and 5% for the heavier fragments, respectively [46].

- **Calorimeter (CAL)**

The calorimeter is the most downstream detector, placed just beyond the TW, designed to measure the fragments kinetic energy needed to compute their mass. Since FOOT will work at a relatively low beam intensity, the ideal material for the calorimeter was a dense crystal, with high light yield and no strict requirements on the response speed.

The high density of the  $320\ Bi_4Ge_3O_{12}$  (BGO) crystals ( $\rho = 7.13\text{g/cm}^3$ ), guarantees a high stopping power, that, coupled to a light yield of  $\approx 10\ \text{photon/keV}$ , meets such requirements.

Each bar composing the calorimeter has a truncated pyramid shape with a front face of about  $2 \times 2\text{cm}^2$ , a back face of about  $3 \times 3\text{cm}^2$  and a length of 24 cm.

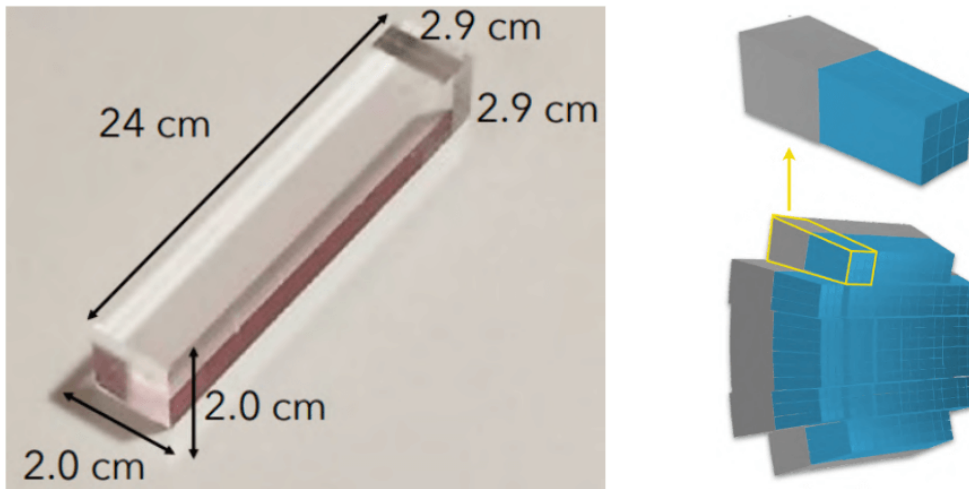


*Figure (2.13) – One of the BGO crystals without its wrapping (left) and a schematic view of the FOOT calorimeter arrangement (right), with the crystals (in blue) housed in their supports (in grey)*

The signal of each crystal is collected by a matrix of 25 SiPMs with an active surface of  $2 \times 2\text{cm}^2$  and a microcell pitch of  $15\ \mu\text{m}$  that provides a linear response in the energy range up to 10 GeV [47].

Each SiPM matrix is coupled to a readout board designed to match the dimensions of the SiPMs with integrated temperature sensors.

The Front-end boards are then interfaced with the WaveDAQ system as the SC and TW detectors, with the signal sampled at 1 Gsample/s, allowing a measurement based on both the signal amplitude and its integral, as well as a shape analysis.

Several tests have been performed in a wide energy range in order to choose the optimal combination of SiPM array, readout configuration and BGO wrappings materials.

A very good linearity response is achieved in the whole investigated energy range and the measured energy resolution is below 2%, meeting the experiment requirements [48][49].

### Trigger and data acquisition system

The Data Acquisition (DAQ) system designed for the FOOT electronic setup is designed to acquire the largest sample size with a high accuracy in a controlled and online-monitored environment.

To avoid any source of systematic errors due to the trigger selection, the SC detector, which is the fastest detector of the electronic setup, is used to generate a *Minimum Bias Trigger* for the data acquisition, with a trigger fired whenever the multiplicity of the readout channel group above thresholds exceeds a programmable value (*Majority Trigger*).

When needed, a fragmentation trigger asking for signals outside the central bars of the TW can also be used, in addition to a prescaled Minimum Bias trigger, to enhance the fraction of recorded fragmentation events.

All the trigger logics are managed by a fully programmable CAEN V2495 board [50].

The maximum acquisition rate in Minimum Bias modality is dictated by the slowest detectors of the electronic setup, which is the MIMOSA 28 chips in the VTX and ITR, with a frame readout time of 180  $\mu$ s.

Therefore the electronic setup can operate at a theoretical maximum rate of about 5 kHz, with a foreseen 1 kHz target acquisition rate to avoid pile up in the pixel detectors.

The DAQ system uses a flexible hierarchical distributed system based on specific detector read out systems paired to different computers that communicate through

optical fibers, USB and Ethernet cables, as showed in figure 2.14.

The system control is hosted on a master PC used to run the DAQ GUI interface to start/stop a single run, control and configure other nodes in the system and collect data from the various subsystems. An Ethernet switch connected to the master PC is used to collect all the data from the detectors via 1Gbps ethernet connections to each the detector specific readout systems:

- the tracking system, based on terasic's DE10[41] (for the VTX and the ITR) and De10-Nano[51] (for the MSD)
- the WaveDAQ system (for the SC, TW and CAL)
- a VME to PCI Optical Link (for the trigger logic board and the BM readout)

The DAQ system is also equipped with a set of online monitoring tools that can collect run related information from each VME board or readout system at a rate  $\approx$ Hz, depending on the specific sub-detector system, and provide them to the network of PCs connected to the experiment.

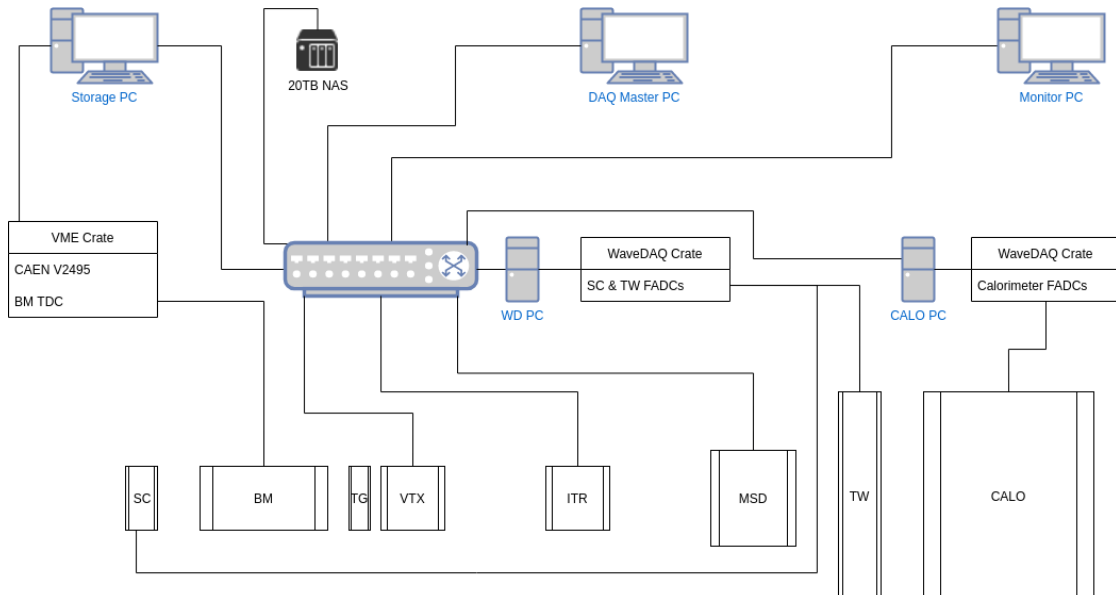


*Figure (2.14) – DAQ logical scheme*

A storage PC is used during the data taking to collect all the detectors data on a

fast SSD disk at a maximum rate of 400 MB/s. The data are sent in a second phase to a dedicated NAS system ( $> 20$  TB) to store all the FOOT experiment measurements.

### 2.3.2 Emulsion spectrometer

An emulsion spectrometer (ES) was included in the FOOT setup to characterize the production of low Z fragments ( $Z \leq 3$ ) with an angular acceptance increased to approximately  $70^\circ$ .

The ability of these kind of detectors to separate and measure the various fragments produced by ion beams at therapeutic energies has already been demonstrated [52] thanks to their high spatial resolution (sub-micrometer) when tracking ionizing particles.

The ES is placed behind the SC and BM that are used for beam monitoring purposes and to control the beam flux on the ES active surface to avoid spatial pile up of events.

The emulsion film used in the FOOT experiment are similar to the those used in the OPERA experiment [53], and consists of two  $70\text{ }\mu\text{m}$  thick sensitive layers made of  $0.2\text{ }\mu\text{m}$   $\text{AgBr}$  crystals dispersed in a gelatin binder and placed on either side of a  $210\text{ }\mu\text{m}$  plastic base, for a total thickness of  $350\text{ }\mu\text{m}$  and an area of  $12 \times 10\text{cm}^2$ .

The ES will be placed on a remotely controlled table allowing the detector to be moved in a plane horizontal to the direction of the incident beam, to evenly distribute the beam across the surface of the ES.

When a ionizing particle passes through the nuclear emulsion film it creates a latent image that, after a chemical process called *development*, transforms into a series of clusters of silver particles called *grains*, that have an average diameter of  $0.6\text{ }\mu\text{m}$ .

Grain density is proportional to the ionization of charged particles in the detector's dynamic range with a value of about 30 to 50 grains/ $100\text{ }\mu\text{m}$  for a minimum ionizing particle [54].

To measure the energy loss of highly ionizing particles such as carbon ions, after exposure and before development, the emulsion film are treated with an additional process called *refreshing*: by keeping the films at a certain temperature ( $> 30^\circ\text{C}$ ) and relative humidity ( $\approx 98\%$ ), tracks from particles with lower ionization strength are

partially or completely removed.

The separation of particles with different ionizing strengths, and therefore with different charges, can be accomplished by combining data from several films that have undergone different refreshing treatments (figure 2.15).

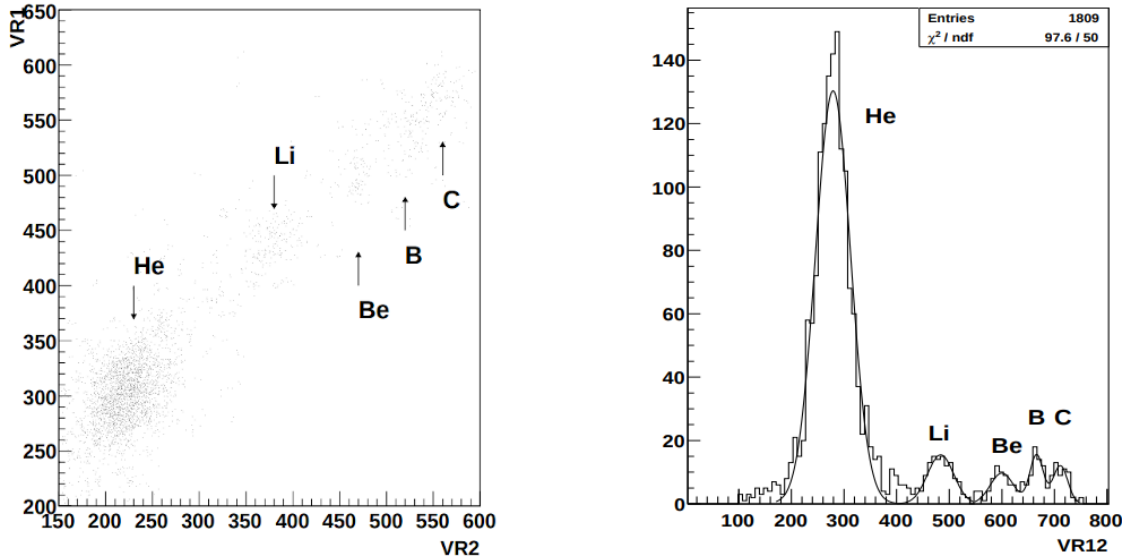


**Figure (2.15)** – Separation between He, Li, Be, B and C ions from the fragmentation of carbon nuclei in an emulsion chamber (from [54])

After development, the emulsions are scanned using an automated system running on GPUs [55].

The resulting image is then analyzed with specialized software to recognize aligned dark pixel clusters, that represent the tracks produced by the impinging particle.

A straight sequence of pixels in the emulsion defines a *micro-track*. Two aligned micro-tracks belonging to the upper and lower layers of the emulsion film form a *base-track* that has accuracy of about  $0.3\mu\text{m}$  for the position and of about  $1.2\text{ mrad}$  for the angle.

Base-tracks aligned along different films are connected to form *volume-tracks* and the propagation of segments from one emulsion layer to another reconstructs the particle track in the detector.

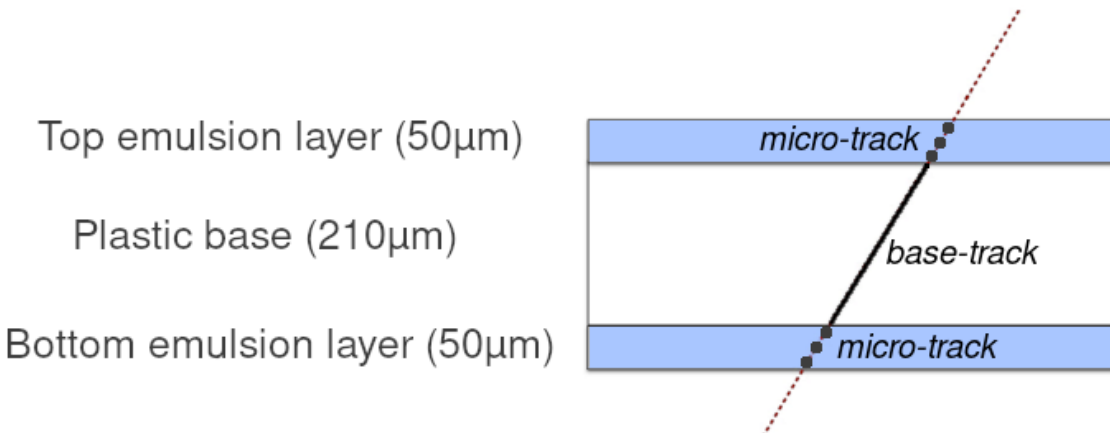


**Figure (2.16)** – Scheme of the track reconstruction of a charged particle traversing an emulsion film

The Emulsion Spectrometer for the FOOT experiment has been designed with passive materials alternated to nuclear emulsions films, divided into three sections with different purposes:

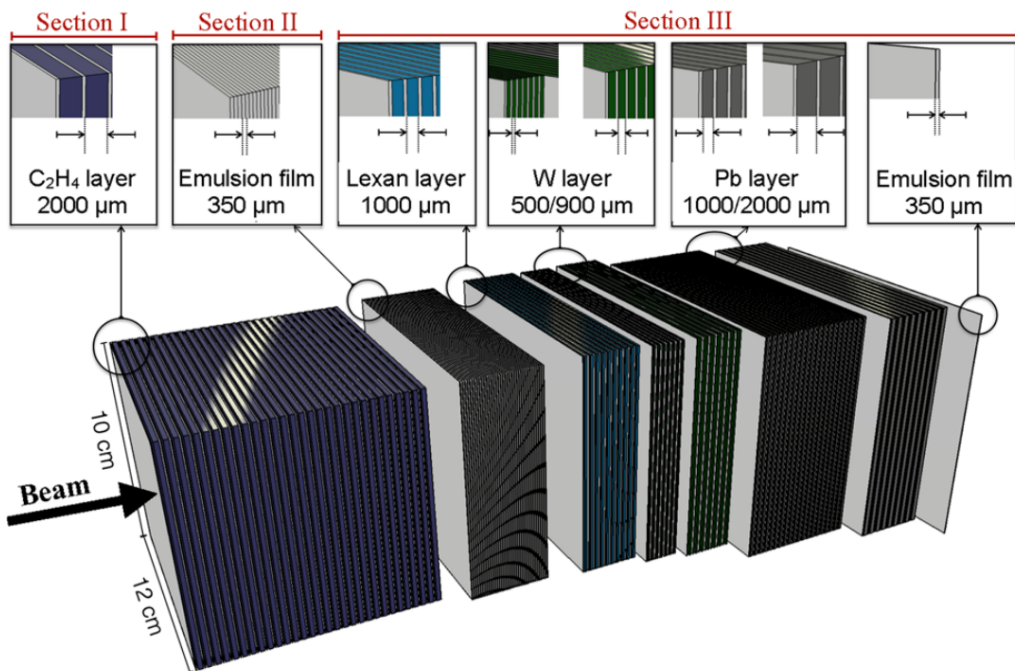


**Figure (2.17)** – Structure of the emulsion spectrometer (from [56])

- **Interaction and vertexing region** The first section consists of several unit cells composed of a layer of target material, carbon or  $C_2H_4$ , alternating with an emulsion film.

Whenever the ion beam interacts within the cells of this section, a secondary fragment is emitted and detected by the following regions of the spectrometer, enabling the reconstruction of the interaction vertex and position.

The length of this spectrometer section is optimized for each data taking according to MC simulation based on FLUKA code, to achieve a statistically significant number of interactions.

- **Charge identification region** The second section is entirely composed of emulsion films, which aim to reconstruct the charge of lighter fragments (H, He, Li).

The energy loss of the fragments, and hence their charge, can be reconstructed from the density of the grains.

The combination of several films, which have undergone different refreshment treatments after exposure, makes it possible to overcome the influence of saturation for particles with different ionizations, extending the dynamic range of the emulsions.

The elementary cells consists of four emulsion films, each of which is treated at different temperatures during the refresh process.

- **Momentum measurement region** The last section is composed of emulsion films interleaved with layers of passive absorbers made of high-Z material such as Lexan, W and Pb, with the lower Z passive layers placed at the beginning of the stack and the higher Z layers at the end.

The section length, the number of passive layers and their thicknesses are set according to the incident beam energy.

Measuring the length of the whole particle track, its momentum will be estimated on the basis of the correlation between range and kinetic energy.

The fragments momentum can be instead estimated through the Multiple Coulomb Scattering method [57][58].

The range and MCS methods are two independent procedures to measure energy and momentum, thus allowing for isotopic determination of the fragments.

## 2.4 Expected performances

To evaluate the experiment expected performances, the complete detector geometry and materials are simulated to properly assess interactions in all active detectors and secondary particle production in off-target fragmentation processes for different combinations of ion beams, beam kinetic energy and targets.

The Monte Carlo simulation measurements provide the fundamental quantities related to each FOOT detector sub-system: times in SC, fired cells in BM, fired pixels in VTX and ITR detectors, energy released in MSD strips, and time and energy released in TW bars and calorimeter crystals.

The reconstruction of the quantities of interest, like hits, clusters, tracks, TOF, fragment charge Z and kinetic energy, is performed locally for each detector.

To estimate the detector capability in identifying the fragments in terms of charge and mass, the experimental resolutions of the fundamental quantities necessary for particle identification, when available, have been included in the MC simulation by means of a Gaussian smearing.

The Time Of Flight (TOF), energy loss ( $\Delta E$ ) and kinetic energy ( $E_{kin}$ ) resolutions implemented in the simulation have been extracted from the results obtained during specific test beams for SC, TW and for calorimeter.

Momentum ( $p$ ) resolution has been evaluated by means of dedicated MC simulations using a standard Kalman tracking algorithm.

The resolution obtained for the quantities of interest are thus

- $\sigma(p)/p \approx 3 - 5\%$
- $\sigma(TOF) \approx 70 - 250 ps$
- $\sigma(E_{kin})/E_{kin} \approx 1.5 - 2.5\%$
- $(\Delta E)/\Delta E \approx 3 - 10\%$

where the best performances are obtained for the heaviest fragments.

The measurements of all the quantities allows the identification of a nuclear fragment

by reconstructing its charge and mass number: the charge  $Z$  of the fragment is measured by means of the TW detector, as shown in figure 2.18.

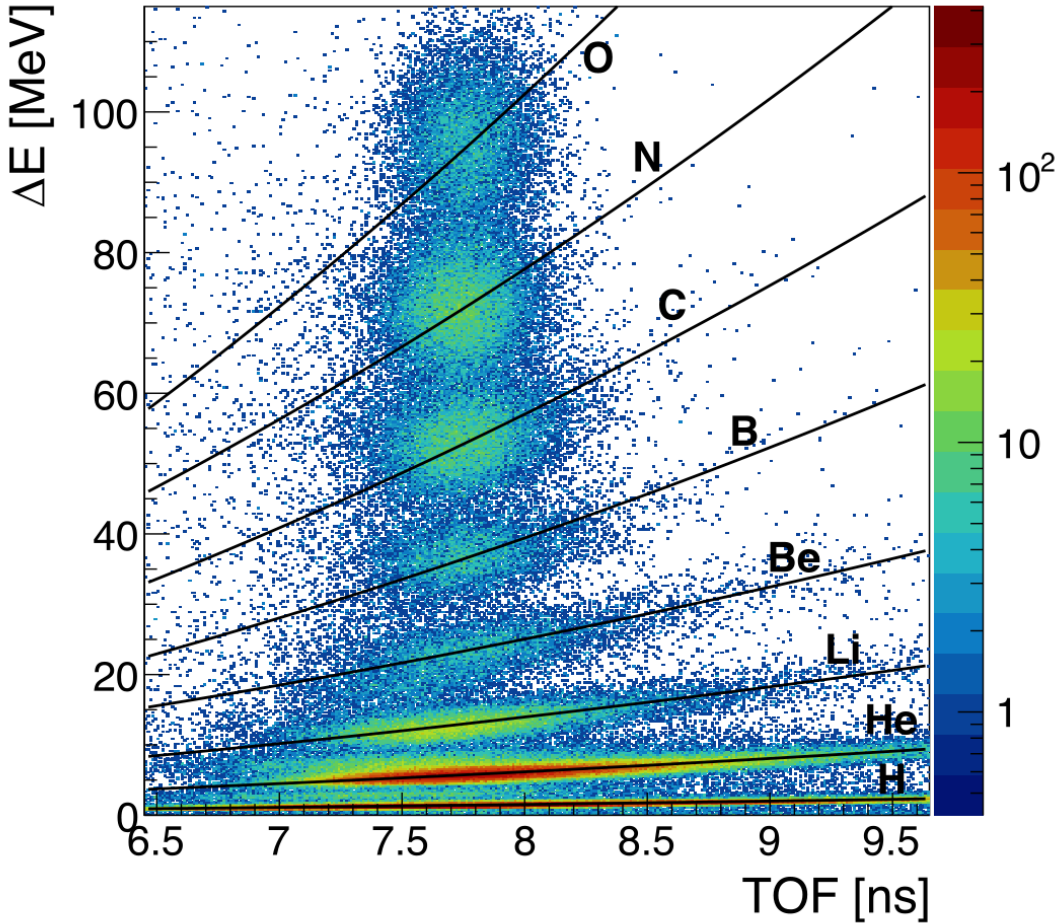


*Figure (2.18) – Fragments charge identification in TW using the energy release in the scintillators  $\Delta E$  and the TOF calculation performed together to the SC (from [31])*

The TW resolution allows the discrimination of eight regions in the  $\Delta E$ -TOF plane, related to different fragment charges.

For each region a Bethe-Bloch curve, parametrized as a function of the *time of flight* measured by the detector, can be used to fit the MC simulation results to describe the average energy loss of fragments of the same charge  $Z$  impinging on TW with different angles, kinetic energies, TOF and path lengths  $L$ .

For each fragment it is then possible to choose the closest Bethe-Bloch curve in the  $\Delta E - TOF$  plane to retrieve the charge, with a fragment charge mis-identification  $< 4\%$ .

The fragments charge measurement, when coupled to the rigidity ( $p/Z$ ) provided by the magnetic spectrometer, allows to compute the momentum  $p$ .

By using the measurement of  $p$ ,  $TOF$  and  $E_{kin}$  it is then possible to have three different, correlated, measurements of the fragment mass, with the mass identification resolution directly related to the precision achieved on  $p$ ,  $TOF$  and  $E_{kin}$ .

Figure 2.19 shows the carbon isotopes mass resolution dependence on each of the three parameters ( $TOF$ ,  $p$ ,  $E_{kin}$ ).

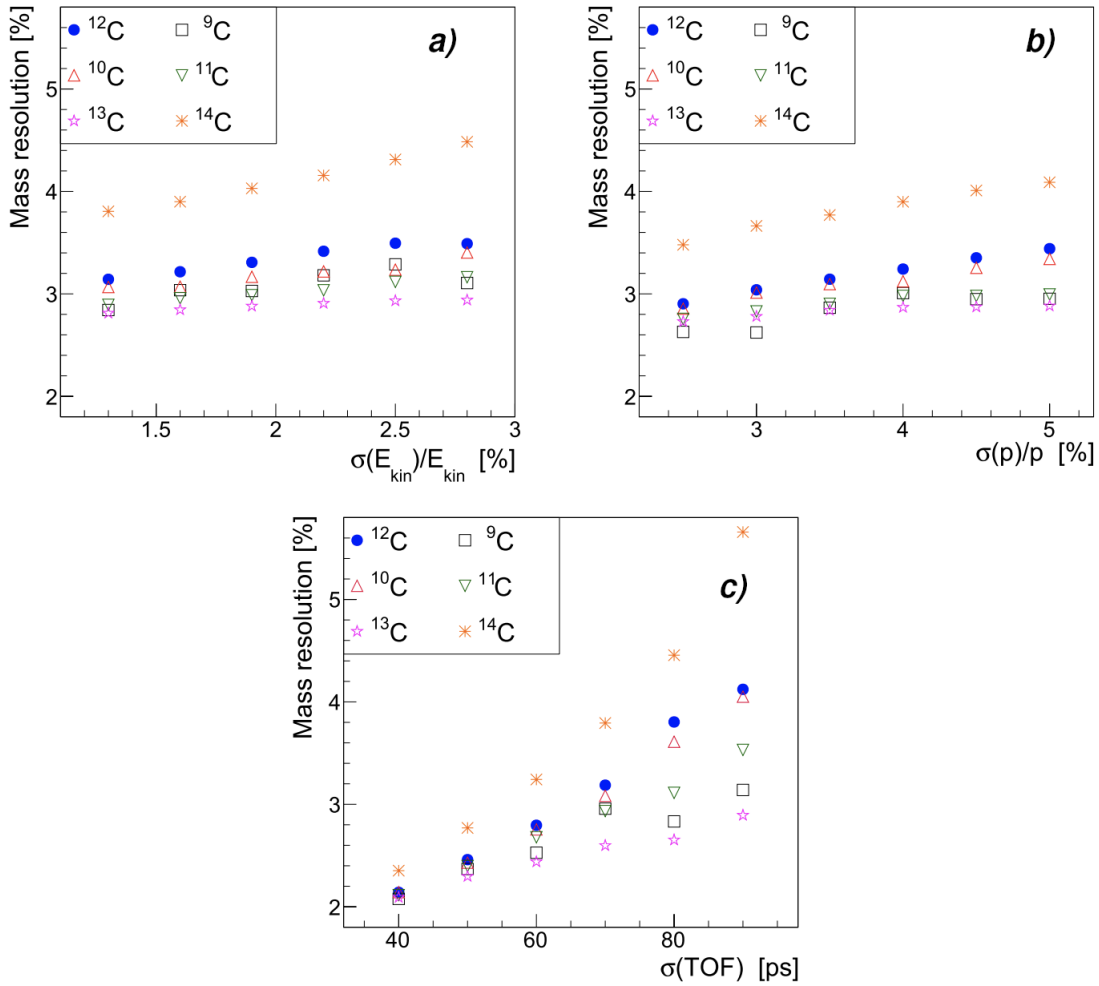


**Figure (2.19)** – Mass resolution of the identified isotopes of carbon ions as a function of: a) kinetic energy resolution b) momentum resolution and c) carbon ions TOF (from [31])

In order to get the best mass estimation, taking advantage of the measurement redundancy, a standard  $\chi^2$  minimization approach or an Augmented Lagrangian Method (ALM) [59] approach can be pursued, performing a fit to the mass values.

The two fit procedures lead to compatible results, and the final mass resolution ranges between 3% for  ${}^1C$  to 6% for protons.

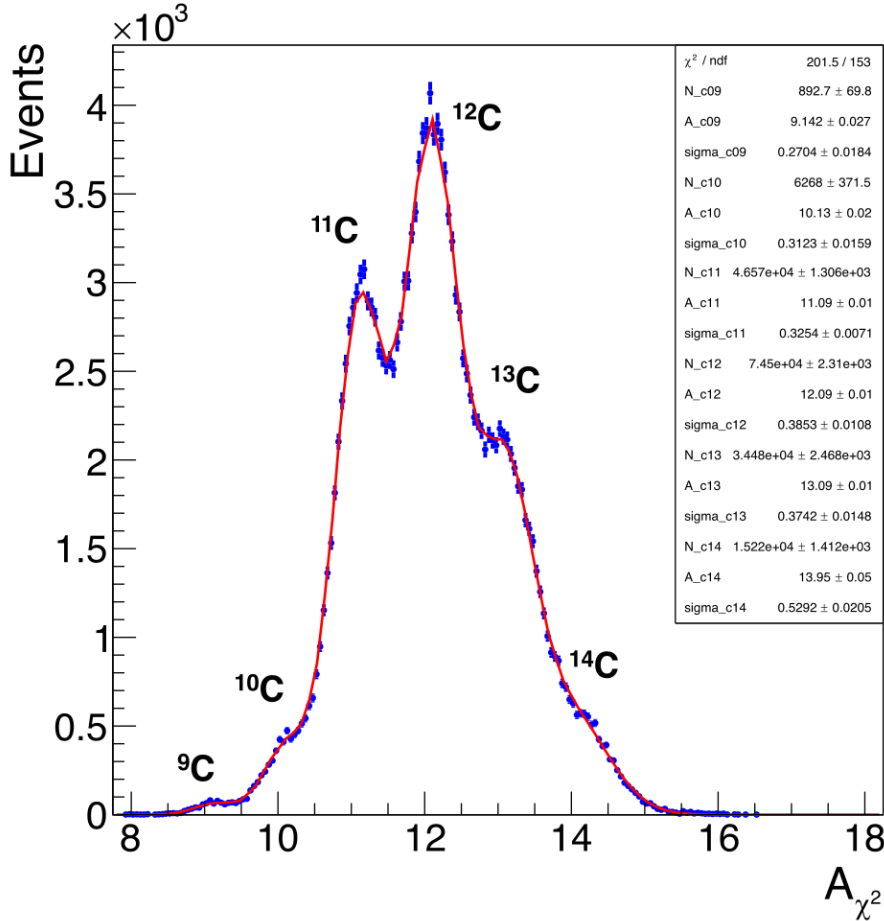


Figure (2.20) – An example of mass number determination obtained with the  $\chi^2$  fit for the carbon fragments (from [31])

Additionally, the  $\chi^2$  of the selected fit procedure can be used to exclude the events with a worse mass determination. Figure 2.20 shows an example of mass number determination obtained with the  $\chi^2$  minimization fit in the case of carbon ions fragmentation studies for the case of  $\sigma(\text{TOF}) \approx 70\text{ps}$ ,  $\sigma(p)/p \approx 3.7\%$  and  $\sigma(E_{\text{kin}})/E_{\text{kin}} \approx 1.5\%$ .



# CHAPTER 3

---

## Silicon position detectors

---

### 3.1 Short introduction to track detectors

A crucial requirement of many physics experiments is the measurement of particle trajectories: tracking of particles provides information about the interaction point, the decay path of unstable particles, angular distributions and, when the particle is deflected by a magnetic field, its momentum.

Track detectors, used intensively in particle physics since early 1930s, came in various forms and used different materials but they all exploit the same basic principle of operation: charged particles deposit some of their energy by ionizing the traversed medium.

The charge generated by such ionization then either directly shows the path of the crossing particle or is collected by means of dedicated electronic and subsequently analyzed.

The mean rate of energy loss by moderately relativistic charged heavy particles is well-described by the “Bethe equation” (1.3), as introduced in chapter 1.3.1, that can be rearranged as

$$-\frac{dE}{dx} = \frac{\xi}{x} \left[ \ln \left( \frac{2m_e v^2 W_{max}}{I^2(1-\beta^2)} \right) - 2\beta^2 - \delta(\beta\gamma) \right] \quad (3.1)$$

where

$$\xi = 0.1535 \frac{\rho z^2 Z}{A\beta^2} \text{ and } x \text{ is the target thickness in cm} \quad (3.2)$$

However, this mean is weighted by rarer events with large single-collision energy deposits (known as *knock-on electrons* or  *$\delta$ -rays*), so even with hundreds of events a dependable value for the mean energy loss cannot be easily obtained.

A more easily measured value is the most probable energy loss. The most probable energy loss in a detector is considerably below the mean given by the Bethe equation.

## 3.2 Charged particle signals in thin detectors

The Bethe-Bloch equation only describes the average energy loss per unit length.

When charged particles pass through a material, they undergo a large number of interactions and transfer only a small part of their initial kinetic energy in each of these collisions, so that the energy of the incident particle slowly decreases.

Due to the stochastic nature of these processes, the energy loss distribution of a monochromatic beam is not a delta function, even in a homogeneous target.

### 3.2.1 Energy loss in thin silicon layers

If the target can be considered thick, then the total energy lost by the particle is the sum of many small independent energy releases, which can be thought of as Gaussian distributed.

Consequently, in this case, the distribution of energy losses is well approximated by a Gaussian function: conversely, if the absorber is thin, less energy deposition events occur and the effect of a single hard interaction with a large energy transfer plays a major role in the shape of the distribution.

This results in a distribution that is strongly asymmetric, with a tail in the high energy region of the distribution, and for which the moments of the distribution, like mean or variance, are undefined.

This kind of distribution was firstly parametrized by Lev Landau and is thus commonly known as a *Landau distribution*[60].

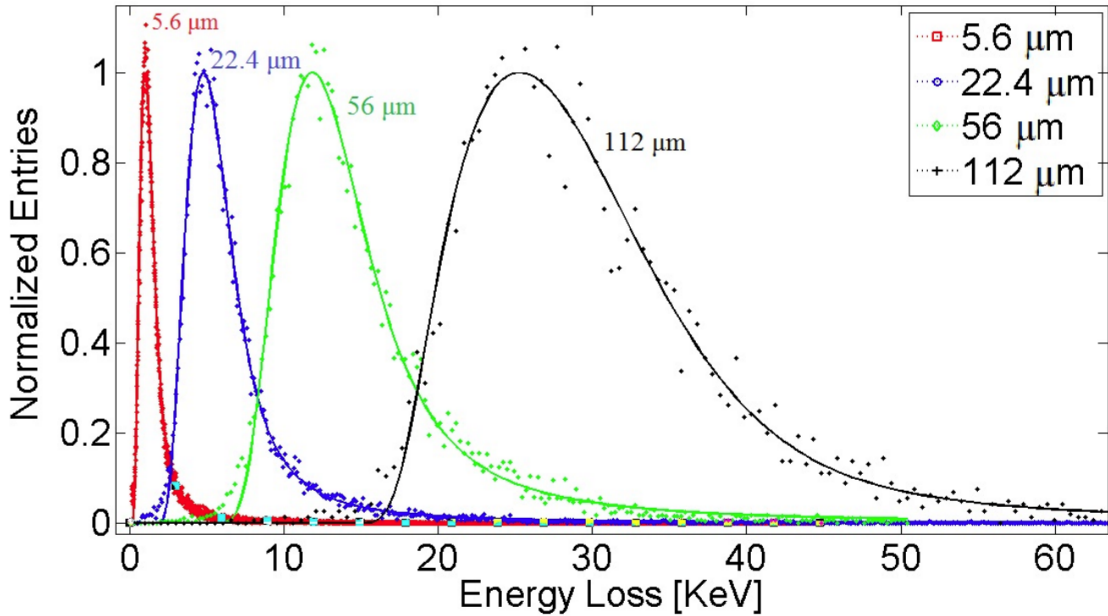


*Figure (3.1) – Energy loss distributions 12GeV protons for several silicon thicknesses (from [61])*

The probability density function written originally by Landau can be defined by the complex integral:

$$\Phi(x) = \frac{1}{2\pi i} \int_{a-i\infty}^{a+i\infty} e^{s \ln(s) + xs} ds \quad (3.3)$$

where  $a$  is an arbitrary real number.

The solutions for the mean energy loss value have different regions of applicability defined by the discriminating parameter  $\kappa = \xi/W_{max}$  where  $W_{max}$  is the maximum transferable energy in a single collision and  $\xi$  is defined as in equation (3.2). For values of  $\kappa \gg 1$ , the distribution is well approximated by a Gaussian distribution while for the region where  $\kappa < 0.01$ , Landau solved the problem under two assumptions

1. the mean energy loss is much lower than the maximum energy transfer possible (that is,  $W_{max} \rightarrow \infty$ )
2. the mean energy loss is much higher than the electrons binding energy, which can be treated as free

with the resulting distribution given by

$$f_L(\epsilon, x) = \frac{\phi(\lambda)}{\xi} \quad (3.4)$$

where

$$\phi(\lambda) = \frac{1}{\pi} \int_0^\infty e^{(-\pi y/2)} \cos(y \ln y + \lambda y) dy \quad (3.5)$$

The function  $f_L(\epsilon, x)$  has a maximum for  $\lambda \approx -0.229$ : the energy loss corresponding to this maximum is the *most probable energy-loss*  $\epsilon_{mp}$  [62].

Vavilov[63] later introduced a physical limit for the variable  $W_{max}$ , demonstrating that for  $\kappa \rightarrow 0$ , the Landau parameter  $\lambda$  approaches

$$\lambda \rightarrow \frac{1}{\xi} (\epsilon - \langle \epsilon \rangle) - \beta^2 - \ln \left( \frac{\xi}{W_{max}} \right) - 1 + C_E \quad (3.6)$$

where  $C_E = 0.577215$  is the Euler constant and  $\langle \epsilon \rangle$  is the mean energy loss in a medium of thickness  $x$ , corresponding to

$$\langle \epsilon \rangle = \xi \left[ \ln \left( \frac{2m_e v^2 W_{max}}{I^2(1-\beta^2)} \right) - 2\beta^2 - \delta(\beta\gamma) \right] \quad (3.7)$$

It has been shown with experimental data[64] that the solutions from Landau and Vavilov are almost equivalent for  $\kappa \lesssim 0.06$ , a conditions that for a typical  $300\mu\text{m}$  thick detector is achieved for protons with momenta approximately larger than  $0.5 \text{ GeV}/c$ .

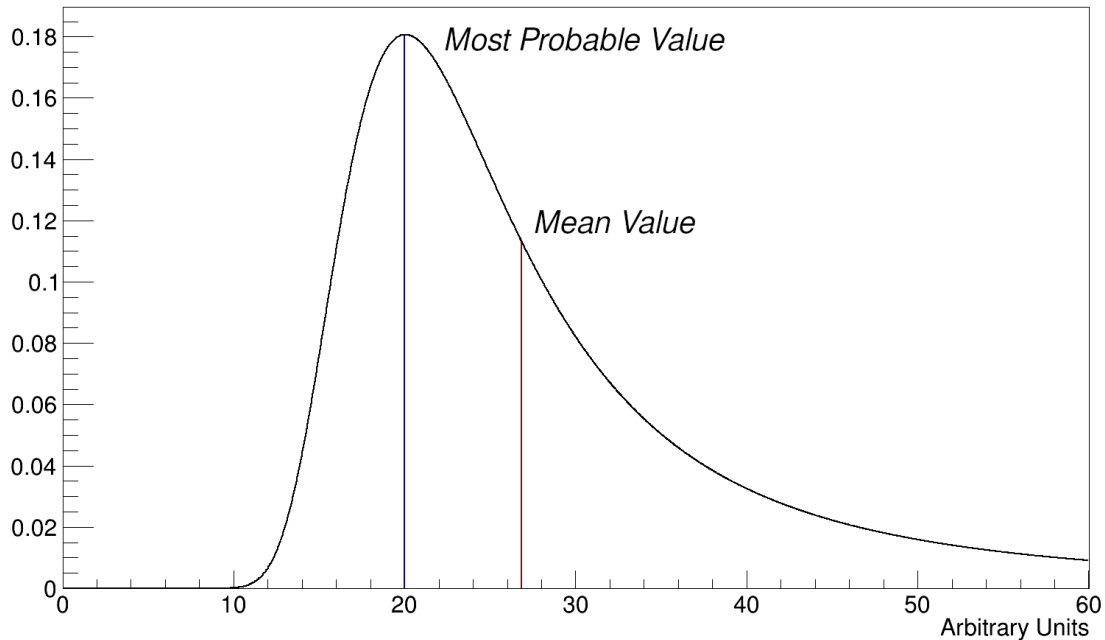


*Figure (3.2) – A generic Landau distribution, showing the difference between its Most Probable Value and its Mean Value*

### 3.3 Interaction of photons with silicon detectors

The behaviour of photons in matter is profoundly different from that of charged particles: the lack of an electric charge prevents photons from having anelastic scattering with the atomic electrons of the detector bulk which, as seen in section 1.3, is the main mechanism by which charged particles (heavy and low energy electrons) interact.

The most significant processes involved in the passage of photons in matter are:

- Photoelectric effect
- Compton effect
- Production of electron-positron pairs

The energy on which these interactions take place ranges from energies of the order of eV for the photoelectric effect up to energies of the order of several MeV for Compton scattering and pair production.

In the case of a photon travelling inside a semiconductor material, if the energy  $E_v$  of the photon is larger than the width of the bandgap  $E_g$  and smaller than 100 keV, the photon is absorbed primarily due to the photoelectric effect: in this process the energy of the photon is transferred to one of the electrons in the valence band, which is then lifted to the conduction band, producing an electron-hole pair. Figure 3.3 shows the mass attenuation coefficient in silicon, that is the fraction of photons absorbed from a monochromatic photon beam per unit mass.

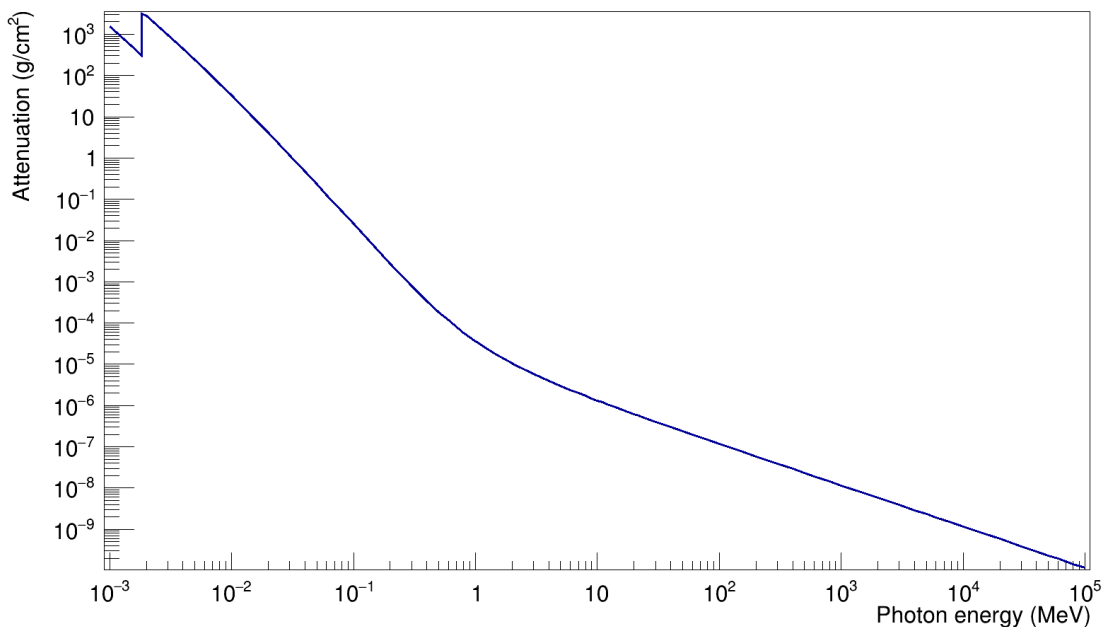


**Figure (3.3)** – Mass Attenuation Coefficients in Silicon (data from [65])

In the case of X-rays, the photon is more likely to interact with one of the innermost electrons. After the interaction an hole in the electronic structure forms paired by an electron with kinetic energy equal to that of the incident photon.

The low-energy electron moves through the material, transferring all its energy to external electrons of the atoms of the material, creating many e-h pairs in a limited volume.

The hole is filled by an electron that thus generates a photon that interacts to produce a second photoelectron that loses all its energy in a small space. If the charge-carrier collection element is sufficiently large, both signal contributions from the two photo-

electrons are collected by a single readout channel.

The intensity of the light penetrating through silicon drops exponentially as  $I = I_0 e^{-\alpha z}$ , where  $\alpha$  is the photon absorption probability per unit length and  $z$  is the depth.

The decrease in the intensity of the beam is not due, as in the case of charged particles, to a decrease in the energy of the photons, but rather to a reduction in the number of photons in the beam due to their absorption.

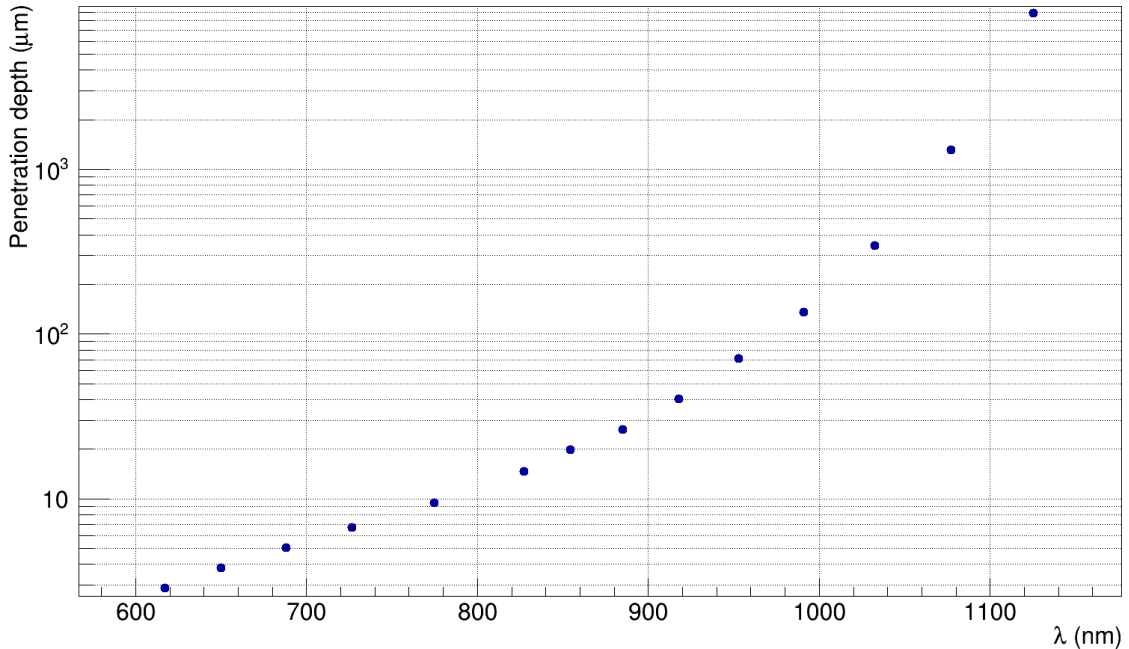


*Figure (3.4) – Penetration depth of light calculated from measurement performed on high purity silicon (adapted from [66])*

Photons of relatively high energies are able to interact with a large number of electrons, and therefore have a high probability of being absorbed in the first few microns of the material they pass through, while photons that are only able to be absorbed by valence electrons have a high probability of passing through the material without interacting.

Figure 3.4 shows the penetration depth of photons into silicon as a function of their wavelength: the width of the bandgap for Si, for example, is  $E_g \approx 1.11\text{eV}$  [67], corresponding to a photon wavelength of  $1130\text{nm}$ , for a penetration depth of  $\approx 900\mu\text{m}$ .

### 3.4 Current technology: silicon detectors

Starting from the 1980s, most track detectors used in modern high-energy physics experiments are semiconductor based detectors.

The most commonly used material is silicon, but germanium, gallium-arsenide and diamond are also useful in some applications.

Semiconductor track detector are basically a set of p-n junction diodes operated at reverse bias. This forms a sensitive region depleted of mobile charges and sets up an electric field that sweeps ionization charge to the electrodes.

Typically an asymmetric structure is used with, for example, a highly doped  $p^+$  electrode and a lightly doped  $n$  bulk region, commonly called backplane, so that the depletion region extends predominantly into the lightly doped volume (figure 3.5). To allow a better ohmic contact, the backplane is metalized with an aluminum deposit.

The electrodes of a solid-state track detectors are usually segmented in the form of strips or pads. A thin silicon oxide (e.g.  $SiO_2$ ) layer is deposited on the bulk surface between each strip, to achieve surface passivation of the detector that protects the silicon surface against degradation from the interaction with the environment [68].

Integrated circuit technology allows the formation of high-density micron-scale electrodes on large (10–15 cm diameter) wafers, providing excellent position resolution.

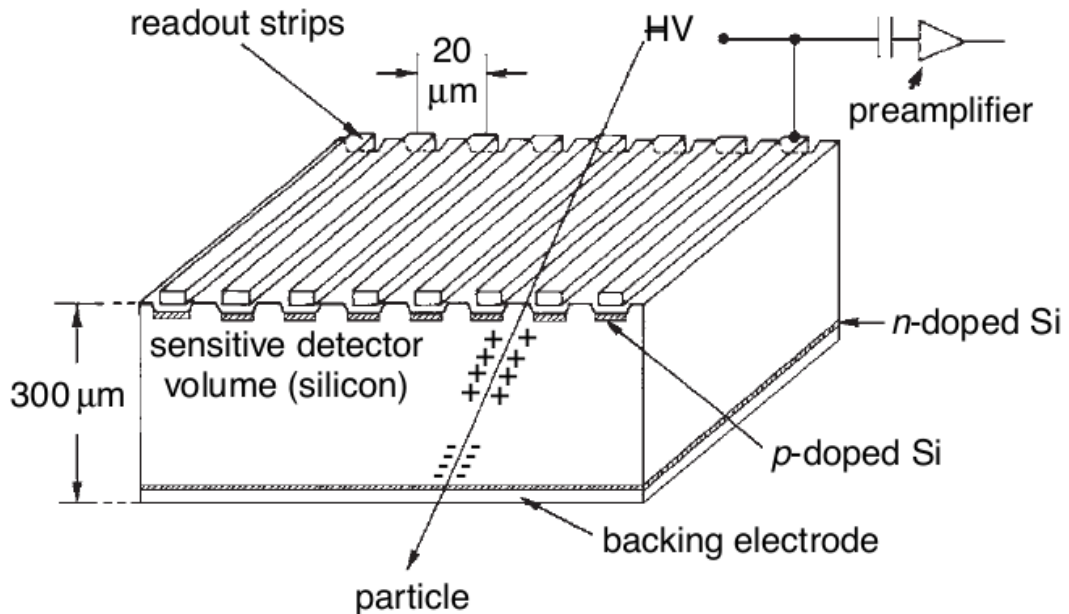


*Figure (3.5) – Typical structure of a single-face microstrip silicon detector, not to scale, from [69]*

The detector thickness is thus chosen as a compromise between two competing factors: the material traversed by the charged particle must be enough to create a sufficiently large number of electron-hole pairs without introducing an excessive deviation from the original trajectory, due to multiple scattering, or increasing the probability of production of secondary particles in the case of experiments using low energy particles.

For a typical detector an adequate value is found to be 300  $\mu\text{m}$  resulting in a total collected charge well above the noise level of available electronics: in this case, considering the most probable energy loss in silicon for a minimum ionizing particle (MIP) of about 270  $e\text{V}/\mu\text{m}$ , the resulting produced charge is  $\approx 2.2 \times 10^4$  electron-hole pairs.

The optimal pitch is determined by the carrier diffusion and by the spread due to delta electrons. In the case of a binary readout, assuming that a particle track fires a single channel the position resolution is simply  $\sigma = \text{readout pitch}/\sqrt{12}$ . Resolution can be improved if charge from the particle is shared by more channels and with the use of analog readout, where the position is reconstructed from the center of charge of the fired channels, with the contribution of each channel weighted by their signal.

In many applications, in order to minimize the number of acquisition channels, not all the strips are connected to the readout circuitry. Typical readout schemes are based on alternating connections every n strips (the charge collected on not connected strips is capacitively transmitted to the neighbor readout strip) in a configuration called *floating strip readout*: the charge distribution via capacitive coupling with the readout strips allows a spatial resolution on the order of 10  $\mu\text{m}$  or even better [70].

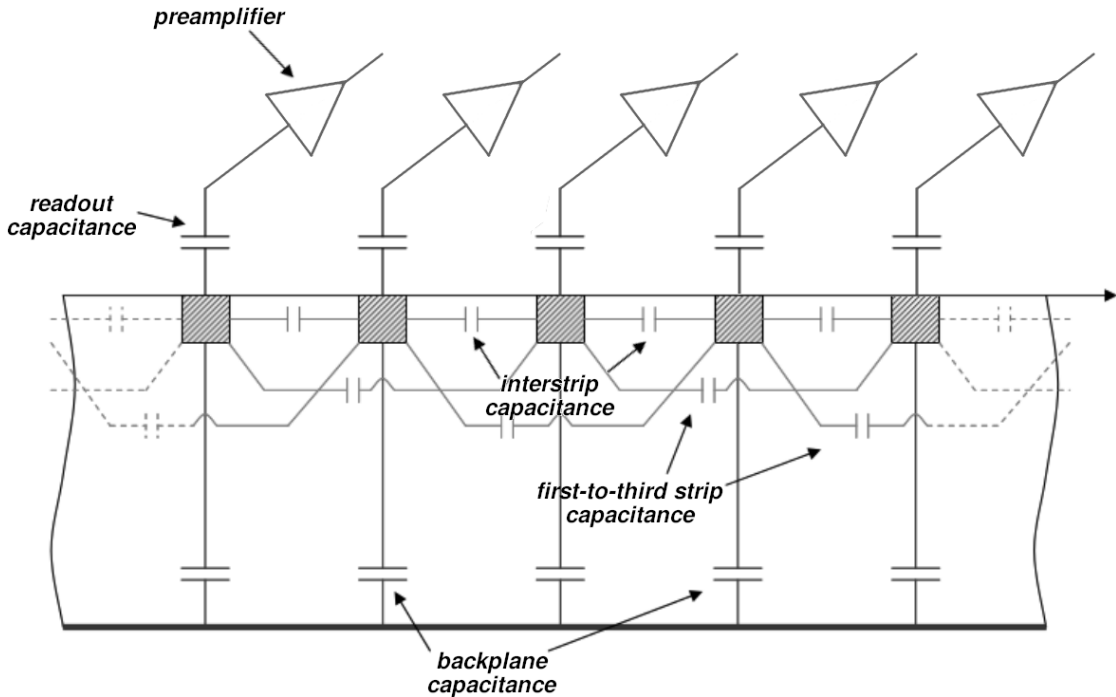


*Figure (3.6) – Equivalent electric diagram of capacitive couplings in a silicon strip detector*

Typical detectors are operated at full depletion: to provide the necessary bias voltage many different configurations are used. The simplest solution is to ground all strips and positively bias the n-side.

This solution has the drawback that only strips connected to the readout electronics are biased, forbidding the use of a floating strip configuration.

The biasing may be realized through a the readout preamplifier (DC coupling configuration) alternatively via AC coupling: a capacitor, either implemented on the electronics board, or directly on the silicon detector strips, is connected between the strips and the amplifiers.

This method has the benefit of decoupling the readout circuit from the bias line, preventing amplifier saturation due to high current leaking strips.

To reduce the number of connections required (providing direct contact of every strip with bias line would be usually impractical) a number of different solutions exist:

- **Polysilicon Bias:** strips are connected to a common bias line through deposition of polycrystalline silicon lines. To achieve high resistance values winding ploy structures are deposited.

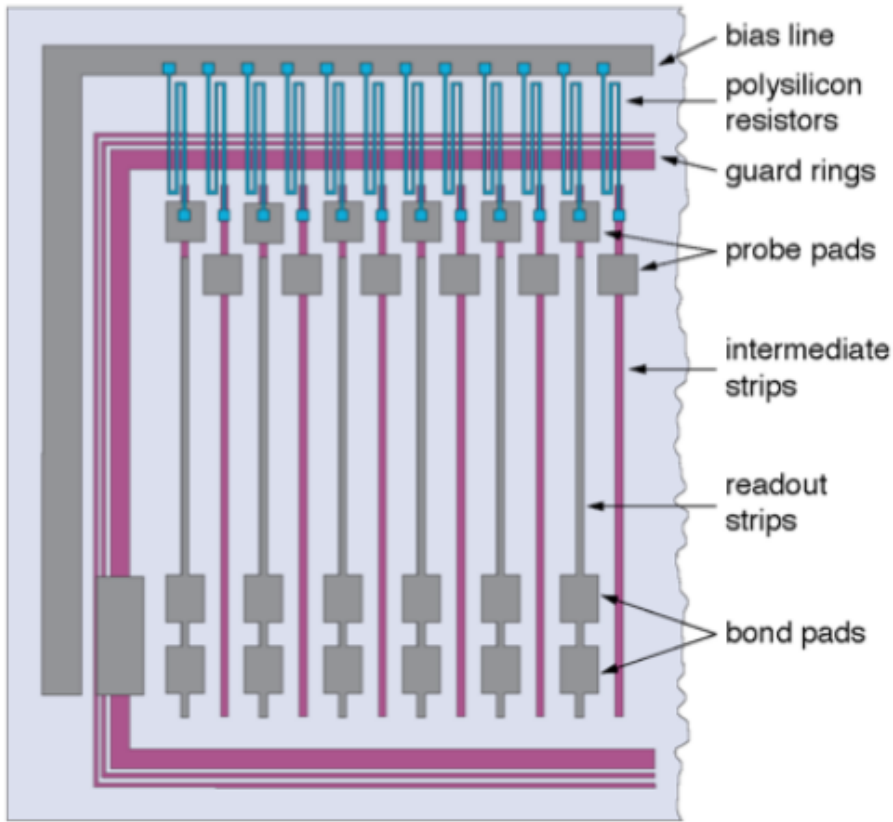


*Figure (3.7) – Polysilicon lines bias (adapted from [71])*

- **Punch-trough Bias:** a guard ring is ground and backplane is biased. As the bias voltage increases, the guard ring depletion zone increases and merges with the strip depletion zone. The result is that the strips have a positive potential with respect to the bias line and the guard ring reverse biased. With this method all the strips are at the same voltage, though not directly connected.

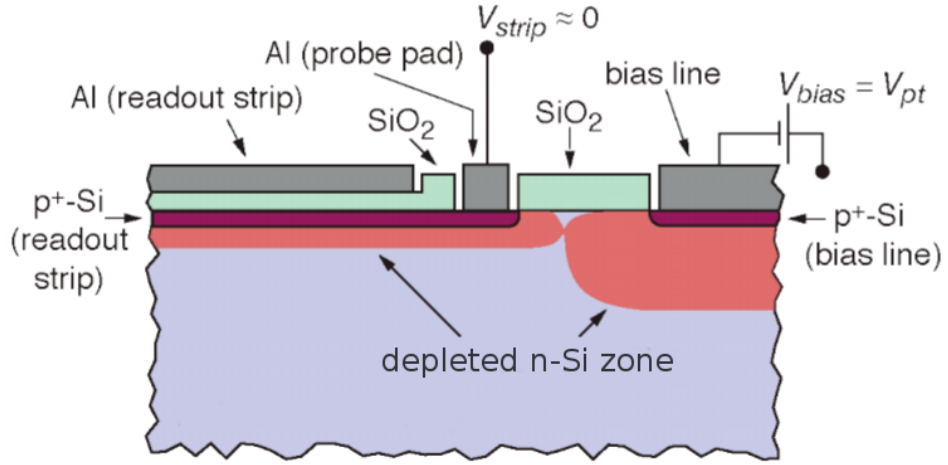


*Figure (3.8) – Punch-trough bias (adapted from [71])*

- **FOXFET Bias:** two strip  $p^+$  implants are source and drain of a field effect transistor. A gate is implemented on top of the  $SiO_2$  isolation. A dynamic resistance between drain and source can be adjusted controlling gate voltage.

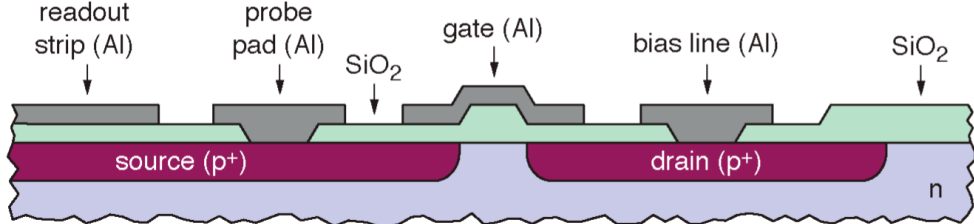


*Figure (3.9) – FOXFET based bias (adapted from [71])*

### 3.4.1 Signal generation in a microstrip detector

Semiconductor detectors output a signal that depends on the number of electron-hole pairs generated by the ionization of the bulk by a traversing charged particle.

While the exact shape and value for a certain particle depends on the characteristics of the detector (material, doping, etc.), the signal is mainly determined by the electric current induced by the ionization charges moving in the vicinity of the electrode, following the Shockley–Ramo theorem [72][73].

### Shockley-Ramo's theorem

The initial current induced by a single charge as determined by the theorem is defined by

$$i = \frac{qv}{d} \quad (3.8)$$

where  $q$  is the charge,  $v$  is its instantaneous velocity and  $d$  is the distance between the electrodes.

The total ionization charge depends on the particle type and energy, but for Minimum Ionizing Particles a value of  $\approx 80$  electron-hole pairs per micron of track length is used.

The value  $d$  is closely related to the *depletion region* thickness: at the interface of two semiconductors of p and n type, the electrons of the n-type diffuse into the p type, and the holes from the p type to the n-type region.

When no external voltage is applied, the diffusion of carriers provides a contact potential  $U_C$  which is of the order of 1V.

When an external positive voltage is applied to the n region (also known as *reverse bias*), the depletion layer depth increases and the electron–hole pairs released by particles interacting in the depletion area are separated by the electric field and the carriers are collected by the electrodes inducing the signal.

Electron–hole pairs created beyond the depletion layer, on the other hand, do not induce an electric pulse since the electric field outside the p-n junction is negligible due to the high charge-carrier concentration.

The width of the depletion area can be then expressed as

$$d = \sqrt{2\epsilon(U + U_C)\mu\rho_d} \quad (3.9)$$

where  $U$  is the external *bias voltage*,  $\epsilon$  is the dielectric constant if the material,  $\mu$  is the mobility of the main charge carriers and  $\rho_d$  is the specific resistivity of the semiconductor: for typical values found in silicon detectors, a  $150\mu\text{m}$  thick sensor has then a theoretical depletion layer depth of around 20V.

To make sure the detector is operated in a condition where the bulk was completely depleted, and thus the signal is the highest possible, the bias voltage chosen for detector operation is actually set at a much higher value than the one previously calculated, in what is commonly called *overdepletion*.

### Signal charge fluctuations and Fano factor

Given a fixed energy deposit in the detector bulk, it is important to not only know the magnitude of the signal generated but also its fluctuations, as they ultimately determine the minimum signal threshold and the relative energy resolution  $\Delta E/E$ .

When measuring the energy resolution of a semiconductor or gas detector, a lower value is found than the theoretical prediction derived assuming a Poissonian statistic.

Since ionisation processes are not completely independent but are linked to discrete electronic shells, the Poissonian statistic cannot be used and a correction must be introduced.

Fano first estimated the statistical fluctuations of the number of ions produced by constant amounts of radiation energy in a gas [74], and has been consequently calculated also for semiconductor materials like silicon and germanium [75] [76].

A simplified calculation of the Fano factor in a semiconductor can be derived assuming that the deposited energy can only be absorbed by either phonon production or the formation of a mobile charge pair [77].

The sums of the energies going into lattice excitation and ionization will then be equal to the deposited energy  $E_0$

$$E_0 = E_{ion}N_{ion} + E_xN_x \quad (3.10)$$

where  $E_{ion}$  is the semiconductor bandgap and  $E_x$  is the average phonon energy and where it's assumed that the variance  $\sigma_{ion} = \sqrt{N_{ion}}$  and  $\sigma_x = \sqrt{N_x}$ .

For a given energy deposited in the material, a fluctuation in excitation must be balanced by an equivalent fluctuation in ionization, and averaging over many events this means that the variances of the two processes must be equal

$$E_{ion}\sigma_{ion} = E_x\sigma_x \longrightarrow \sigma_{ion} = \frac{E_x}{E_{ion}}\sqrt{N_x} \quad (3.11)$$

Combining (3.10) and (3.11) and defining the number  $N_Q$  of charge pairs formed as the total deposited energy  $E_0$  divided by the average energy  $E_i$  required to produce such a pair, we obtain

$$\sigma_{ion} = \sqrt{\frac{E_0}{E_i}} \sqrt{\frac{E_x}{E_{ion}} \left( \frac{E_i}{E_{ion}} - 1 \right)} \longrightarrow \sigma_Q = \sqrt{F N_Q} \quad (3.12)$$

where  $F$  is the *Fano factor*, which for the case of silicon and germanium is  $F \approx 0.1$ . This result gives an estimation for the intrinsic resolution of semiconductor detectors as  $\Delta_{FWHM} = 2.35E_i\sqrt{F N_Q}$ .

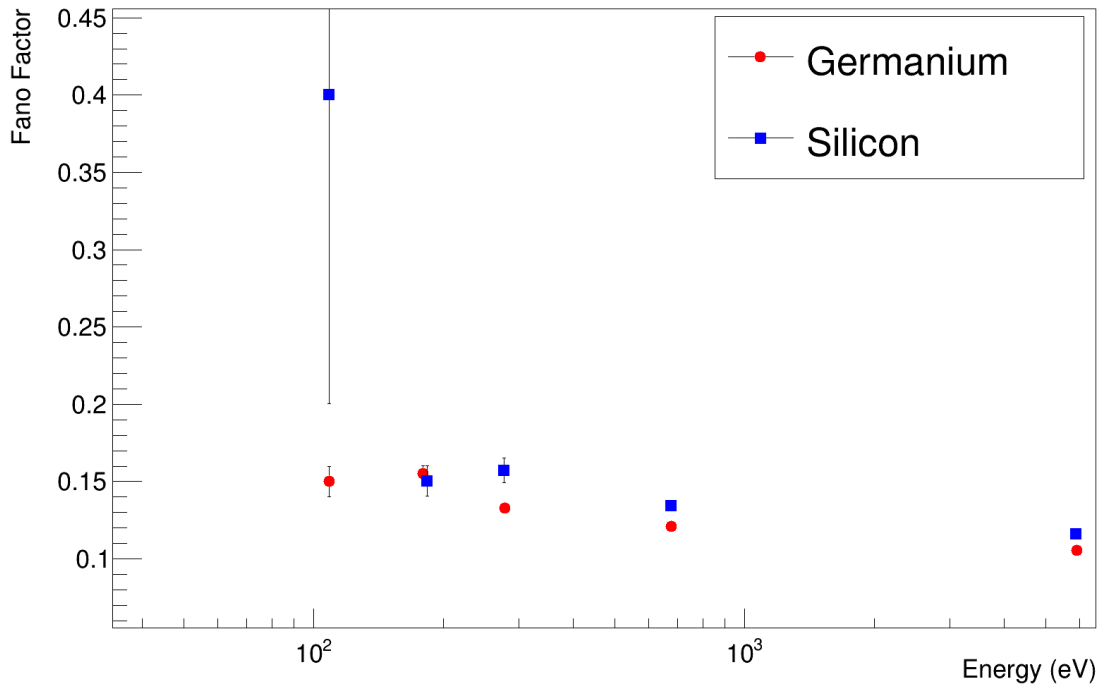


Figure (3.10) – Fano factors for Silicon and Germanium for different energies (data from [76])

The presence of the Fano factor makes so that the variance in the signal for a fixed energy deposit in a semiconductor is only relevant for very low energies, while in most cases the electronic noise is the dominant contribution.

### Noise in a silicon microstrip detector

In addition to the statistical fluctuations intrinsic to the physical processes in the interaction and generation of the signal, additional noise sources coming from both the detector itself and its readout electronics exists.

Noise is generally expressed in terms of *Equivalent Noise Charge* (ENC), i.e. the corresponding number of electrons if the noise contribution were a real signal.

The main sources to the total ENC come from the preamplifier circuitry and the silicon detector itself, with the different contributions that sum up quadratically

$$ENC = \sqrt{ENC_{I_L}^2 + ENC_{R_p}^2 + ENC_{R_s}^2 + ENC_C^2} \quad (3.13)$$

with a *shot noise* term coming from the detector leakage current

$$ENC_{I_L} = \frac{e}{2} \sqrt{\frac{I_L t_p}{q_e}} \quad (3.14)$$

a *parallel thermal noise* coming from bias resistance

$$ENC_{R_p} = \frac{e}{q_e} \sqrt{\frac{k_b T t_p}{2 R_p}} \quad (3.15)$$

a *serial thermal noise* coming from the strip metalization resistance

$$ENC_{R_s} = C_d \frac{e}{q_e} \sqrt{\frac{k_b T R_s}{6 t_p}} \quad (3.16)$$

and a *load capacitance* term

$$ENC_C = a + \frac{b}{t_p} C_d \quad (3.17)$$

In equations 3.14 to 3.17  $e$  is the Euler number,  $k_B$  the Boltzmann constant,  $q_e$  the electron charge,  $t_p$  the preamplifier shaping time,  $T$  the operating temperature,  $a$  and  $b$  preamplifier specific constant parameters.

All the noise behaviours have a direct impact on the sensor design, which have to take into account the expected signal levels to avoid noise levels of the same amplitude, with a subsequent decrease in the *signal to noise ratio* (S/N) of the detector.

In particular, it's evident that while some of the sources are easily lowered (with the use of silicon with lower leakage current, high parallel resistance and small series one, and lower operating temperature), some of the contributions are inevitable depending on the applications: namely, noise necessarily increases with strip length while the preamplifier shaping time contributes to different competing terms.

Given that noise contributions from 3.14 and 3.17 depend respectively on  $\sqrt{t_p}$  and  $1/\sqrt{t_p}$ , an optimal shaping time which minimizes the total noise exists, as shown in figure 3.11.

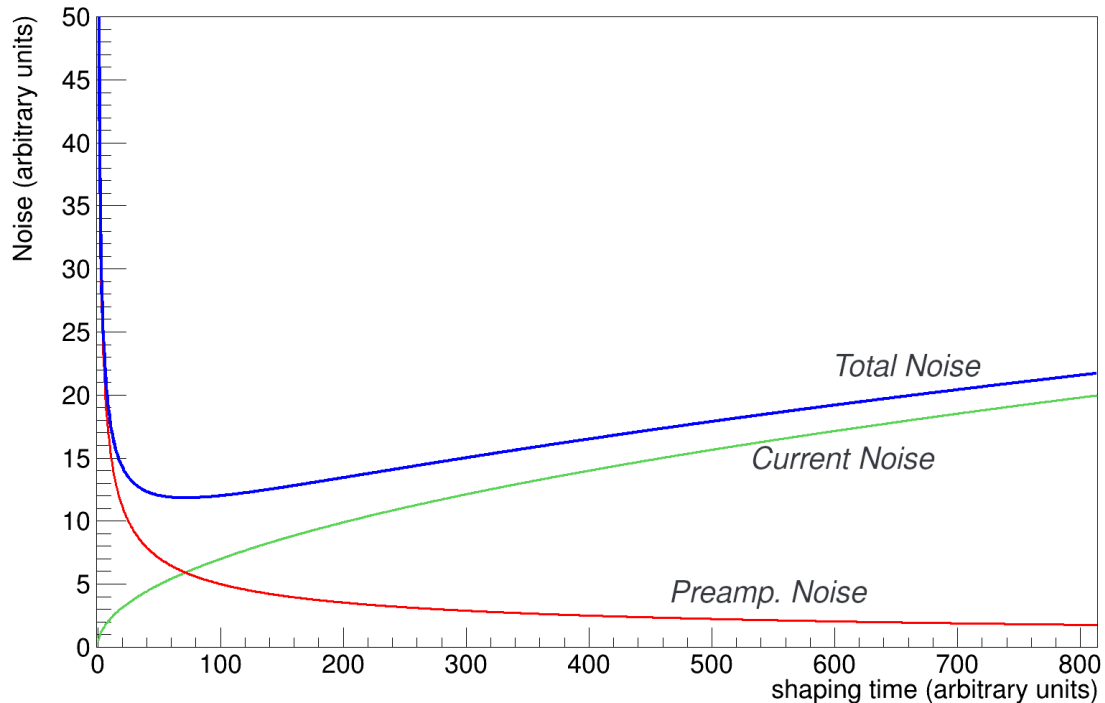


Figure (3.11) – Contributions of current noise and preamplifier noise to the total ENC noise



## CHAPTER 4

---

### The FOOT Micro Strip Detector

---

The FOOT Micro Strip Detector (MSD) apparatus is the last tracking station of the magnetic spectrometer, located downstream of the magnets and about 35 cm away from the target, and consists of 6 layers of silicon microstrip sensors, organized in three x-y stations with mutually orthogonal sensors.

The purpose of this detector is to provide information about the spatial location of the tracks needed for the momentum reconstruction of the fragments, but it also provides information about the energy loss of the fragments.

Each plane is equipped with two single-sided silicon strip detectors placed front-to-front to measure the two orthogonal views perpendicular to the beam direction of the apparatus. Each single detector is made of one AC-coupled silicon microstrip sensor, read-out by ten IDE1140 ASIC chips [78].

The silicon sensors, made by Hamamatsu Photonics, are 150 $\mu\text{m}$  thick, less than half of the typical thickness of silicon microstrip detectors used in past physics experiment to reduce the effect of Multiple Coulomb Scattering and further fragmentation of projectiles, and have a 96 mm  $\times$  96 mm active area segmented in 1920 strips with a 50  $\mu\text{m}$  implantation pitch.

An innovation in the sensor design to simplify the assembly procedure is the implementation of the pitch adapter from strips to ASIC channels directly on-silicon (Fig. 4.1 right). In this way an external pitch adapter became unnecessary, and the microbonding procedure complexity is reduced.

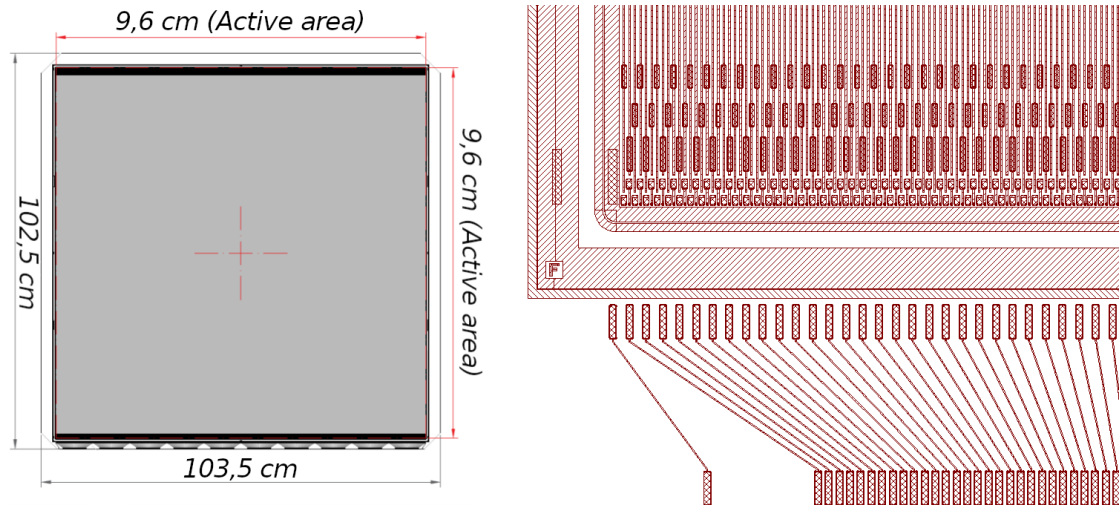


**Figure (4.1)** – Mechanical drawings of a silicon sensor from Hamamatsu (left) and close up of the on-silicon pitch adapter (right)

In order to reduce the number of the readout channels and maintain a good performance in terms of spatial resolution the readout is performed with a floating strip approach with a final readout pitch of  $150 \mu m$ , with two floating strips for every readout strip: this should allow to go from a 43 micrometer digital spatial resolution below the 35 micrometers requested by the FOOT CDR.

Table 4.1: Silicon specifications from Hamamatsu

<b>Thickness</b>	$150 \mu m$
<b>Overall dimensions</b>	$102.5 mm \times 103.5 mm$
<b>Active area</b>	$96 mm \times 96 mm$
<b>Total number of strips</b>	1920

Continued on next page

Table 4.1: Silicon specifications from Hamamatsu (Continued)

<b>Thickness</b>	$150 \mu m$
<b>Readout strips in FOOT</b>	640
<b>Readout pitch</b>	$150 \mu m$
<b>Implant pitch</b>	$50 \mu m$
<b>Mechanical edges</b>	5 mm
<b>Pad dimensions</b>	$80 \times 300 \mu m^2$
<b>Strip width</b>	$40 \mu m$

Table 4.1 summarizes the main characteristics of MSD sensors, as provided by the manufacturer.

## 4.1 The first prototype PE001

### 4.1.1 Assembly procedure

The construction of the first FOOT MSD sensor prototype has been used to develop the assembly procedure and check for the basic electrical performances with and without ionizing radiation.

The assembly procedure for the first FOOT MSD prototype combined established methodologies with some innovative choices and instruments: the basic procedure can be described as follows

- electrical testing of the hybrid board;
- gluing and micro-bonding of the VA1140 chips: the hybrid board, produced by ARTEL S.R.L., already contains all the passive circuitry needed and only the readout ASICs need to be glued and micro-bonded (figure 4.2)
- electrical testing of the ASIC populated hybrid board

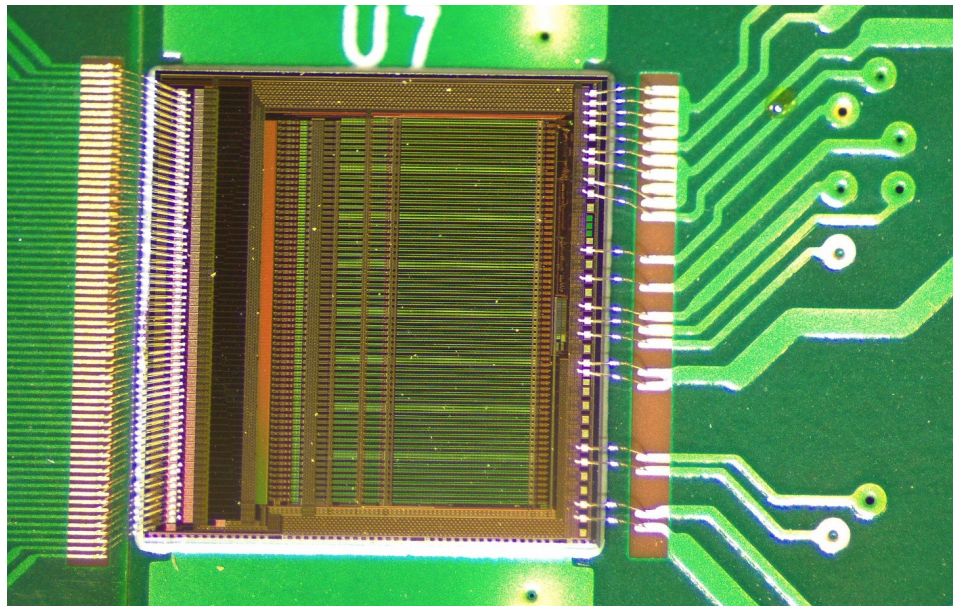


*Figure (4.2) – Closeup of the IDE1140 readout ASICs after gluing and microbonding*

- precise alignment of the hybrid on the assembly jig to ensure the correct positioning of all the components to  $\approx 100 \mu m$  uncertainty (figure 4.3)

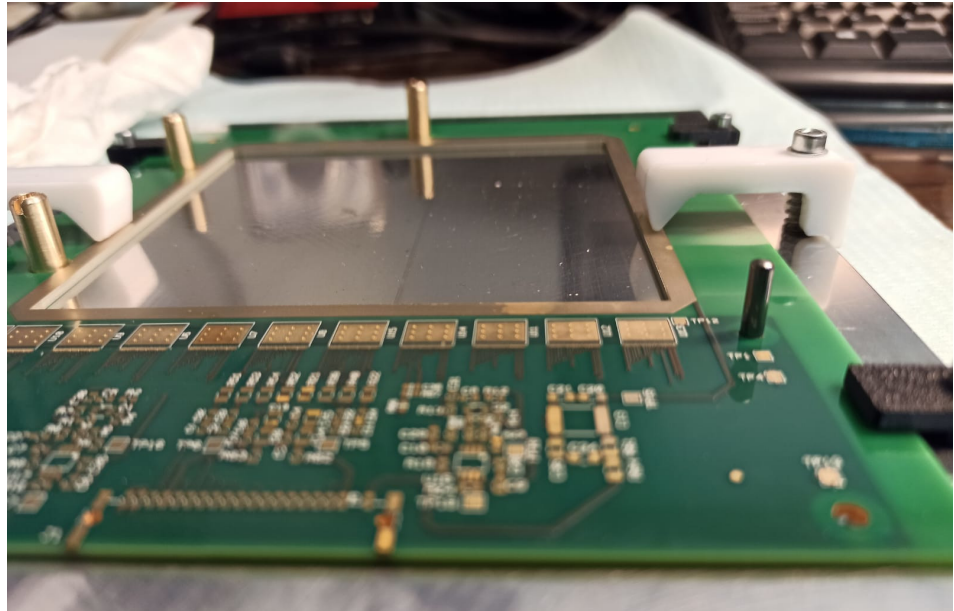


*Figure (4.3) – The hybrid board on its mounting jig*

- glue deposition on the hybrid: silicone for adhesion, conductive to ensure the back potential of the silicon can be provided by an external line
- positioning of the silicon sensor on the hybrid: the pins used to align the hybrid board to the jig are designed in a D-like shape so that, once the sensor is correctly aligned, the flat side of the pins can be used to remove them without damaging the sensor; given the reduced thickness, specific tools to handle the sensor, have been designed and realized, like a 4-pod vacuum suction (figure 4.4, left) and a tool to assure the uniform pressure needed during the glueing of the sensor on hybrid (figure 4.4, right)

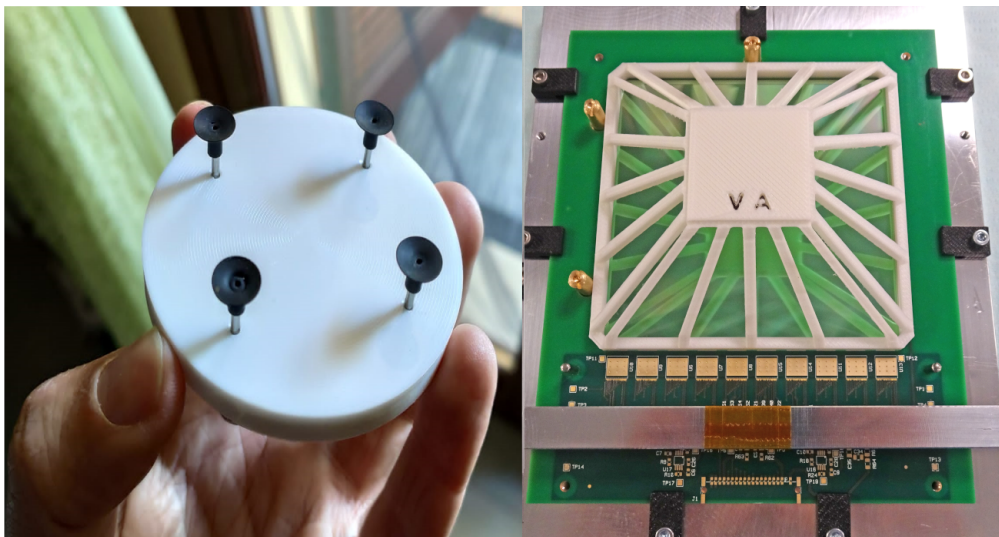


*Figure (4.4) – Custom tools for assembly: pickup tool with 4 suction cups (left); tool to distribute pressure for sensor gluing on hybrid board (right)*

- the silicon sensor is left overnight under pressure while the glue is curing (figure 4.5)
- after curing of the glue, in order to check the alignment and measure the thickness of the detector, the metrology measurement is done and then the wire bonding is performed;
- after assembly, the completed sensor is then electrically tested to check its quality. In the case of anomalous behaviour the detector is inspected and, if needed, reworking is performed.

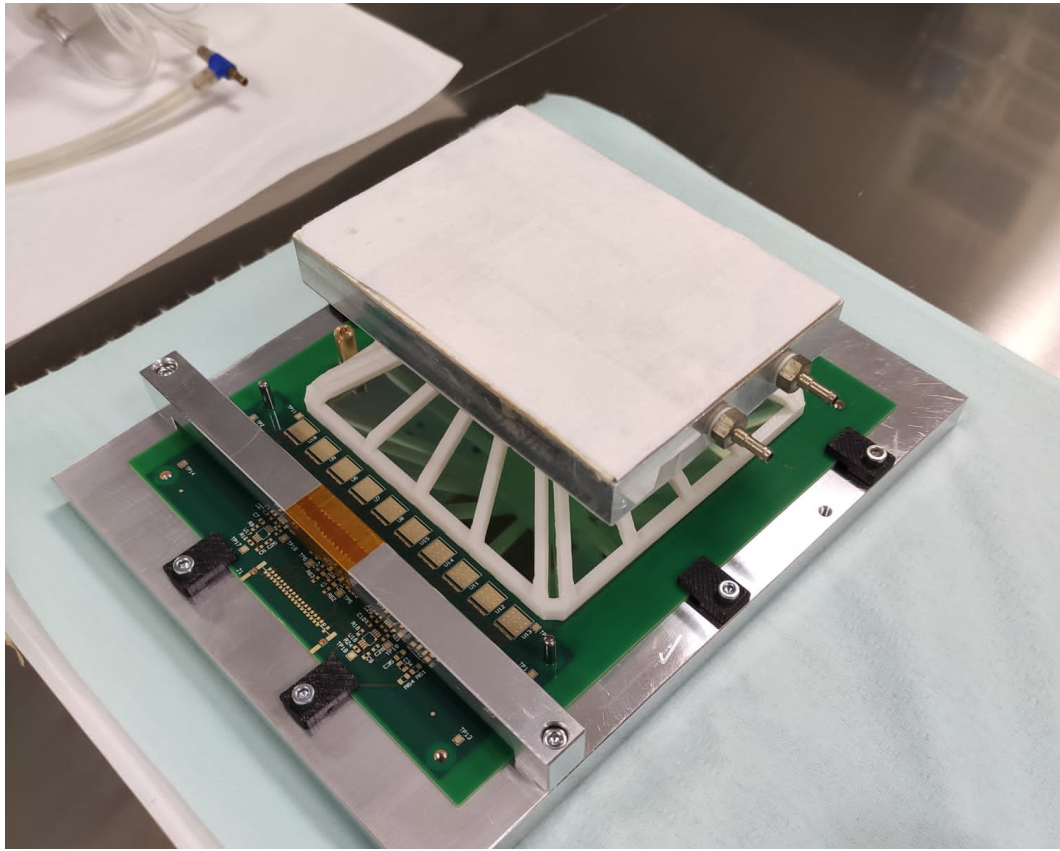


*Figure (4.5) – The silicon curing overnight after gluing on the hybrid board*

#### 4.1.2 Data Acquisition system for the first prototype

The front-end hybrid board collects and amplifies the signals coming from the strips with the use of 10 IDE1140 ASICs (10x64 channels low-noise/ low power high dynamic range preamplifier-shaper circuit) produced by IDEAs.

The VA chips are separated into two independent readout groups: the two groups are read in parallel while the VAs of a same group are serially readout.

Each group has its own amplification circuit, and the differential analog outputs are then transferred to the *miniTRB* test data acquisition boards which contains the ADC circuitry and a FPGA.

The *miniTRB* is a reduced version of the full DAQ system used in the DaMPE experiment [79][80], used in the Perugia laboratories during the construction of the Silicon

Tracker components: this gave a first reliable system to verify the correct functioning of the first prototype while also providing data that can be directly compared with that from older silicon microstrip detectors with similar geometry read out by the same DAQ system.

The board has the task of digitizing the data from the IDE1140 chips, packing them in binary format and sending them to the DAQ program running on the control PC to store them on a hard disk for further offline processing.

The miniTRB can either generate an internal random trigger at 50 Hz or receive an external trigger signal.

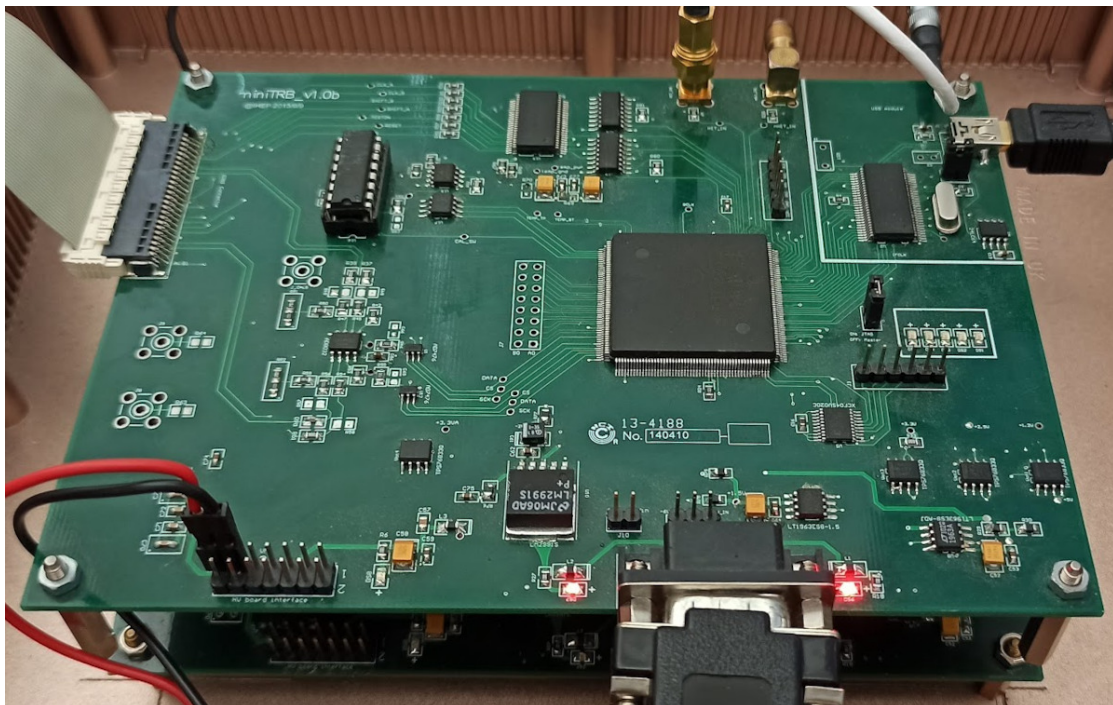


*Figure (4.6) – The miniTRB DAQ system*

#### 4.1.3 Noise performance of the detector

The boards are operated in "raw" mode during the test: at each trigger, the analog signals of all the 640 strips are read-out, pre-amplified and shaped by the VA chips and then digitized.

Before searching for charged particle signals it's of fundamental importance to characterize the noise of the assembled detector.

A *raw event* is defined as the raw content of all the strips of the prototype, i.e. 640 integer values that range from 0 to 4095 ADCs. A set of consecutive events is a *run*.

A *calibration run* is a collection of a minimum of 3000 up to 10000 events, without external radiation source, to calibrate the sensor's response.

Figure 4.7 shows an example of one raw event from a calibration run of the FOOT PE001 prototype sensor: all channels have a value between 140 and 300 ADCs mainly determined by the ADC offset, the difference among the readout channels of the IDE1140 chips and the sensor characteristics.

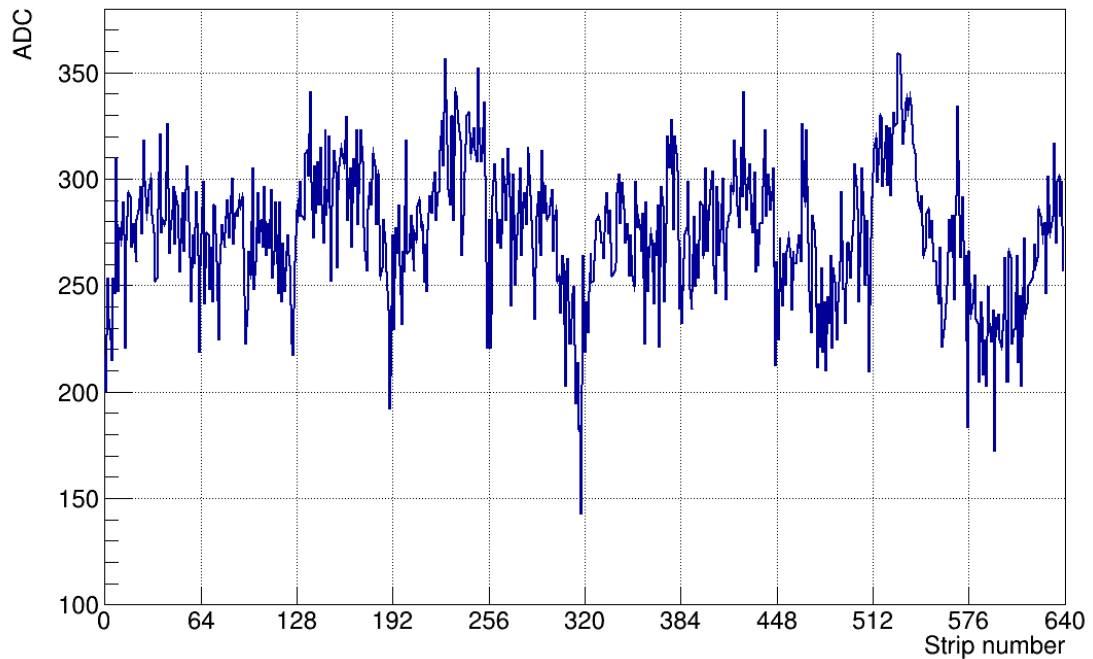


**Figure (4.7) – Sample raw event display for a pedestal run**

The average response of the single strips in the absence of an external stimulus needs be determined and then subtracted to equalize the single strip response. As an example, Fig. 4.8 shows the raw output in ADC of strip # 600 during a calibration run.

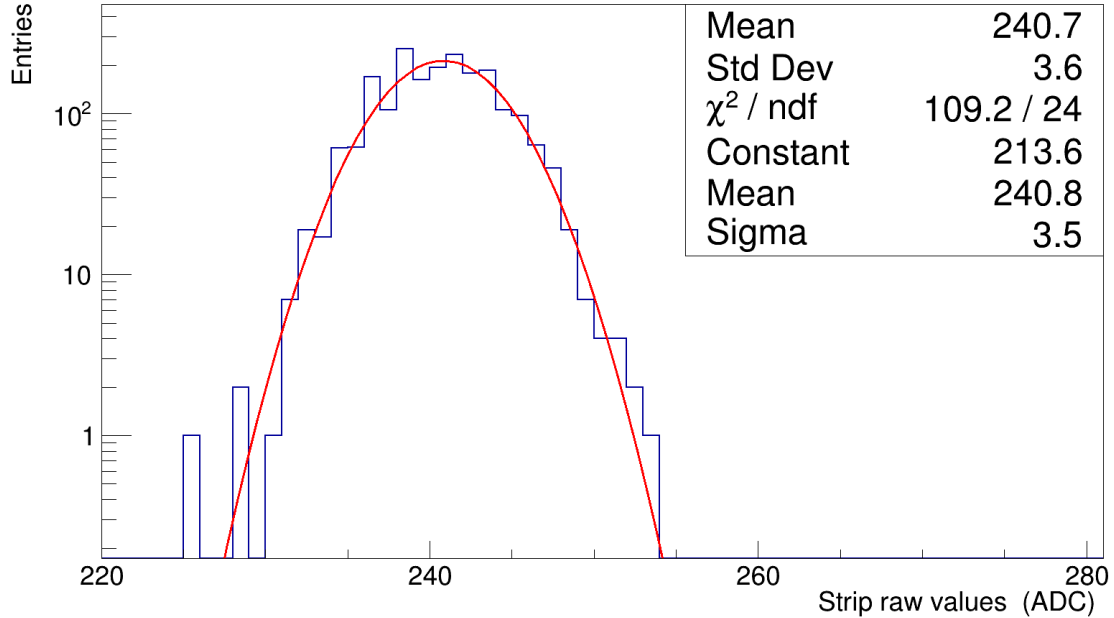


Figure (4.8) – Distribution of raw output values for strip # 600.

The distribution width, 31 ADC, is roughly double of the expected signal Most Probable Value (MPV) for a MIP [81], so it is evident the importance of strip by strip response equalization.

The pedestal of a channel is its base-level without signal and it's determined by properties of the readout circuitry and detector geometry, and is defined as

$$\text{ped}_i = \frac{1}{N} \sum_i^{N_j} (\text{ADC}_{ij}) \quad (4.1)$$

From the widths of the distributions for the pedestals (RMS) it is possible to gain information on the presence of strips with anomalous behavior: a distribution that is too narrow, compared to the others, is usually an indication of a malfunctioning strip.

The fact that its noise oscillates too little (around an average value that can be either much lower or much higher than that of the rest of the strips) can be an indication of an electronic problem (e.g. a bad microbonding) or, more rarely, a problem with the strip itself (such as, for example, the presence of shorts between several strips or physical damage of the metalization layer).

Figure 4.9 shows the distribution of all the pedestals of the PE001 prototype.

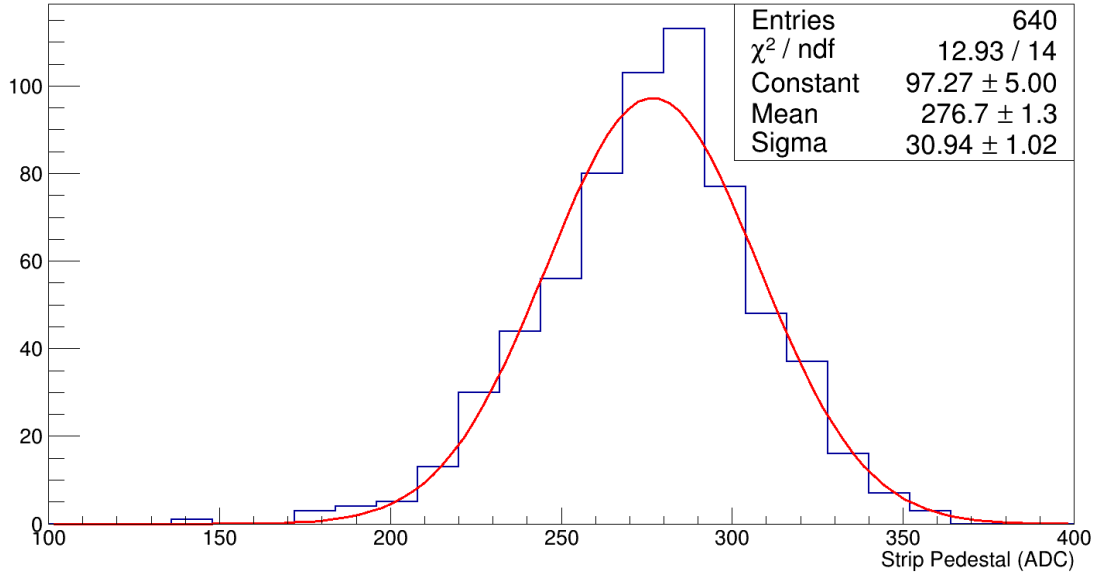


Figure (4.9) – Typical pedestal values for the assembled detector

The next step in the equalization procedure is subtracting the collective signal variation for each event caused by the pickup of external electromagnetic noise. This step is known as *Common mode noise subtraction*: common mode noise (CN) is the average deviation of all the channels of a readout ASIC at the same time.

For each ASIC, the common mode noise of event  $j$  is calculated as

$$\text{CN}_j = \frac{1}{N_j} \sum_i^{N_j} (\text{ADC}_{ij} - \text{ped}_i) \quad (4.2)$$

where  $N_j$  is the number of normal strips within the ASIC (noisy or dead strips are excluded). Usually  $N_j$  is 64, the total channel number of the IDE1140, but if bad strips exist, the CN is computed excluding the bad channels until there are at least 16 good channels, otherwise (number of bad channels  $> 48$ ), all channels of the ASIC are blocked.

Fig. 4.10 shows the distribution of the CN for one IDE1140 for all the events collected during one calibration run. The distribution is well represented by a Gaussian, where the fit has a width of  $\approx 3$  ADC counts: this corresponds to about 20-25% the predicted signal of a MIP [81], so it is important to subtract this deviation from the ideal 0 value

on a event by event basis.

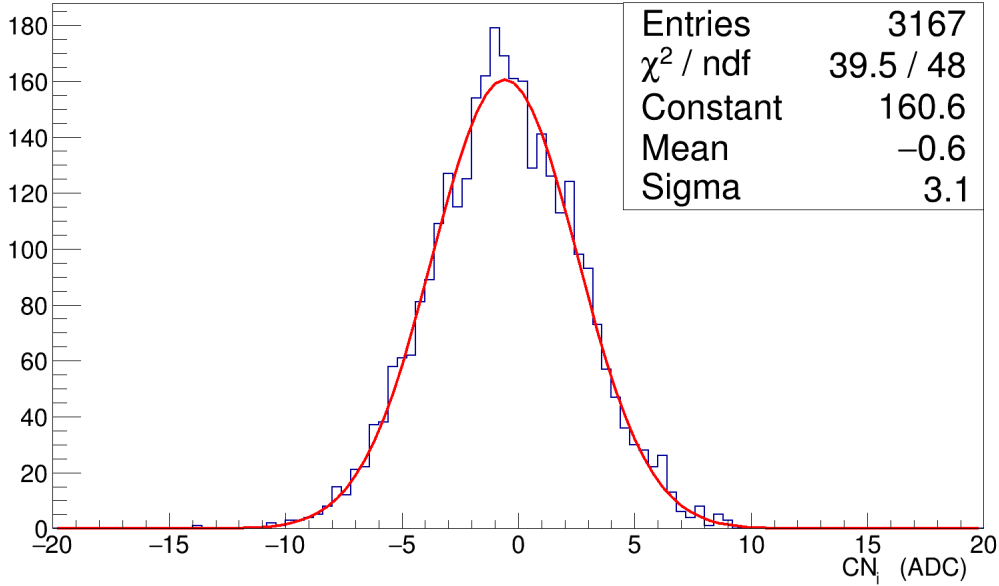


Figure (4.10) – Common mode noise distribution for one chip for a calibration run.

The final reduced value for each channel is thus

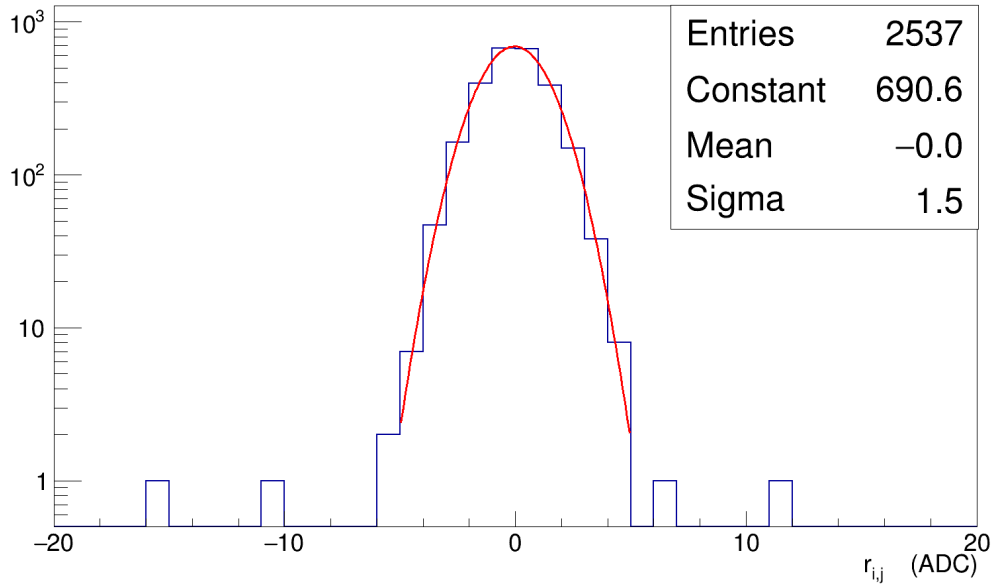
$$r_{ij} = \text{ADC}_{ij} - \text{ped}_i - \text{CN}_j \quad (4.3)$$

Fig. 4.11 shows as an example the  $r_{ij}$  distribution for the same strip as figure 4.8.

After pedestal and common noise mode are subtracted, the sigma of each channel can be computed from the raw data as

$$\sigma_i = \sqrt{\frac{1}{N} \sum_{j=1}^N (\text{ADC}_{ij} - \text{ped}_i - \text{CN}_j)^2} \quad (4.4)$$

The  $\sigma$  value of each channel is crucial to define a uniform criteria to evaluate if a signal is due to a noise fluctuation or not.



*Figure (4.11)* – Distribution of  $r_{ij}$  values for strip # 600.

This is typical of all the strips, as shown in figure 4.12, with an average value of  $1.54 \pm 0.12$  ADC. From this value and the average pedestal value, the dynamic range available is  $\approx 2500$  times the single strip noise.

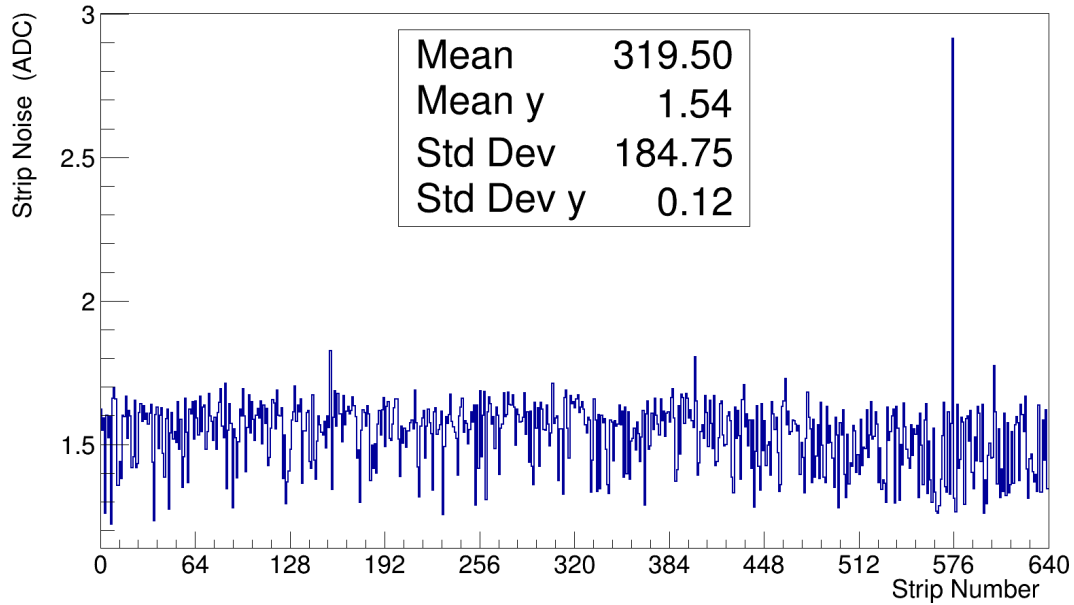


*Figure (4.12)* – Strip noise profile for all FOOT\_PE001 strips.

### Pedestal stability

To assess long-term stability of the detector, a dedicated acquisition spanning over several hours and without exposure to external ionizing radiation has been done while keeping the same detector's operational settings: a dataset where no signal source is present was acquired using an internal 50Hz periodic trigger generated by the onboard FPGA.

To check the time trend of pedestals, corresponding values are first graphed as function of the number of events for each strip. Knowing the rate of the trigger and the number of events acquired it's then possible to infer the time elapsed during data acquisition.

Noise and pedestal are expected to be quite stable since the tests are performed in a controlled lab environment with no external sources of noise like magnetic fields or other detectors working. Fig. 4.13 shows the raw value for one strip as a function of time over 3000 events, corresponding to 30 seconds. The fluctuations around the average value lie within  $\pm 8$  ADCs, and are due to both single strip noise than common mode fluctuations.

Each graph was then fitted first with a polynomial of degree one, to evaluate a possible drift of the pedestal in time.

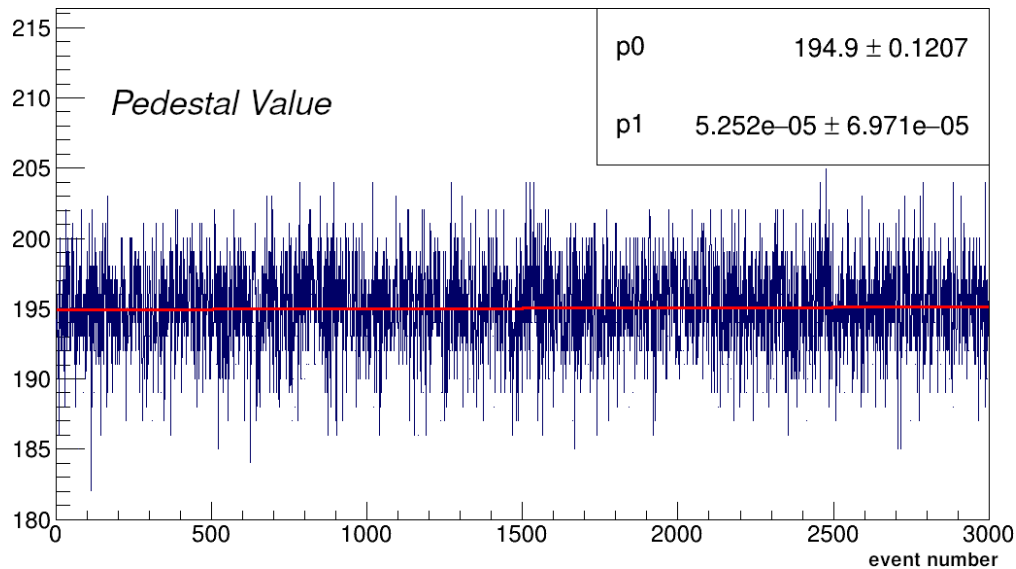


*Figure (4.13) – Typical pedestal value as function of the event number and its fit with a pol1*

To better visualize medium and long term effects, pedestal values were averaged every 3000 events (that is, every 60 seconds), and the resulting graph was once again fitted with a polynomial of degree one (figure 4.14).

The fit seem to be in agreement with the data and we can therefore conclude that the noise presents at most a very slight temporal dependence in a window of a few hours.

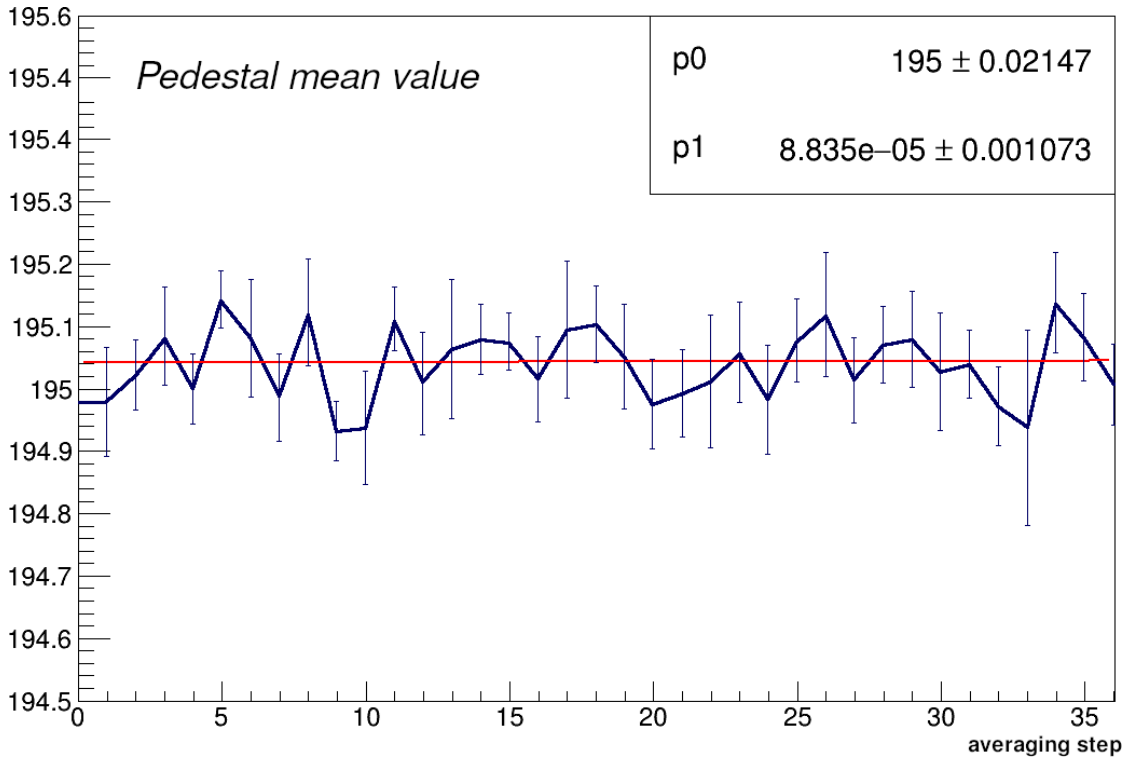


Figure (4.14) – Typical pedestal value trend after averaging every 3000 events and its fit with a pol1

The distribution of slopes for all strips is well represented by a Gaussian with mean value  $0.000 \pm 0.001$  ADC/minutes.

From this result, it could be inferred that the single strip pedestals are stable at the level of the single strip noise (2-3 ADC units) over  $\approx 10$  hours for  $\approx 99\%$  of the strips, at least in the laboratory environment.

Hence for data taking it should be safe to assume that a calibration run taken at a certain point in time would be valid for few hours.

### Common mode uniformity across the sensor

Given that common mode noise is the result of an external noise source (like electromagnetic noise or noise on the power lines), the resulting value mode can in principle change for each electronic base unit.

In the case of the FOOT prototype under study, this could be a single front-end IDE1140 ASIC chip, or one of the ADC circuits.

Common mode is as a general rule computed and subtracted for each event on a front-end ASIC basis (i.e. the smallest electronic base unit), as defined in equation 4.1.3.

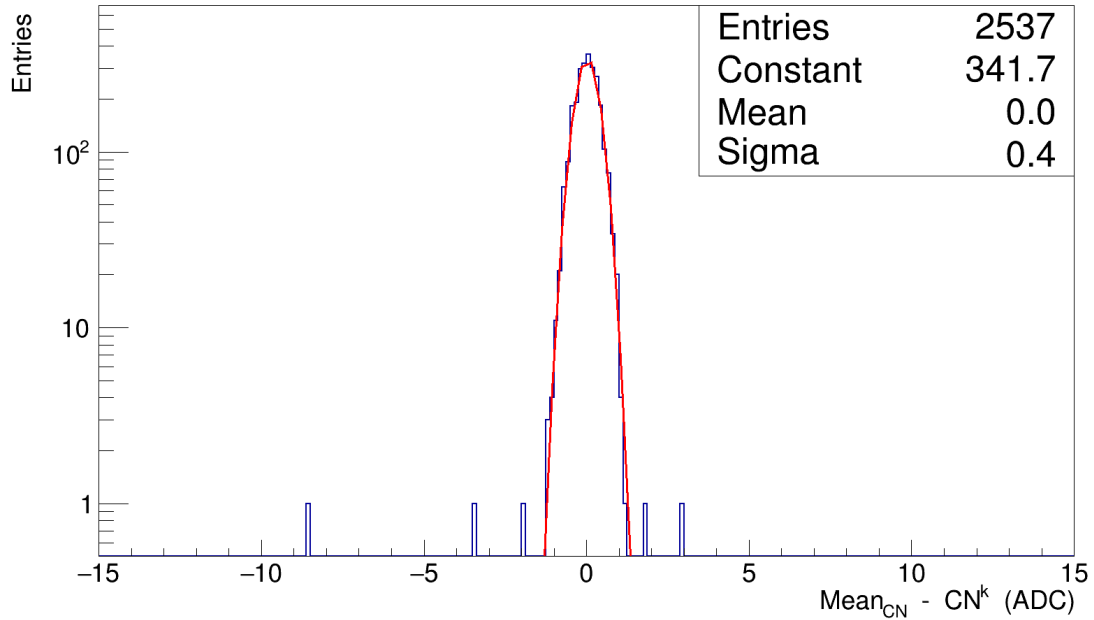


*Figure (4.15) – Distribution of difference between  $CN_j$  for chip # 2 and the average of the remaining four chips read by the same ADC.*

If one or more chips have so many strips with signal such that  $CN_j$  could not be computed, the  $CN_j$  value from other chips could be used. Hence the study of the  $CN_j$  uniformity across the whole sensor is an important task.

Figure 4.15 shows the distribution of the event-by-event difference of the Common Mode computed for one IDE1140 chip with respect to the average value of the other four chips read by the same ADC.

The difference is compatible with 0, so there is no substantial difference in using one chip or another.

Finally the difference in common mode computation due to the different ADC chains is reported in figure 4.16 and shows again an average difference compatible with 0, confirming the possibility to use other chips to compute the Common Mode correction event by event.

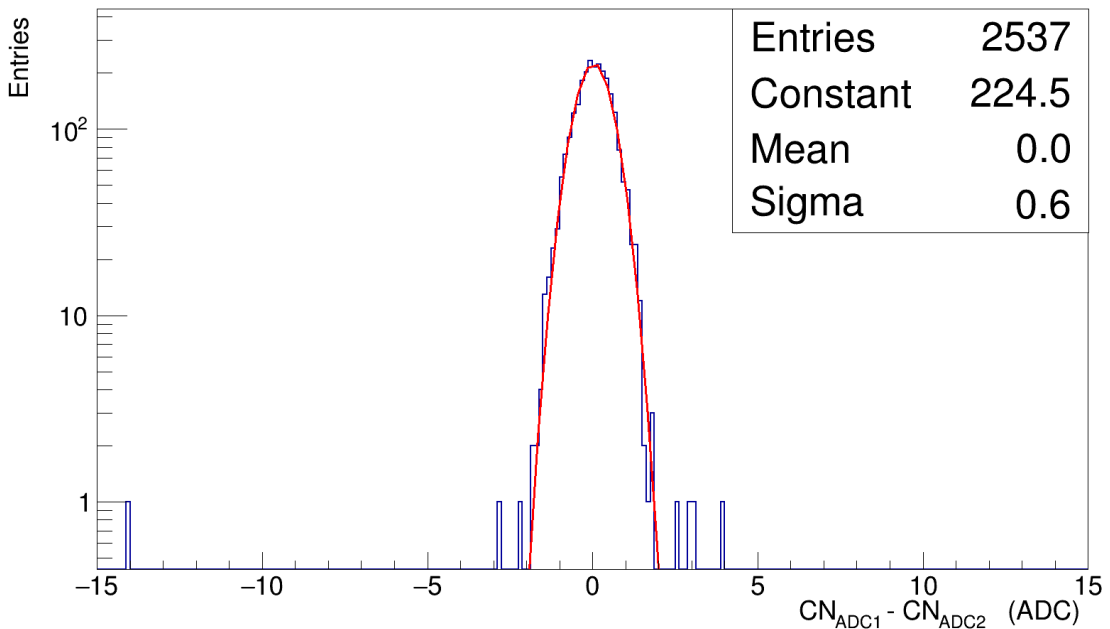


*Figure (4.16) – Distribution of the difference between  $CN_j$  computed for chips read by ADC1 and ADC2.*

#### 4.1.4 Characterization with cosmic muons data

A charged particle passing through the silicon sensor will deposit energy along the track creating e-h pairs and the drift of the charge carriers toward the electrodes will generate a signal, as explained in section 3.4.1.

The energy deposited in the silicon bulk depends on both the particle type and energy, and a value of  $\approx 24000$  e-h pairs for  $300 \mu\text{m}$  track length is used for Minimum Ionizing Particles. An external electric potential to deplete the entire thickness of the sensor assures the collection of the produced charges.

The depth of the depletion zone in the silicon bulk after a biasing voltage is applied can be calculated as [82]

$$w \approx \sqrt{\frac{2\epsilon|V|}{e|N_{eff}|}} \quad (4.5)$$

from which the full depletion voltage can be approximately written as

$$V_{depletion} \approx \frac{d^2}{2\epsilon\mu\rho} \quad (4.6)$$

where  $d$  is the sensor thickness,  $\mu$  is the charge carrier mobility in the bulk and  $\rho$  the specific resistivity of the bulk.

For a  $150\mu m$  thick sensor the complete depletion should then be reached at  $\approx 20$  V, which is compatible with the value provided by the vendor for the sensor used to build the FOOT\_PE001 prototype of 25V.

The bias voltage chosen for all the tests was set at 50V to work in the *over depletion* regime to assure a complete charge collection efficiency and thus obtain the highest possible signal.

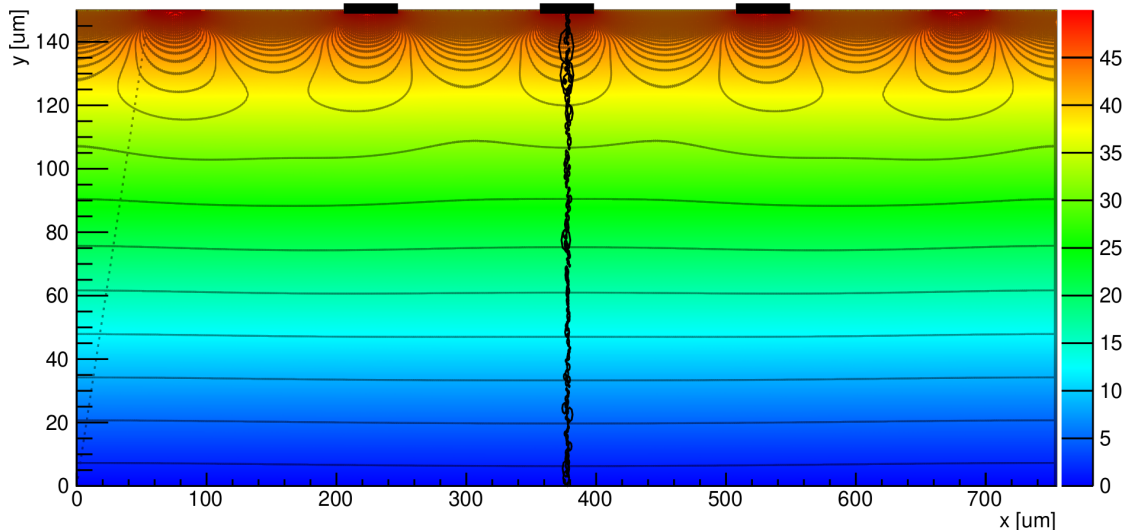


**Figure (4.17)** – MIP interaction in the silicon detector simulated with Weightfield2

The *Weightfield2* software package [83] has been used to simulate the interaction of a MIP particle in a *p* over *n* sensor with a 25V depletion voltage reverse biased at 50V detector (same as the FOOT\_PE001).

Figure 4.17 shows the track generated by the interaction of a MIP particle in the detector: the colour scale represents the calculated drift potential in the detector bulk with superimposed the equipotential lines and the energy released along the path of the particle in a portion comprising three readout strips.

Figure 4.18 shows the spatial charge distribution for the electrons generated by the ionization of the particle crossing the bulk under one of the readout strips.

The lateral distribution is of the order of a few micrometers even taking into account the thermal diffusion. Hence, due to the intense electric field, the charge will be collected solely on that strip.

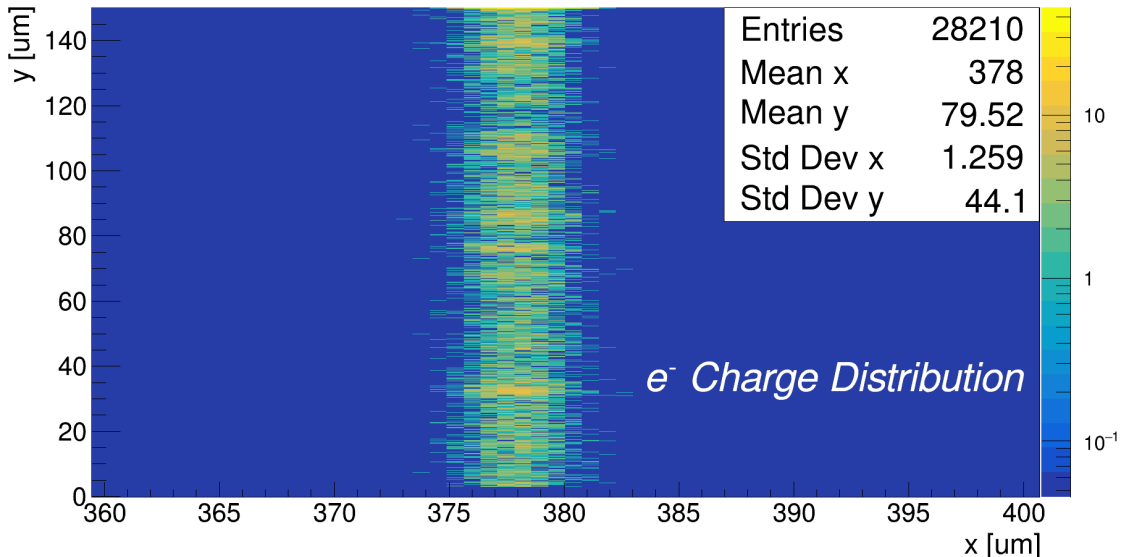


*Figure (4.18) – Charge distribution in the detector bulk for the ionization electrons*

If the track passes in the region between two strips (even if unconnected), the charge collection and signal formation are split between the two strips: in a floating strip configuration, the induced current by an unconnected strip will be shared with some loss with respect to the connected ones.

This signal subdivision depends in a non-trivial way on the track's position with respect to the electrodes, the number of floating strips and their characteristics: a reduction of up to 50% of the full signal is possible [84].

An algorithm to find the complete signal even if split among several adjacent strips is needed, and it should produce as observable the *cluster*.

The cluster finding is performed offline on each event, after pedestal and common mode noise subtraction, as shown schematically in figure 4.19: starting from the reduced value in equation (4.3), the cluster finding algorithm starts by parsing the reduced values in memory and seeks the cluster seed.

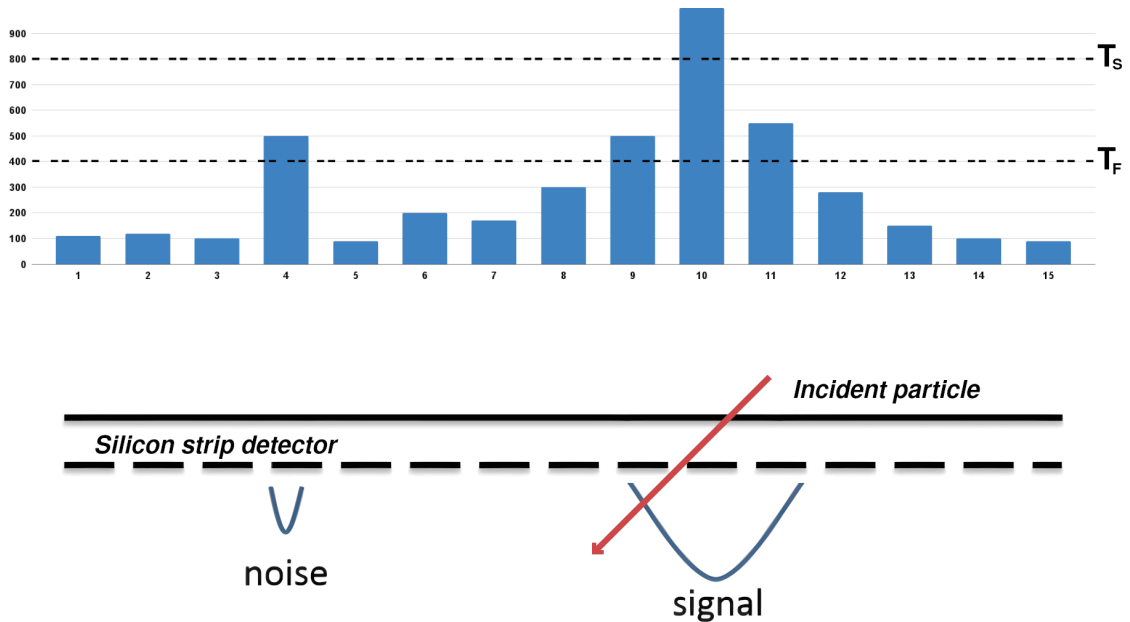


Figure (4.19) – Clustering algorithm

A cluster seed is defined as a channel with the reduced value  $r_{ij} > T_{s_i}$ , where  $T_{s_i}$  is the *seed threshold* of the channel  $i$  defined as a multiple of the sigma value for that channel: when a cluster seed is found, channels before and after are checked for values over the *fire threshold*  $T_f$ , until  $r_{ij} < T_f$ .

The properties of a cluster to be determined are:

- cluster width, i.e. the number of strips belonging to the cluster;

- cluster charge, i.e. the sum of the strip signal for the strips belonging to the cluster;
- cluster position, i.e. the presumed position of the incoming charged particle;

The first real data acquisition of the detector has been performed with the same DAQ system used for noise performance studies.

Trigger signal is no more generated randomly by the FPGA but is provided by the digitization of the signal produced by cosmic rays muons in a plastic scintillator placed under the detector read by a phototube, as shown in figure 4.20.

The entire setup is enclosed in a shielding box to protect the detector and the DAQ from light and from electromagnetic noise.

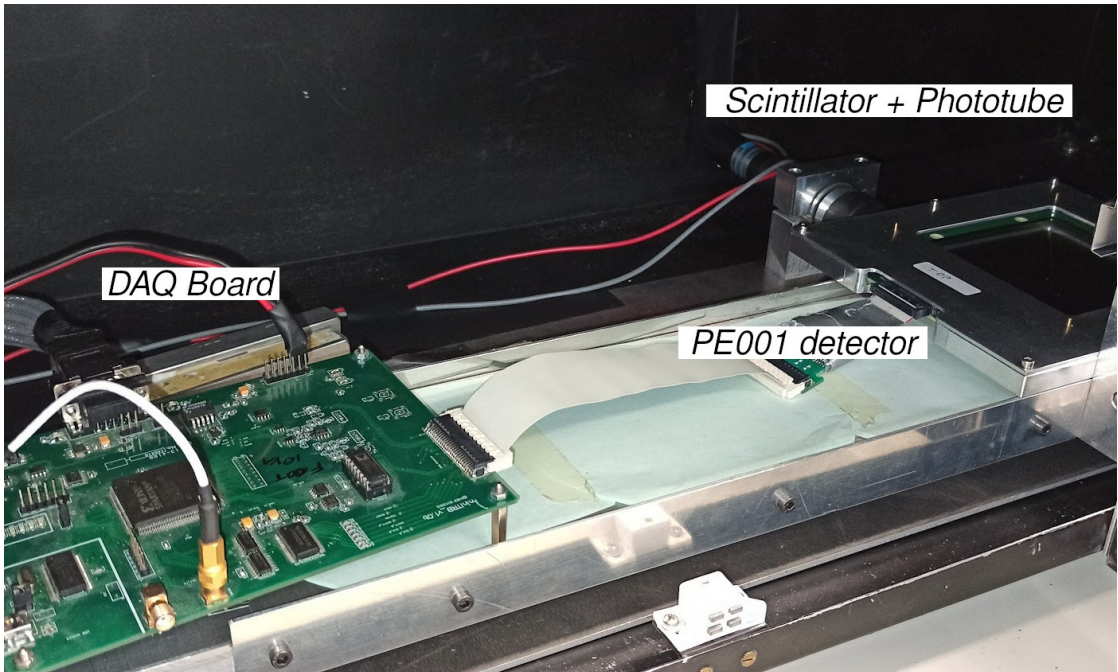


*Figure (4.20) – Setup used for the acquisition of cosmic muons data*

To define the proper  $T_s$  threshold to be used, the probability for one strip to be over the threshold due to noise needs to be minimized: a probability of less than 0.1% will only result in 1 of the 640 strips to fire due to noise fluctuations every 2 events.

Figure 4.21 shows the cumulative distribution of the strips with  $r_{ij}$  over threshold as a function of the threshold.

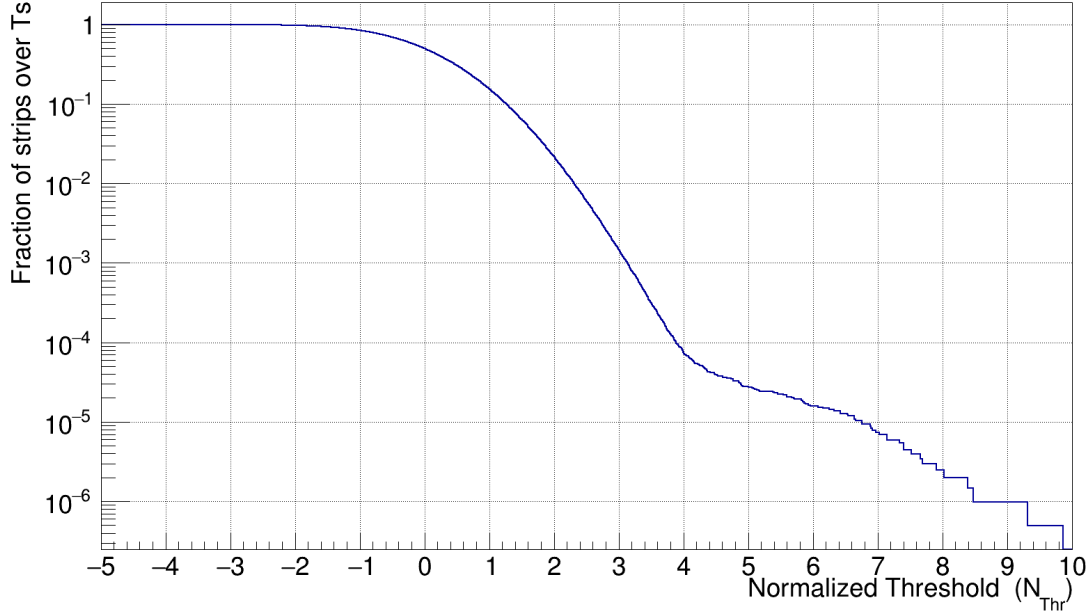


Figure (4.21) – Integral distribution of strips greater than seed threshold  $T_s$  vs seed threshold.

In the case of MIPs, a value of  $4 \sigma_i$  gives a negligible probability to have one strip over the threshold in one event.

For this reason, values of  $T_s = 4\sigma$  and  $T_f = 2\sigma$  were chosen for the clustering of data acquired with cosmic muons.

Given a certain ENC for the detector, and the signals  $S_i$  of the strips at positions  $x_i$  that are included in the cluster, the *center of gravity* (or COG) is defined as

$$COG = \sum_i S_i x_i \Big/ \sum_i S_i \quad (4.7)$$

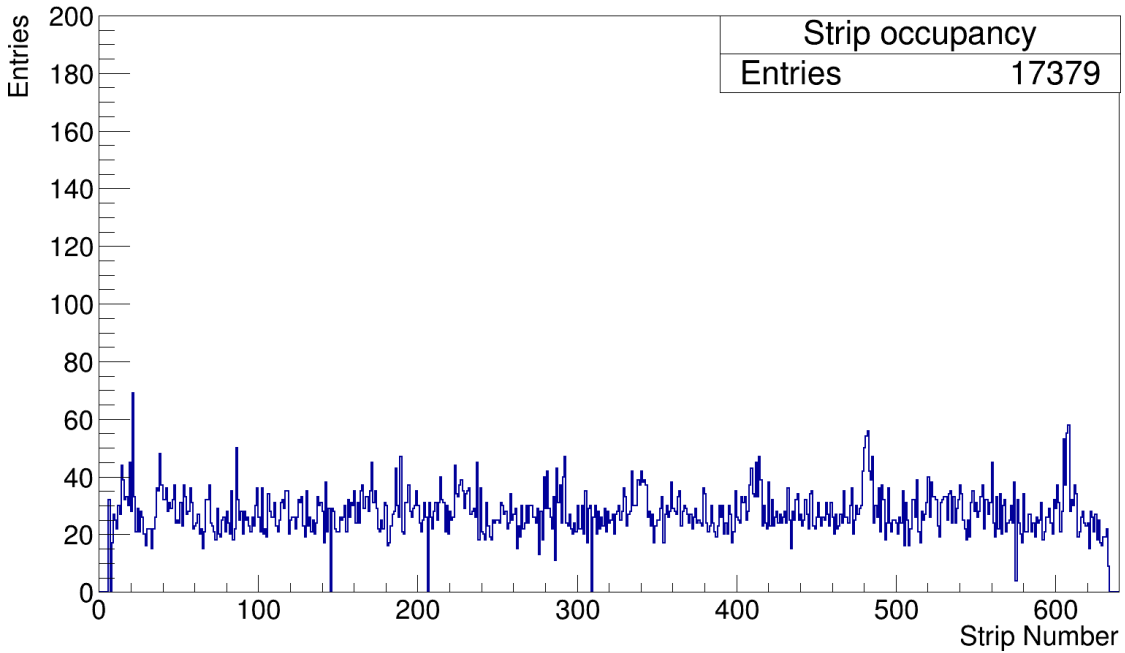
It has been proven that the spatial resolution is slightly dependent on the position of the impact point with respect to the collecting strips, and, for a given position, it is linearly dependent on the  $ENC/S$  ratio [85].

Choosing the impact point  $P$  for which the spatial resolution is worst it can be shown [86] that

$$\frac{\sigma_{COG}}{P} \propto a \frac{ENC}{S} \quad (4.8)$$

where  $a$  is a coefficient that depends on the hypothesis on noise and on the number of strips that make up the cluster.

Figure 4.22 shows the distribution of clusters position for clusters exceeding the seed threshold for one run, where the cluster position is determined with the COG algorithm: given that the scintillator used for triggering purposes was wide enough to span across the silicon sensor active area the distribution is, as expected, flat.



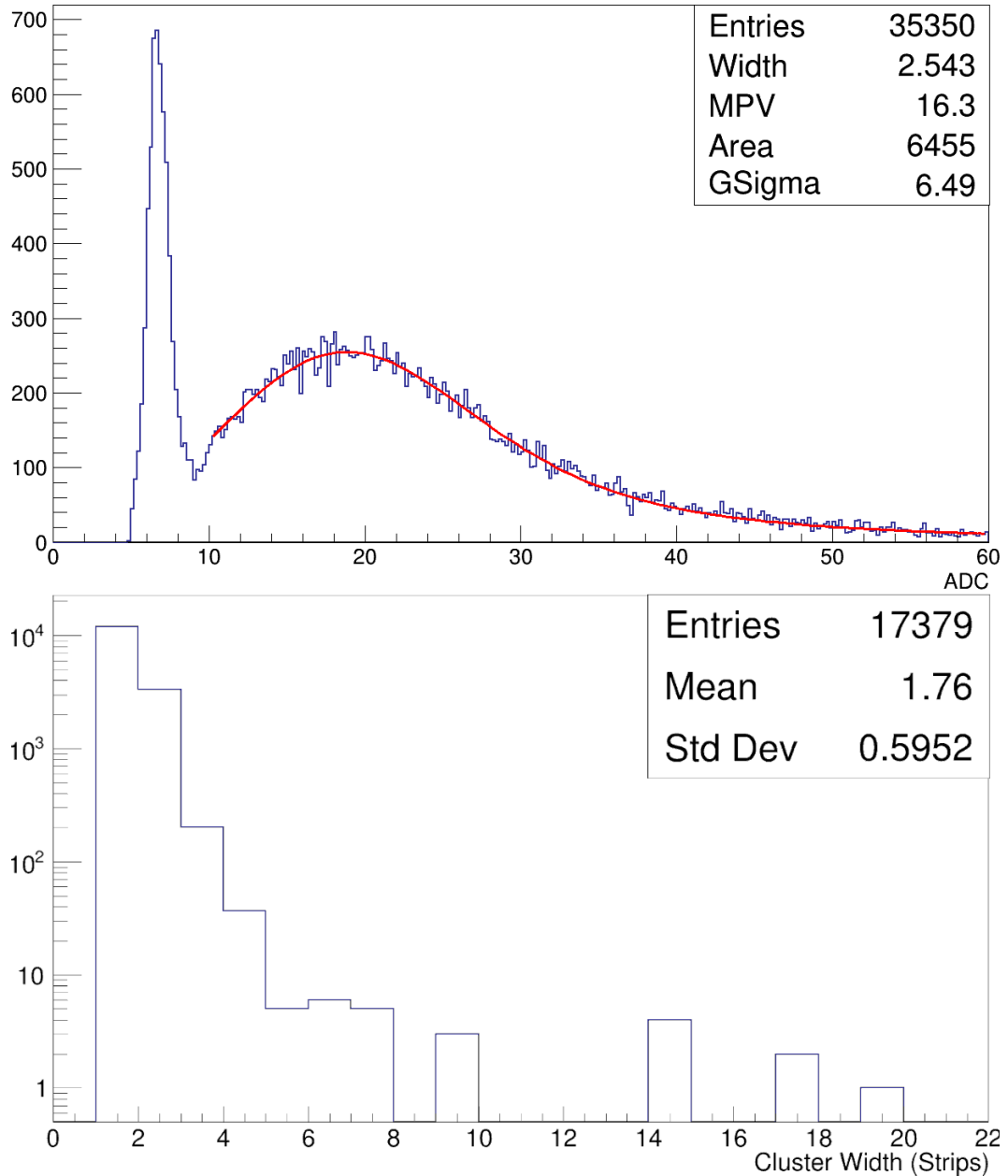
*Figure (4.22) – Strip occupancy for a cosmic muons run*

Figure 4.23 show the distributions of the reconstructed cluster signal (top) and cluster width (bottom) for one of the runs: as expected from data taken in the past with similar detectors [87][88] the charge distribution follows a Landau-like distribution with a clearly defined peak and a long tail for higher energy clusters.

Distributions for cluster signals were fitted with a convolution of a Gaussian function with a Landau function, giving as a result a Most Probable Value of  $\approx 16.3$  ADC, a value that is consistent with the predicted value from data acquired with a  $300 \mu m$  thick detector with the same DAQ system [88], for a Signal to Noise ratio of about 10.

Assuming a most probable value of  $\approx 12000$  electron-hole pairs generated by a single MIP, this results in an estimated value of  $2.6 keV/ADC$ .

Cluster width distribution (figure 4.23, bottom) show a prevalence of clusters with a single and a double strips: this is to be expected from particles impinging perpendicularly to the detector and releasing their energy in a region that is mostly confined either under a readout strip or between two of them.



**Figure (4.23)** – Cluster signal (top) and width (bottom) distribution for cosmic muons data

#### 4.1.5 Signal dependence on DAQ parameters

An important set of measurements performed with the new setup was a fine tuning of the DAQ system timing parameters: under normal mode of operation the input current of the 64 readout ASIC channels is fed to the pre-amplifier stage and, after a triggering event, is integrated by the shaper stage.

Once the peak is reached, an external signal needs to be applied to sample the value at the correct point in time. After the sampling, the multiplexed output stage is activated to sequentially read the values of all the channels, which are then given in input to the ADC chip.

To obtain the highest possible signal output, the delay between the triggering signal and the sampling signal needs to be tuned to match the time at which the shaper has peak value.

Figure 4.24 shows a schematic view of all the control signals needed for the correct functioning of the readout ASIC.

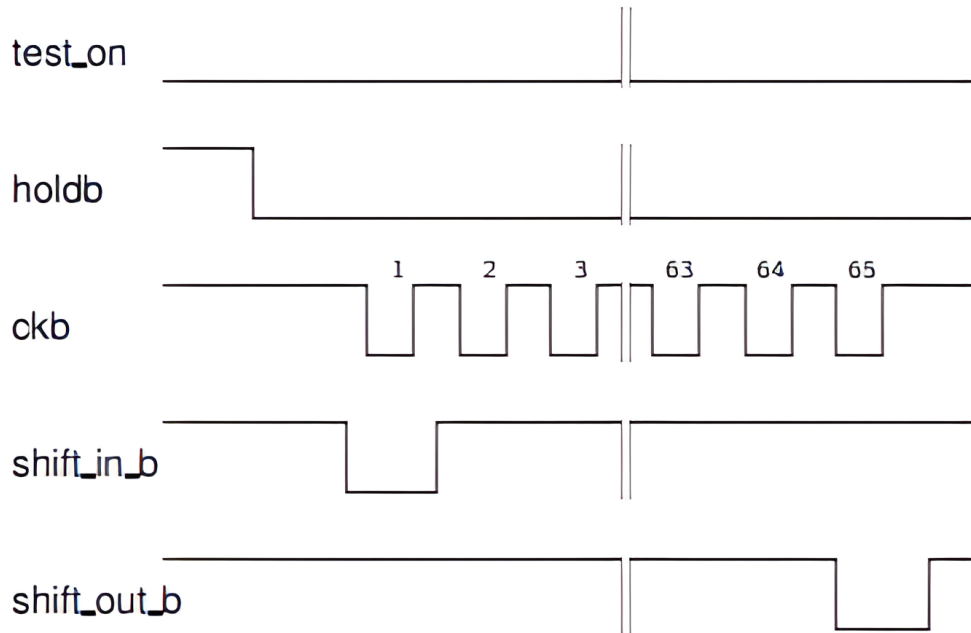


*Figure (4.24) – Readout ASIC control scheme*

To find the ideal working point, a scan of the values for this delay has been performed with the use of a radioactive Strontium-Yttrium (90) source with 19 mm diameter, using the setup shown in fig. 4.25. Strontium-90 is a pure beta-emitter with a maximum energy of 0.546 MeV and an half-life of 28.8 years, while its daughter nuclei Yttrium-90 has a shorter half-life of 64 hours and decays itself, via 2.28 MeV beta emission, into stable Zirconium-90.

The difference in decay rates of the two components implies a radioactive source that is at secular equilibrium [89].



*Figure (4.25) – Setup used for 90Sr data acquisitions*

Beta electrons are emitted over a continuous energy spectrum and deposit their energy along the full path in the detector before reaching the scintillator: only the higher part of the spectrum can actually generate a trigger for the acquisition, giving an energy deposit that is very close to that of a Minimum Ionizing Particles, while the lower energy electrons release all their energy in the silicon detector and therefore can not reach the scintillator beneath it.

Moreover, in order to get a low enough rate of particles, avoiding so saturation of readout electronics and limiting the number of lost events due to dead time in DAQ systems, thresholds for scintillator were set so that only the highest energy electrons could trigger the system, avoiding noise and spurious events coming from "dark counts" signals.

Data was acquired using the naked (non collimated)  $^{90}\text{Sr}$  radioactive source: figure 4.26 shows the spatial distribution in millimeters for the reconstructed clusters generated by the electrons of the naked  $^{90}\text{Sr-Y}$  source: a Gaussian fit of the distribution returns a value for  $\sigma$  of  $\approx 5\text{mm}$ , which is comparable with the expected values from the geometrical acceptance.

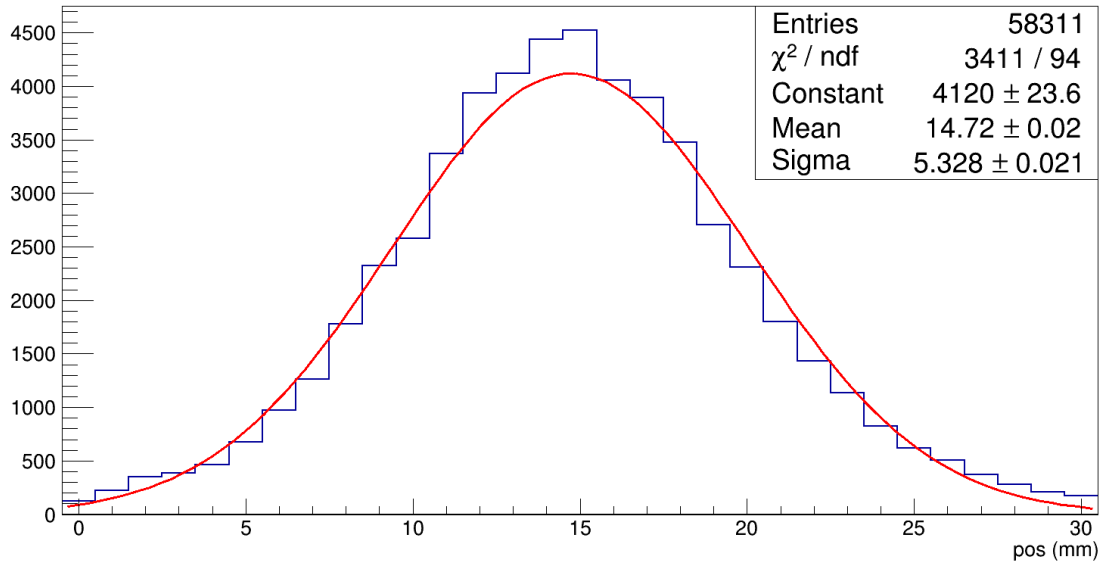


*Figure (4.26) – Reconstructed spatial distribution of the clusters*

Varying the sampling signal delay from 3 to  $12\ \mu\text{s}$ , the allowed range by the DAQ system's onboard FPGA, signal distributions were then fitted with a Landau (Landau convoluted with a Gaussian) function to retrieve the MPV for each value of the delay.

This values were then used to produce the characteristic curve of the readout ASIC to choose the optimal working point for subsequent data acquisitions (that is the value of the delay that maximizes the reconstructed output signal): as shown in fig.4.27, a value of  $\approx 8\mu\text{s}$  gives the highest possible signal.

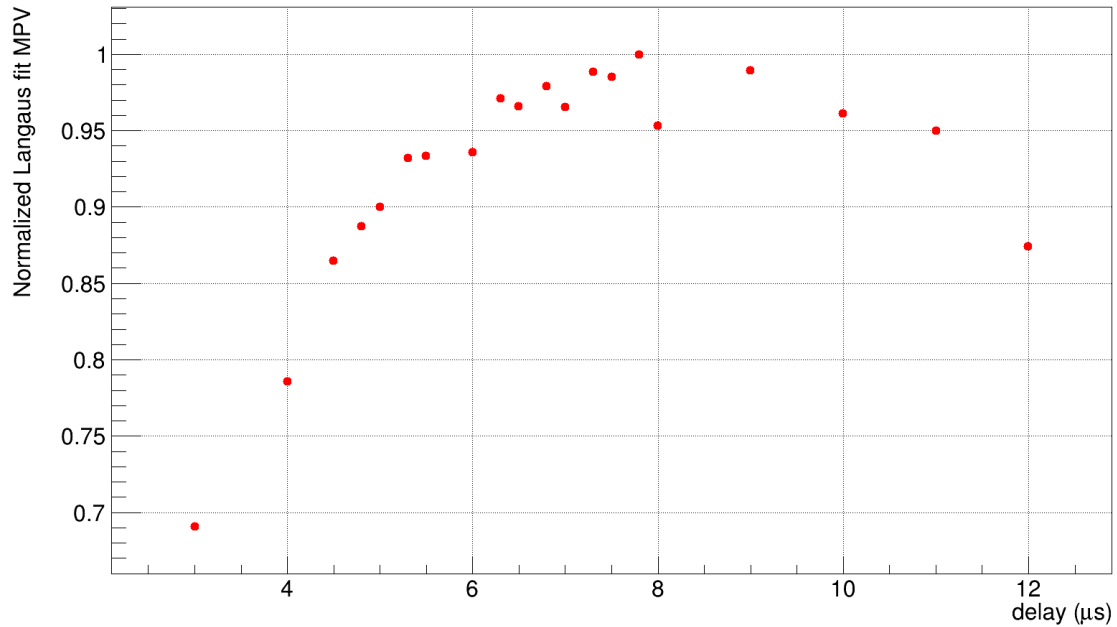


Figure (4.27) – IDE1140 response as a function of delay from trigger to the sampling the signal

## 4.2 Characterization of the detector with photon sources

### 4.2.1 Energy calibration with a radioactive photon source

Due to the characteristic signal deposition distributions of charged particles traversing a thin sensor, absolute calibration of the energy response is typically not possible for silicon microstrip detectors: the intrinsic fluctuations of the deposited energy, as described in 3.2.1, give raise to a Landau-Vavilov distribution for which the moments, like mean or variance, are undefined.

A conversion factor from ADC to deposited eV is thus not generally calculated for such detectors, and particle identification only relies on a relative calibration of the response based on the Z of the incident particle.

An attempt to perform such an energy calibration has been performed for the FOOT MSD detectors: the new calibration method under test is based on the premise that it is possible to measure the full energy possessed by the ionising particles used a stimulus.

The particles chosen for this task are photons from a radioactive source and X-ray

fluorescence: as discussed in section 3.3, the interaction mechanism of photons with the silicon bulk will result in an energy deposit that is approximately that of a Minimum Ionizing Particle ( $\approx 42\text{keV}$  under the assumption of a most probable value of  $\approx 12000$  electron-hole pairs generated): for example, Americium-241 decays mainly via alpha decay, with a weak gamma ray byproduct 59.5409 keV for the most part, with little amounts of other energies such as 13.9 keV, 17.8 keV and 26.4 keV (figure 4.28), while fluorescence photons from Gadolinium-64 and Tin-50 have energies of 42.5keV and 25.27keV respectively.

Starting from the value of  $2.6\text{keV}/\text{ADC}$  previously obtained from data with cosmic muons, a cut around 8 ADC will result in a cut of  $\approx 20\text{keV}$ , allowing in principle the identification of signal from all the photon species over the detector noise.

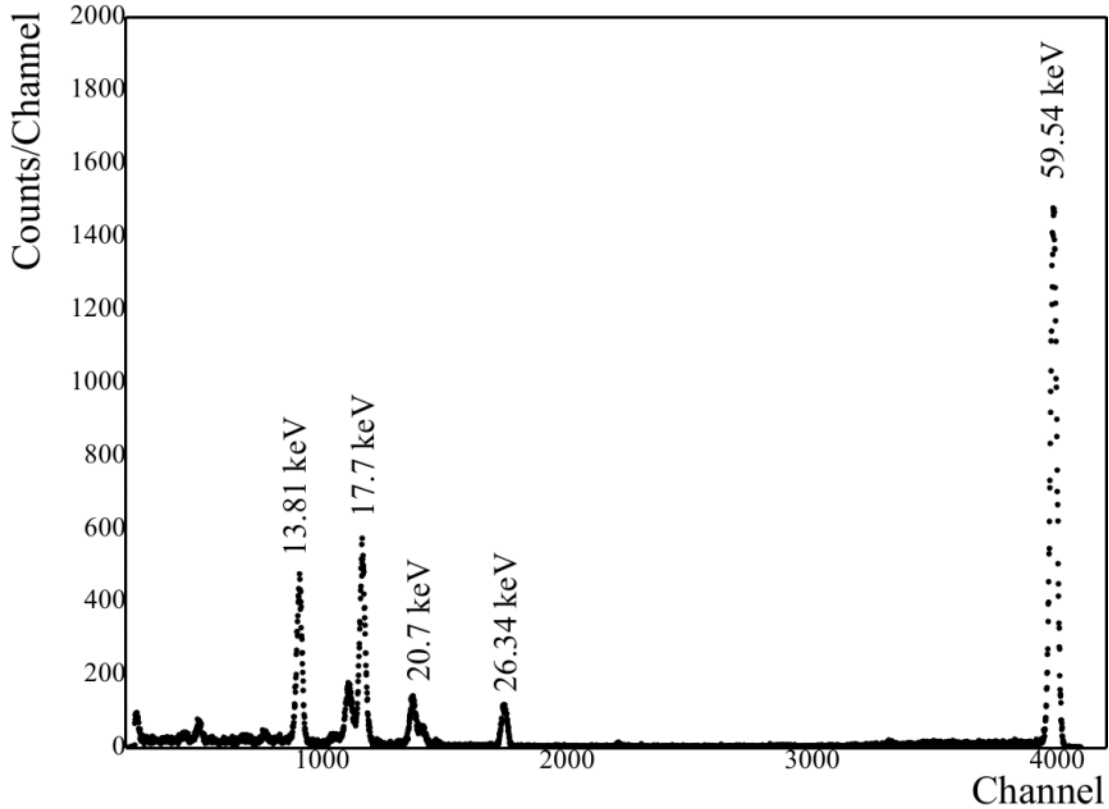


*Figure (4.28) – A typical spectrum of  $^{241}\text{Am}$  (from [90])*

The major obstacle of this type of analysis is the impossibility of using an external trigger for the acquisition like in the case of charged particles because the photons being

used which will be completely absorbed. It was therefore necessary to acquire with a random trigger at a fixed frequency of 50Hz, the maximum reliable rate that could be accepted by the miniTRB DAQ system previously described.

This resulted in two main complications

- a very long acquisition time is required to accumulate significant statistics, since in most events there is no signal
- When the passage of a photon occurs in the acquisition time window, it is not certain that the signal is sampled at its maximum peak

As a consequence of this, the distribution for the signal will be the result of a convolution between the Gaussian expected in the case in which the signal was sampled at its maximum peak and the shaping time function shown in figure 4.27.

Moreover, the detector geometry (150  $\mu\text{m}$  readout pitch, 150  $\mu\text{m}$  sensor thickness) guarantees that the photoelectron resulting from the interaction of the photon with the silicon bulk, which has an energy of the order of tens of keV, will be contained both laterally and vertically below one strip for most of the cases, and hence the signature to be searched for would be a single strip with signal.

The strip signal distributions in figure 4.29 (without  $^{241}\text{Am}$  source) and in figure 4.30 (with  $^{241}\text{Am}$  source) show the difference due to the photon emitting source: the peak around 0 ADC due to noise of the detector is clearly visible, while a tail for higher ADC values appears.

Data without the photon source was used to evaluate the background given by cosmic muons and has been subsequently subtracted.

Given the impossibility to directly retrieve the signals parameters from the raw signal distributions, a toy Monte-Carlo simulation was exploited.

The components of the simulation are:

- The experimental signal's spectrum from cosmic rays is used to attribute an energy deposition to each generated interaction in the silicon.
- The signal from photon energy deposition is modeled as a Gaussian distribution

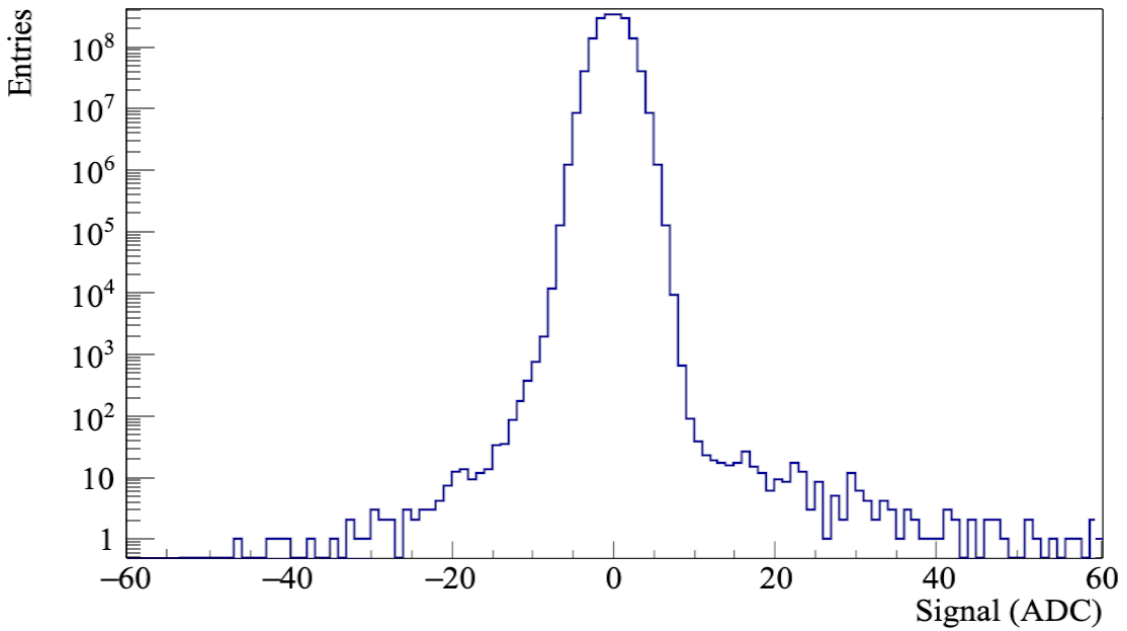


**Figure (4.29)** – Strip signal distribution without  $^{241}\text{Am}$  source. The tail on the right is due to cosmic rays interactions.

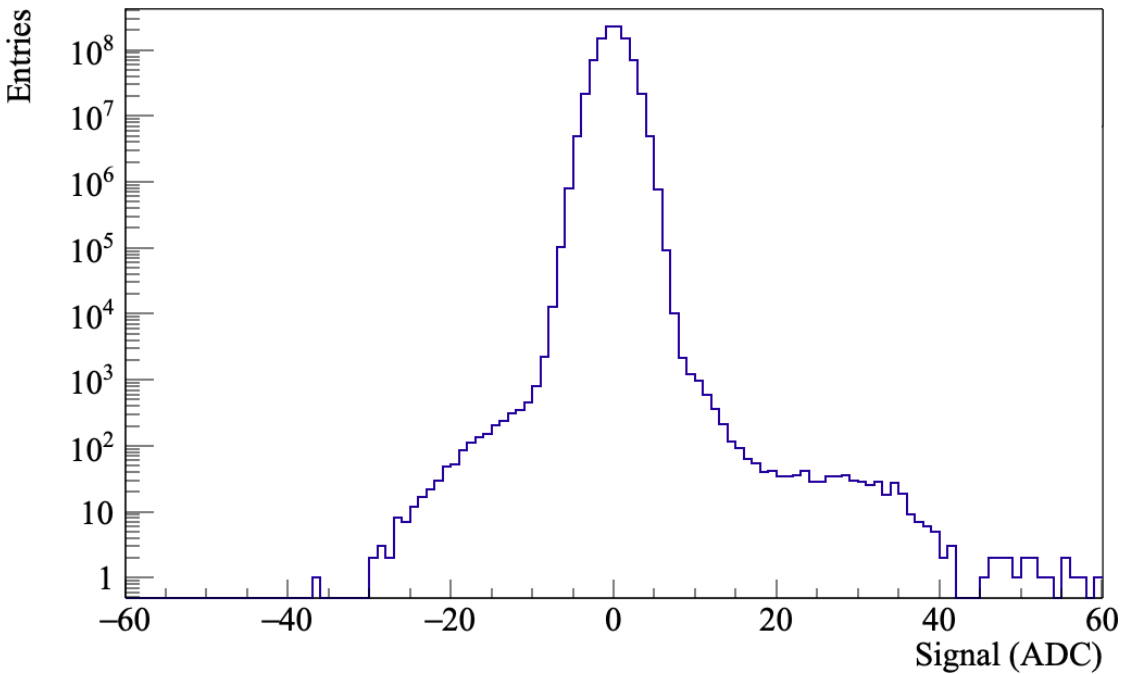


**Figure (4.30)** – Strip signal distribution with  $^{241}\text{Am}$  source. The tail on the right is due to sum of  $^{241}\text{Am}$  photons and cosmic rays interactions.

with fixed mean and sigma chosen in different ranges, [xx,yy] ADC and [ww,zz] ADC respectively near the expected values.

- The time of interaction with respect to internal trigger start is described as a uniform distribution and the signal is then obtained using a shaping response function derived from the data in figure 4.27

$$\begin{aligned}
 & - \text{ for } t \in [0,10] \mu\text{s} \quad ADC_0 = a \cdot \frac{1+b \cdot e^{-t/c}}{1+d \cdot e^{-t/c}} \\
 & - \text{ for } t \in [10,35] \mu\text{s} \quad ADC_1 = a_1 + b_1 \cdot t \\
 & - \text{ for } t \notin [0,35] \mu\text{s} \quad ADC_2 = 0
 \end{aligned}$$

- The number of simulated events for cosmic background per each trigger is normalized to the experimental measurement at a fixed threshold (10 ADC).

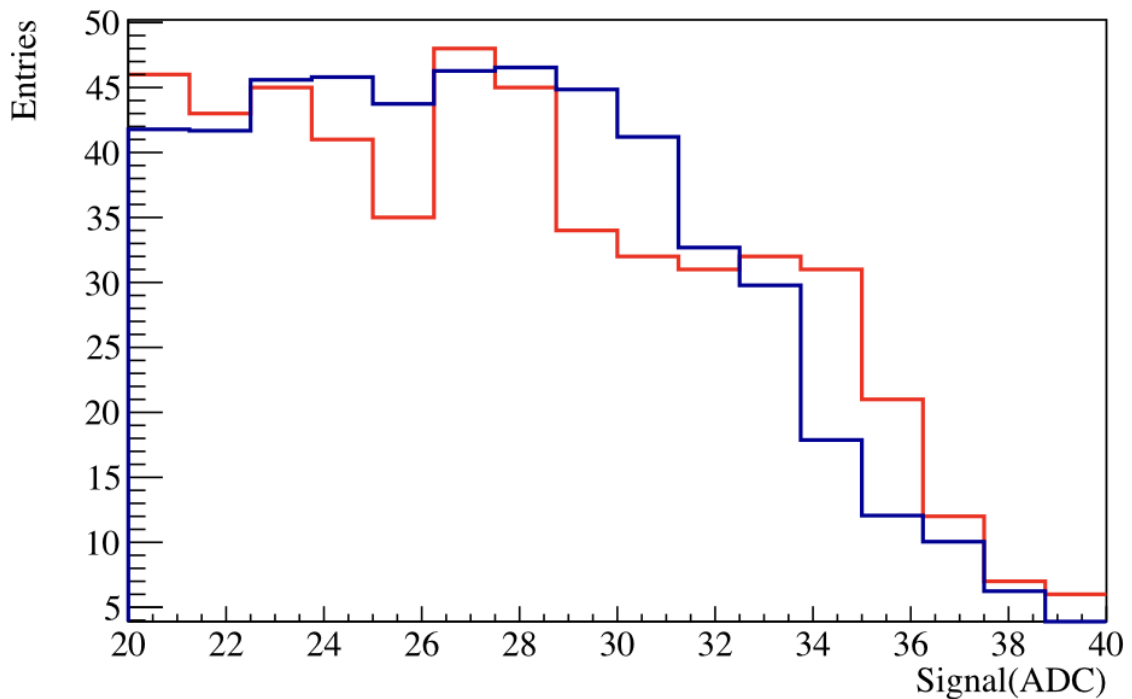


*Figure (4.31) – Distribution of the simulated signal (blue line) and experimental data (red line) for one of the simulated datasets*

The output of the simulation for a choice of the  $(\mu, \sigma) = (25.0, 3.0)$  starting pair is shown in fig.4.31 (blue line) together with the experimental data (red line) with the reproduced shape that qualitatively agrees with experimental data.

At this point it's possible to vary the values assumed by the two parameters in order to find the signal that best matches the experimentally measured one.

For each pair of values a data set is simulated to obtain a distribution that represents a particular parametric hypothesis for the signal while the experimental one represents the sample evidence which, supplemented with a priori knowledge, is used to statistically verify the validity of the hypothesis made.

From each simulated dataset it is thus possible to obtain a value of the  $\chi^2$  parameter as

$$\chi^2 = \sum_{i=0}^n \frac{(y_i^{exp} - y_i^{sim})}{\sigma_{exp}^2} \quad (4.9)$$

where  $y_i$  identifies the number of entries in the  $i$ -th bin.

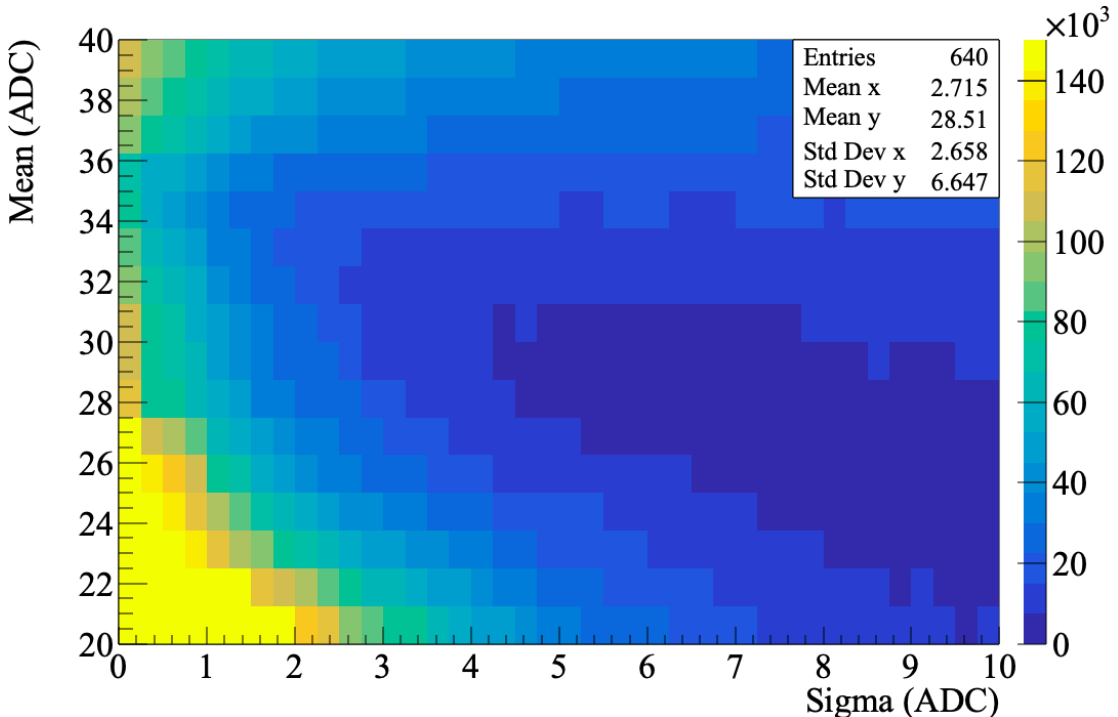


**Figure (4.32)** – 2D distribution of the  $\chi^2$  value obtained for each simulated  $(\mu, \sigma)$  pair in the case of  $^{241}Am$  photons

Figure 4.32 shows the 2D distribution of the  $\chi^2$  value obtained for each simulated  $(\mu, \sigma)$  pairs: the search for the optimal pair of parameters for the simulated signal is

therefore a minimization problem for a  $\chi^2$  function that depends on two parameters and for which a multidimensional confidence interval can therefore be estimated, which in the case under study is expected to be an elliptical surface, given the possible correlation between the two parameters.

Such simulations have then been performed for data taken not only with  $^{241}Am$  photons but also with fluorescence photons from an X-Ray source impinging on different target materials, to then extract the values for the deposited energy and, subsequently, to generate a calibration curve for the energy response of the signal [91].

Table 4.2 shows the values obtained for the different photon sources.

	Photon energy (keV)	$\hat{\mu}$	$\hat{\sigma}$	Calibration coef. (keV/ADC)
$^{241}Am$	59.54	$29.9 \pm 0.4$	$4.4 \pm 0.3$	$2.0 \pm 0.3$
$^{64}Gd$	42.50	$17.8 \pm 0.3$	$4.0 \pm 0.2$	$2.4 \pm 0.5$
$^{50}Sn$	25.27	$14.3 \pm 0.3$	$2.0 \pm 0.1$	$1.7 \pm 0.2$

Table (4.2) – Energy calibration parameters calculated with different photon sources (adapted from [91])

### 4.2.2 Characterization of the detector with an infrared laser

To further characterize the detector, a setup using an infrared laser has been used: for a light wavelength of 1058 nm, the expected penetration depth is about  $800\mu m$ .

The wavelength of the laser has been chosen to match as closely as possible the optimal value for silicon, as discussed in section 3.3.

The integrated energy loss of a laser pulse with initial energy  $E_0$  up to a depth  $z$  is described by

$$E(z) = E_0(1 - e^{-z\alpha}) \quad (4.10)$$

from which it is possible to obtain an expression of the energy lost per unit path, in a similar manner to the stopping power defined for charged particles

$$\frac{dE}{dx} = E_0\alpha e^{-z\alpha} \quad (4.11)$$

A pulse of laser light of this wavelength will thus traverse the whole thickness of the detector, producing a column of electron and hole pairs which are nearly uniformly distributed along the laser beam path inside the silicon bulk.

Data acquired with the infrared laser has been therefore used to make a further check of the optimal value to be used for the shaping time delay discussed in section 4.1.5 being able to avoid the problems caused by the low signal-to-noise ratio of MIPs and the intrinsic fluctuations resulting from the use of charged particles.

The response of the readout IDE1140 ASIC is presented in figure 4.33: the characteristic response curve can be well reconstructed from experimental data, confirming the value of  $\approx 8\mu\text{s}$  already found with data from  $^{90}\text{Sr}$  electrons.

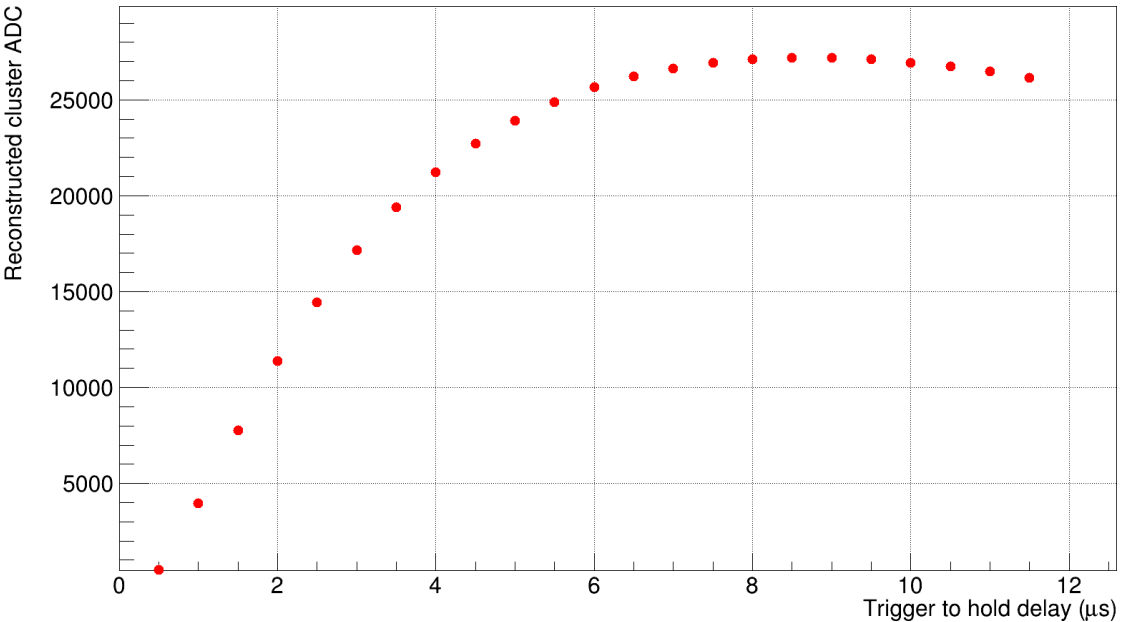


*Figure (4.33) – IDE1140 response as a function of delay from trigger to the sampling the signal from the pulsed laser*

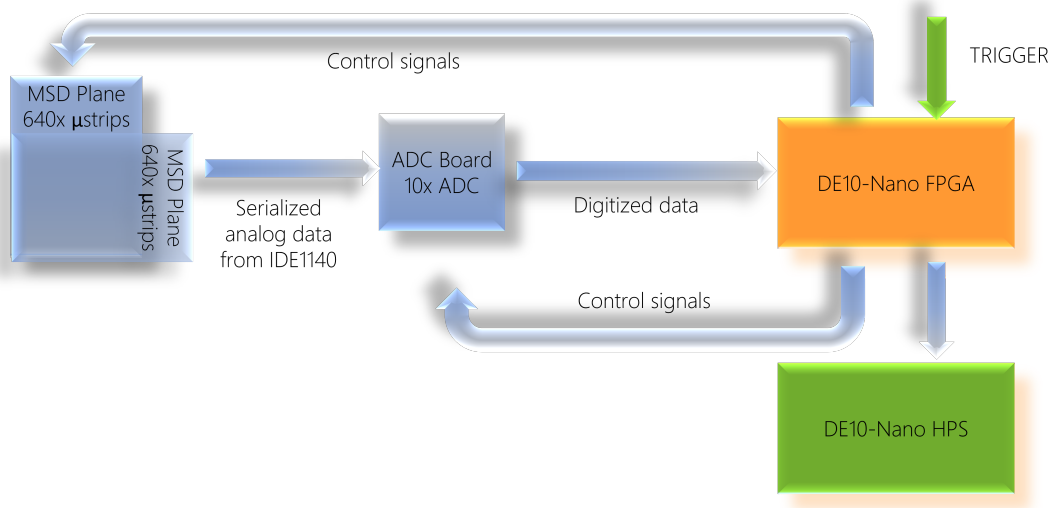
### 4.3 The new DAQ system for the FOOT MSD

The new data acquisition system developed for the MSD subsystem is based on the core principles of scalability and adaptability to the multiple different conditions, as requested by the full FOOT experiment.

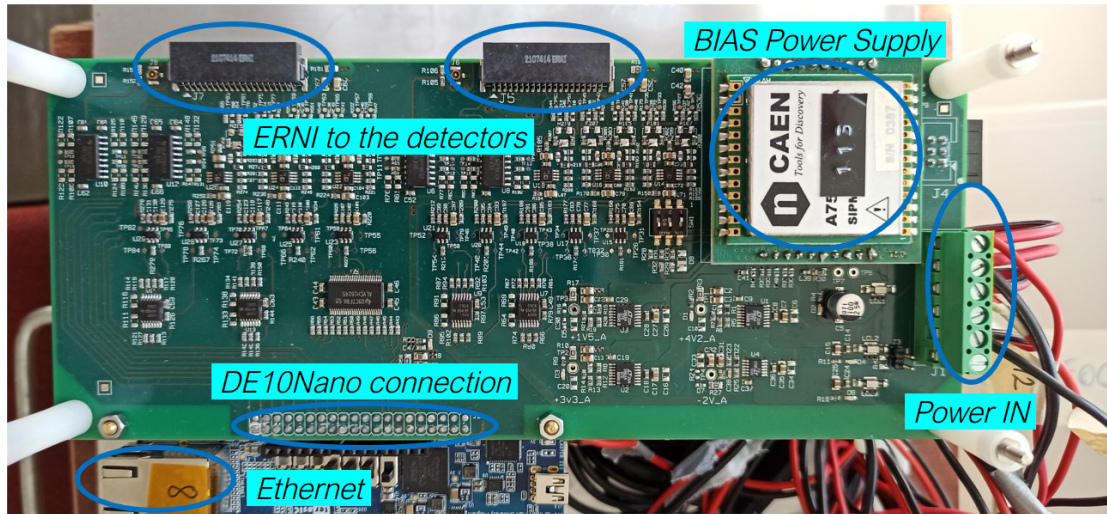
#### 4.3. THE NEW DAQ SYSTEM FOR THE FOOT MSD

Figure 4.34 shows a scheme of the MSD DAQ subsystem, consisting of two main components: the ADC board and the DAQ board.

The ADC board (figure 4.35) hosts the ADCs to digitize the signals coming from the IDE1140 outputs on the hybrid boards, while the DAQ board embeds the controller of all of the other subsystems and the interface toward the central system.



*Figure (4.34) – Scheme of the MSD DAQ subsystem*



*Figure (4.35) – Close up of one of the FOOT MSD ADC boards*

Each ADC board (figure 4.35) reads one x-y plane, i.e. two microstrip detectors, connected via two 40-pin ERNI connectors with the use of ten 12-bit 3-MspS AD7276A[92] ADCs and each of them digitizes two IDE1140 outputs.

The number of IDE1140s read by each ADC, and thus the total number of ADCs, was chosen to guarantee a maximum dead time below  $500\ \mu\text{s}$ . The board also includes one of the CAEN AD7585DU described in section 4.3.1 to generate the bias voltage for the x-y plane and the buffers/drivers for the DAQ board, which is controlled by an I<sub>2</sub>C bus via a dedicated connector on the board.

The ADC board directly plugs to the DAQ board, i.e. a Terasic DE10-Nano board, a commercial board that is the core unit of the x-y plane readout with an Intel Cyclone V System-On-Chip device that integrates an Intel FPGA with a Cortex-A9 ARM-based hard processor system (HPS) CPU, assisted by 1GB of fast DDR3 SDRAM and 1 gigabit ethernet capabilities.

The Cyclone V controls both the IDE1140s and ADCs (with its FPGA side), collects their digital output, and communicates with the central DAQ system (with its CPU side). Everytime the central DAQ system issues a trigger signal, the FPGA starts the readout procedure:

1. wait for the IDE1140 shaper to reach its peak (with a programmable value derived from the measurements performed in section 4.1.5)
2. start the IDE1140s readout process with a signal on their *shift in* line
3. enable the *hold* of the sample-&-hold circuitry
4. activate the ADCs by deasserting their chip select
5. feed the ADCs' serial clock to synchronize their output
6. sample the incoming serial data from the ADCs and parallelize them in 16-bit shift registers
7. feed the IDE1140s a clock to multiplex in output all of the microstrip values

Steps 4) to 7) are then repeated for all the 128 strips that are multiplexed to each ADC.

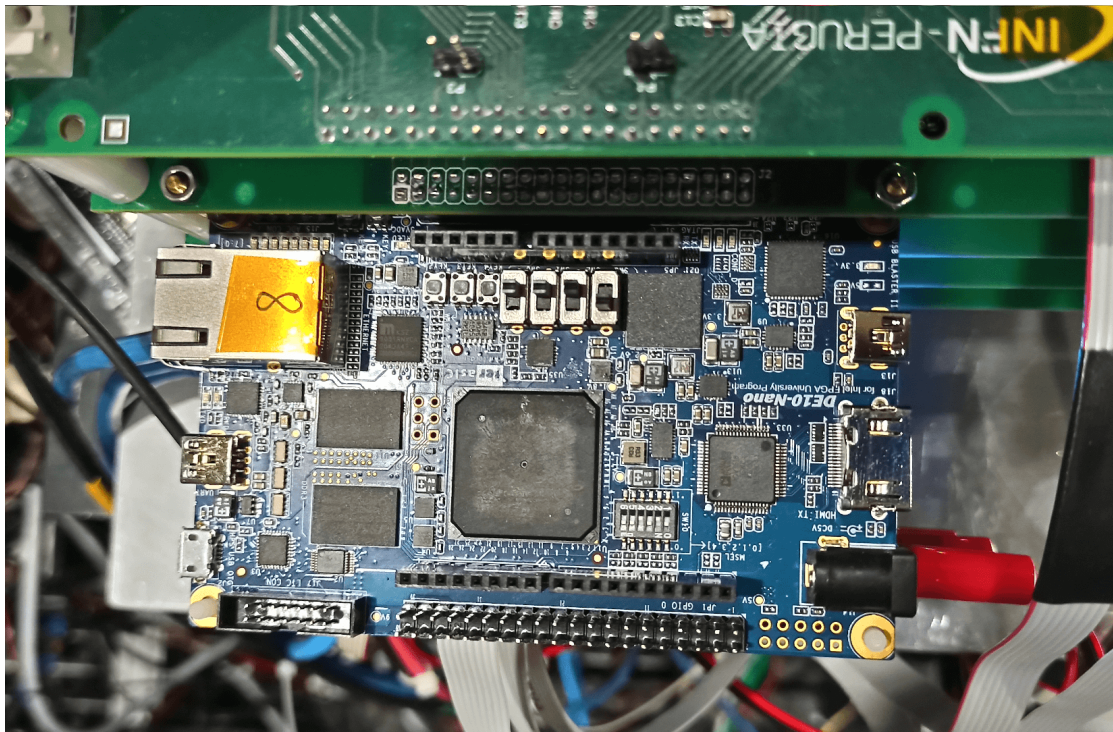


*Figure (4.36) – Close up of one of the Terasic DE10-Nano boards*

The ten streams of parallel output generated in this way from the ADCs are interleaved to form a 32-bit wide packet, that is encapsulated with a header and a trailer.

The header contains the packet length, a progressive number of triggers occurred, and a timestamp computed from an external 1-MHz clock that can be used to verify data integrity and synchronization.

The resulting event packet length is thus fixed to 1280 bytes for a single detector, 2560 bytes for one ADC board.

No further processing is performed on the packet, with no impact on the capabilities of the complete system to run at the required trigger rates foreseen for the FOOT experiment (section 2.3.1).

A dedicated compression algorithm running either on FPGA or CPU is foreseen for the future to further decrease the necessary bandwidth and memory occupation of the data stream.

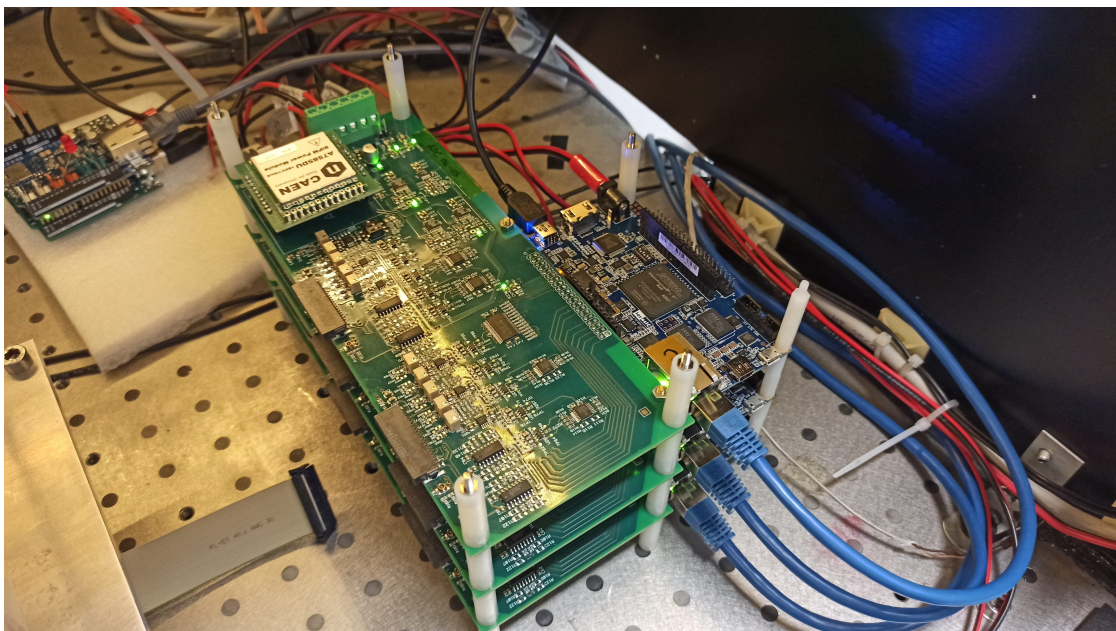


*Figure (4.37) – Photo of the complete assembled DAQ system during preliminary tests in the laboratory*

The DE10-Nano HPS communicates with the FPGA via an AXI interface, with a maximum throughput of 100 Gbps.

The FPGA writes the events directly into the HPS memory via Direct Memory Access (DMA), to guarantee the maximum use of the AXI interface bandwidth.

The HPS runs an embedded Linux distribution developed by Terasic, with custom software running to perform all the MSD related tasks.

Communications to the DAQ central for system slow control, monitoring, and physics data transfer occur on a TCP channel over the 1Gbps Ethernet interface of the board.

Finally, a patch-panel completes the system with the needed electrical interface toward the central trigger control unit. The received signals of trigger, clock, and reset provided by the central DAQ trigger system are converted from LVDS to single-ended 3.3-LVTTL and fan-out for all of the DE10-Nano boards.

The single-ended busy lines from all the DE10-Nano are then converted to LVDS signals to be sent to the central trigger control unit.

### 4.3.1 CAEN A7585DU Silicon Power Supply

The A7585DU Silicon Power Supply is a compact high voltage regulator originally designed by CAEN S.p.A. in close collaboration with Nuclear Instruments s.r.l [93] for SiPM biasing.

For this reason, an input low-dropout regulator (LDO) and an output filter operate to minimize the output noise and the variations of the requested output voltage.

Each module can provide up to 10 mA and the output voltage can be regulated between 20V and 85V with a resolution of 1mV and great time stability (as shown in figure 4.38), making it suitable for the biasing of the produced MSD detectors at full depletion voltage for extended periods of time.

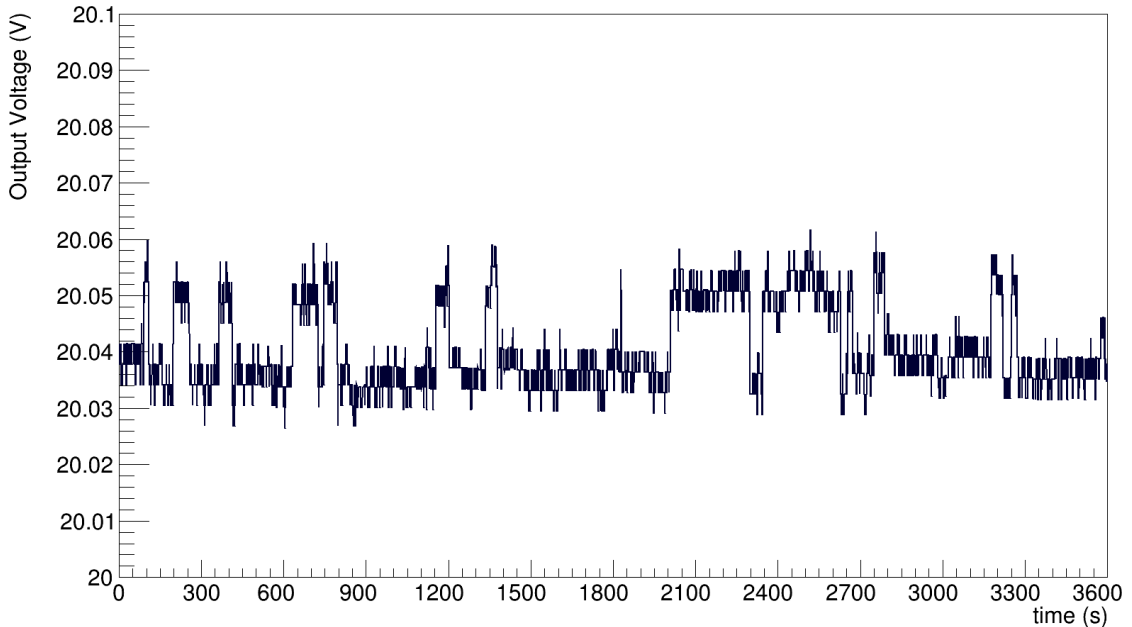


*Figure (4.38) – Output voltage as a function of time for a requested 20V bias voltage*

The A7585DU integrates a USB to UART bridge to control it via a serial connection with the provided software and both digital (UART and I2C) and analog control interface that are runtime selectable by a single pin or a digital command.

To increase the flexibility of the biasing power supply system, the A7585DU located on the FOOT ADC boards (as described in section 4.3) are controlled remotely by an

Arduino Uno microcontroller board: commands to be sent to the power supply modules are received over the local network shared with the DAQ boards by the Arduino board running an Ethernet Shield add-on.

A server running on the Arduino board listens for the power supply commands and transmits them to the targeted module via the I2C bus.

Each module on the I2C bus can be directly addressed both to change its functioning parameters and for real-time output voltage and output current monitoring, with up to 16 different manageable modules with a single Arduino Uno board.

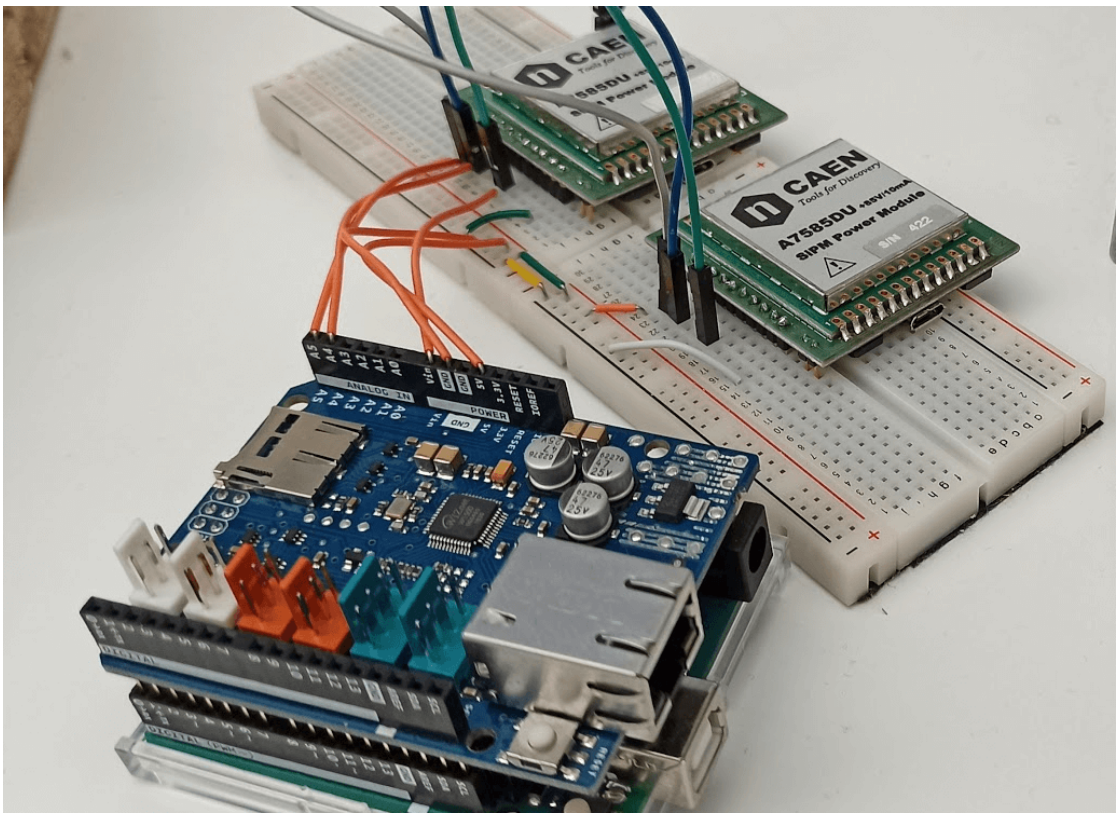


*Figure (4.39) – Two AD7585DU power supply modules controlled via I2C bus by Arduino Uno*

## 4.4 Construction and testing of the complete MSD subsystem

A total of 32 single sided microstrip detectors have been assembled over the span of several months, following the successful procedure developed for the first prototype, as explained in section 4.1.

Figure 4.40 shows the characteristic I-V curves of the naked silicon sensors provided by Hamamatsu: all of the provided sensors show the correct behaviour, with leakage currents within the limits of the power supply used, making them suitable for the construction of the detectors.

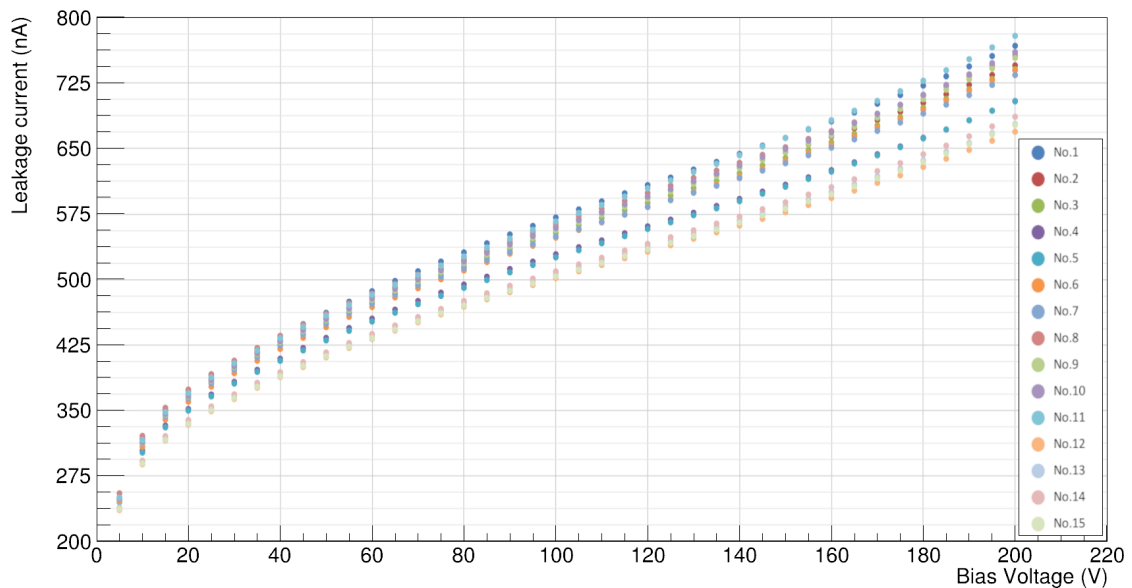


*Figure (4.40) – I-V curves for the naked silicon sensors as provided by the manufacturer*

The I-V curves have then been remeasured after the assembly, with figure 4.41 showing an example of such measurements: as expected, the absolute value of the leakage current of the detector shows a slight increase due to the presence of the bias voltage filtering circuitry on the hybrid, while the overall shape does not change significantly.

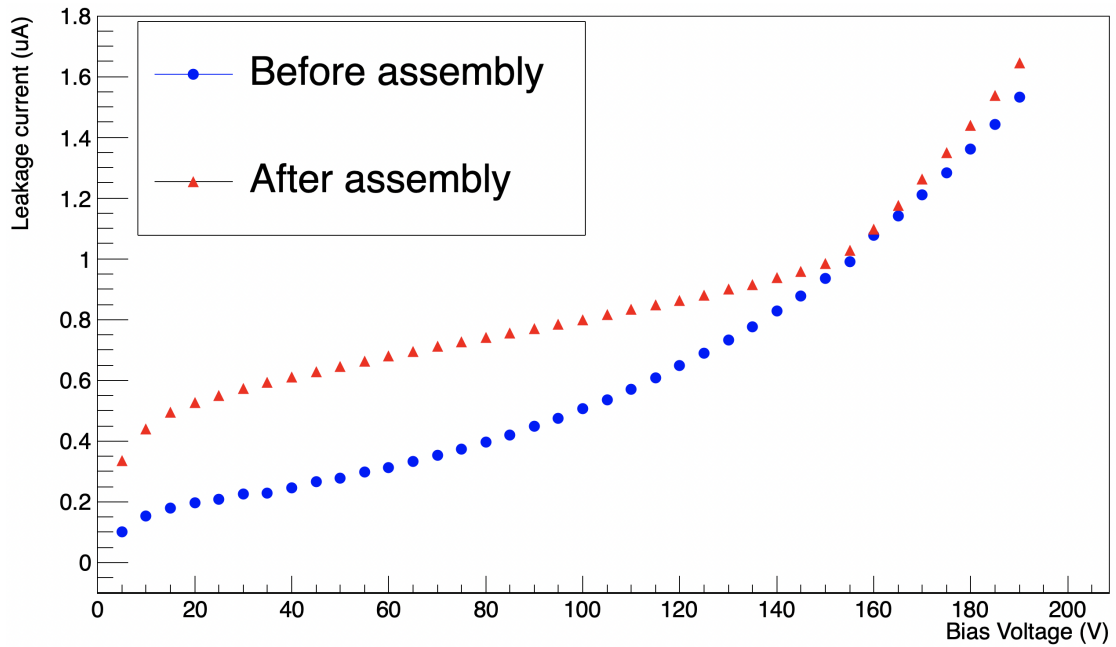


Figure (4.41) – I-V curve for one of the silicon sensors before and after the detector assembly

This confirms the average full depletion voltages provided by the manufacturer of  $\approx 23$ V, and the subsequent choice of a biasing voltage of 50V to ensure the operation in overdepletion regime.

Noise performance have been evaluated at several steps during the assembly procedure to assure the correct functioning of each detector.

Particularly important is the evaluation of pedestal and sigma of all channels after the micro-bonding of the readout ASICs with the hybrid PCB, and after the micro-bonding of the silicon channel with the readout chips.

Figure 4.42 and 4.43 show the difference in the computed pedestals and sigmas for one of the detector in the two steps described: the noise introduced by the silicon is well within 1 ADC, with the pedestal value change being negligible in view of dynamic range performance and no introduction of noisy channels by the silicon bonding procedure.

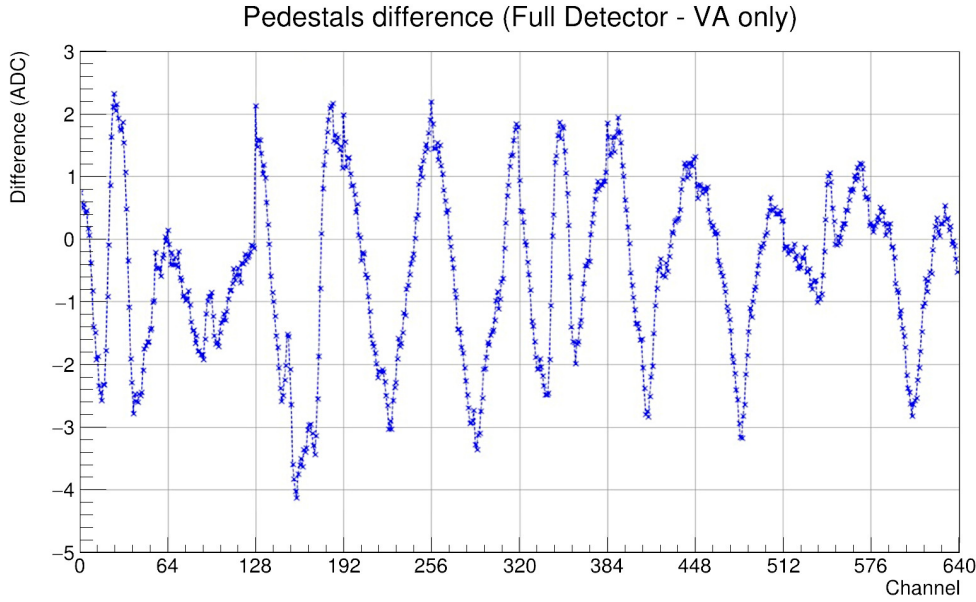


*Figure (4.42) – Difference in pedestals after silicon bonding for one of the detectors*

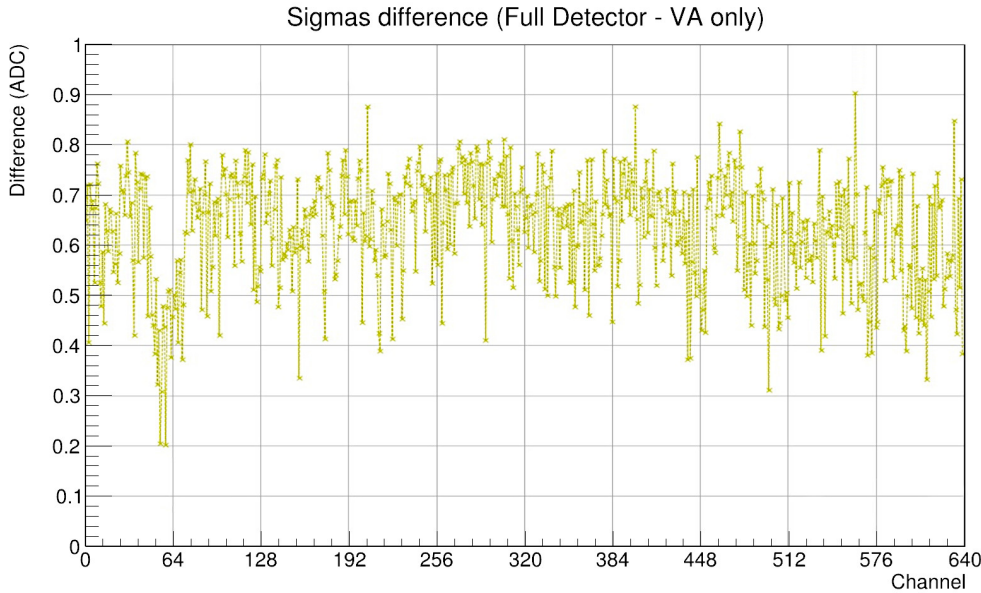


*Figure (4.43) – Difference in sigmas after silicon bonding for one of the detectors*

Figure 4.44 show the noise distributions of all the tested detectors: the pedestal distribution, while presenting substructures deriving mostly from the non uniformity

of the baseline levels of the different ADC boards, is well contained in the 100-700 range, with a mean value of  $\approx 368$  ADC. This value is close to the planned value for the ADC baseline level, ensuring the availability of a wide portion of the dynamic range.

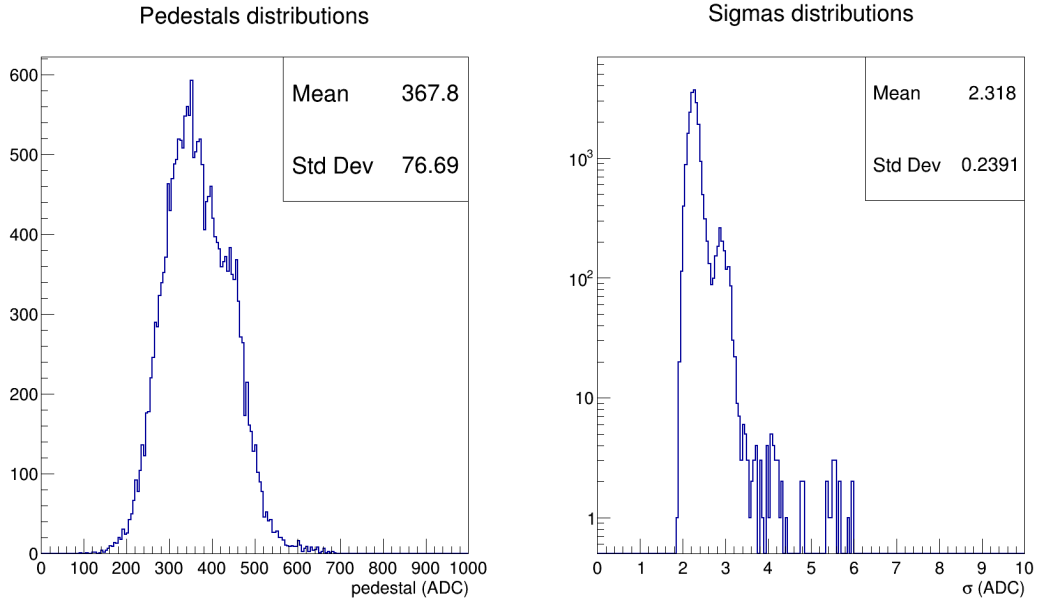


*Figure (4.44) – Pedestals and noise distributions for all the assembled FOOT silicon microstrip detectors*

The sigmas distribution shows that most of the channels of all the constructed detectors have a noise between 2 and 3 ADC, with only a low number of strips presenting an higher level of noise: this was ensured by thoroughly testing all the detectors at each step of their assembly procedure, giving the possibility of fixing either single channels or entire readout chips that presented abnormal behaviour.

# CHAPTER 5

---

## Detector response to charged particles at the accelerators

---

The FOOT Microstrip Silicon Detector will give information about the track position to contribute to the momentum reconstruction, but it will also measure the fragments  $\Delta E$ . It is thus important to characterize both its tracking capabilities (namely, its spatial resolution and detection efficiency) and its response to different particles that are not at the ionizing minimum, as foreseen for the fragments that will be produced in the different setups needed for the goal measurements of the FOOT experiment.

To do this, a series of tests at the accelerators have been performed in different facilities after the construction and testing performed in the laboratory, to gather data with different particles species at several energies.

Section 5.1 will briefly describe the different experimental setups used and their main goals, while sections 5.2 to 5.4 will present the results of the analysis performed on data from the various data campaigns.

## 5.1 Experimental setups

Three main data campaign at the accelerators have been performed during the last year to acquire data to characterize the performance of the complete MSD subsystem: sections 5.1.1 to 5.1.3 will describe the setups used and their goals, while sections 5.2 to 5.4 will present the first results of the analysis of the data acquired.

### 5.1.1 Trento 2021 Data Campaign

The first data campaign to test the complete MSD subsystem was performed in June 2021 at the *Proton Therapy Center* (PTC) in Trento [94], Italy's newest hadrontherapy oncology centre, equipped with two treatment chambers with a 360° adjustable proton beam and a room entirely dedicated to research.

The latter (shown in figure 5.1) is made available for both Italian and European experiments for both clinical and other purposes, such as the test of the various FOOT experiment components.

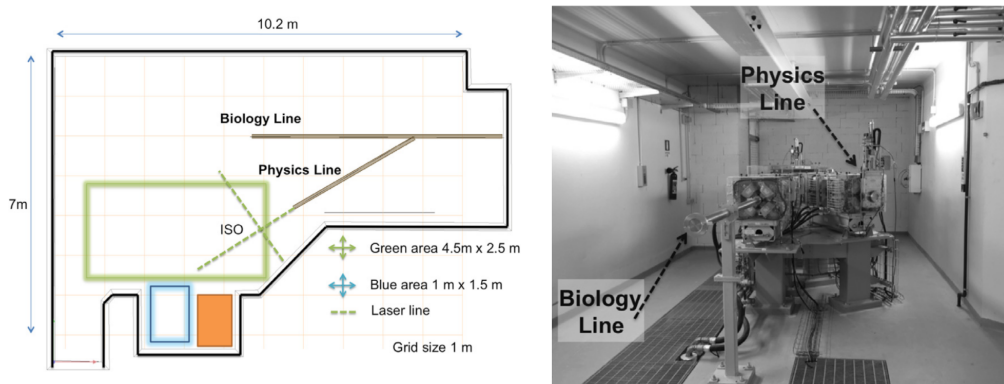


**Figure (5.1)** – Schematic view (left) and a photo (right) of the experimental room at the Trento Proton-therapy centre (from [95])

Figure 5.2 shows a 3D render of the setup used during the test: three X-Y pairs have been exposed to proton beams at several energies (from 70 MeV to 228 MeV) primarily to test the response of the detectors to particles that are not at the minimum of ionization and to verify the system performance in terms of noise outside the controlled environment of the lab where the first tests were performed.

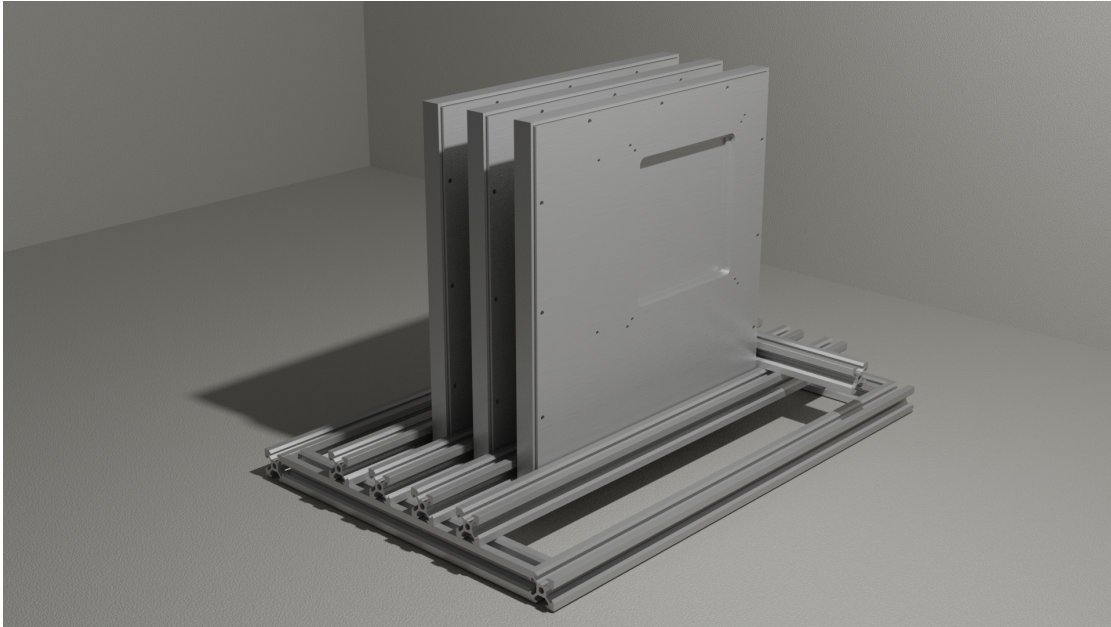


*Figure (5.2) – 3D render of the MSD setup used at Trento*

### Integration with the FOOT DAQ system

Another fundamental goal of the test performed at Trento was the integration of the MSD subsystem with the central TDAQ software developed by the experiment: figure 5.3 shows a screenshot of the FOOT TDAQ Software running during one of the acquisitions, while figure 5.4 shows that data fragments received from the MSD subsystem is correctly decoded.

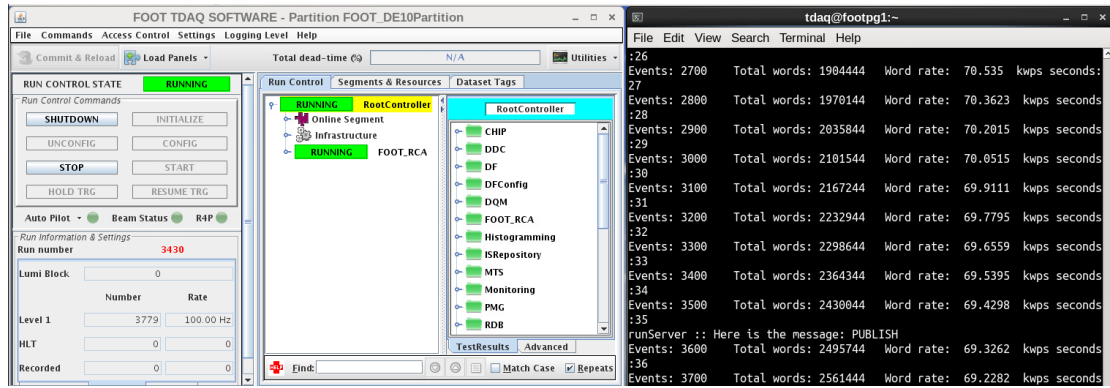


*Figure (5.3) – The FOOT TDAQ Software running with the MSD subsystem during the test*

The MSD DAQ, described in section 4.3 correctly received the trigger and clock signals from the central DAQ system while correctly sending the busy signals from the DE10Nano boards and the data digitized from the ADC boards.

```
DAQ trigger 1
TAMSDataNtuRaw::Action():: I'm going to charge 4 number of fragments
*****
NtuRaw hits
*****
Sens:: 2 View:: 1 Strip:: 204
Sens:: 2 View:: 1 Strip:: 417
DEMSDEvent DATA:
Channel ID (hex): 463432
Time in seconds: 1622887231
Time in microseconds: 169986
Number of Event: 1
Data size: 656
Detector Header: eadebabab
Board Header: badcafe3
HW Event Number: 1
Trigger Counter (hw): 1
BCO counter: 6657
```

*Figure (5.4) – Data received from the MSD subsystem is correctly decoded*

A total of 367GB over the course of the three days of data taking have been acquired, with no major problems and the system correctly running for several hours: trigger was provided by the coincidence of two thin plastic scintillator placed after the detectors, with an average trigger rate during a single data run varied between  $\approx 400\text{Hz}$  and  $\approx 2.0\text{k}\text{Hz}$ .

### 5.1.2 GSI 2021 Data Campaign

A second data campaign has been performed in July 2021 at the GSI Helmholtz Centre for Heavy Ion Research (German: GSI Helmholtzzentrum für Schwerionenforschung) in Darmstadt[96], with a primary beam of Oxygen ions at 200 MeV/u and 400 MeV/u.

The main goals of the data campaign were for the FOOT experiment to acquire data with an almost complete setup (only the *Inner Tracker* and the magnets are missing), testing the capabilities of the full DAQ system running with all the different subsystems, and to acquire the first fragmentation data that will be used to make the first integral cross-section measurements. Trigger is provided by the start counter detector, as described in section 2.3.1.

At the same time, a subset of the data, with and without targets, can be used by the various sub-detectors to study their performance and their response to heavy charged particles.

Figure 5.5 shows a photo of the MSD setup, where the same mechanical setup described in section 5.1.1 is used. Figure 5.6 shows an event display of the complete setup generated by the SHOE (*Software for Hadrontherapy Optimization Experiment*) software package used by the FOOT experiment.

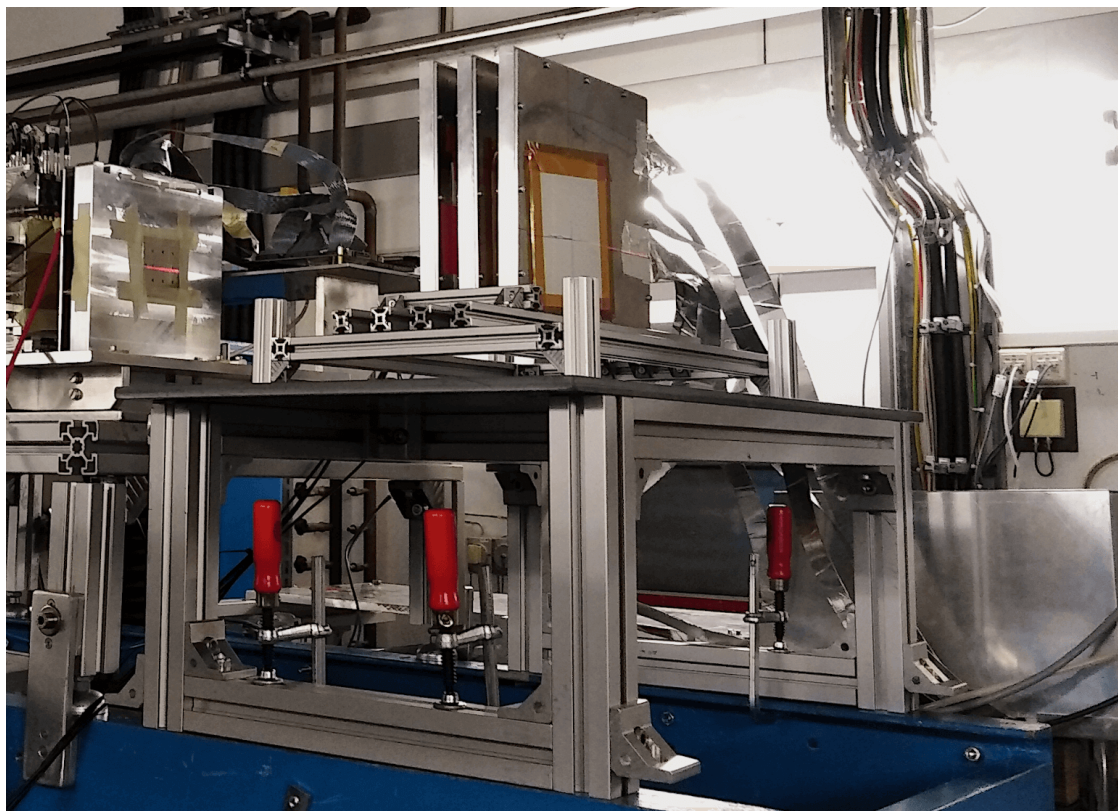
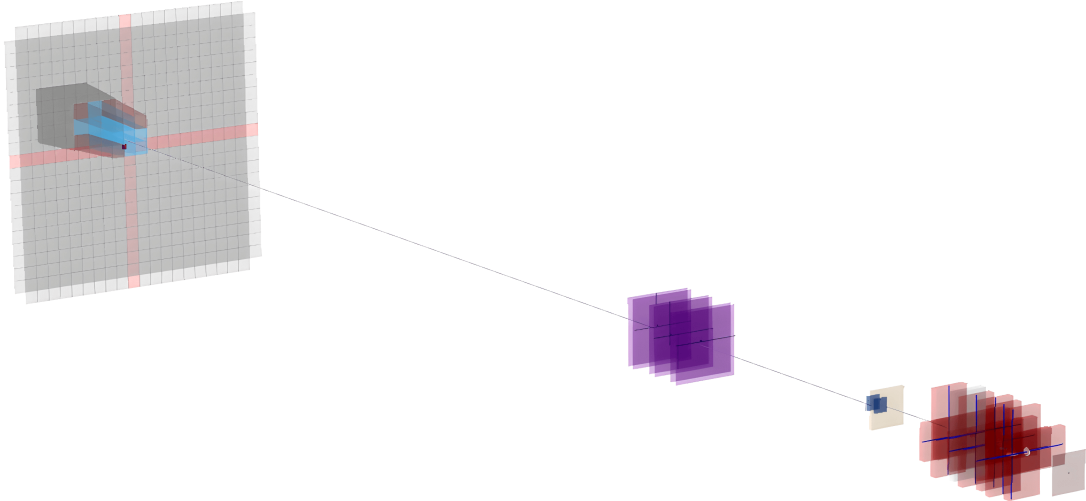


*Figure (5.5) – Photo of the FOOT MSD setup used at GSI*

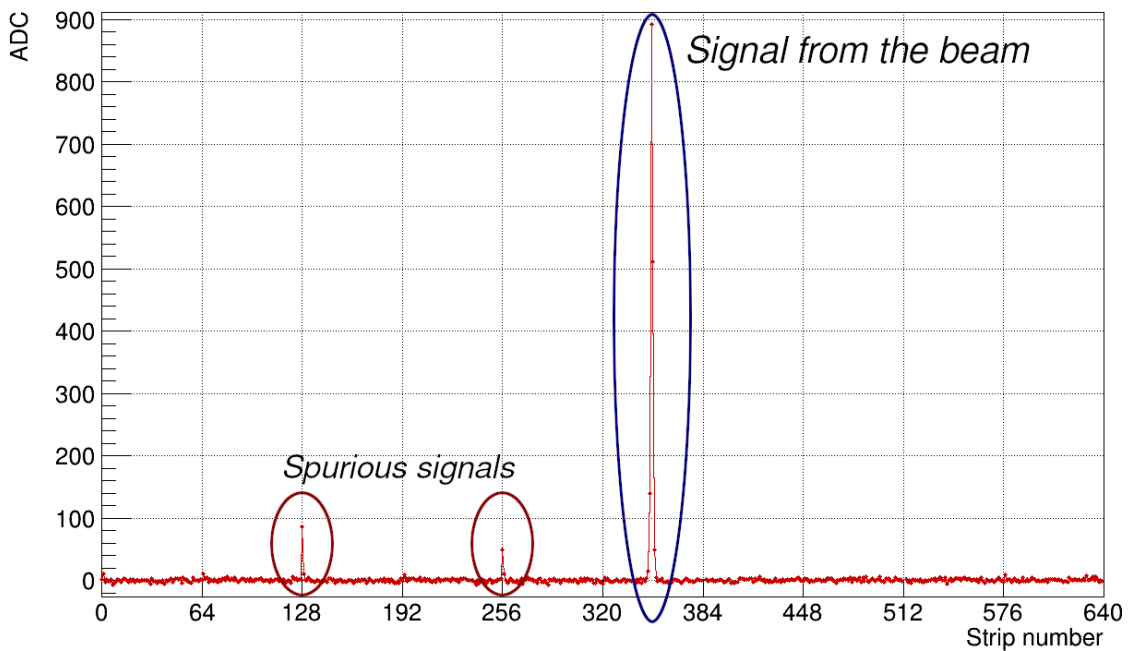
As for the Trento data taking, the first fundamental measurement for the MSD sub-system was a noise characterization: due to the different environment new behaviours can be observed when compared to data acquisitions in the controlled lab environment.

Figure 5.7 shows one such observed behaviour: when plotting the pedestal subtracted data from one of the events, the signal coming from the heavy ion is clearly

visible, but a series of smaller peaks appear in correspondence of channels at the start of new readout ASICs due to noise induced on the control signals, with the subsequent need to mask off these channels from all subsequent analysis. This results in a loss of 10 channels for each detector, for a total of 1.6% of all the readout channels.



*Figure (5.6) – SHOE event display of the complete FOOT setup used at GSI*



*Figure (5.7) – Pedestal subtracted raw data for one of the MSD detectors at GSI test*

### 5.1.3 CNAO 2021 Data Campaign

A final data campaign has been performed in December 2021 at *Centro Nazionale di Adroterapia Oncologica* (CNAO), the only centre in Italy able to provide hadrontherapy treatments using protons and carbon ions and one of the only six facilities worldwide that are able to do so.

In addition to providing hadrontherapy treatments, CNAO is also a Research and Development Centre whose activities range from clinical research to radiobiological and translational research, and collaborates closely with experiments like FOOT, providing the expertise and beam time necessary.

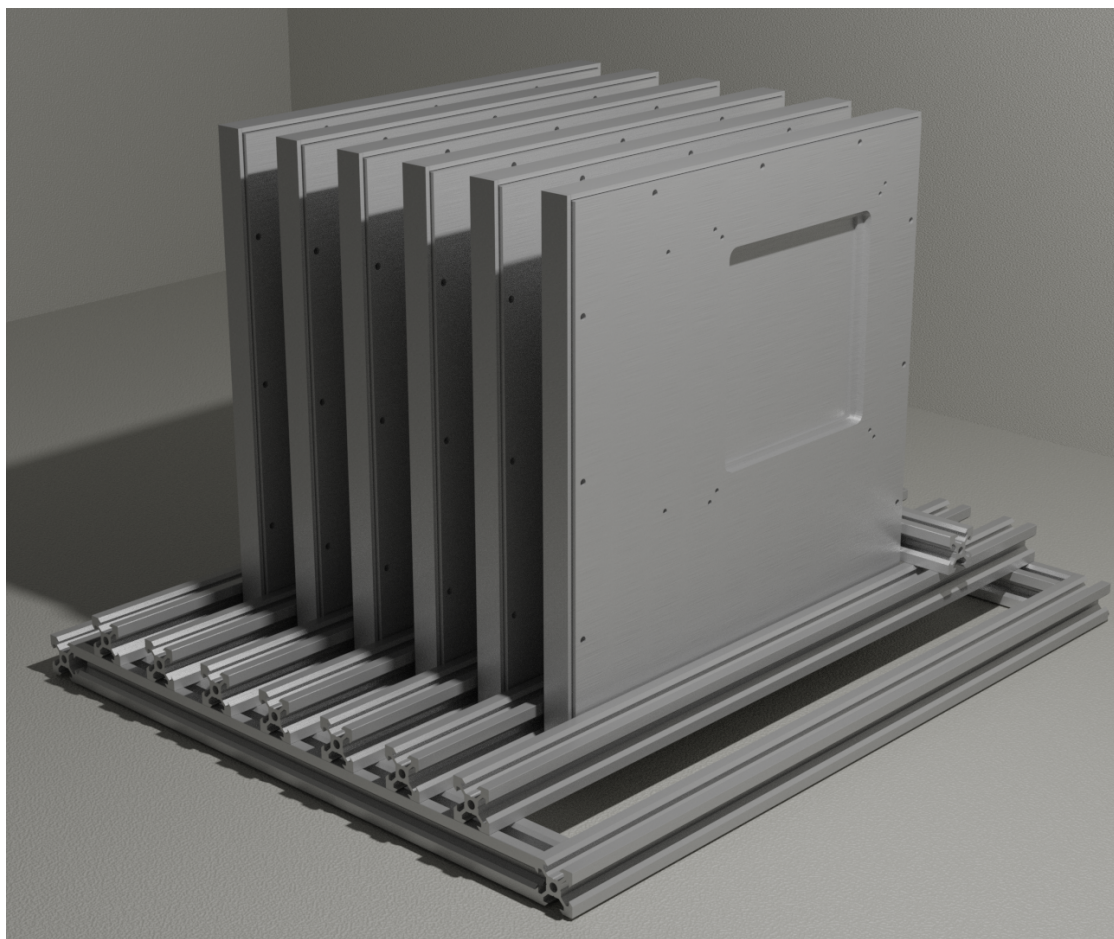


*Figure (5.8) – 3D render of the MSD setup used at CNAO*

Figure 5.8 shows a render of the setup used: six X-Y pairs have been exposed to carbon beams at several energies (from 115 MeV/u to 400 MeV/u) to complement the measurements carried out with protons and oxygen ions of the two previous data campaigns, in order to better understand the performance and response of the detector to charged particles.

The number of detector that are readout is also increased to verify the scalability of the modular DAQ system developed. Trigger is provided by a thin plastic scintillator placed at the exit of the beam pipe, before the detectors.

#### **5.1.4 Noise performance at the accelerators**

The noise performance of all the detectors has been tested for each data taking, similarly to what was already done in the controlled laboratory conditions as described in section 4.1.3.

Pedestal values for each channel were calculated after every few hours, accordingly to the stability windows found during the characterization of the prototype, and the Common Mode noise was monitored for each data run at the different conditions.

One particular series of tests has been performed to verify the light tightness for each x-y plane, assembled with the two backplane facing the exterior to use their metalization to screen the ambient light.

Figure 5.9, shows the distributions of the common mode noise for two different runs where additional protective beam windows covers were present or removed.

No meaningful change in the distribution is observed when the cover is removed and the back of the silicon sensor is exposed to ambient light, proving that the metalization layer on the back of the silicon is enough to shield the silicon, ensuring light tightness of the X-Y assembly without the need of additional material.

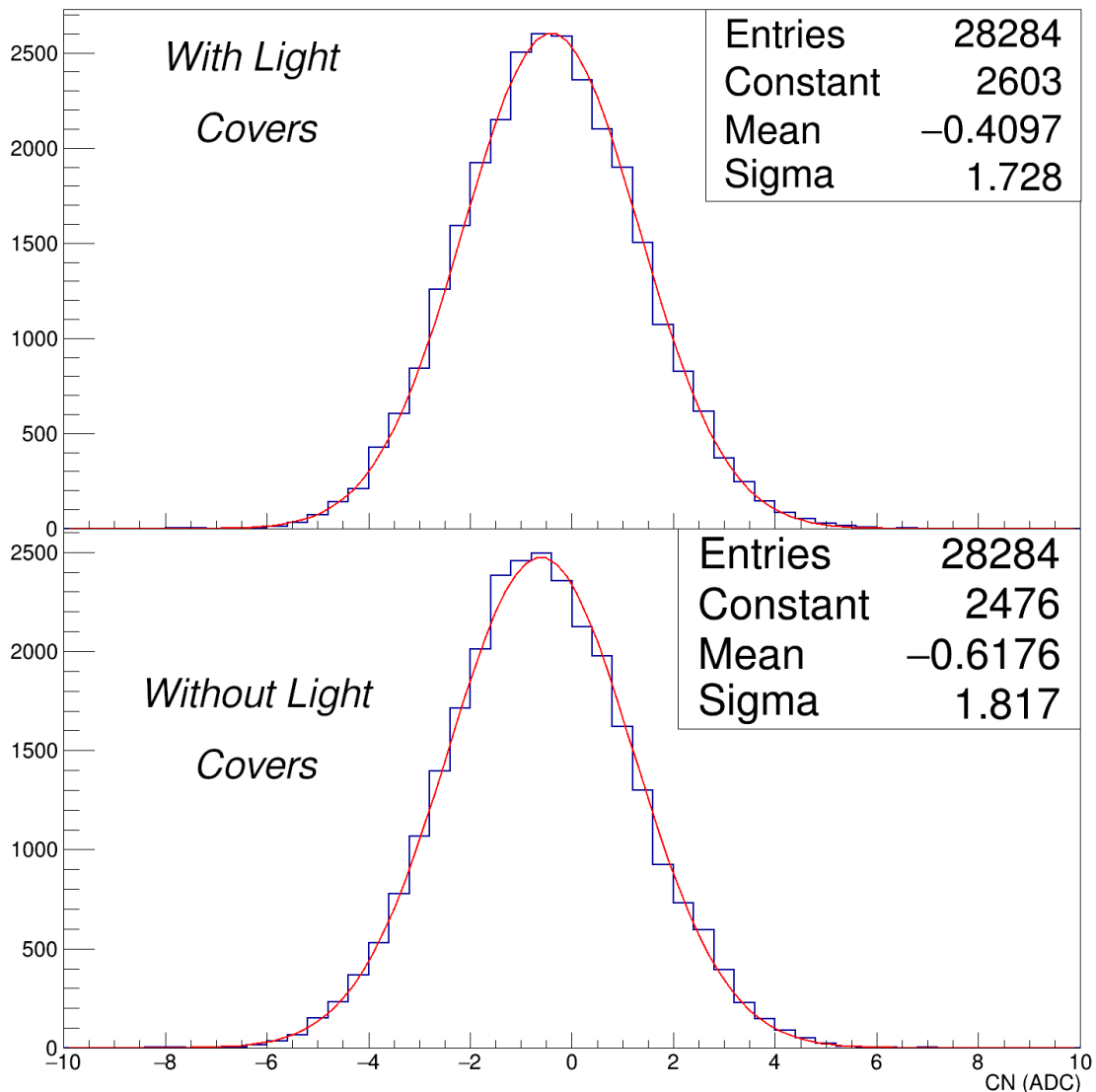


*Figure (5.9) – Common Noise distribution for a run with (top) and without (bottom) protective beam windows covers*

## 5.2 Detection efficiency

The total efficiency of a detector derives from two main contributions, one intrinsic and one geometric:

- intrinsic: it takes into account the fact that a detector, actually crossed by a particle, may not detect it. This is an intrinsic property of the detector itself, and is an unavoidable contribution to the total efficiency.
- geometric: a particle, due to the geometric position of the detectors with respect to the beam or their alignment, may not hit a particular layer, thus leaving no visible sign of its passage. By varying the position of the detectors, or ideally by making them infinitely large, this contribution can be completely eliminated.

In cases where the geometrical contributions to the efficiency are considered negligible, as in the case of detectors that are very large compared to the beam source, very close to it or in the limit of infinite extension, it is possible to define the intrinsic efficiency of the  $i$ -th detector simply as

$$\epsilon_i = \frac{m_i}{N} \quad (5.1)$$

where  $m_i$  is the number of counts recorded by the  $i$ -th detector and  $N_{tot}$  the total number of events with a particle passing through the detector.

The algorithm for the calculation of the intrinsic efficiency for a setup with  $n$  detectors then requires simply the reconstruction of a track for the events where the  $n - 1$  recorded a hit and calculate the intersection of said track with the  $i$ -th under study to check for the presence of a reconstructed hit in the neighboring of the intersection point.

A further hypothesis necessary for the algorithm to correctly work is that the intrinsic noise of the detector channels does not produce false positives, i.e. signals attributable to the passage of a particle.

To study this effect it has been chosen to collect signal, without a cut on seed threshold, from a group of 8 strips around the point where the track intersects the second plane and from a group of 8 strips away from it, with each group of strip signals summed to obtain a fixed width cluster. Figure 5.10 shows the result for a sample run with data from 400 MeV  $^{16}O$ .

When looking at the signal collected from the group of strips near the track intersection (top) two clearly distinguishable peaks are present far from the noise levels of the detector. The double peak structure is due to the dependence of the charge collection

with respect to the particle impact position, as it will be explained in section 5.3.

Conversely, when looking at the mean signal collected away from the track intersection (bottom), the values obtained are comparable with the value expected for the sum of the noise of said strips when no particle is present.

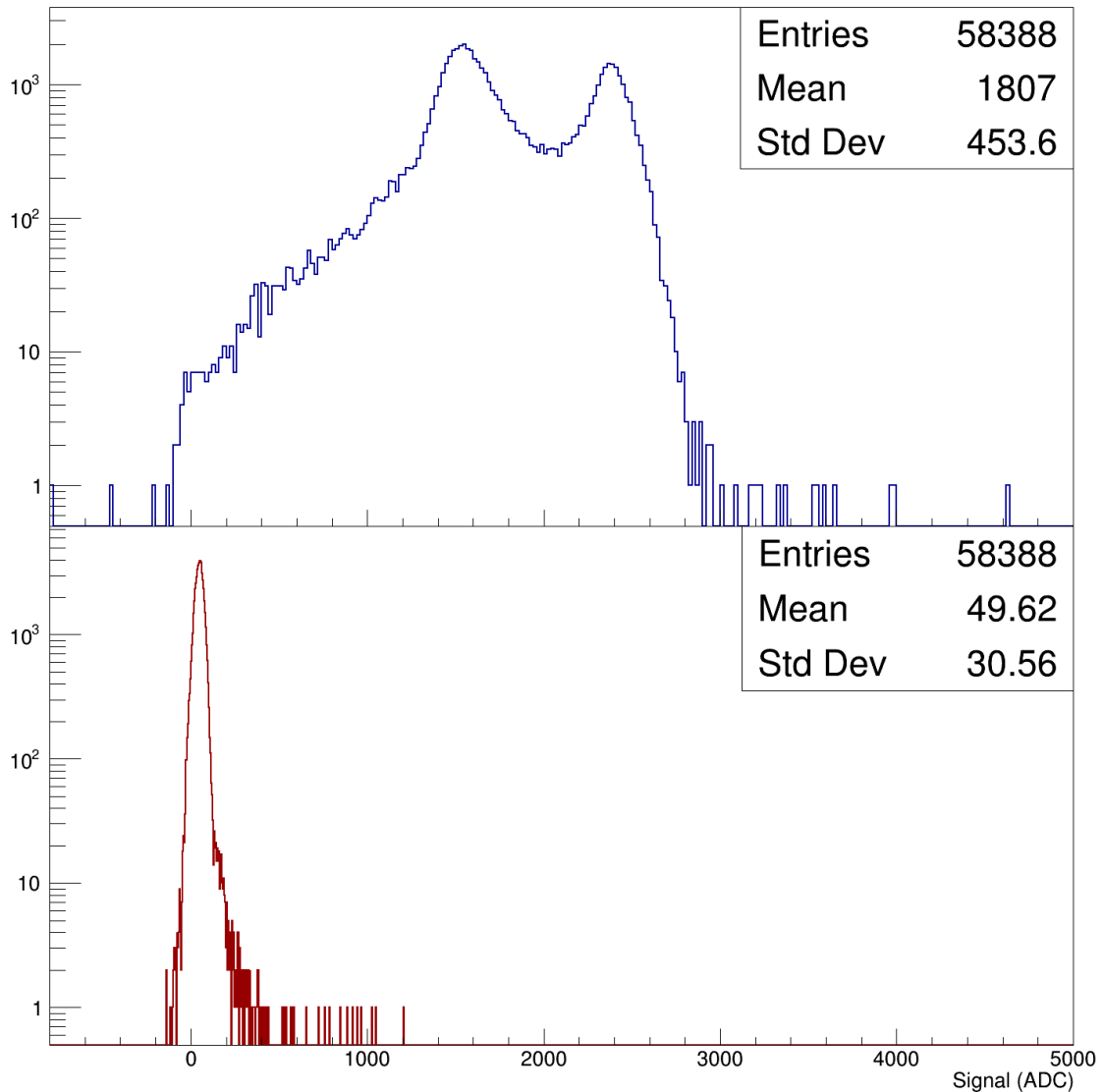


*Figure (5.10) – Signal from a group of 8 strips around the track intersection (top) and away from it (bottom)*

By varying the cut in ADC for the two histogram of both the signal and the noise, and calculating their integral it is possible to obtain the efficiency (figure 5.11) and the number of fake clusters (figure 5.12).

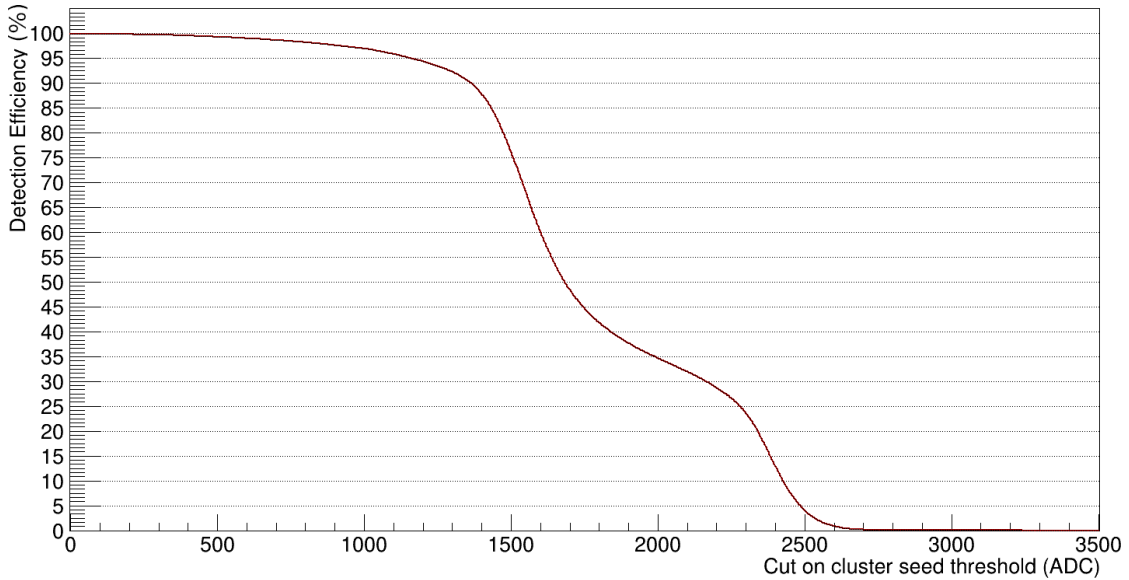


Figure (5.11) – Detection efficiency for a 400 MeV  $^{16}\text{O}$  beam

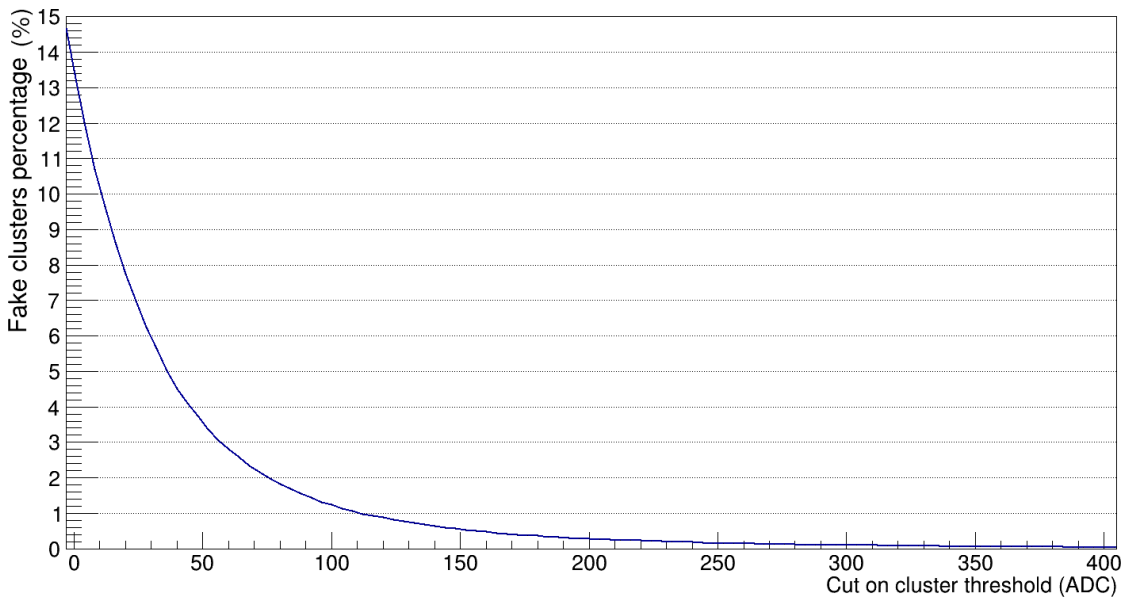


Figure (5.12) – Reconstructed "fake" clusters for a 400 MeV  $^{16}\text{O}$  beam

As an example, in the case of data from a 400 MeV/u Oxygen beam: with a cut on the *seed* threshold of 50 times the single strip noise (about 100 ADC on average), it is possible to collect less than 1% of noise and obtain more than 99% detection efficiency.

The procedure shows a good performance of all the detectors and it also allows the choice of the optimal ADC threshold cut for the different data samples in order to obtain an high purity in the cluster reconstruction.

## 5.3 Response of the detector to charged particles

After assessing the correct behaviour of all the detectors in terms of noise performance, data from the test conducted at the accelerators were used to study the response of the detector to particles that, unlike the case of the first prototype described in section 4.1, are not at the minimum of ionization.

### 5.3.1 Response to protons

The study of response of the detector to protons has been performed with the data acquired at the *Trento Proton Therapy* facility in June 2021 with the use of proton beams at 6 different energies (70 MeV, 112 MeV, 137 MeV, 159 MeV, 198 MeV, 228 MeV).

Figure 5.13 shows the number of detectors with at least one reconstructed cluster per each event for the highest (228 MeV, top) and lowest (70 MeV, bottom) energies, with a cut on the *seed* strip of 8 times the single strip noise (about 15 ADC on average).

In both cases, for most of the events all the detectors recorded at least one hit, with data acquired at the highest energy presenting a slightly larger percentage of events where some detectors are missing.

This is partly due to the lower signal obtained for higher energy incoming particles that don't cross the high threshold used to increase the purity of the dataset analyzed, as explained in section 5.2.

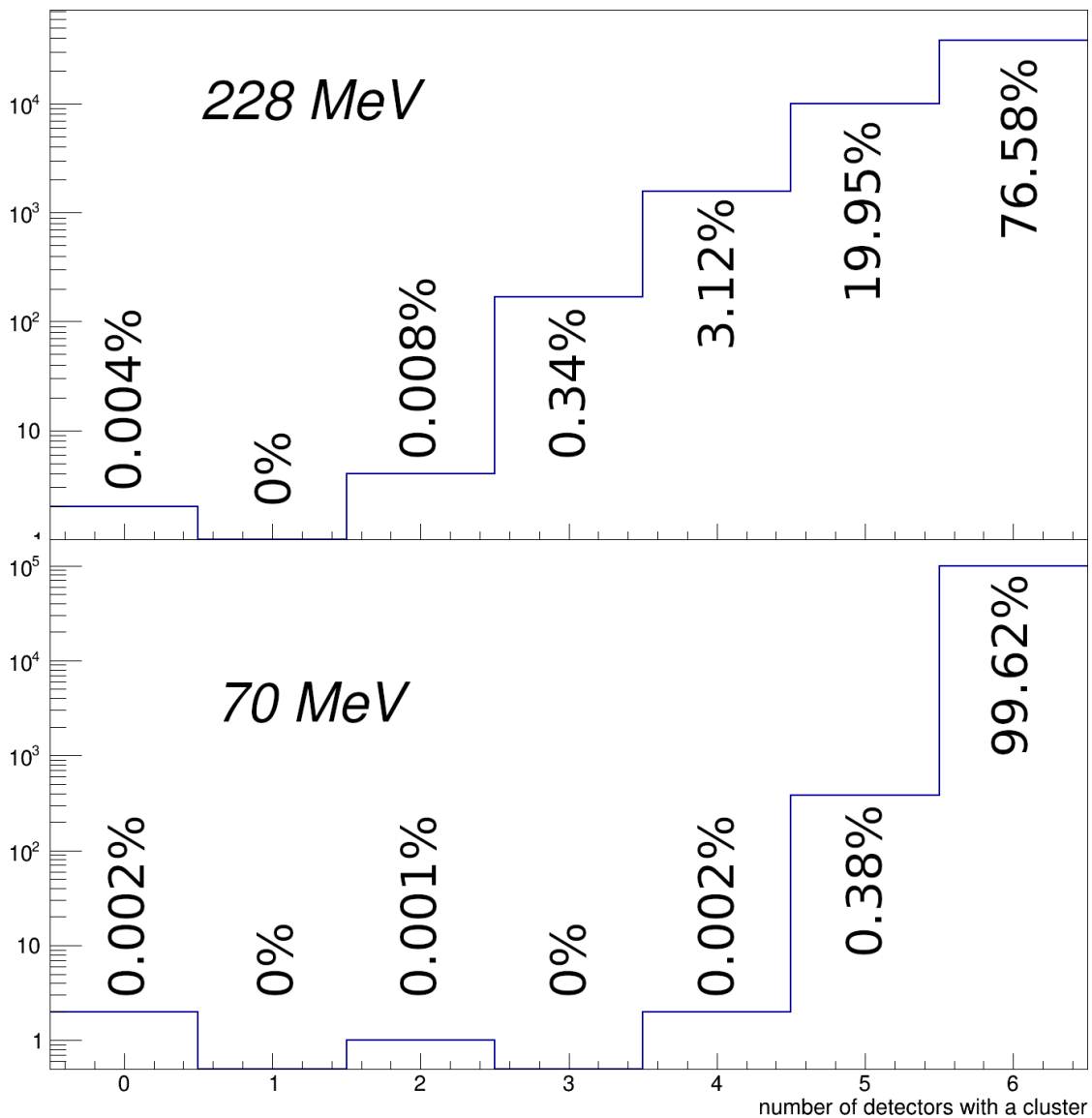
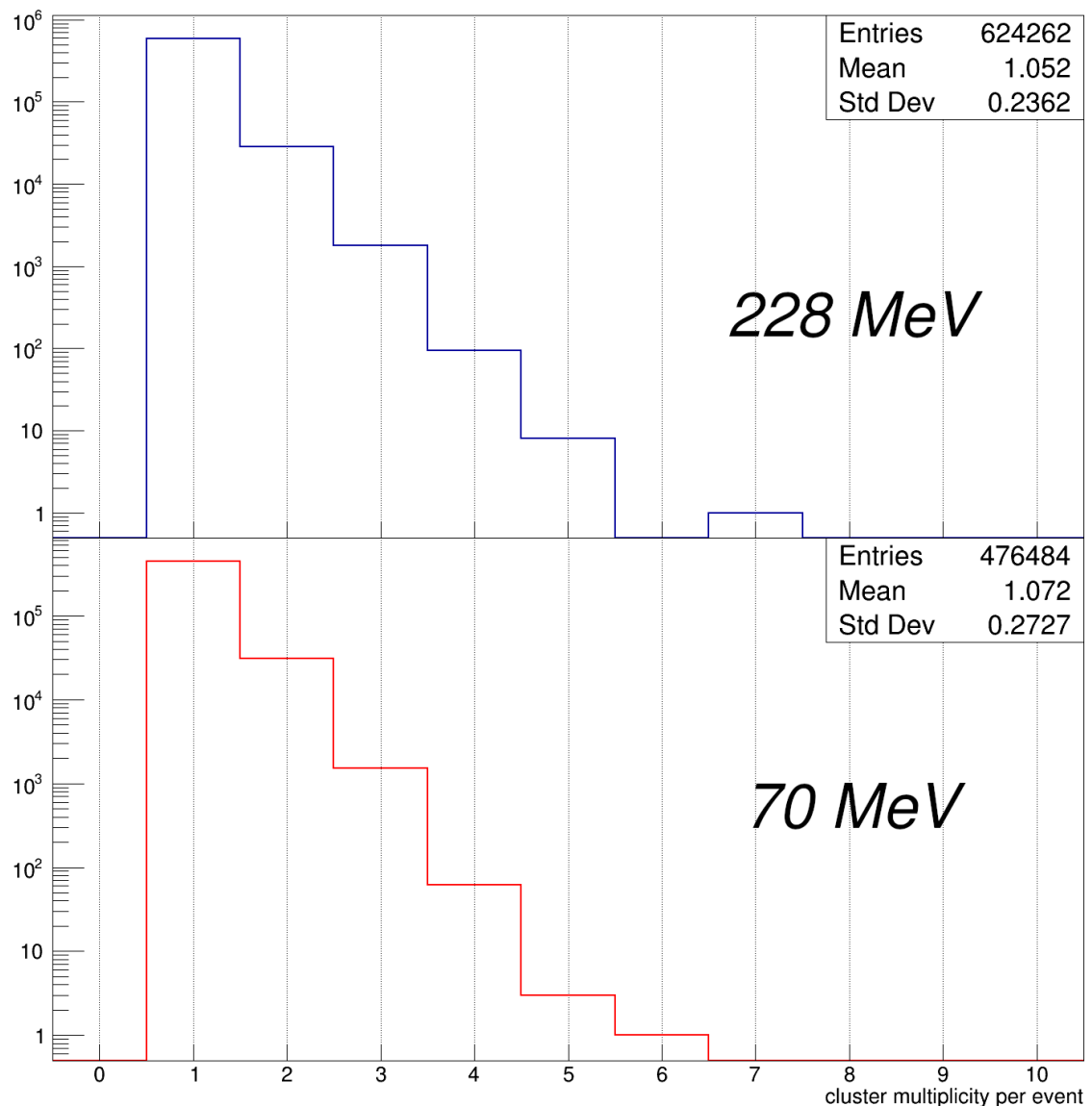


Figure (5.13) – Number of detectors with a reconstructed clusters at 228 MeV (top) and 70 MeV (bottom)

This choice is also reflected in the cluster multiplicity obtained that, as shown in figure 5.14, is on average close to 1, indicating of a low number of clusters incorrectly reconstructed from noise.



*Figure (5.14) – Cluster multiplicity distributions for reconstructed clusters at 228 MeV (top) and 70 MeV (bottom)*

Figure 5.15 and 5.16 show the mean cluster multiplicity and the mean cluster width calculated for all the detectors as a function of the energy: the values obtained present, as expected, a negligible dependence on the incoming particle energy.

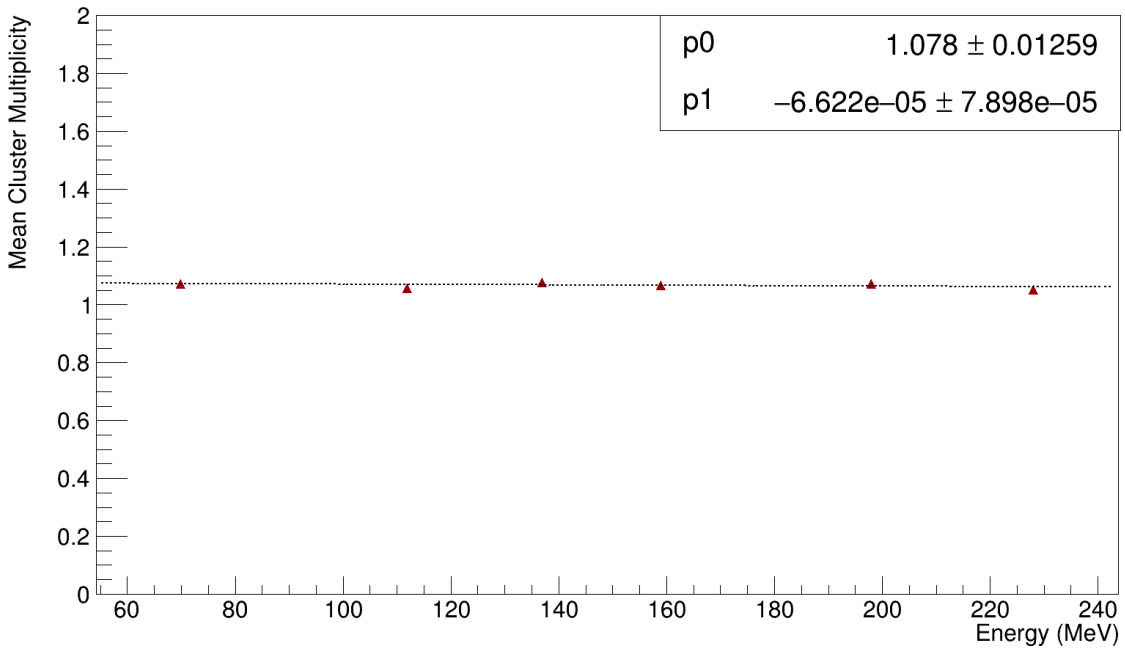


Figure (5.15) – Mean cluster multiplicity as a function of the incoming Proton energy

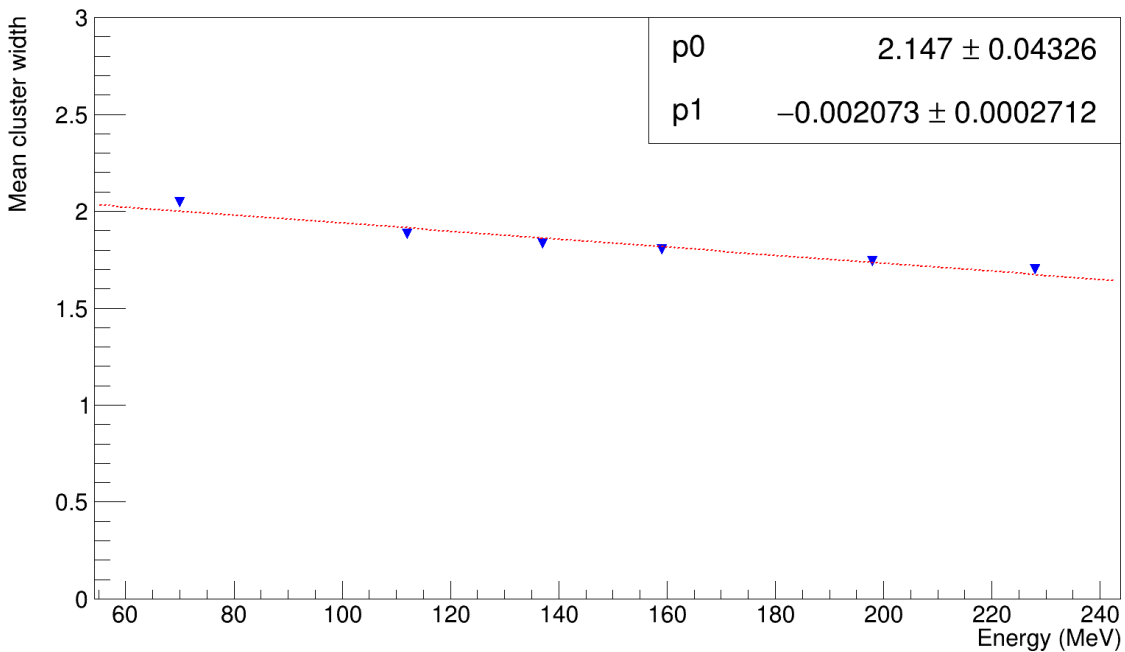
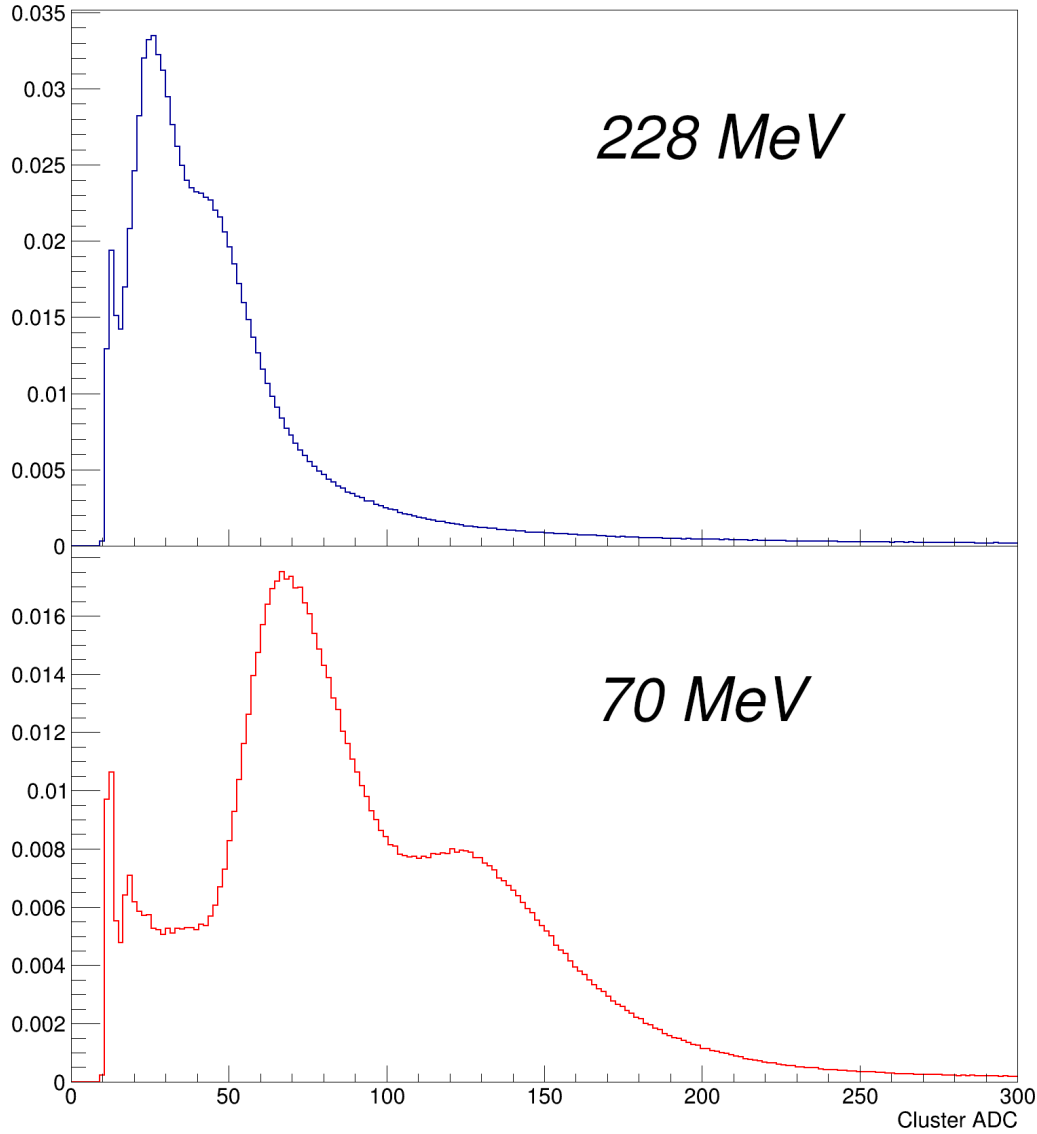


Figure (5.16) – Mean cluster width as a function of the incoming Proton energy

The cluster ADC content distributions for the highest (228 MeV, top) and lowest (70 MeV, bottom) energies is shown in figure 5.17, where a clear double peak shape is identifiable in both cases.

This effect is a widely known characteristic of silicon microstrip detectors where the readout strategy employs *floating strips* [97] [98] and is related to the non linear charge collection between two different readout strips.



*Figure (5.17) – Cluster ADC distributions for reconstructed clusters at 228 MeV (left) and 70 MeV (right)*

In order to study the behaviour of the charge collection in function of the impact point between the readout strips we define the  $\eta$  variable as follows

$$\eta = \frac{S_L}{S_L + S_R} \quad (5.2)$$

where  $S_L$  and  $S_R$  are the two highest signals in the cluster.

The variable  $\eta$  as defined is a parameter that is closely related to the charge-sharing between adjacent strips.

It can be alternatively thought of as the center of gravity in units of the readout strip pitch of the two consecutive readout strips with the maximum amplitudes.

The effect of the capacitive coupling gives rise to the presence of peaks in the  $\eta$  distribution. The resulting charge division between the strips is thus non linear, because, if this was the case, the  $\eta$  distribution should be flat.

Figure 5.18 shows the  $\eta$  distribution observed for one of the detectors.

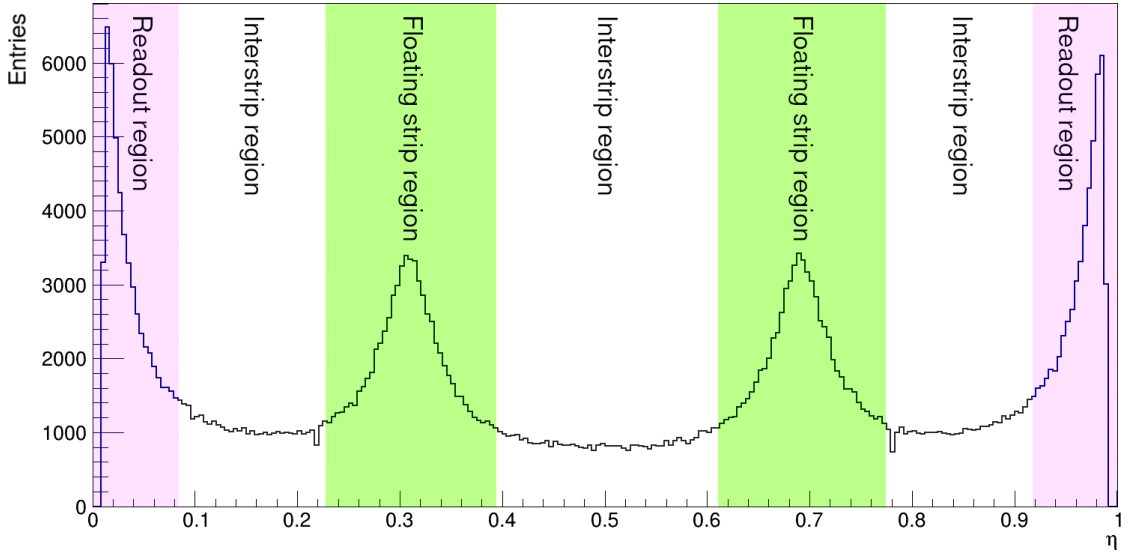


**Figure (5.18) – Distribution of cluster  $\eta$  values with the different regions of interest highlighted (data from Protons at 70 MeV)**

The charge collection efficiency is approximately 100% for particles that hit the sensor near the read-out strip, while near the floating strips is smaller, as some of the ionization charge can recombine before it can drift to one of the neighboring readout

strip, resulting in a lower total collected charge.

The different highlighted regions correspond to the distinct  $\eta$  intervals that can be used during analysis: 1) read out strip region; 2) interstrip region and 3) floating strip region.

The correlation between the strip implantation structure and the peaks of the  $\eta$  is evident, with peaks around one third and two thirds of the region in between two readout strips.

A value of  $\eta$  close to 0 or 1 corresponds to the readout strip incidence, while  $\eta$  values close to 0.3 or 0.6 correspond to the floating strip incidence.

The effect of the charge loss is clearly visible in figure 5.19, where the contributions from clusters from different  $\eta$  regions reveal the origin of the double peak structure of the general cluster ADC distribution.

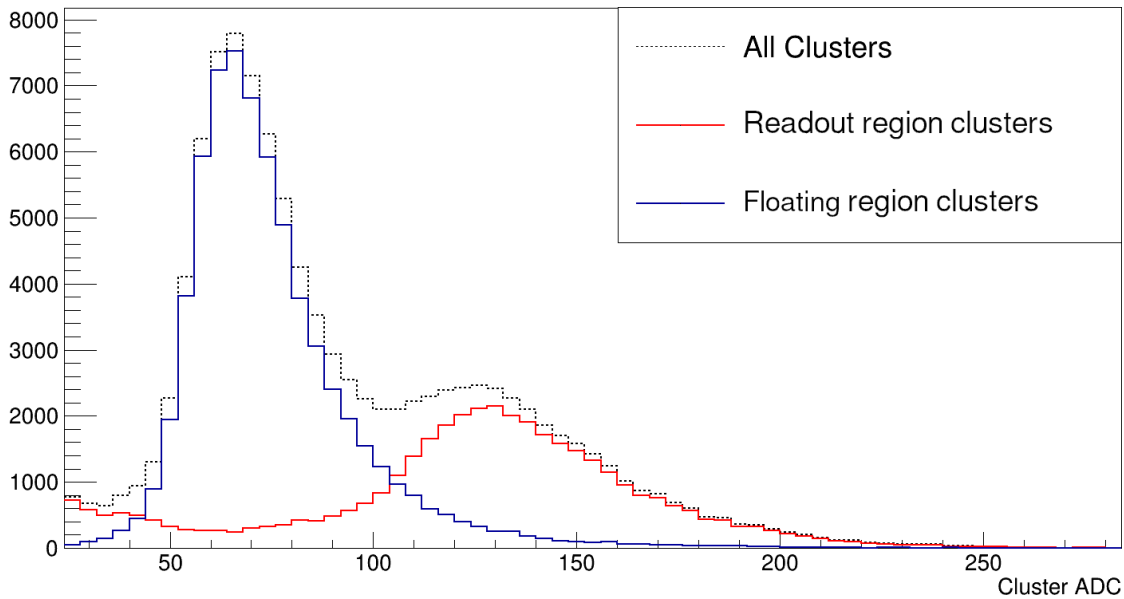


**Figure (5.19)** – ADC distributions for reconstructed clusters in the readout strip region (red) and floating strip region (blue) content at 70 MeV

Figure 5.20 shows as an example the cluster amplitudes for 70 MeV incident protons as a function of  $\eta$  where the black points represent the most probable values of the Langaus fit for each  $\eta$  bin.

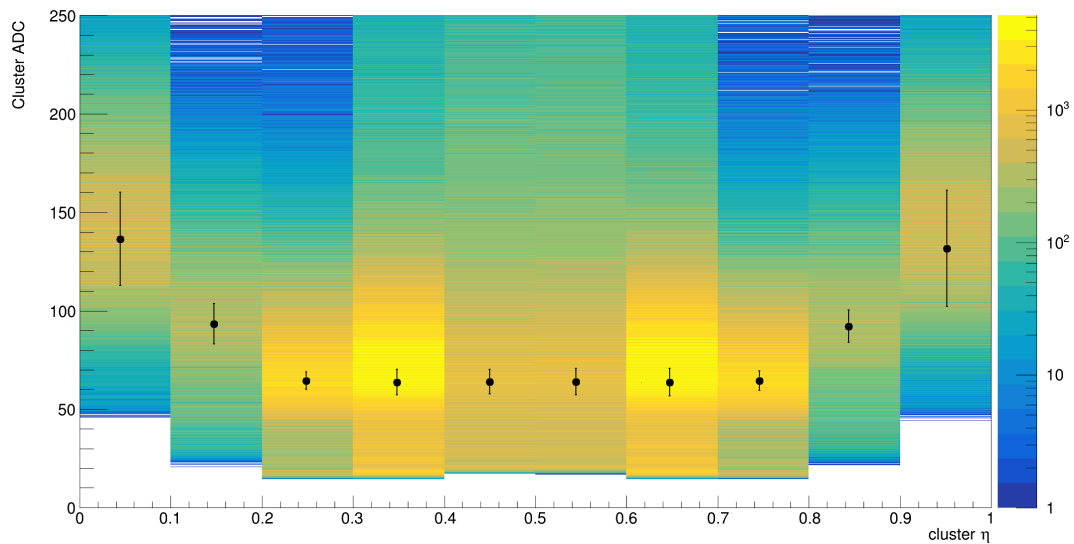


*Figure (5.20)* – Cluster ADC content as a function of the  $\eta$  parameter for 70 MeV protons

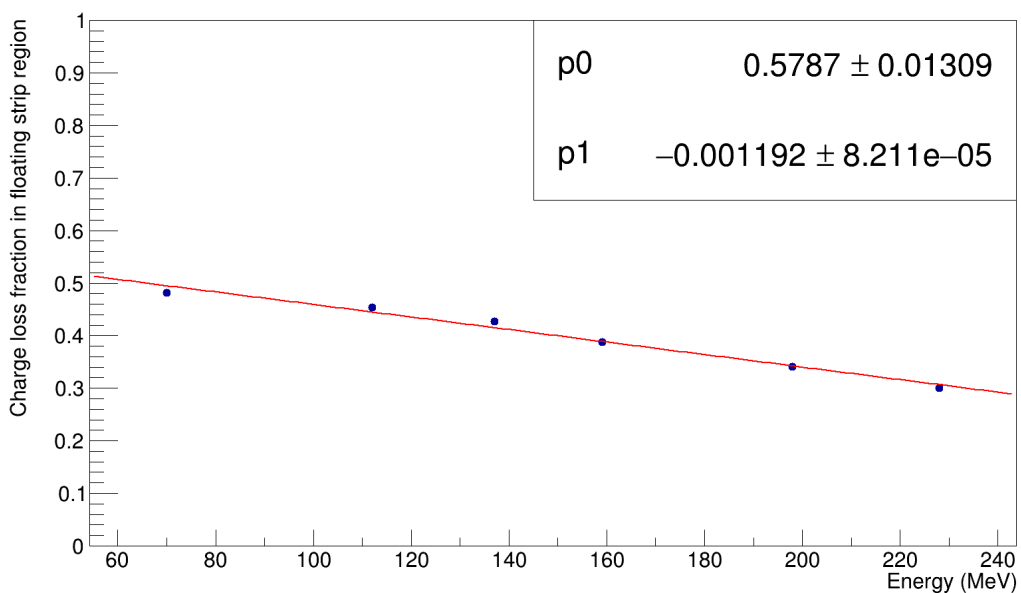


*Figure (5.21)* – Charge loss fraction of clusters in the floating strip region as a function of the Proton energy

The difference in the MPVs between the floating strip incidence region and the readout strip incidence region shows a charge loss varying from 30% to about 50% for protons hitting near a floating strip, as shown in figure 5.21, with a dependence on the

energy of the incoming particle and thus of the deposited energy in the detector. The unexpected dependence on the energy for will be investigated in future with the help of an evolution of the laser setup previously used in section 4.2.2.

The results of the analysis for the cluster ADC content at all energies, together with the predictions from the Bethe-Bloch formula and MonteCarlo simulations for the different proton beams impinging on the microstrip detector performed with the FLUKA package, are shown in figure 5.22: the simulated energy deposit in both cases has been converted to ADC with the conversion factor computed in section 4.2.

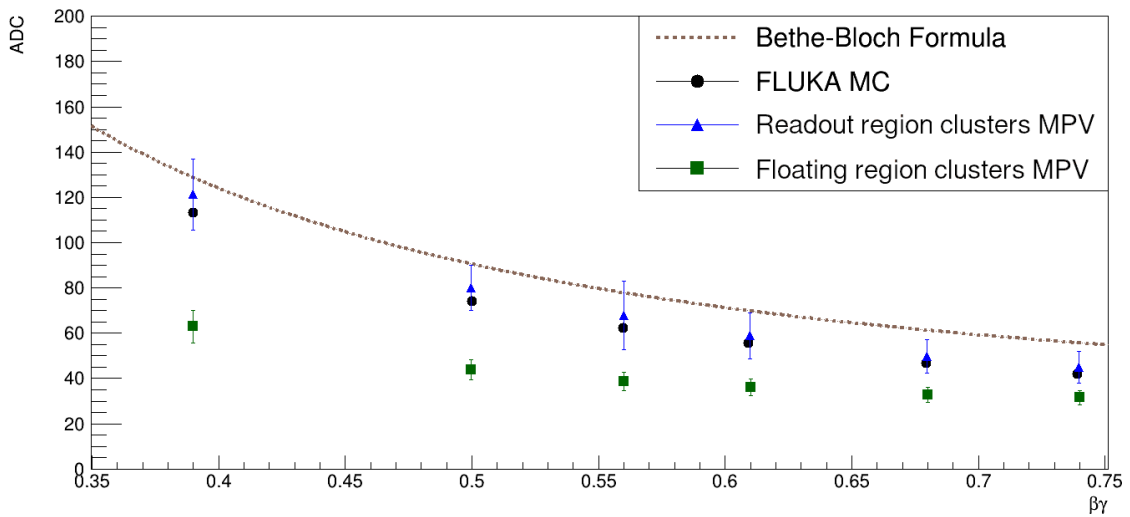


*Figure (5.22) – Response of the detector to protons at different energies compared with the Bethe-Bloch formula and FLUKA simulations*

While the data from clusters hitting near a readout strip is in good agreement with both the predictions, the data from clusters hitting near floating strips does not due to the charge loss effect observed.

A correction of the cluster charge as a function of the impact point of the incoming particle is thus foreseen for the future to improve the charge and energy resolutions of the detectors.

### 5.3.2 Response of the detector to heavy ions

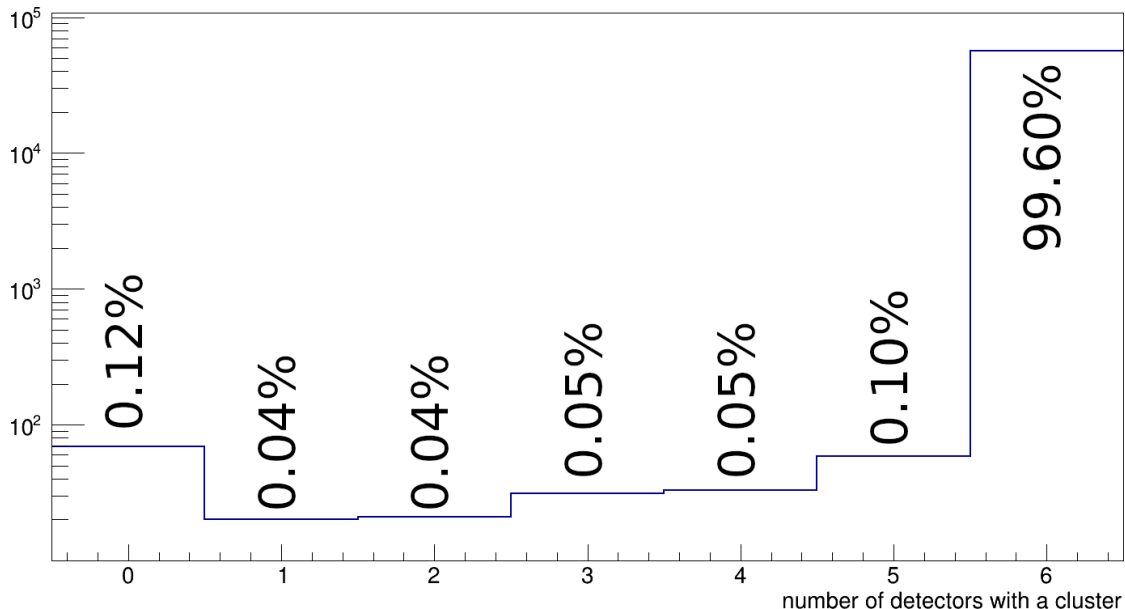
The same analysis has been performed on data acquired at the data campaigns at GSI in July 2021 and at CNAO in December 2021, to verify the response of the detector to heavy charged particles.

Data has been acquired with Oxygen ions at two different energies (200 MeV/u and 400 Mev/u) and Carbon ions at five different energies (115 Mev/u, 160 Mev/u, 200 Mev/u, 300 Mev/u and 400 Mev/u).

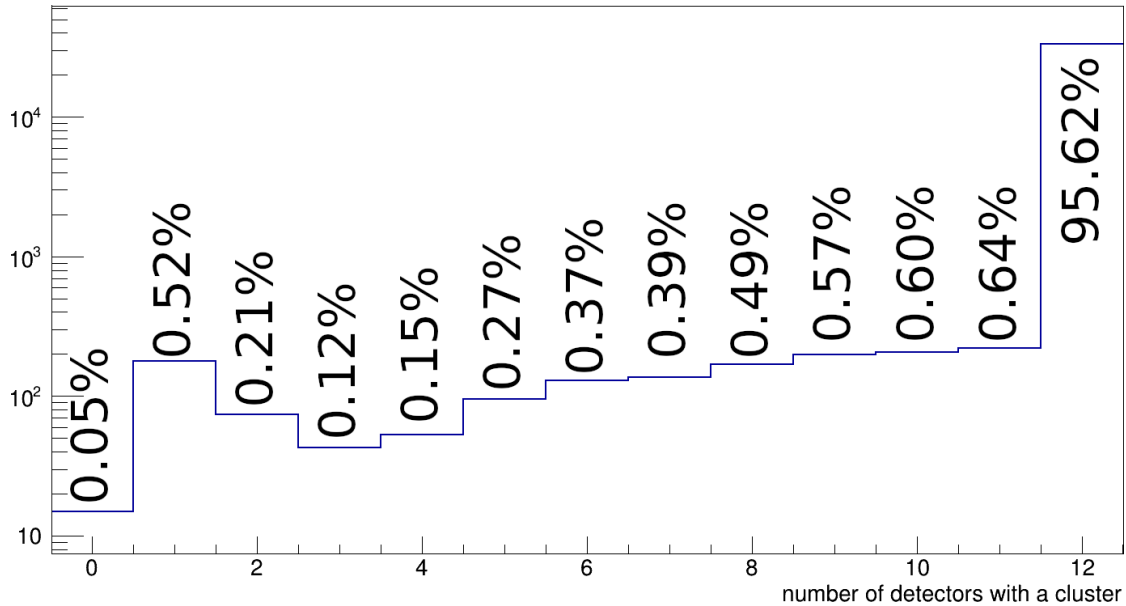
Figure 5.24 and 5.23 show the number of detectors with at least one reconstructed cluster per each event in the case of Oxygen and Carbon ions at 400 MeV/u.

As in the case of the data for protons the cluster reconstruction thresholds have been chose to increase the purity of the dataset analyzed.

This results is in most cases in events where all the detectors (6 in the case of the data from the GSI campaign and 12 in the case of data from the CNAO one) recorded at least one hit.



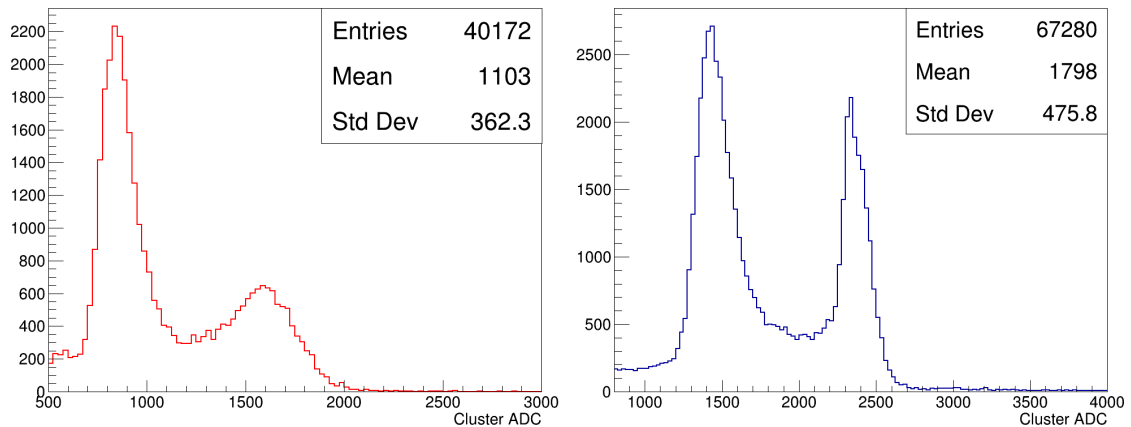
*Figure (5.23) – Number of detectors with a reconstructed clusters for Oxygen at 400 MeV/u*



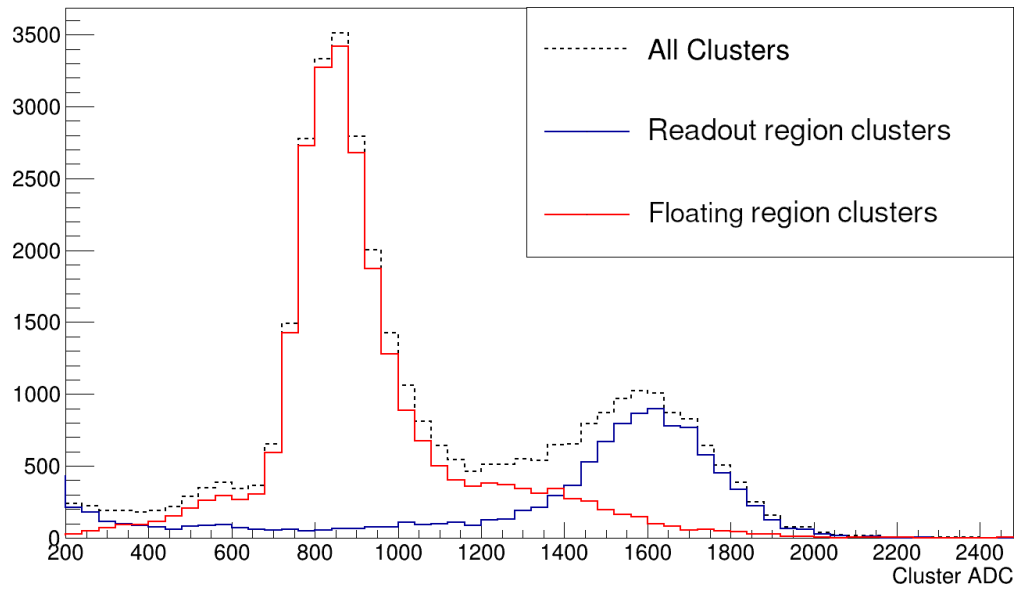
**Figure (5.24)** – Number of detectors with a reconstructed clusters for Carbon at 400 MeV/u

Figure 5.25 shows the cluster ADC content distributions for Carbon (left) and Oxygen (right) at 400 MeV/u: once again a clear double peak shape is identifiable, as in the case of data from protons, coming from the different contributions to the cluster ADC distributions of clusters hitting near a readout or a floating strip.

Figure 5.26 shows the role of the two different contributions in the case of Carbon ions at 400 MeV/u, with similar results obtained from Oxygen data.



**Figure (5.25)** – Sample ADC distributions for reconstructed clusters for Carbon (left) and Oxygen (right) at 400 MeV/u



**Figure (5.26)** – ADC distributions for reconstructed clusters in the readout strip region (blue) and floating strip region (red) of Carbon ions at 400 MeV/u

The dependence of the cluster total ADC content on the  $\eta$  parameter of the cluster is once again evident from the data: figure 5.27 shows the cluster amplitudes for 400 MeV/u incident oxygen ions as a function of  $\eta$  where the black points represent the most probable values of the Langaus fit for each  $\eta$  bin.

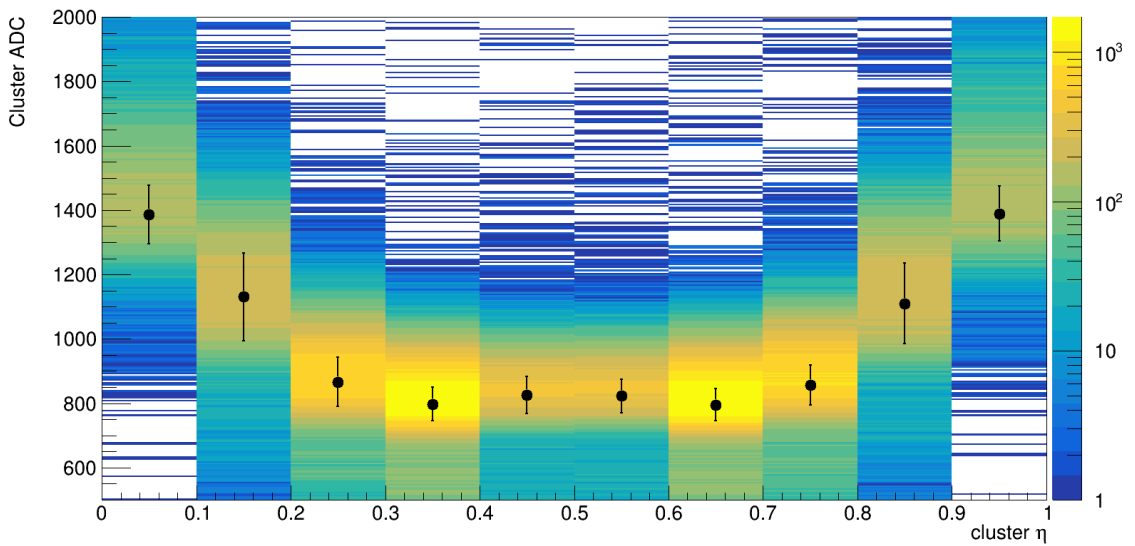


**Figure (5.27)** – Cluster ADC content as a function of the  $\eta$  parameter for 400 MeV/u Carbon

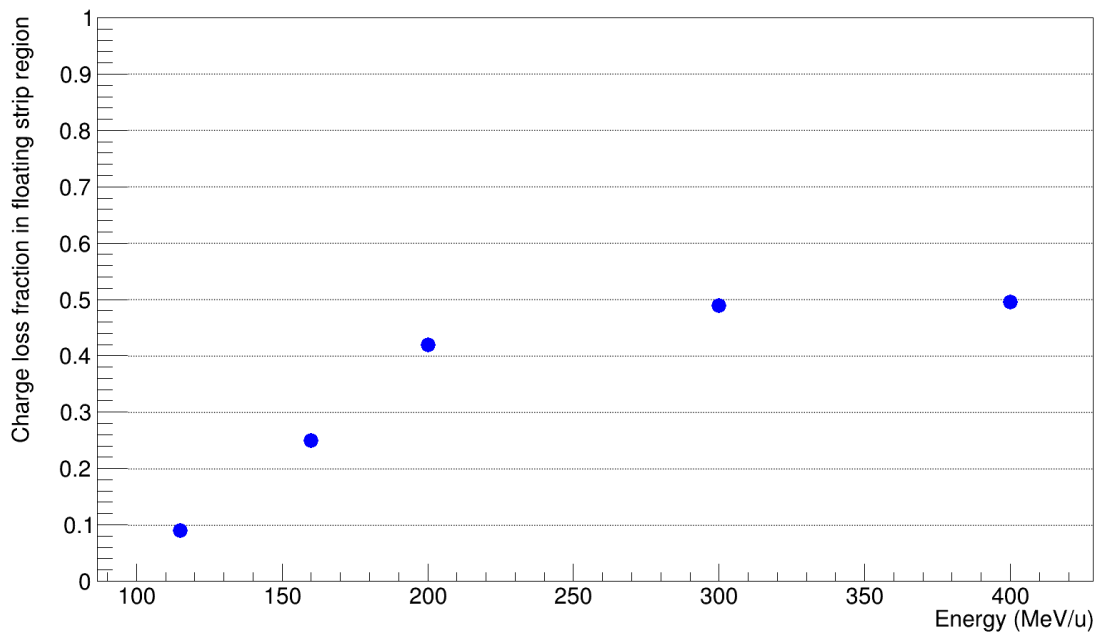


**Figure (5.28)** – Charge loss fraction of clusters in the floating strip region as a function of the Carbon ion energy

The difference in the MPVs between the floating strip incidence region and the readout strip incidence region shows a charge loss up to approximately 50% for ions at 400 MeV/u hitting near a floating strip, as shown in figure 5.28 for the case of Carbon data.

The measured charge loss appears to decrease with the increase of the deposited energy of the particle starting from energies around 200 MeV/u.

This behaviour suggests a possible saturation regime of the detector and/or readout electronic: assuming that the single readout channel saturates at a certain energy, the reconstructed clusters for particles hitting near a readout strip will all have similar ADC content, even for increasing deposited energy.

Conversely, clusters from particles hitting near a floating strip that experience charge collection loss will have single channel values below the saturation level that increase with increasing deposited energy.

The two effect combine to give a charge loss fraction that decreases with the incoming particle energy.

Figure 5.29 shows that the percentage difference of the MPV value calculated for one of the detectors, as a function of the  $\eta$ , is within 5% of the average of the others. This imposes a lower boundary on the resolution of the deposited charge.

Similarly to the case of proton data, predictions for the ADC content of the clusters have been made with both the Bethe-Bloch formula and with dedicated FLUKA simulations for each ion species at each energy.

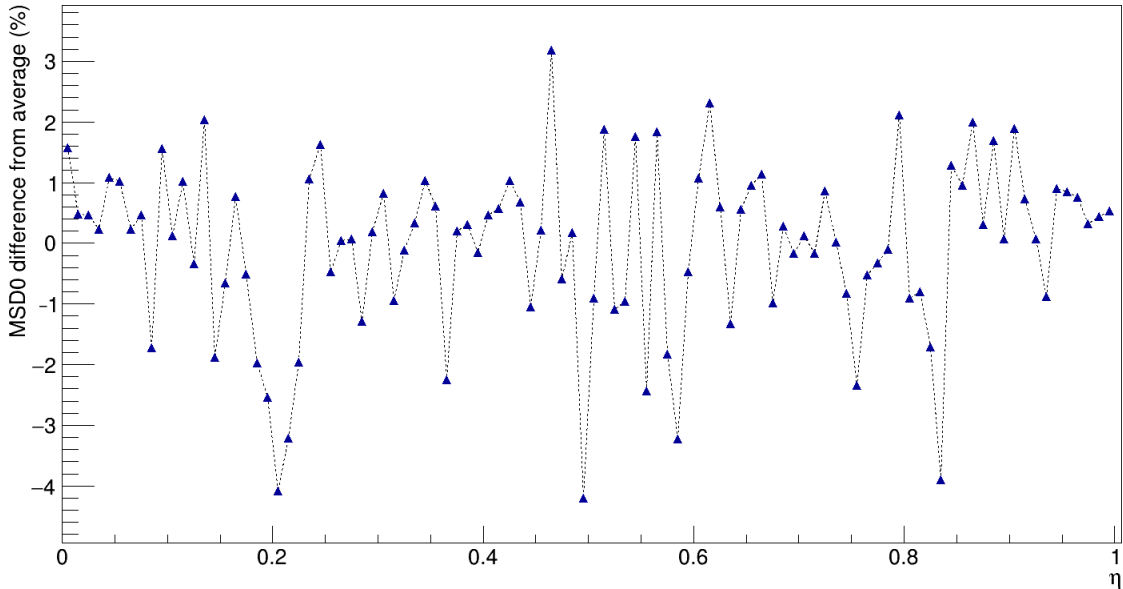


*Figure (5.29) – Percentage deviation of one of the detectors as a function of  $\eta$*

Figure 5.30 shows the results for Carbon data: data from clusters that hitting near a readout strip are once again in agreement with the predictions, while clusters hitting nearer to a floating strip are affected by the charge loss effects as in the case of data from Protons.

For Oxygen ions, results are shown in figure 5.31: differently from the previous results obtained from Protons and Carbon, data at the lowest energy (200 MeV/u) show a deviation from the predictions for both families of clusters, with all clusters giving similar results once again hinting at saturation behaviour of the detector.

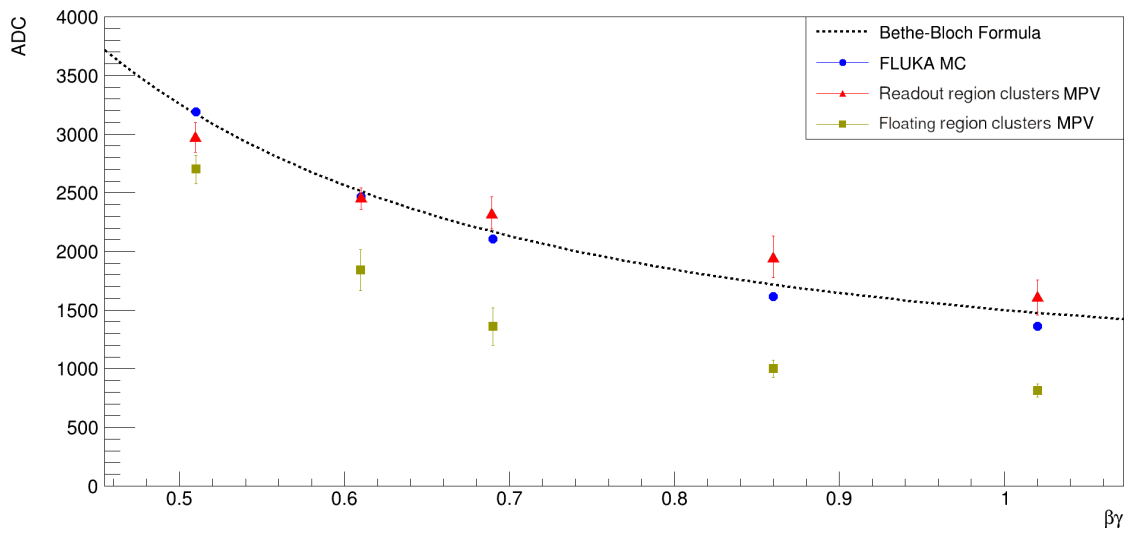


Figure (5.30) – Response of the detector to Carbon ions at different energies compared with the Bethe-Bloch formula and FLUKA simulations

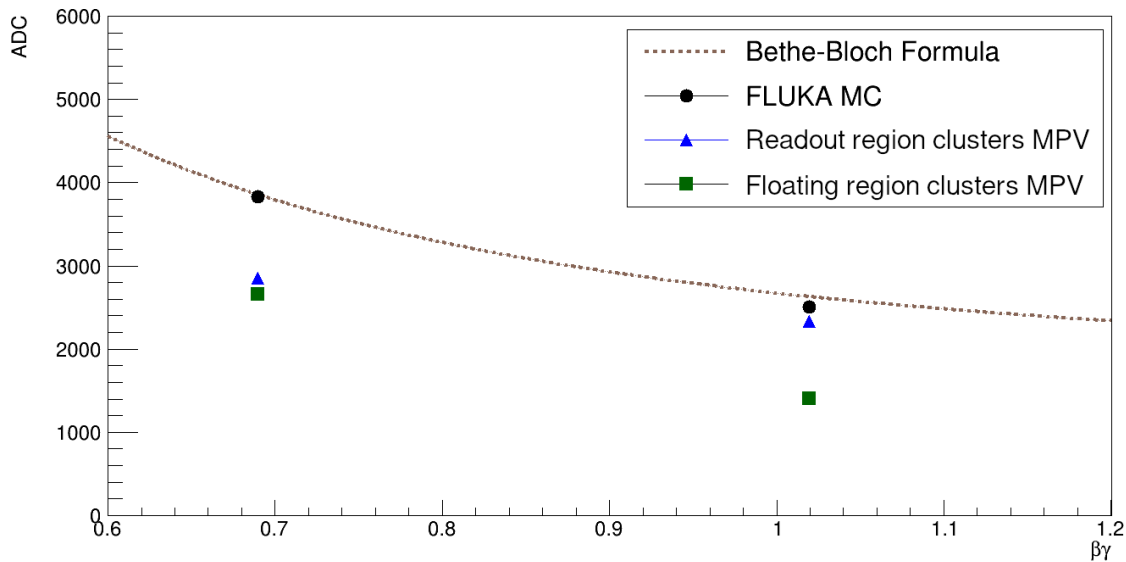


Figure (5.31) – Response of the detector to Oxygen ions compared with the Bethe-Bloch formula and FLUKA simulations

Further studies are planned in the future to analyse the anomalous behaviour found with heavy ions, using a laser-focused optical system, dedicated SPICE simulations of the electrical behaviour of the detector and data campaigns with different particles.

## 5.4 Computation of alignment parameters

After establishing the behavior of all the detectors the following step is the computation of their alignment parameters that are needed for the correct computation of the spatial resolution performance of the detectors.

Mechanical assembly of the detectors pairs in a single system only allows for a millimetre precision in the relative alignment of the different sensors pairs. Moreover, the assembly of the two single detectors in a single pair can introduce additional misalignment.

Under the assumption that

- Each detector can have a shift in the X (Y) direction and a rotation around the Z axis
- The offset and rotation lay both in the XY plane

correlation of hit positions for all pair of ladders is enough to extract alignment constants, as illustrated in figure 5.32.

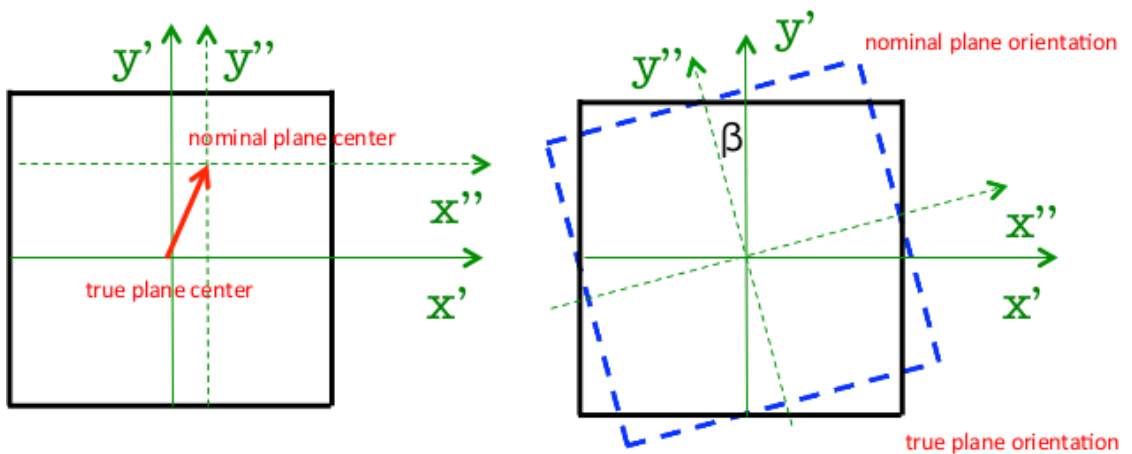


Figure (5.32) – Effects of rigid shifts and rotations

In particular, rigid shifts in the X (Y) direction can be simply evaluated using the average value of the hit occupancy distribution. Correlation between position in two adjacent planes can then be used to extract rotation parameters.

The first step is to determine the distribution of events for each X and Y view of each detector. Using the mean value of this distribution, the displacement to be applied to the detector in each direction can be determined.

This method, which is simple to implement, makes it possible to carry out an initial rough alignment, which will then be perfected with subsequent procedures.

Figure 5.4 shows an example of such a distribution for the first detector to be used as reference in the alignment procedure in one of the coordinates in which the reconstructed beam profile is clearly not centered on the detector sensitive area.

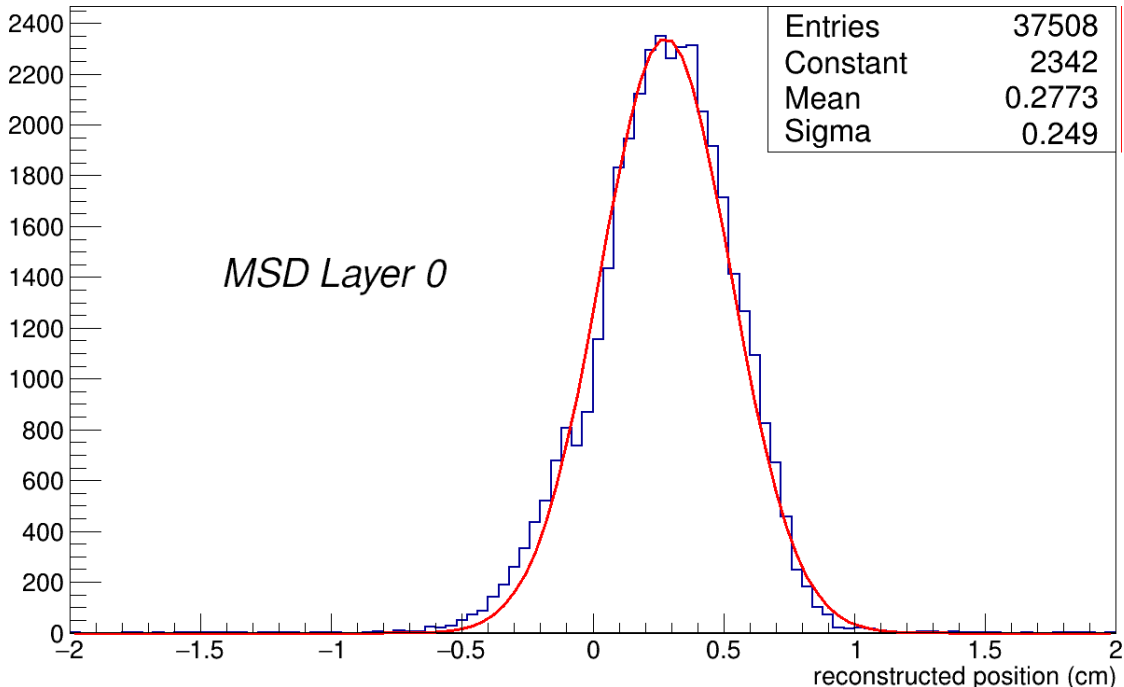
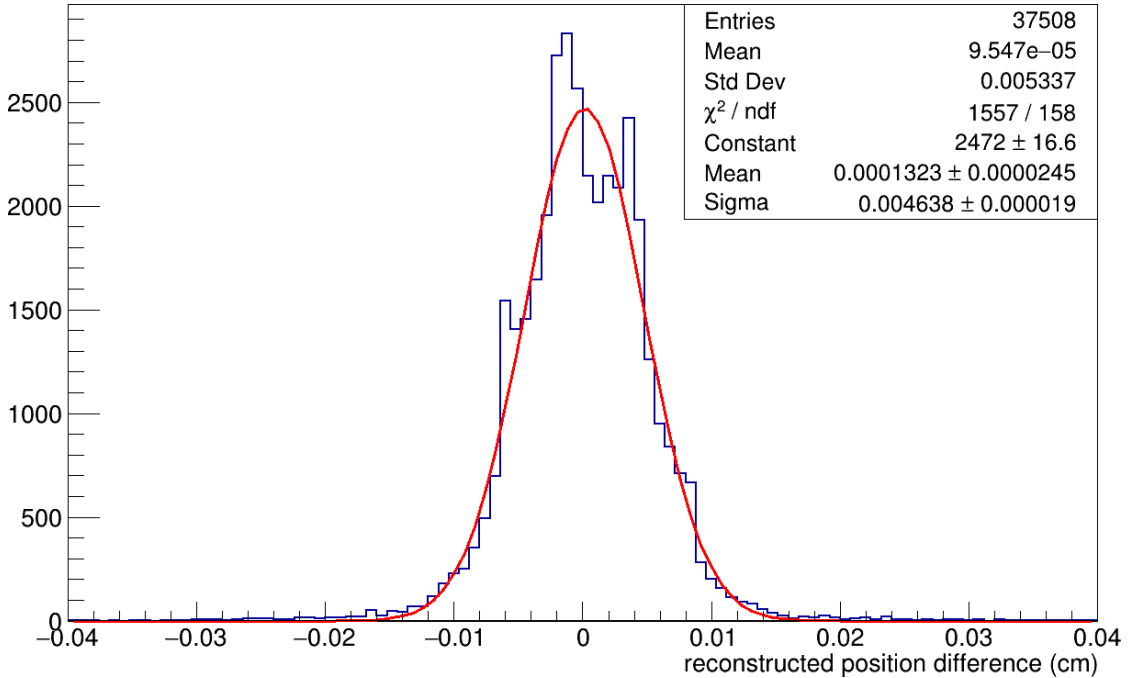


Figure (5.33) – Reconstructed beam profile on the first detector (to be used as reference in the alignment)

Once the previous step has been carried out, a relative alignment between the various layers is performed using the difference in the reconstructed position of the hits between each pair of detectors measuring the same coordinate (figure 5.4). Each coordinate is treated independently in this step.

This method, as well as providing further information about the shifts, compared to the zero-order approximation performed earlier, can also be used to determine any rotations between planes.

In the case in which one of the detectors involved in the computation of the hits position difference is rotated, the average value of the distribution of these differences will be, in absolute value, higher than in the case in which only planes with rigid shifts and no relative rotation are involved.



**Figure (5.34)** – Difference in reconstructed beam profile of the first detector with another one measuring the same coordinate

The final iterative step consists in performing a bias fit of the hits measured by the tracker: rather than using a straight line in the three spatial dimensions, it is preferable to consider two independent tracks in the XZ and YZ planes respectively.

The measurement of the fit parameters of the line is not performed numerically, but analytically with the *ordinary least squares estimation* method[99]: writing the functional form of the variable  $y = y(x)$ , considering a number of parameters  $\theta_i$  equal to k

$$y(x) = \theta_1 h_1(x) + \theta_2 h_2(x) + \cdots + \theta_k h_k(x) \quad (5.3)$$

with the assumption that the functions  $h_i$  are known, distinguishable (i.e. none of the  $h_i$  are linear combinations of the others), single-valued throughout the domain of the independent variable  $x$  and that  $y(x)$  is linear in the parameters  $\theta_i$  and not in  $x$  itself.

In the case of a straight line fit, the functional form can be reduced to

$$y = f(x) = ax + b \quad (5.4)$$

where  $a$  and  $b$  are the parameters to determine and the independent variable  $x$  represents the distance  $z$  of one of the detectors along the beam axis. It is then possible to define the  $\chi^2$  function as

$$\chi^2 = \sum_{i=1}^n \frac{(y_i - ax_i - b)^2}{\sigma_i^2} \quad (5.5)$$

where  $\sigma_i$  is the standard deviation associated with the variables  $y_i(x)$ , assumed to be normally distributed and in the case under study represent the spatial resolutions of the detectors

Performing the partial derivatives of equation 5.5 with respect to  $a$  and  $b$ , and imposing a minimum condition for the variable  $\chi^2$

$$\begin{aligned} \frac{\partial \chi^2}{\partial a} &= -2 \sum_{i=1}^n \frac{(y_i - ax_i - b)x_i}{\sigma_i^2} = 0 \\ \frac{\partial \chi^2}{\partial b} &= -2 \sum_{i=1}^n \frac{(y_i - ax_i - b)}{\sigma_i^2} = 0 \end{aligned} \quad (5.6)$$

and defining the following terms

$$\begin{aligned} A &= \sum_{i=1}^n \frac{x_i}{\sigma_i^2} & B &= \sum_{i=1}^n \frac{1}{\sigma_i^2} & C &= \sum_{i=1}^n \frac{y_i}{\sigma_i^2} \\ D &= \sum_{i=1}^n \frac{x_i^2}{\sigma_i^2} & E &= \sum_{i=1}^n \frac{x_i y_i}{\sigma_i^2} & F &= \sum_{i=1}^n \frac{y_i^2}{\sigma_i^2} \end{aligned} \quad (5.7)$$

equations 5.6 become

$$\begin{aligned} 2(-E + aD + bA) &= 0 \\ 2(-C + aA + bB) &= 0 \end{aligned} \quad (5.8)$$

from which it's possible to obtain the fit parameter estimators

$$\begin{aligned} \hat{a} &= \frac{EB - CA}{DB - A^2} \\ \hat{b} &= \frac{DC - EA}{DB - A^2} \end{aligned} \quad (5.9)$$

It can be proven that the obtained estimators are indeed *unbiased* (that is, the estimator's expected value and the true value of the parameter being estimated are equal) and do not depend explicitly from  $\sigma_i$ .

Once the fit has been made, the distributions of the residuals can be constructed, for each plane and for each view, in order to obtain information on the entity of the shift to be made.

Defining the position of the track on the silicon ladder as *IP*, residuals can be evaluated as  $\text{res} = \text{IP} - \text{cog}$ , where *cog* is the center of gravity of the cluster (see figure 5.35).

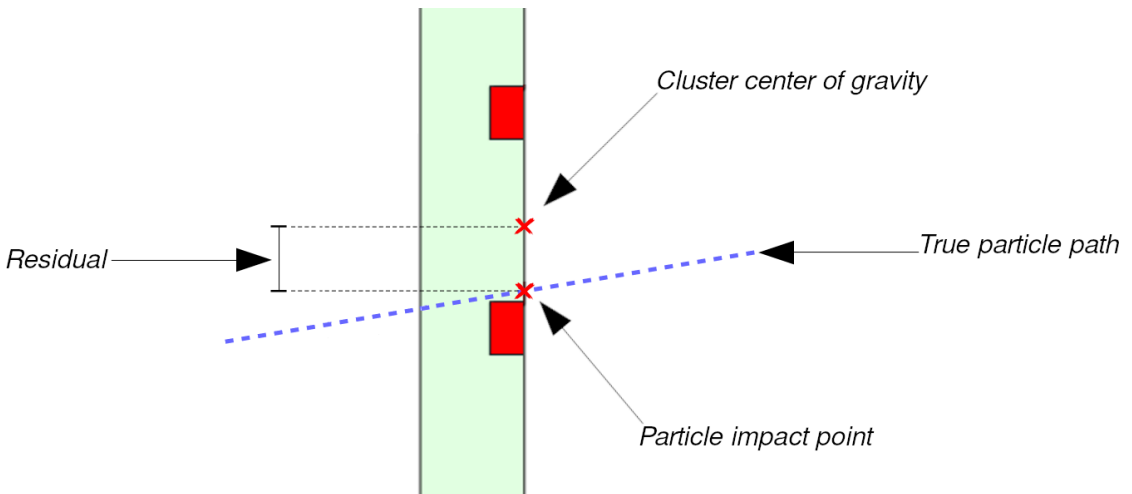


*Figure (5.35) – Track residual working principle*

Simultaneously to the measurement of the rigid displacements, the rotation angles of the planes must also be evaluated; to do this, a TProfile is created to display the mean value of Y and its error for each bin in X, which when fitted with a first-order polynomial provides the rotation angle.

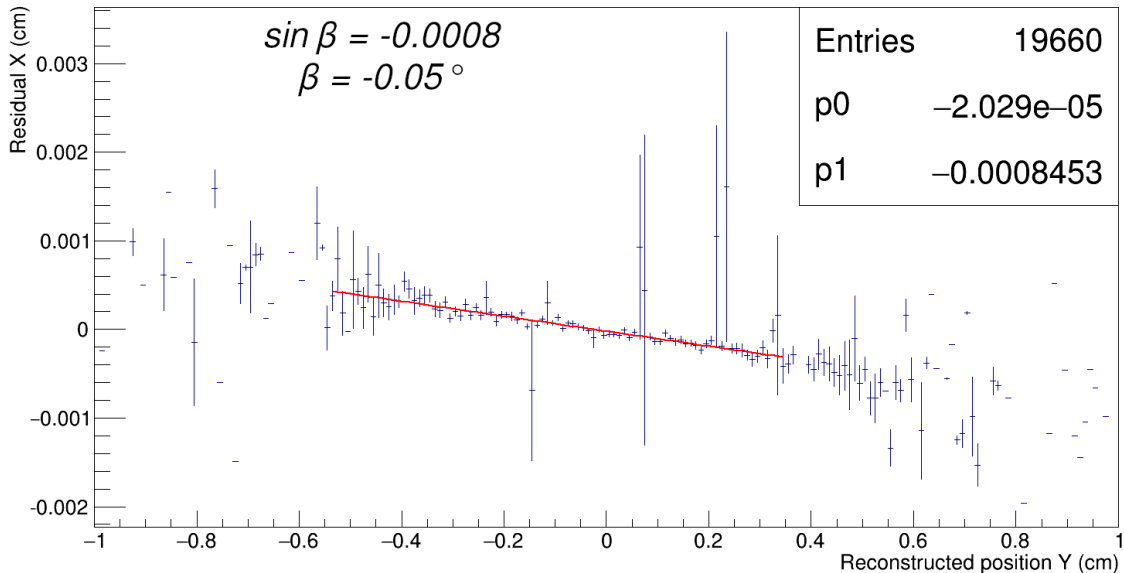


**Figure (5.36)** – TProfile of the reconstructed position in the X coordinate versus the track residual in the Y coordinate for the first pair of detectors

Figure 5.4 shows the TProfile of the reconstructed position in the X coordinate versus the track residual in the Y coordinate for the first pair of detectors before the start of the iterative alignment procedure.

The relative angular misalignment of the two detectors measuring the XY coordinates in the first tracking station gives rise to an evident dependence of the track residual value in one coordinate with the reconstructed position in the other coordinate.

The iterative procedure is thus performed on a reduced data sample for each configuration with the request that each event contains exactly one reconstructed hit in each detector.

This, combined with the use of the highest energy available at each data taking, reduces the potential errors in the computation of the alignment parameters due to track mismatches (where the biased track is performed with a reconstructed hit that

does not correspond to a real particle) and the effect of Multiple Coulomb Scattering.

The number of iterations used is of the order of some hundreds, and convergence is observed for all the parameters. Shifts and rotations of all planes are carried out simultaneously only if the absolute value of both operations is greater (within one sigma) than the relative experimental error, since it would not make sense to shift and rotate below this limit.

## 5.5 Spatial resolution of the detectors

The spatial resolution of the detector is a fundamental parameter for the tracker system which tells how good the position measurements made with the system can be.

As a starting assumption, the resolution should be independent of the detector considered, as all of them are by construction equal and are independently read in the same manner.

Ignoring this hypothesis, however, the measurement of this parameter is performed for all the detectors under test. For the resolution measurement, only events with all hits on all planes and all views will be used, for the same reasons as previously explained for the alignment iterative procedure.

The first step is to measure the distribution of the unbiased residuals for each of the  $n$  detectors: this is evaluated by not including the  $i$ -th plane in the fit, i.e. by only performing a  $(n-1)$ -point fit.

This distribution should be wider than the one obtained through a  $n$ -point fit, because, by not including the  $i$ -th point, the line interpolating the points will no longer be constrained to pass near the point itself.

The unbiased distribution of the residuals is then a convolution of two different distributions, one due to the same intrinsic resolution of the detector and the other due to the errors of the linear fit

$$\sigma_{res}^2 = \sigma^2 + \sigma_{fit}^2 \quad (5.10)$$

where  $\sigma_{res}^2$  indicates the standard deviation of the total distribution of residuals,  $\sigma$

the contribution of the pure residuals (and thus the resolution we are looking for) and  $\sigma_{fit}$  is the contribution due to the linear fit.

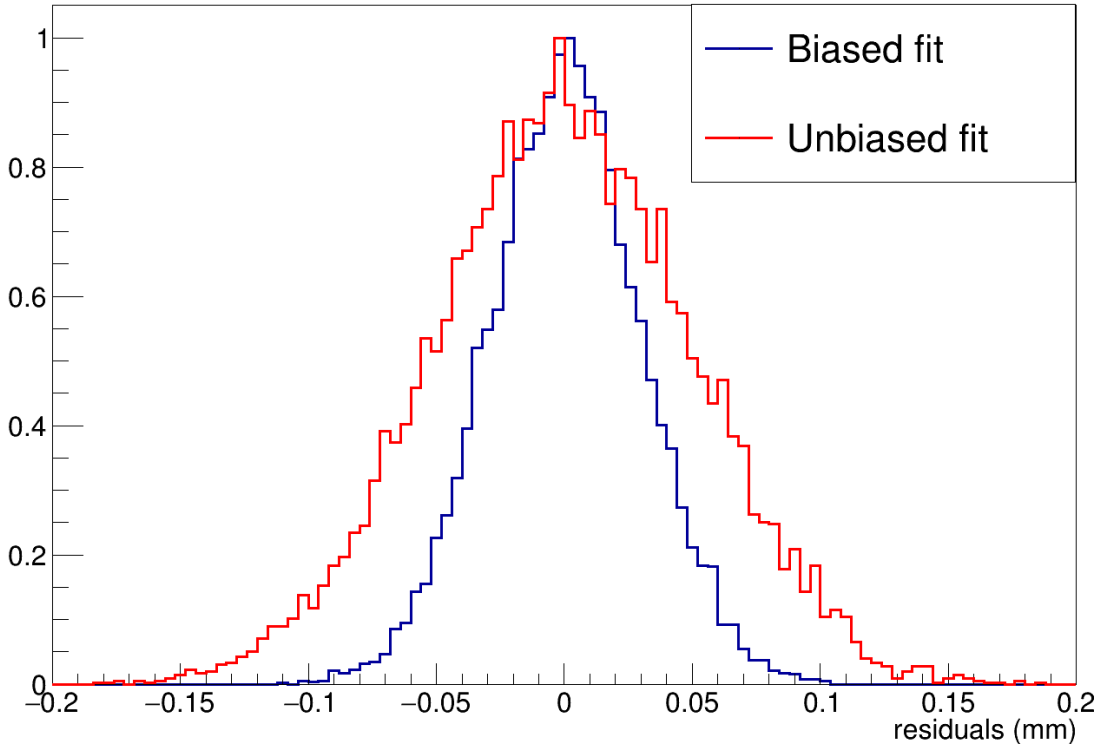


*Figure (5.37) – Effect of biased and unbiased linear fit for the calculation of track residuals*

The equation can be factored by taking into account that the parameters of the track, the intercept and the angular coefficient, are not independent of each other.

Considering that the covariance matrix for the linear fit parameters

$$U = \frac{\sigma^2}{N(\bar{z}^2 - \bar{z}^2)} \begin{pmatrix} \bar{z}^2 & -\bar{z} \\ -z & 1 \end{pmatrix} \quad (5.11)$$

and that the variance on the measure of a point for the straight line fit is equal to

$$\sigma_{int}^2 = U_{00} + z^2 U_{11} + 2z U_{01} \quad (5.12)$$

where  $z$  denotes the distance of a detector along the beam axis,  $\bar{z}$  is the mean of the distances of the detectors and  $\bar{z}^2$  the mean of their squares.

It is possible to factor equation 5.10 in the following way

$$\sigma_{res}^2 = \sigma^2 \left[ 1 + \frac{1}{N(\bar{z}^2 - \bar{z}^2)} (\bar{z}^2 + z^2 - 2\bar{z}z) \right] = \alpha \sigma^2 \quad (5.13)$$

From which the resolution of a detector at a certain distance  $z$  can be simply obtained from the residual distribution as  $\sigma = \sigma_{res}/\sqrt{\alpha}$ .

Figure 5.38 shows the results for the spatial resolutions computed for the different experimental setups described in section 5.1: the values obtained are to be compared to the expected resolution for a digital readout of the detector, namely

$$\sigma \approx \frac{\text{readout pitch}}{\sqrt{12}} \approx 43\mu\text{m} \quad (5.14)$$

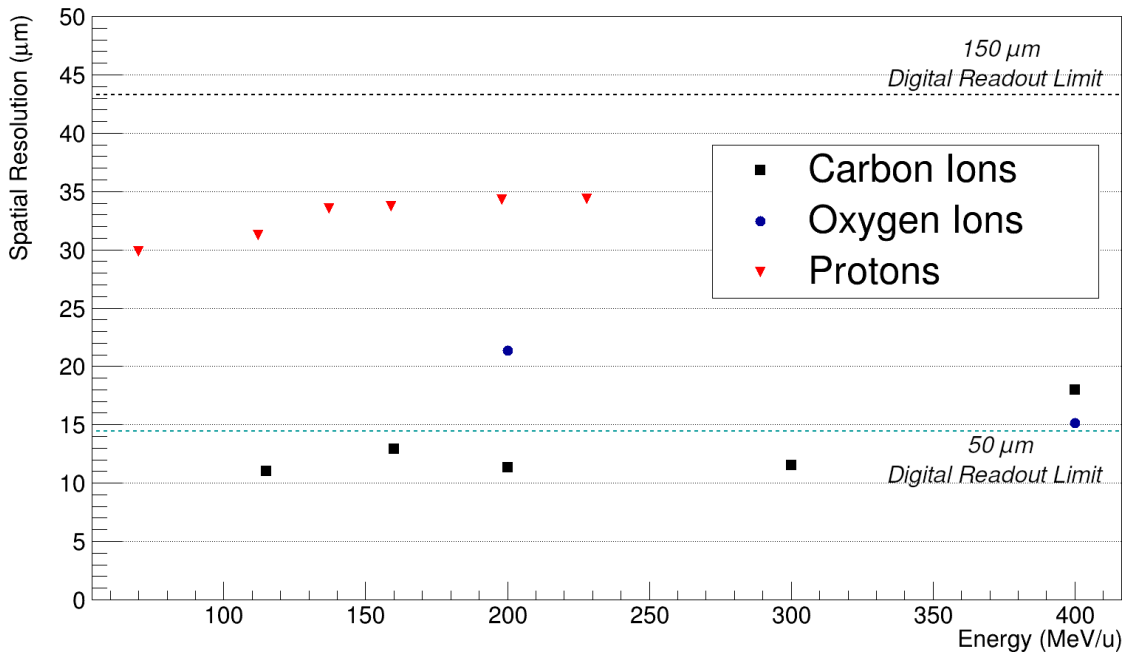


**Figure (5.38)** – Computed spatial resolutions from experimental data and comparison with digital readout limits for 150  $\mu\text{m}$  and 50  $\mu\text{m}$

In the case of data from protons, were the mean cluster width is slightly less than 2

strips, the improvement over the digital readout is small, while still indicating that the detector performs within the required specs of the experiment.

Conversely, for data taken with Carbon and Oxygen ions, where the mean cluster width is much higher, the improvement is significant, with a resolution value that is closer to the value expected for a  $50\mu m$  readout pitch, thanks to the presence of the floating strips and the much higher Signal to Noise ratio obtained.



# CHAPTER 6

---

## Conclusions

---

The FOOT (FragmentatiOn Of Target) experiment is designed to measure the differential cross sections ( $d^2\sigma/d\Omega dE$ ) of fragments produced in nuclear interactions relevant both for particle therapy applications, where the current state of the art shows a lack of experimental data required to improve the treatment planning systems both in proton-therapy and heavy ion therapy, and in the framework of space radioprotection, where data on nuclear interactions can be used to optimize the shielding of the spaceship for long term space missions.

The work presented in this thesis focuses on the studies needed to define the development first of the prototypes and then of the final sensors to be used for the *Microstrip Silicon Detector* (MSD), which constitutes the last station of the tracking and one of the two systems to measure the  $dE/dx$  of the fragments.

In particular, several tests were carried out in the laboratory and on particle beams at accelerators for Hadrontherapy in Italy, such as the synchrotron at the *Centro Nazionale di Adroterapia Oncologica* (CNAO) in Pavia and the proton accelerator at the *Protontherapy Centre* in Trento.

The first part of the work was dedicated to the study of the performance in terms

of noise and dynamic range of the readout electronics that would have been then used for the final detectors, with various tests carried out both in the laboratory and at the accelerators, to study the performance of the new IDE1140 ASIC production by Ideas to compare them with the version previously used in other experiments.

The tests focused above all on the study of the response in terms of signal at different energies and angles of the incident beam for an evaluation of the dynamic range in view of the construction of the final detector.

The development work then continued with the construction of the first prototype of a thin  $150\mu m$  sensor, whose correct operation in terms of noise and leakage current was verified in the laboratory, and was then subjected to characterisation work with ionising and photon sources in the laboratory, which was then integrated with test campaigns at accelerators.

At the same time, the development of the software dedicated to reading and analysis continued in order to adapt it to the requirements of the new readout electronics, also in anticipation of the use of the final Data Acquisition system planned for the experiment.

A study was then carried out on the construction of a power supply system to achieve the reverse polarization of the detectors needed for their operation: the performance in terms of stability and noise of different power supply systems was evaluated, and a system consisting of a chip produced by CAEN that could be integrated into the ADC boards of the MSD system was then chosen. The remote control and monitoring of this system was also designed using an Arduino system and its performance were verified.

The second part of the work focused mainly on completing the construction and characterisation of the complete Microstrip Silicon Detector system.

The sensors produced were tested throughout the production chain first in the laboratory, similarly to the first prototype, to ensure their operation and performance in terms of noise/signal. When possible, further tests were carried out at the accelerators to test the operation of the complete setup that will be used by the FOOT experiment: this involved verifying the operation not only of the individual sensor, but also of the acquisition chain which, unlike the prototype, uses more performance electronics designed and developed in Perugia.

The complete setup was then integrated into the central DAQ system of the FOOT

---

experiment thanks to the collaboration with the Bologna group responsible for the global DAQ during a first joint data acquisition at the accelerator of the *Centro di Protonterapia* of Trento in June 2021. This allowed a verification of the proper functioning of the acquisition system and a first characterization of the response of the proton detectors of interest for the FOOT experiment.

The success of the construction from the point of view of performance and integration with the rest of the experiment have allowed to perform the first official data acquisition of the FOOT experiment at the accelerator of the *GSI Helmholtz Centre for Heavy Ion Research* in Darmstadt in July 2021.

A final test has been carried out at the *Centro Nazionale di Adroterapia Oncologica* (CNAO) in Pavia. The data acquired in these last two campaigns allowed the characterisation of the response of the detectors to heavy charged particles such as Carbon and Oxygen in terms of noise performance, signal, cluster characteristics and spatial resolution.

In parallel to the hardware work and to the analysis of the data acquired during the various tests, the collaboration with the software development group of the experiment has allowed the integration of the MSD system in the simulation and reconstruction framework that will be used by the entire collaboration for the joint analysis of the data acquired during the summer and for future data taking at the accelerators in Italy and Europe.

Further improvements for both online and offline software will be possible starting from the groundwork performed in this thesis, namely the complete understanding of the electronic saturation effects for the highest energy deposits in the detectors and the  $\eta$  corrections for the spatial and energy resolutions.

Nonetheless, the MSD system has been fully constructed and shows excellent preliminary performance in terms of noise and tracking capabilities that are well within the requirements of the FOOT experiment.



---

## Bibliography

---

- [1] H. Sung et al. "Global Cancer Statistics 2020: GLOBOCAN Estimates of Incidence and Mortality Worldwide for 36 Cancers in 185 Countries". CA: A Cancer Journal for Clinicians 71.3 (2021), pp. 209–249. doi: <https://doi.org/10.3322/caac.21660>.
- [2] E. M. Ferlay J et al. "Global Cancer Observatory: Cancer Today. Lyon, France: International Agency for Research on Cancer". Available from: <https://gco.iarc.fr/today>. Accessed [03 August 2021]. 2020.
- [3] P. G. Corrie. "Cytotoxic chemotherapy: clinical aspects". Medicine 36.1 (2008). Oncology, pp. 24–28. issn: 1357-3039. doi: <https://doi.org/10.1016/j.mpmed.2007.10.012>.
- [4] R. R. Wilson. "Radiological Use of Fast Protons". Radiology 47.5 (1946). doi: 10.1148/47.5.487.
- [5] "Dose Depth Curves". Available from [https://commons.wikimedia.org/wiki/File:Dose\\_Depth\\_Curves.svg](https://commons.wikimedia.org/wiki/File:Dose_Depth_Curves.svg). Accessed [22 June 2022].
- [6] P. Zyla et al. "Review of Particle Physics". PTEP 2020.8 (2020), p. 083C01. doi: 10.1093/ptep/ptaa104.
- [7] M. Würl et al. "Dosimetric impact of the low-dose envelope of scanned proton beams at a ProBeam facility: comparison of measurements with TPS and MC calculations". IOP Publishing 61.2 (Jan. 2016), pp. 958–973. doi: 10.1088/0031-9155/61/2/958.

- [8] N. Bohr. "The Penetration of Atomic Particles Through Matter". Det Kgl. Danake videnskabernes selskab. Mathematick-fysiske meddelelser, XVIII 8. Hafner Publishing Company, 1948.
- [9] B. M.J. et al. "ESTAR, PSTAR, and ASTAR: Computer Programs for Calculating Stopping-Power and Range Tables for Electrons, Protons, and Helium Ions (version 1.2.3). Available from: <http://physics.nist.gov/Star>. Accessed [25 October 2021].
- [10] R. Serber. "Nuclear Reactions at High Energies". Phys. Rev. 72 (11 Dec. 1947), pp. 1114–1115. doi: [10.1103/PhysRev.72.1114](https://doi.org/10.1103/PhysRev.72.1114).
- [11] K. Gunzert-Marx et al. "Secondary beam fragments produced by 200 MeV  $\mu$ - $^{112}\text{C}$  ions in water and their dose contributions in carbon ion radiotherapy". 10.7 (July 2008), p. 075003. doi: [10.1088/1367-2630/10/7/075003](https://doi.org/10.1088/1367-2630/10/7/075003).
- [12] F. Tommasino and M. Durante. "Proton Radiobiology". Cancers 7.1 (2015), pp. 353–381. doi: [10.3390/cancers7010353](https://doi.org/10.3390/cancers7010353).
- [13] D. Richter. "Treatment planning for tumors with residual motion in scanned ion beam therapy". PhD thesis. Darmstadt: Technische Universität, July 2012.
- [14] M. W. Charles. "ICRP Publication 103: Recommendations of the ICRP". Radiation Protection Dosimetry 129.4 (May 2008), pp. 500–507. issn: 0144-8420. doi: [10.1093/rpd/ncn187](https://doi.org/10.1093/rpd/ncn187).
- [15] "Tumor therapy with heavy charged particles". Progress in Particle and Nuclear Physics 45 (2000), S473–S544. issn: 0146-6410. doi: [https://doi.org/10.1016/S0146-6410\(00\)00112-5](https://doi.org/10.1016/S0146-6410(00)00112-5).
- [16] "Prescribing, Recording, and Reporting Proton-Beam Therapy". 7.2 (Dec. 2007), pp. 1–8. doi: [10.1093/jicru\\_ndm021](https://doi.org/10.1093/jicru_ndm021).
- [17] W. Chu and W. T. "Overview of Light-Ion Beam Therapy". LBNL (Jan. 2006).
- [18] N. Nishida et al. "Angiogenesis in cancer". 2.3 (Aug. 2006), pp. 213–219. doi: [10.2147/vhrm.2006.2.3.213](https://doi.org/10.2147/vhrm.2006.2.3.213).
- [19] R. H. Thomlinson and L. H. Gray. "The Histological Structure of Some Human Lung Cancers and the Possible Implications for Radiotherapy". 9.4 (Dec. 1955), pp. 539–549. doi: [10.1038/bjc.1955.55](https://doi.org/10.1038/bjc.1955.55).

- [20] Y. Furusawa et al. "Inactivation of Aerobic and Hypoxic Cells from Three Different Cell Lines by Accelerated  $^3\text{He}$ -,  $^{12}\text{C}$ - and  $^{20}\text{Ne}$ -Ion Beams". *Radiation Research* 154.5 (2000), pp. 485–496. doi: [10.1667/0033-7587\(2000\)154\[0485:IOAAHC\]2.0.CO;2](https://doi.org/10.1667/0033-7587(2000)154[0485:IOAAHC]2.0.CO;2).
- [21] L. H. Gray et al. "The Concentration of Oxygen Dissolved in Tissues at the Time of Irradiation as a Factor in Radiotherapy". *26.312* (Dec. 1953), pp. 638–648. doi: [10.1259/0007-1285-26-312-638](https://doi.org/10.1259/0007-1285-26-312-638).
- [22] D. J. Indelicato et al. "Consensus Report From the Stockholm Pediatric Proton Therapy Conference". *96.2* (Oct. 2016), pp. 387–392. doi: [10.1016/j.ijrobp.2016.06.2446](https://doi.org/10.1016/j.ijrobp.2016.06.2446).
- [23] E. V. Bellinzona et al. "Biological Impact of Target Fragments on Proton Treatment Plans: An Analysis Based on the Current Cross-Section Data and a Full Mixed Field Approach". *Cancers* 13.19 (2021). issn: 2072-6694. doi: [10.3390/cancers13194768](https://doi.org/10.3390/cancers13194768).
- [24] C. Zeitlin and C. La Tessa. "The Role of Nuclear Fragmentation in Particle Therapy and Space Radiation Protection". *Frontiers in Oncology* 6 (2016). issn: 2234-943X. doi: [10.3389/fonc.2016.00065](https://doi.org/10.3389/fonc.2016.00065).
- [25] W. R. Webber, J. C. Kish, and D. A. Schrier. "Total charge and mass changing cross sections of relativistic nuclei in hydrogen, helium, and carbon targets". *Phys. Rev. C* 41 (2 Feb. 1990), pp. 520–532. doi: [10.1103/PhysRevC.41.520](https://doi.org/10.1103/PhysRevC.41.520).
- [26] J. Dudouet et al. "Double-differential fragmentation cross-section measurements of 95 MeV/nucleon  $^{12}\text{C}$  beams on thin targets for hadron therapy". *Phys. Rev. C* 88 (2 Aug. 2013), p. 024606. doi: [10.1103/PhysRevC.88.024606](https://doi.org/10.1103/PhysRevC.88.024606).
- [27] M. Toppi et al. "Measurement of fragmentation cross sections of  $^{12}\text{C}$  ions on a thin gold target with the FIRST apparatus". *Phys. Rev. C* 93 (6 June 2016), p. 064601. doi: [10.1103/PhysRevC.93.064601](https://doi.org/10.1103/PhysRevC.93.064601).
- [28] G. Battistoni et al. "Overview of the FLUKA code". *Annals of Nuclear Energy* 82 (2015). Joint International Conference on Supercomputing in Nuclear Applications and Monte Carlo 2013, SNA + MC 2013. Pluri- and Trans-disciplinarity, Towards New Modeling and Numerical Simulation Paradigms, pp. 10–18. issn: 0306-4549. doi: <https://doi.org/10.1016/j.anucene.2014.11.007>.

- [29] T. Böhlen et al. “*The FLUKA Code: Developments and Challenges for High Energy and Medical Applications*”. Nuclear Data Sheets 120 (2014), pp. 211–214. issn: 0090-3752. doi: <https://doi.org/10.1016/j.nds.2014.07.049>.
- [30] G. Battistoni et al. “*The FLUKA Code: An Accurate Simulation Tool for Particle Therapy*”. Frontiers in Oncology 6 (2016), p. 116. issn: 2234-943X. doi: [10.3389/fonc.2016.00116](https://doi.org/10.3389/fonc.2016.00116).
- [31] G. Battistoni et al. “*Measuring the Impact of Nuclear Interaction in Particle Therapy and in Radio Protection in Space: the FOOT Experiment*”. Frontiers in Physics 8 (2021), p. 555. issn: 2296-424X. doi: [10.3389/fphy.2020.568242](https://doi.org/10.3389/fphy.2020.568242).
- [32] A. e. a. Alexandrov. "FOOT CDR V3-1. Sept. 2018. doi: [10.13140/RG.2.2.35295.30883](https://doi.org/10.13140/RG.2.2.35295.30883).
- [33] V. Vlachoudis. “*FLAIR: a Powerful but User Friendly Graphical Interface for Fluka*”. Apr. 2009.
- [34] A. S. D. (AdvanSiD). NUV SiPMs Chip Scale Package. Available from: <https://advansid.com/products/product-detail/asd-rgb-nuv-3s-p>. Accessed [27 October 2021].
- [35] G. Traini et al. “*Performance of the ToF detectors in the FOOT experiment*”. FATA 2019. Acireale, Italy, Sept. 2019. doi: [10.1393/ncc/i2020-20016-5](https://doi.org/10.1393/ncc/i2020-20016-5).
- [36] L. Galli et al. “*WaveDAQ: An highly integrated trigger and data acquisition system*”. Nucl. Instrum. Meth. A 936 (2019). Ed. by G. Batignani et al., pp. 399–400. doi: [10.1016/j.nima.2018.07.067](https://doi.org/10.1016/j.nima.2018.07.067).
- [37] Z. Abou-Haidar et al. “*Performance of upstream interaction region detectors for the FIRST experiment at GSI*”. 7.02 (Feb. 2012), P02006–P02006. doi: [10.1088/1748-0221/7/02/p02006](https://doi.org/10.1088/1748-0221/7/02/p02006).
- [38] Y. Dong et al. “*The Drift Chamber detector of the FOOT experiment: Performance analysis and external calibration*”. Nuclear Instruments and Methods in Physics Research Section A: Accelerators, Spectrometers, Detectors and Associated Equipment 986 (2021), p. 164756. issn: 0168-9002. doi: <https://doi.org/10.1016/j.nima.2020.164756>.
- [39] I. Valin et al. “*A reticle size CMOS pixel sensor dedicated to the STAR HFT*”. 7.01 (Jan. 2012), pp. C01102–C01102. doi: [10.1088/1748-0221/7/01/c01102](https://doi.org/10.1088/1748-0221/7/01/c01102).

- [40] G. Contin et al. "The STAR Heavy Flavor Tracker (HFT): focus on the MAPS based PXL detector". Nucl. Part. Phys. Proc. 273-275 (2016). Ed. by M. Aguilar-Benítez et al., pp. 1155–1159. doi: [10.1016/j.nuclphysbps.2015.09.181](https://doi.org/10.1016/j.nuclphysbps.2015.09.181).
- [41] "terasIC DE10-Standard Cyclone V FPGA board". Available from: <https://www.terasic.com/cgi-bin/page.pl?CategoryNo=167&No=1081>. Accessed [29 October 2021].
- [42] N. Simos et al. "Demagnetization of Nd<sub>2</sub>Fe<sub>14</sub>B, Pr<sub>2</sub>Fe<sub>14</sub>B, and Sm<sub>2</sub>Co<sub>17</sub> Permanent Magnets in Spallation Irradiation Fields". IEEE Trans. Magnetics 54.5 (2018), pp. 1–10. doi: [10.1109/TMAG.2017.2769040](https://doi.org/10.1109/TMAG.2017.2769040).
- [43] W. de Boer et al. "Measurements with a CMOS pixel sensor in magnetic fields". Nuclear Instruments and Methods in Physics Research Section A: Accelerators, Spectrometers, Detectors and Associated Equipment 487.1 (2002). 3rd International Workshop on Radiation Imaging Detectors, pp. 163–169. issn: 0168-9002. doi: [https://doi.org/10.1016/S0168-9002\(02\)00960-9](https://doi.org/10.1016/S0168-9002(02)00960-9).
- [44] A. Nomerotski et al. "PLUME collaboration: Ultra-light ladders for linear collider vertex detector". Nuclear Instruments and Methods in Physics Research Section A: Accelerators, Spectrometers, Detectors and Associated Equipment 650.1 (2011). International Workshop on Semiconductor Pixel Detectors for Particles and Imaging 2010, pp. 208–212. issn: 0168-9002. doi: <https://doi.org/10.1016/j.nima.2010.12.083>.
- [45] m. Morrochi et al. "Development and characterization of a Δ E-TOF detector prototype for the FOOT experiment". Nuclear Instruments and Methods in Physics Research Section A: Accelerators, Spectrometers, Detectors and Associated Equipment 916 (Oct. 2018). doi: [10.1016/j.nima.2018.09.086](https://doi.org/10.1016/j.nima.2018.09.086).
- [46] E. Ciarrocchi et al. "The ΔE-TOF detector of the FOOT experiment: Experimental tests and Monte Carlo simulations". Nuclear Instruments and Methods in Physics Research Section A: Accelerators, Spectrometers, Detectors and Associated Equipment 936 (2019). Frontier Detectors for Frontier Physics: 14th Pisa Meeting on Advanced Detectors, pp. 78–79. issn: 0168-9002. doi: <https://doi.org/10.1016/j.nima.2018.08.117>.

- [47] “*Design and performance of the Calorimeter for the FOOT experiment2020*”. Il Nuovo Cimento C 43.405 (Oct. 2020), pp. 1–7. issn: 03905551, 03905551. doi: 10.1393/ncc/i2020-20123-3.
- [48] “*Design and performance of the Calorimeter for the FOOT experiment*”. Il Nuovo Cimento C 43.405 (Oct. 2020), pp. 1–7. issn: 03905551, 03905551. doi: 10.1393/ncc/i2020-20123-3.
- [49] L. Scavarda. “*The Foot Experiment: Measuring Proton and Light Nuclei Fragmentation Cross Sections up to 700 MeV/A*”. 84.4 (Apr. 2020), pp. 480–484. doi: 10.3103/s1062873820040267.
- [50] “*CAEN V2495 Programmable Logic Unit PLUS*”. Available from: <https://www.caen.it/products/v2495/>. Accessed [29 October 2021].
- [51] “*terasic DE10-Nano Kit Cyclone V FPGA board*”. Available from: <https://www.terasic.com.tw/cgi-bin/page/archive.pl?CategoryNo=167&No=1046>. Accessed [29 October 2021].
- [52] G. D. Lellis et al. “*Measurement of the fragmentation of Carbon nuclei used in hadron-therapy*”. 853.1 (Mar. 2011), pp. 124–134. doi: 10.1016/j.nuclphysa.2011.01.019.
- [53] T. Nakamura et al. “*The OPERA film: New nuclear emulsion for large-scale, high-precision experiments*”. Nuclear Instruments and Methods in Physics Research Section A: Accelerators, Spectrometers, Detectors and Associated Equipment 556 (Jan. 2006), pp. 80–86. doi: 10.1016/j.nima.2005.08.109.
- [54] G. D. Lellis et al. “*Emulsion Cloud Chamber technique to measure the fragmentation of a high-energy carbon beam*”. 2.06 (June 2007), P06004–P06004. doi: 10.1088/1748-0221/2/06/p06004.
- [55] A. Alexandrov et al. “*The Continuous Motion Technique for a New Generation of Scanning Systems*”. 7.1 (Aug. 2017). doi: 10.1038/s41598-017-07869-3.
- [56] G. Galati et al. “*Charge identification of fragments with the emulsion spectrometer of the FOOT experiment*”. Open Physics 19 (July 2021), pp. 383–394. doi: 10.1515/phys-2021-0032.

- [57] N. Agafonova et al. “*Momentum measurement by the multiple Coulomb scattering method in the OPERA lead-emulsion target*”. 14.1 (Jan. 2012), p. 013026. doi: [10.1088/1367-2630/14/1/013026](https://doi.org/10.1088/1367-2630/14/1/013026).
- [58] G. D. Lellis et al. “*Momentum measurement by the angular method in the Emulsion Cloud Chamber*”. Nucl. Instrum. Meth. A 512 (2003), pp. 539–545. doi: [10.1016/S0168-9002\(03\)02016-3](https://doi.org/10.1016/S0168-9002(03)02016-3).
- [59] W. S. Cho et al. “*OPTIMASS: a package for the minimization of kinematic mass functions with constraints*”. Journal of High Energy Physics 2016.1 (Jan. 2016). doi: [10.1007/jhep01\(2016\)026](https://doi.org/10.1007/jhep01(2016)026). url: [https://doi.org/10.1007/jhep01\(2016\)026](https://doi.org/10.1007/jhep01(2016)026).
- [60] L. D. Landau. “*On the energy loss of fast particles by ionization*”. J. Phys. 8 (1944), pp. 201–205.
- [61] S. Meroli, D. Passeri, and L. Servoli. “*Energy loss measurement for charged particles in very thin silicon layers*”. 6.06 (June 2011), P06013–P06013. doi: [10.1088/1748-0221/6/06/p06013](https://doi.org/10.1088/1748-0221/6/06/p06013).
- [62] C. Leroy. “*Silicon Solid State Devices and Radiation Detection*”. Singapore: World Scientific Pub. Co, 2012. isbn: 9789814390040.
- [63] P. V. Vavilov. “*Ionization losses of high-energy heavy particles*”. Sov. Phys. JETP 5 (1957), pp. 749–751.
- [64] D. W. Aitken, W. L. Lakin, and H. R. Zulliger. “*Energy Loss and Straggling in Silicon by High-Energy Electrons, Positive Pions, and Protons*”. Phys. Rev. 179 (2 Mar. 1969), pp. 393–398. doi: [10.1103/PhysRev.179.393](https://doi.org/10.1103/PhysRev.179.393).
- [65] M. Berger et al. XCOM: Photon Cross Section Database (version 1.5). Available from: <https://physics.nist.gov/PhysRefData/Xcom/html/xcom1.html>. Accessed [15 April 2022]. 2010.
- [66] I. Abt et al. “*Characterization of silicon microstrip detectors using an infrared laser system*”. Nuclear Instruments and Methods in Physics Research Section A: Accelerators, Spectrometers, Detectors and Associated Equipment 423.2 (1999), pp. 303–319. issn: 0168-9002. doi: [https://doi.org/10.1016/S0168-9002\(98\)01337-0](https://doi.org/10.1016/S0168-9002(98)01337-0).

- [67] K. W. Böer and U. W. Pohl. Semiconductor Physics. Springer International Publishing, 2020. doi: [10.1007/978-3-319-06540-3](https://doi.org/10.1007/978-3-319-06540-3). url: <https://doi.org/10.1007/978-3-319-06540-3>.
- [68] F. Hartmann. “*Basic Principles of a Silicon Detector*”. Evolution of Silicon Sensor Technology in Particle Physics. Berlin, Heidelberg: Springer Berlin Heidelberg, 2009, pp. 1–96. isbn: 978-3-540-44774-0. doi: [10.1007/978-3-540-44774-0\\_1](https://doi.org/10.1007/978-3-540-44774-0_1).
- [69] R. P. Horisberger. “*Solid state detectors*” (Dec. 1991), 33 p.
- [70] B. Alpat et al. “*The internal alignment and position resolution of the AMS-02 silicon tracker determined with cosmic-ray muons*”. Nuclear Instruments and Methods in Physics Research Section A: Accelerators, Spectrometers, Detectors and Associated Equipment 613.2 (2010), pp. 207–217. issn: 0168-9002. doi: <https://doi.org/10.1016/j.nima.2009.11.065>.
- [71] M. Krammer et al. “*Silicon detectors*”. Institute of High Energy Physics, Vienna, Austria (2011).
- [72] W. Shockley. “*Currents to Conductors Induced by a Moving Point Charge*”. Journal of Applied Physics 9.10 (1938), pp. 635–636. doi: [10.1063/1.1710367](https://doi.org/10.1063/1.1710367).
- [73] S. Ramo. “*Currents Induced by Electron Motion*”. Proceedings of the IRE 27.9 (1939), pp. 584–585. doi: [10.1109/JRPROC.1939.228757](https://doi.org/10.1109/JRPROC.1939.228757).
- [74] U. Fano. “*Ionization Yield of Radiations. II. The Fluctuations of the Number of Ions*”. Phys. Rev. 72 (1 July 1947), pp. 26–29. doi: [10.1103/PhysRev.72.26](https://doi.org/10.1103/PhysRev.72.26).
- [75] J. Palms, P. Venugopala Rao, and R. Wood. “*A Fano factor measurement for silicon using low energy photons*”. Nuclear Instruments and Methods 76.1 (1969), pp. 59–60. issn: 0029-554X. doi: [https://doi.org/10.1016/0029-554X\(69\)90289-4](https://doi.org/10.1016/0029-554X(69)90289-4).
- [76] B. Lowe. “*Measurements of Fano factors in silicon and germanium in the low-energy X-ray region*”. Nuclear Instruments and Methods in Physics Research Section A: Accelerators, Spectrometers, Detectors and Associated Equipment 399.2 (1997), pp. 354–364. issn: 0168-9002. doi: [https://doi.org/10.1016/S0168-9002\(97\)00965-0](https://doi.org/10.1016/S0168-9002(97)00965-0).
- [77] H. Spieler. "Semiconductor detector systems. Oxford New York: Oxford University Press, 2005. isbn: 9780198527848.

- [78] I. D. E. AS. IDE1140. Available from: <https://ideas.no/products/ide1140/>. Accessed [26 September 2020].
- [79] J. Chang et al. “*The DArk Matter Particle Explorer mission*”. Astroparticle Physics 95 (2017), pp. 6–24. issn: 0927-6505. doi: <https://doi.org/10.1016/j.astropartphys.2017.08.005>.
- [80] F. Zhang et al. “*Design of the readout electronics for the DAMPE Silicon Tracker detector*”. Chin. Phys. C 40.11 (2016), p. 116101. doi: [10.1088/1674-1137/40/11/116101](https://doi.org/10.1088/1674-1137/40/11/116101). arXiv: [1606.05080](https://arxiv.org/abs/1606.05080) [physics.ins-det].
- [81] G. Silvestre and FOOT Collaboration. “*Evaluation of double-sided silicon microstrip sensor for the FOOT experiment*”. Nuclear Instruments and Methods in Physics Research Section A: Accelerators, Spectrometers, Detectors and Associated Equipment 936 (Nov. 2018). doi: [10.1016/j.nima.2018.10.190](https://doi.org/10.1016/j.nima.2018.10.190).
- [82] M. Krammer. “*Silicon detectors in High Energy Physics experiments*”. Scholarpedia 10.10 (2015). revision #197033, p. 32486. doi: [10.4249/scholarpedia.32486](https://doi.org/10.4249/scholarpedia.32486).
- [83] F. Cenna et al. “*Weightfield2: A fast simulator for silicon and diamond solid state detector*”. 796 (Oct. 2015), pp. 149–153. doi: [10.1016/j.nima.2015.04.015](https://doi.org/10.1016/j.nima.2015.04.015).
- [84] D. Lietti et al. “*A microstrip silicon telescope for high performance particle tracking*”. Nuclear Instruments and Methods in Physics Research A 729 (Nov. 2013), pp. 527–536. doi: [10.1016/j.nima.2013.07.066](https://doi.org/10.1016/j.nima.2013.07.066).
- [85] G. Landi. “*Properties of the center of gravity as an algorithm for position measurements*”. Nuclear Instruments and Methods in Physics Research Section A: Accelerators, Spectrometers, Detectors and Associated Equipment 485.3 (2002), pp. 698–719. issn: 0168-9002. doi: [https://doi.org/10.1016/S0168-9002\(01\)02071-X](https://doi.org/10.1016/S0168-9002(01)02071-X).
- [86] V. Radeka and R. A. Boie. “*Centroid finding method for position-sensitive detectors*”. Nuclear Instruments and Methods 178.2 (1980), pp. 543–554. issn: 0029-554X. doi: [https://doi.org/10.1016/0029-554X\(80\)90836-8](https://doi.org/10.1016/0029-554X(80)90836-8).
- [87] B. Alpat et al. “*The AMS silicon tracker readout: performance results with minimum ionizing particles*”. Nuclear Instruments and Methods in Physics Research Section A: Accelerators, Spectrometers, Detectors and Associated Equipment 439.1 (2000), pp. 53–64. issn: 0168-9002. doi: [https://doi.org/10.1016/S0168-9002\(99\)00864-5](https://doi.org/10.1016/S0168-9002(99)00864-5).

- [88] P. Azzarello et al. “*The DAMPE silicon–tungsten tracker*”. Nuclear Instruments and Methods in Physics Research Section A: Accelerators, Spectrometers, Detectors and Associated Equipment 831 (2016). Proceedings of the 10th International “Hiroshima” Symposium on the Development and Application of Semiconductor Tracking Detectors, pp. 378–384. ISSN: 0168-9002. doi: <https://doi.org/10.1016/j.nima.2016.02.077>.
- [89] M. de Bruin. “*Glossary of terms used in nuclear analytical chemistry (Provisional)*”. 54.8 (Jan. 1982), pp. 1533–1554. doi: [10.1351/pac198254081533](https://doi.org/10.1351/pac198254081533).
- [90] D. Demir, M. Eroğlu, and A. Turşucu. “*Studying of characteristics of the HPGe detector for radioactivity measurements*”. Journal of Instrumentation 8.10 (Oct. 2013), P10027–P10027. doi: [10.1088/1748-0221/8/10/p10027](https://doi.org/10.1088/1748-0221/8/10/p10027).
- [91] F. Peverini. “*Test prototipi sensore a micro strip di silicio per l'esperimento FOOT*”. MA thesis. Università degli studi di Perugia - Dipartimento di Fisica e Geologia, 2020.
- [92] AD7276. Available from: <https://www.analog.com/en/products/ad7276.html>. Accessed [28 November 2020].
- [93] “A7585D/DU”. Available from: <https://www.caen.it/products/a7585/>. Accessed [30 October 2021].
- [94] *Centro di Prototerapia di Trento*. Available from: <https://prototerapia.provincia.tn.it/>. Accessed [03 January 2022].
- [95] F. Tommasino et al. “*Proton beam characterization in the experimental room of the Trento Proton Therapy facility*”. Nuclear Instruments and Methods in Physics Research Section A: Accelerators, Spectrometers, Detectors and Associated Equipment 869 (2017), pp. 15–20. ISSN: 0168-9002. doi: <https://doi.org/10.1016/j.nima.2017.06.017>. URL: <https://www.sciencedirect.com/science/article/pii/S0168900217306654>.
- [96] *GSI Helmholtzzentrum für Schwerionenforschung*. Available from: [https://www.gsi.de/en/about\\_us](https://www.gsi.de/en/about_us). Accessed [03 January 2022].

- [97] B. Alpat et al. “*Charge determination of nuclei with the AMS-02 silicon tracker*”. Nuclear Instruments and Methods in Physics Research Section A: Accelerators, Spectrometers, Detectors and Associated Equipment 540.1 (2005), pp. 121–130. issn: 0168-9002. doi: <https://doi.org/10.1016/j.nima.2004.11.012>.
- [98] R. Qiao et al. “*Charge reconstruction of the DAMPE Silicon-Tungsten Tracker: A preliminary study with ion beams*”. Nuclear Instruments and Methods in Physics Research Section A: Accelerators, Spectrometers, Detectors and Associated Equipment 886 (2018), pp. 48–52. issn: 0168-9002. doi: <https://doi.org/10.1016/j.nima.2018.01.007>.
- [99] G. Cowan. Statistical Data Analysis. Oxford science publications. Clarendon Press, 1998. isbn: 9780198501558.
- [100] K. Bethge. Medical applications of nuclear physics. Berlin New York: Springer-Verlag, 2004. isbn: 9783540208051.
- [101] J. S. Lilley. Nuclear physics : principles and applications. Chichester New York: J. Wiley, 2001. isbn: 9780471979364.
- [102] G. Tejedor. Radiation damage in biomolecular systems. Springer, 2012. isbn: 9789400725638.
- [103] M. d’Ávila Nunes. Hadron therapy physics and simulations. Springer, 2013. isbn: 9781461488989.
- [104] “*Formulae and Methods in Experimental Data Evaluation With Emphasis on High-energy Physics. Vol. 1: General Glossary, Glossary Group Theory*” (1984). Ed. by R. K. Bock et al.
- [105] D. Schardt, T. Elsässer, and D. Schulz-Ertner. “*Heavy-ion tumor therapy: Physical and radiobiological benefits*”. Rev. Mod. Phys. 82 (1 Feb. 2010), pp. 383–425. doi: [10.1103/RevModPhys.82.383](https://doi.org/10.1103/RevModPhys.82.383).
- [106] F. Rademakers et al. root-project/root: v6.20/04. 2020. doi: [10.5281/ZENODO.3895855](https://doi.org/10.5281/ZENODO.3895855).
- [107] G. Ambrosi. “*The AMS Silicon Tracker readout system: design and performance*”. Nuclear Instruments and Methods in Physics Research Section A: Accelerators, Spectrometers, Detectors and Associated Equipment 435.1 (1999), pp. 215–223. issn: 0168-9002. doi: [https://doi.org/10.1016/S0168-9002\(99\)00587-2](https://doi.org/10.1016/S0168-9002(99)00587-2).

- [108] B. Adeva et al. “*The construction of the L3 experiment*”. Nuclear Instruments and Methods in Physics Research Section A: Accelerators, Spectrometers, Detectors and Associated Equipment 289.1 (1990), pp. 35–102. issn: 0168-9002. doi: [https://doi.org/10.1016/0168-9002\(90\)90250-A](https://doi.org/10.1016/0168-9002(90)90250-A).
- [109] *Centro Nazionale di Adroterapia Oncologica*. Available from: <https://fondazionecnao.it/>. Accessed [03 January 2022].
- [110] D. J. Indelicato et al. “*Consensus Report From the Stockholm Pediatric Proton Therapy Conference*”. 96.2 (Oct. 2016), pp. 387–392. doi: [10.1016/j.ijrobp.2016.06.2446](https://doi.org/10.1016/j.ijrobp.2016.06.2446). url: <https://doi.org/10.1016/j.ijrobp.2016.06.2446>.
- [111] R. Turchetta. “*Spatial resolution of silicon microstrip detectors*”. Nuclear Instruments and Methods in Physics Research Section A: Accelerators, Spectrometers, Detectors and Associated Equipment 335.1 (1993), pp. 44–58. issn: 0168-9002. doi: [https://doi.org/10.1016/0168-9002\(93\)90255-G](https://doi.org/10.1016/0168-9002(93)90255-G).
- [112] I. Thorlabs. Cube-Mounted Pellicle Beamsplitters. Available from: [https://www.thorlabs.com/newgroupage9.cfm?objectgroup\\_id=4138](https://www.thorlabs.com/newgroupage9.cfm?objectgroup_id=4138). Accessed [04 March 2022].
- [113] J. Buck. Fundamentals of optical fibers. Hoboken, N.J: John Wiley & Sons, 2004. isbn: 978-0-471-22191-3.
- [114] W. Demtröder. Laser spectroscopy. Berlin: Springer, 2016. isbn: 978-3-662-49542-1.
- [115] M. A. Green. “*Self-consistent optical parameters of intrinsic silicon at 300K including temperature coefficients*”. Solar Energy Materials and Solar Cells 92.11 (2008), pp. 1305–1310. issn: 0927-0248. doi: <https://doi.org/10.1016/j.solmat.2008.06.009>.